Pulse-Sequence Approaches for Multidimensional Electronic Spectroscopy of Ultrafast Photochemistry

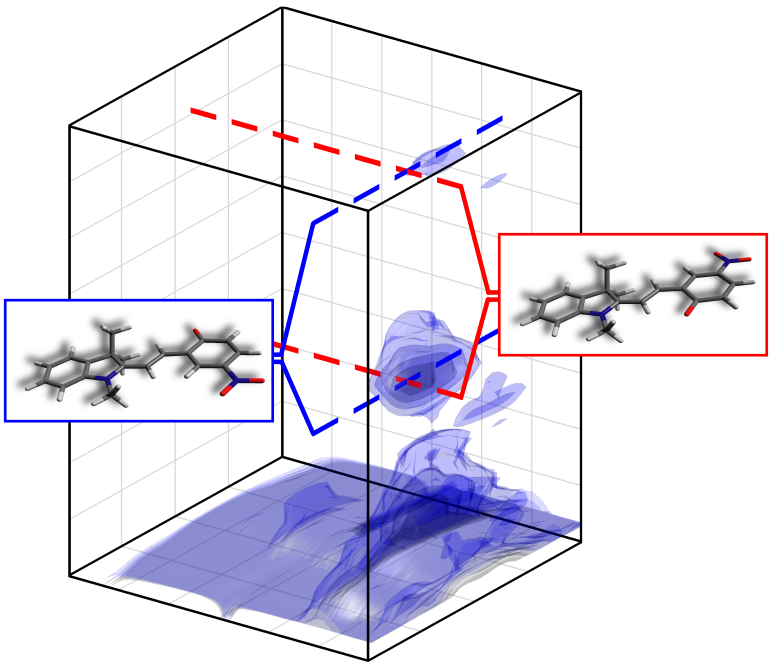

Dissertation zur Erlangung des naturwissenschaftlichen Doktorgrades der Julius-Maximilians-Universität Würzburg

vorgelegt von

Stefan Rützel

aus Marktredwitz

Würzburg 2014

Eingereicht bei der Fakultät für Chemie und Pharmazie am _____

Gutachter der schriftlichen Arbeit
1. Gutachter: Prof. Dr. T. Brixner
2. Gutachter: _____

Prüfer des öffentlichen Promotionskolloquiums
1. Prüfer: Prof. Dr. T. Brixner
2. Prüfer: _____
3. Prüfer: _____

Datum des Promotionskolloquiums: _____

Doktorurkunde ausgehändigt am _____

List of Publications

[1] C. Consani, S. Ruetzel, P. Nuernberger, and T. Brixner.
Quantum Control Spectroscopy of Competing Reaction Paths in a Molecular Switch.
in preparation (2014).

[2] S. Ruetzel, M. Diekmann, P. Nuernberger, C. Walter, B. Engels, and T. Brixner.
Photoisomerization Among Ring-Open Merocyanines. Part I: Reaction Dynamics and Wave-Packet Oscillations Induced by Tunable Femtosecond Pulses.
submitted for publication (2014).

[3] C. Walter, S. Ruetzel, M. Diekmann, P. Nuernberger, T. Brixner, and B. Engels.
Photoisomerization Among Ring-Open Merocyanines. Part II: A Computational Study.
submitted for publication (2014).

[4] S. Ruetzel, M. Diekmann, P. Nuernberger, C. Walter, B. Engels, and T. Brixner.
Multidimensional Spectroscopy of Photoreactivity.
Proceedings of the National Academy of Sciences of the United States of America (2014), doi: 10.1073/pnas.1323792111.

[5] S. Ruetzel, M. Kullmann, J. Buback, P. Nuernberger, and T. Brixner.
Tracing the Steps of Photoinduced Chemical Reactions in Organic Molecules by Coherent Two-Dimensional Electronic Spectroscopy Using Triggered Exchange.
Physical Review Letters **110**, 148305 (2013).

[6] S. Ruetzel, M. Kullmann, J. Buback, P. Nuernberger, and T. Brixner.
Exploring Higher-Lying Electronic States of a Molecular Switch by Coherent Triggered-Exchange 2D Electronic Spectroscopy.
EPJ Web of Conferences **41**, 05001 (2013).

[7] S. Rützel, A. Krischke, and T. Brixner.
The von Neumann Representation as a Joint Time–Frequency Parameterization for Polarization-Shaped Femtosecond Laser Pulses.
Applied Physics B: Lasers and Optics **107**, 1–9 (2012).

[8] M. Kullmann, S. Ruetzel, J. Buback, P. Nuernberger, and T. Brixner.
Reaction Dynamics of a Molecular Switch Unveiled by Coherent Two-Dimensional Electronic Spectroscopy.
Journal of the American Chemical Society **133**, 13074–13080 (2011).

[9] S. Ruetzel, C. Stolzenberger, F. Dimler, D. J. Tannor, and T. Brixner.
Adaptive Coherent Control Using the von Neumann Basis.
Physical Chemistry Chemical Physics **13**, 8627–8636 (2011).

[10] D. Reitzenstein, T. Quast, F. Kanal, M. Kullmann, S. Ruetzel, M. S. Hammer, C. Deibel, V. Dyakonov, T. Brixner, and C. Lambert.
Synthesis and Electron Transfer Characteristics of a Neutral, Low-Band-Gap, Mixed-Valence Polyradical.
Chemistry of Materials **22**, 6641–6655 (2010).

[11] S. Ruetzel, C. Stolzenberger, S. Fechner, F. Dimler, T. Brixner, and D. J. Tannor.
Molecular Quantum Control Landscapes in von Neumann Time-Frequency Phase Space.
Journal of Chemical Physics **133**, 164510 (2010).

Parts of this thesis have been published in some of the peer-reviewed journal articles listed on pp. iii–iv. An overview of adapted passages and the corresponding page numbers can be found in the table below. The sources of adapted figures are additionally indicated at the end of the corresponding figure captions.

Publication		Use	Dissertation
[2]	(submitted)	figures adapted, new text	pp. 70–88
[4]	pp. 1–2	figures adapted, text reproduced, modified, and extended	pp. 88–89
	pp. 2–4, SI pp. 1–2	figures adapted, text reproduced	pp. 94–103
	pp. 4–6, SI pp. 2–5	figures adapted, text reproduced and modified	pp. 103–108
	SI pp. 2–4	figures adapted, new text	pp. 70–71
	SI pp. 3–10	figures and tables adapted, text reproduced	pp. 159–164
[5][1]	pp. 1–2	figures adapted, text reproduced, modified and extended	pp. 110–113
	pp. 2–4	figures adapted, text reproduced, modified, and extended	pp. 121–130
[6]	pp. 1–3	figures adapted, new text	pp. 121–130
[8][2]	pp. 1–2	figures adapted, new text	pp. 111–113
	pp. 2–6	figures adapted, new text	pp. 114–120
[7][3]	pp. 1–2	figures adapted, text reproduced, modified, and extended	pp. 132–135
	pp. 2–8	figures adapted, text reproduced, modified, and extended	pp. 140–150

[1]Reproduced and adapted with permission from Physical Review Letters **110**, 148305 (2013). © (2013) by the American Physical Society.

[2]Reproduced and adapted with permission from Journal of the American Chemical Society **133**, 13074–13080 (2011). © (2011) by the American Chemical Society.

[3]Reproduced and adapted with permission from Applied Physics B: Lasers and Optics **107**, 1–9 (2012). © (2012) by Springer Science+Business Media.

Contents

1 Introduction

Chemical reactions form the basis of our everyday lives. Many of these everyday reactions occur upon irradiation of light, for instance, in the primary event of vision, in photosynthesis, or in the formation of vitamin D in the human skin upon sun irradiation. It is therefore obvious that light can also be employed as a tool to initiate and study chemical processes in a well-controlled laboratory environment. Following the course of such chemical reactions from the reactant over reaction intermediates to the products in real time requires the ability to follow the motion of molecules and atoms on unimaginable short time scales on the order of only a few femtoseconds (1 fs = 10^{-15} s). Since conventional (e.g. thermal) light sources are not capable of providing the necessary temporal resolution, studies on photochemical and photophysical processes were limited to the observation of the formed products for a long time while the reaction path remained practically inaccessible.

The field of time-resolved optical spectroscopy was revolutionized by the development of laser sources capable of generating light pulses in the visible spectral range with durations of only a few femtoseconds, which led to the foundation of a new research field, termed *femtochemistry* [12, 13]. In 1999, Ahmed H. Zewail was awarded the Nobel Prize in Chemistry for his pioneering contributions to this field. In femtochemistry, femtosecond pulses are used to initiate and probe photochemical transformations such as photodissociation, photoionization, or photoisomerization reactions, providing unique and unprecedented insights into molecular photodynamical processes.

Nevertheless, the full technological potential of ultrafast spectroscopy has so far only rarely been exploited, as these techniques are in general capable of capturing much more information than typically utilized. This is exemplified by the fact that the 'workhorse' of ultrafast spectroscopy – the pump–probe technique – is in its simplest form a third-order technique and thus provides information in up to three temporal or spectral dimensions. Yet, for many years only a small fraction of the available spectroscopic information was taken into account by considering simple slices along a single dimension, for example, along the pump–probe delay time. As a consequence, identifying all species involved in a reaction is often impossible since the signatures of reactants, intermediates, and products overlap in many cases which in return implies that a reaction product might not be isolated from the signatures of other reagents. This is a major issue especially in cases with low reaction quantum yields.

As a significant technological improvement compared to the pump–probe scheme, coherent two-dimensional electronic spectroscopy was established in the late 1990s as an optical analog of two-dimensional nuclear magnetic resonance. This method spreads the information along two independent frequency dimensions, associated with the system's absorption and emission frequencies [14–20]. In this way, frequency correlations are resolved and couplings are directly visualized. So far, this technique was exclusively

applied to purely *photophysical* phenomena, such as energy transfer in natural or artificial light harvesting [21–24] or exciton dynamics in multichromophores [25–28], but never for the time-resolved study of *photochemical* transformations. While several investigations of photochemical exchange in the infrared spectral region with vibrational transitions (two-dimensional infrared spectroscopy) were reported in the literature [29–35], studies with electronic excitations were so far limited to phenomena in which the excited species return to their initial configurations after a short time such as in excited-state charge-transfer processes [36, 37].

Beyond the two-dimensional approach, also coherent three-dimensional experiments on photophysical systems were reported very recently in the infrared [38–40] and visible spectral range [41–46], in which the signal is additionally mapped onto a third frequency axis accounting for dynamics (such as coherences) that occur after the first two light–matter interactions.

The goal of this thesis is to transfer the method of coherent two- and three-dimensional electronic spectroscopy for the first time to the field of femtochemistry, opening up the science of ultrafast photochemical processes to the multidimensional concept. Several fundamental questions are addressed in the course of this work: Is coherent multidimensional spectroscopy capable of probing molecular reaction dynamics as well as isolating the signatures of the reaction products from all other species? How exactly do different molecular species turn into one another and which electronic states are involved? How is the photochemistry affected when the molecule absorbs a second photon after the initial excitation? And can we provide a joint spectro–temporal formalism for the description of light fields that allows for higher-order and polarization-sensitive experiments?

In order to verify the general capabilities of the approach, well-established experimental techniques are used in the first instance to explore the photodynamics of photoreactive model systems on the basis of their corresponding transient absorption and coherent two-dimensional spectra. In addition, techniques making use of more elaborate pulse sequences, which have so far been limited to the study of vibrational transitions, are implemented in this work also for electronic excitations. This can be used to explore the dynamics initiated upon photoexcitation to higher-lying electronic states. Finally, a new formalism is introduced in this thesis based on the von Neumann time–frequency picture of shaped femtosecond laser pulses. By generalizing this joint time–frequency representation to the description of shaped laser pulses with time-varying polarization profiles, the vectorial character of light–matter interactions can be utilized with applications in polarization-sensitive multidimensional spectroscopy and coherent quantum control.

The discussed experiments can be classified based on the number of associated light–matter interactions, i.e., on the order of the exploited optical nonlinearity. For this reason, this thesis is subdivided into three main chapters containing experiments with third-order (Chap. 4) and fifth-order interactions (Chap. 5), as well as the von Neumann formalism allowing for higher-order nonlinearities (Chap. 6). This work is therefore organized as follows.

The theoretical background of ultrashort laser pulses, their representation in the Fourier domain, conventional joint time–frequency representations, the description of time-varying polarization states, nonlinear optics, and photochemical processes is pro-

vided in Chap. 2.

The experimental techniques required for the implementation of all methods is described in Chap. 3. This includes a short description of the used femtosecond laser source, ultrafast frequency-domain pulse shaping, the employed pulse characterization and compression technique, the experimental setup for transient absorption, and the concept of coherent two-dimensional spectroscopy.

The first experiments are discussed in Chap. 4, in which a model reaction – the *cis-trans* photoisomerization among ring-open nitro-substituted merocyanine isomers – is studied by means of third-order spectroscopies. To gain a picture of the excited-state lifetimes of the system, the associated spectral profiles, and the quantum yield of the reaction, broadband transient absorption measurements in combination with global data analysis are employed in the first part of this chapter. Afterwards, third-order two- and three-dimensional spectroscopy is used to elucidate the mechanism of the photoreaction by analyzing the signal in terms of characteristic vibrational modes associated with the formation of the photoproduct. Results of high-level quantum-chemical calculations performed by our collaborators from the theoretical chemistry department at the University of Würzburg in the group of Prof. B. Engels are also presented.

In Chap. 5, a closely related compound – a dinitro-substituted merocyanine – is characterized by means of novel multidimensional techniques. Coherent two-dimensional spectra are collected to analyze whether the same isomerization reaction as observed in Chap. 4 is part of the photochemistry of this molecule. In order to explore the photochemistry of higher-lying states, a fifth-order technique, termed triggered-exchange two-dimensional spectroscopy, which was so far only available in the infrared regime, is successfully established for the first time for electronic transitions in the visible spectral range.

The von Neumann time–frequency representation for linearly polarized pulses is introduced in Chap. 6. After a short motivation, the formalism is generalized to the description of pulses with shaped polarization profiles and the introduced parameters are illustrated with the help of several example pulse shapes.

Finally, a short summary of this thesis is given in Chap. 7, while in the Appendix supplementary calculated data for the system investigated in Chap. 4 and auxiliary calculations for Chap. 6 are provided.

2 Theoretical Background

Ultrashort laser pulses with durations of only a few femtoseconds (fs) have proven to be a universal tool for research in natural and medical sciences and have applications in technology and industrial manufacturing. In this thesis femtosecond laser pulses are employed for the observation and manipulation of photochemical and photophysical processes in molecules on their fundamental time scales. For this purpose a mathematical basis for the description and a detailed understanding of the underlying physical processes used for generation and manipulation of these laser fields is necessary. Moreover, the photochemical properties and the interactions of light and matter have to be discussed in detail. In this chapter, essential theoretical concepts as well as the mathematical and physical principles of this thesis are explained. Firstly, the mathematical description of femtosecond laser pulses in time- or frequency-domain as well as in the joint time–frequency picture, their time-dependent polarization state, and the spatial properties of Gaussian laser beams are introduced (Sect. 2.1). Also the theory of nonlinear optics is part of this chapter (Sect. 2.2). Finally, the photochemical properties of molecular electronic states and potentials, electronic transitions, and molecular wave packets are discussed (Sect. 2.3).

2.1 Mathematical Description of Ultrashort Laser Pulses

Starting point in the description of electromagnetic waves is the inhomogeneous wave equation for the electric field vector $\vec{E}(\vec{r},t)$ at time t and at the point $\vec{r} = (x,y,z)$ in space that can be derived from Maxwell's equations. Assuming a charge- and current-free nonmagnetic medium it reads [47]

$$\nabla^2 \vec{E}(\vec{r},t) - \frac{1}{c_0^2}\frac{\partial}{\partial t^2}\vec{E}(\vec{r},t) = \mu_0 \frac{\partial}{\partial t^2}\vec{P}(\vec{r},t) \tag{2.1}$$

where $c_0 = 1/\sqrt{\epsilon_0 \mu_0}$ denotes the speed of light in vacuum, μ_0 the permeability constant, and ϵ_0 the permittivity of free space. The source term on the right hand side of Eq. (2.1) consists of the electric polarization $\vec{P}(\vec{r},t)$ that specifies on the one hand how the medium affects the electric field and on the other hand the response of the medium to the external field.

The consequence of the complicated nature of Eq. (2.1) is that in general it can only be solved numerically. However, several simplifications and approximations that are valid for all phenomena discussed in this thesis allow the separation of $\vec{E}(\vec{r},t)$ into a purely time dependent term $\vec{E}(t)$ and a term $u(\vec{r})$ describing the spatial beam profile as a function of the propagation length along the z-axis such that

$$\vec{E}(\vec{r},t) \propto \vec{E}(t)u(\vec{r}). \tag{2.2}$$

Based on this equation both terms will be treated separately in the following subsections before the role of the polarization $\vec{P}(\vec{r},t)$ is discussed.

2.1.1 Frequency- and Time-Domain Pictures

Coherent ultrashort laser pulses can be described by the temporal evolution of the electric field $\vec{E}(\vec{r},t)$. In this subsection, the electric field is treated as linearly polarized, e.g., the electric field vector is located exclusively within a plane of fixed orientation. This plane is perpendicular to the direction of propagation, which is – as mentioned above and without loss of generality – assumed to be the z-direction. The description of femtosecond pulses with a variable polarization state and the spatial beam propagation is discussed in Sects. 2.1.3 and 2.1.4, respectively. If the electric field is considered at a fixed position $z = 0$ in space, the only parameter sufficient to completely characterize the electric field is its amplitude $|\vec{E}(z = 0,t)| = E(t)$ as a function of time. The field $E(t)$ can then be expressed as a product of an oscillation with carrier frequency ω_0 and an envelope function $A(t)$ [48]

$$E(t) = A(t)\cos(\Phi_0 + \omega_0 t). \tag{2.3}$$

The center frequency ν_0 of the light field is given by $\nu_0 = \omega_0/2\pi$. The parameter Φ_0 is the absolute phase, also called *carrier-envelope phase* (CEP) and determines the relationship between the field oscillations and the envelope function. Figure 2.1 illustrates the significance of the CEP. For very short laser pulses with small amounts of optical cycles [few-cycle pulses, Fig. 2.1(a)], the CEP can have a major influence on the temporal evolution of the electric field. For $\Phi_0 = 0$ a cosine-shaped pulse is generated (red), thus, the maximum of the envelope function (gray dashed) and the electric field coincide at time $t = 0$. However, for $\Phi_0 = \pi/2$ a sine-shaped pulse evolves (blue) such that the electric field is zero at $t = 0$ and hence will not reach the maximum value given by the maximum of the envelope. For laser pulses of longer duration the value of Φ_0 is only of minor relevance, as shown in Fig. 2.1(b) for a pulse with an intensity full width at half maximum (FWHM) of 25 fs. In this case, the envelope function varies only slowly during the period of the field oscillation. Therefore, if sufficiently long laser pulses compared to the oscillation period are employed, the so called *slowly varying envelope approximation* (SVEA) is commonly introduced [47]. This approximation states that the carrier envelope phase has practically no effect on the laser pulse shape if the envelope function varies only slowly during the period of a single field oscillation. As the laser system used in this work (see Sect. 3.1) produces laser pulses of a duration longer than 10 fs between the UV and the NIR region, this approximation is valid and will be used in the course of this work. This is also reasonable as the carrier-envelope phase delivered by our system varies on a pulse-to-pulse basis. However, techniques of stabilizing the CEP exist [49, 50] and experiments have also been carried out where the CEP was used as the primary control parameter [51, 52]. In addition, the CEP cannot be determined by common techniques for laser pulse characterization (see Sect. 3.3).

The time-dependent intensity $I(t)$ of the laser pulse is proportional to the squared

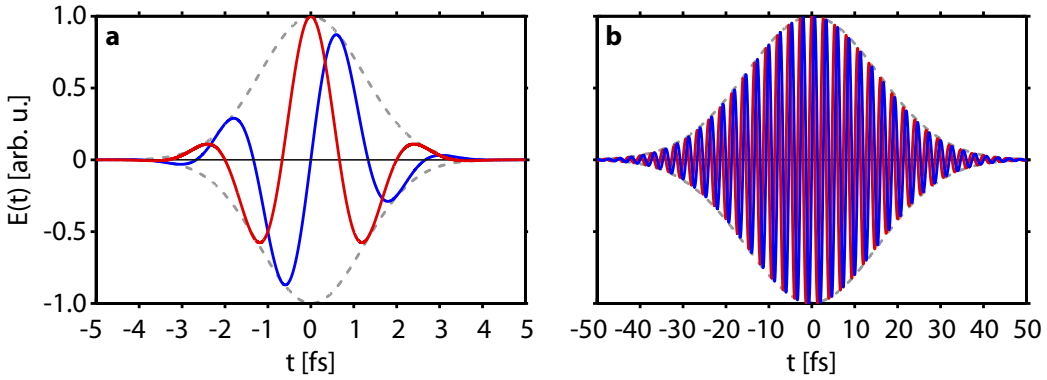

Figure 2.1 | Illustration of the carrier-envelope phase and the slowly varying envelope approximation. (a) A few-cycle cosine laser pulse with a center wavelength of 800 nm, intensity-FWHM of 2 fs, and CEP phase of $\Phi_0 = 0$ (red) is compared to a sine pulse with $\Phi_0 = \pi/2$ (blue). (b) The same case as in (a) is shown, but with an intensity-FWHM of 25 fs.

envelope function

$$I(t) = \frac{1}{2}\epsilon_0 c_0 n A(t)^2 \tag{2.4}$$

where n denotes the refractive index of the medium.

Laser pulses as described by Eq. (2.3) consist of a purely harmonic oscillation of the electric field vector. However, this is in general not the case for pulses that have travelled through media or have been manipulated otherwise, e.g., by a fs pulse shaper. For this reason, a time-dependent phase $\varphi(t)$ has to be added to the phase term in Eq. (2.3) resulting in the following expression for the total temporal phase

$$\Phi(t) = \Phi_0 + \omega_0 t + \varphi(t). \tag{2.5}$$

From this quantity the time-dependent instantaneous frequency is given by the derivative of the phase with respect to time

$$\omega(t) = \frac{\mathrm{d}\Phi(t)}{\mathrm{d}t} = \omega_0 + \frac{\mathrm{d}\varphi(t)}{\mathrm{d}t}. \tag{2.6}$$

The real-valued electric field as a function of time $E(t)$ can be expanded in terms of monochromatic plane waves, which mathematically corresponds to a Fourier transformation

$$E(t) = \frac{1}{\sqrt{2\pi}} \int_{-\infty}^{\infty} \mathrm{d}\omega E(\omega) \mathrm{e}^{\mathrm{i}\omega t} \tag{2.7}$$

where the complex-valued quantity $E(\omega)$ describes the electric field in frequency domain, which in turn is given by the inverse Fourier transform of Eq. (2.7)

$$E(\omega) = \frac{1}{\sqrt{2\pi}} \int_{-\infty}^{\infty} \mathrm{d}t E(t) \mathrm{e}^{-\mathrm{i}\omega t}. \tag{2.8}$$

As $E(t)$ is real valued, the relationship

$$E(\omega) = E^*(-\omega) \tag{2.9}$$

holds, where * denotes the conjugate-complex form. From this symmetry it follows that it is sufficient to consider the electric field for positive frequencies only by defining the quantity $E^+(\omega)$

$$E^+(\omega) = \begin{cases} E(w) & \forall \quad \omega \geq 0 \\ 0 & \forall \quad \omega < 0 \end{cases} \tag{2.10}$$

whereas the negative part of the spectrum is given by

$$E^-(\omega) = \begin{cases} E(w) & \forall \quad \omega < 0 \\ 0 & \forall \quad \omega \geq 0. \end{cases} \tag{2.11}$$

In the same way as $E(t)$ and $E(\omega)$ are connected via a Fourier transformation, there is an inverse function of $E^+(\omega)$ given also by Fourier transformation

$$E^+(t) = \frac{1}{\sqrt{2\pi}} \int_{-\infty}^{\infty} \mathrm{d}\omega E^+(\omega) \mathrm{e}^{\mathrm{i}\omega t} \tag{2.12}$$

$$E^+(\omega) = \frac{1}{\sqrt{2\pi}} \int_{-\infty}^{\infty} \mathrm{d}t E^+(t) \mathrm{e}^{-\mathrm{i}\omega t} \tag{2.13}$$

which is linked to the real valued field via

$$E(t) = E^+(t) + E^-(t) = 2\mathrm{Re}\{E^+(t)\} = 2\mathrm{Re}\{E^-(t)\} \tag{2.14}$$

and to its complex-valued Fourier transformation via

$$E(\omega) = E^+(\omega) + E^-(\omega). \tag{2.15}$$

Since $E^+(t)$ and $E^+(\omega)$ are complex-valued quantities they can be characterized by their amplitudes and phases

$$\begin{aligned} E^+(t) &= \frac{1}{2} A(t) \mathrm{e}^{\mathrm{i}\Phi(t)} \\ &= \sqrt{\frac{I(t)}{2\epsilon_0 c_0 n}} \mathrm{e}^{\mathrm{i}\Phi_0} \mathrm{e}^{\mathrm{i}\omega_0 t} \mathrm{e}^{\mathrm{i}\varphi(t)} \end{aligned} \tag{2.16}$$

$$\begin{aligned} E^+(\omega) &= A(\omega) \mathrm{e}^{-\mathrm{i}\Phi(\omega)} \\ &= \sqrt{\frac{\pi I(\omega)}{\epsilon_0 c_0 n}} \mathrm{e}^{\mathrm{i}\Phi_0} \mathrm{e}^{-\mathrm{i}\varphi(\omega)} \end{aligned} \tag{2.17}$$

where $A(\omega)$ is the spectral amplitude, $\Phi(\omega)$ the spectral phase, and $I(\omega)$ the spectral intensity, i.e., the quantity that is measured by a spectrometer. Due to Eq. (2.9), the relation $-\Phi(\omega) = \Phi(-\omega)$ is valid. The spectral phase is of major relevance since its manipulation will also result in a changed temporal electric field $E(t)$ due to the mutual Fourier relationship in Eq. (2.12) and Eq. (2.13).

The distinction between positive and negative frequencies is made here just for the sake of mathematical correctness. In practice, only positive frequency components and real valued electric fields are considered. Furthermore, the prefactors in Eq. (2.16) and (2.17) are disregarded in the representation of the temporal and spectral fields since in most cases only the shape and not the absolute non-dimensionless value of the electric fields are considered.

As shown in Eq. (2.6) the temporal phase $\Phi(t)$ contains information about the temporal evolution of the instantaneous frequency. In a similar manner the group delay can be defined by the derivative of the spectral phase $\Phi(\omega)$ with respect to the frequency, describing the relative temporal delay of a given spectral component

$$T_g(\omega) = \frac{\mathrm{d}\Phi(\omega)}{\mathrm{d}\omega}. \tag{2.18}$$

In many cases it is convenient to expand the spectral phase in terms of a Taylor series centered around the center frequency ω_0 of the laser pulse spectrum:

$$\Phi(\omega) = \sum_{j=0}^{\infty} \frac{a_j}{j!} \cdot (\omega - \omega_0)^j \tag{2.19}$$

with the Taylor coefficients given by

$$a_j = \left.\frac{\partial^j \Phi(\omega)}{\partial \omega^j}\right|_{\omega_0}. \tag{2.20}$$

In the same way, assuming the temporal evolution of the laser pulse is centered around $t = 0$, the temporal phase $\Phi(t)$ can be expanded in terms of a Taylor series as well:

$$\Phi(t) = \sum_{j=0}^{\infty} \frac{b_j}{j!} \cdot t^j \tag{2.21}$$

where

$$b_j = \left.\frac{\partial^j \Phi(t)}{\partial t^j}\right|_{t=0}. \tag{2.22}$$

The temporal Taylor coefficient of zeroth order describes the absolute CEP phase with $b_0 = \Phi_0 = -\Phi(\omega_0) = -a_0$. The temporal Taylor coefficient of first order accords with the carrier frequency ω_0, whereas the spectral Taylor coefficient of first order determines the temporal shift relative to time zero. The spectral coefficient of second order describes dispersion of second order and consequently the amount of linear group delay [Eq. (2.18)], which leads to a linear change of the instantaneous frequency with time. In the sign

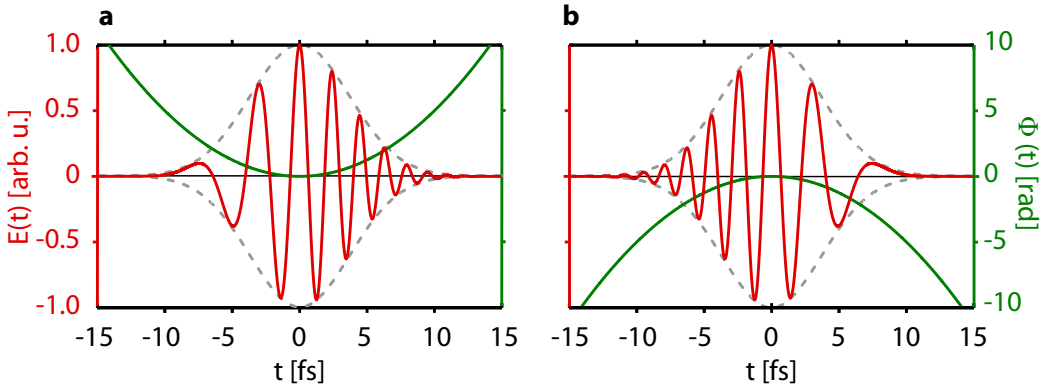

Figure 2.2 | Influence of the linear chirp on the oscillation period of the electric field of a laser pulse. The effect of pulse chirp is demonstrated with a laser pulse of 6 fs duration (FWHM) and (a) $b_2 = +0.05/\text{fs}^2$ and (b) $b_2 = -0.05/\text{fs}^2$ showing an increasing oscillating frequency with time for the positively chirped pulse and a decreasing instantaneous frequency with time for negative chirp.

convention used in this thesis, a positive (negative) second order of spectral phase term also leads to a positive (negative) quadratic temporal phase corresponding to a linearly increasing (decreasing) instantaneous frequency with time and the laser pulse is referred to be linearly positively (negatively) chirped, also called up-chirped (down-chirped). Figure 2.2 illustrates this effect on a laser pulse of 6 fs duration with $b_2 = \pm 0.05/\text{fs}^2$ (green). In the case of up-chirped pulses [Fig. 2.2(a)] the oscillation period of $E(t)$ (red) decreases with time, while it increases for a down-chirp [Fig. 2.2(b)]. Dispersion for shorter laser pulses causes, depending on the amount and order of chirp, in addition a temporal broadening. Therefore, dispersion effects have to be avoided in femtosecond pulse generation. Due to the required broader spectral bandwidth, dispersion has a stronger effect on shorter laser pulses.

Higher phase terms of even order cause chirp values of higher order, i.e., the instantaneous frequency varies non-linearly with time. Odd-numbered phase terms result in pre- or post-pulses and also in a temporal broadening. In order to quantify this effect, the term 'pulse duration' has to be defined more exactly. We now consider a Gaussian-shaped pulse envelope

$$A(\omega) = \frac{E_0}{2} \mathrm{e}^{-\frac{2\ln 2}{\sigma_\omega^2}(\omega-\omega_0)^2} \tag{2.23}$$

where σ_ω denotes the FWHM of the spectral intensity profile $I(\omega)$. Via Fourier transformation the distribution in time-domain

$$A(t) = \frac{E_0 \sigma_\omega}{2} \sqrt{\frac{\pi}{2\ln 2}} \mathrm{e}^{-\frac{\sigma_\omega^2}{8\ln 2} t^2} \tag{2.24}$$

is obtained. In this case the following expression is found for the so called time–bandwidth product

$$\sigma_\omega \sigma_t = 4 \ln 2. \tag{2.25}$$

This equation only holds for pulses with a flat spectral phase function.[1] For pulses with additional non-zero phase terms and different spectral profiles, this equation is generalized by the form

$$\sigma_\omega \sigma_t \geq 2\pi K \tag{2.26}$$

making use of the parameter K characterizing the spectral intensity profile. For Gaussian-shaped spectral intensity profiles with a flat phase $K = 0.441$ is obtained. A laser pulse is referred to as bandwidth-limited if the equation $\sigma_\omega \sigma_t = 2\pi K$ holds. Equation (2.26) corresponds to a time–frequency uncertainty and is a fundamental property of physical quantities linked via Fourier transformation. From this equation it follows that shorter pulses require a broader spectrum.

The effect of different spectral phase functions and intensity profiles on the temporal pulse profile is illustrated exemplarily in Fig. 2.3, where $I(\omega)$ (red) and $I(t)$ (blue) and the spectral and temporal phase functions (green) of corresponding pulse shapes are depicted next to each other. For all pulses [except of (i)–(l)] a Gaussian-shaped spectrum is assumed with 17.7 nm FWHM (corresponds to 25 nm FWHM for $|E^+(\omega)|$). For a flat spectral phase this spectral field corresponds to a Gaussian temporal pulse of 53.3 fs duration [Fig. 2.3(a)]. A linear spectral phase with a slope of $\Phi'(\omega) = 400$ fs shifts the temporal envelope function by the same amount to positive times [Fig. 2.3(b)]. In Fig. 2.3(c) a linearly chirped pulse with $\Phi''(\omega) = 2.5 \cdot 10^4$ fs^2 is shown, leading to a broadening of the temporal pulse structure and a quadratic temporal phase function. In Fig. 2.3(d) it is demonstrated how third-order spectral phase terms affect the pulse sequence resulting in post-pulses with a phase difference of π between successive subpulses. Fourth-order spectral phase terms [Fig. 2.3(e)] cause a third-order chirp and therefore the temporal intensity profile is no longer Gaussian. Spectral phase-steps of π give rise to destructive interference at time $t = 0$ leading to a distinct intensity dip at $t = 0$. Also a phase separation of π is introduced between positive and negative times, as shown in Fig. 2.3(f). The resulting pulse shape can have a significant effect on multiphoton excitation processes [53]. By applying a triangular (piecewise linear) phase function [Fig. 2.3(g)] with the breakpoint at the center wavelength, it is possible to generate double pulses by shifting the corresponding spectral components to different points in time [54–56]. Figure 2.3(h) illustrates the effect of a cosine-shaped spectral phase with an amplitude of π and a frequency of 400 fs. A multipulse sequence is generated of which every subpulse is a copy of the unshaped pulse. These phase functions have applications in spectroscopy and microscopy [57, 58] as well as in quantum control [59, 60]. The influence of the spectral intensity profile is shown in Fig. 2.3(i)–(l). If spectral components at the outer [Fig. 2.3(i)] or inner [Fig. 2.3(j)] part of the spectrum are blocked, the temporal intensity profile as well as the temporal phase is strongly affected leading to temporal smearing of the pulse. By imitating the spectral interference pattern of a Michaelson interferometer [Fig. 2.3(k)] a temporal double pulse is generated of which each subpulse has the same temporal profile as the unshaped pulse. This can be used in various time resolved spectroscopy techniques as for example in coherent two-dimensional spectroscopy in a pump–probe beam geometry, as will be explained in

[1] a flat spectral phase profile is characterized by $\frac{\partial^j \Phi(\omega)}{\partial t^j} = 0$ for $j > 1$

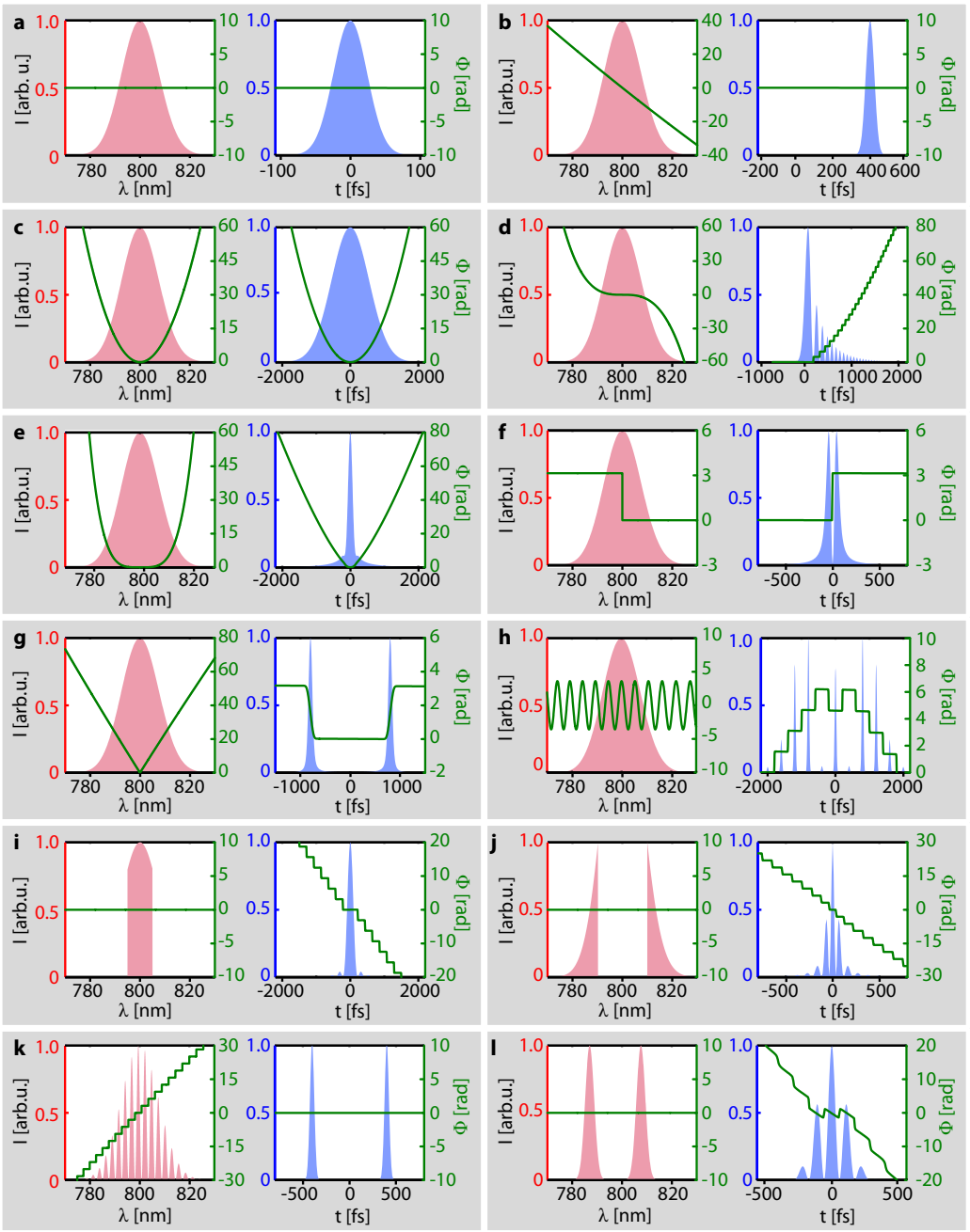

Figure 2.3 | Influence of the spectral intensity profile (blue) and phase (green) on the temporal structure of a laser pulse. The spectral FWHM is 25 nm centered at 800 nm. (a) bandwidth-limited Gaussian pulse with a flat phase; (b) linear phase with $\Phi'(\omega) = 400$ fs; (c) linearly up-chirped pulse with $\Phi''(\omega) = 2.5 \cdot 10^4$ fs^2; (d) $\Phi'''(\omega) = 1 \cdot 10^6$ fs^3; (e) $\Phi''''(\omega) = 1 \cdot 10^8$ fs^4; (f) phase step of π at the center wavelength; (g) generation of a double pulse by applying a triangular phase with the spectral breakpoint at the center wavelength; (h) cosine phase with an amplitude of π and frequency of 400 fs; (i) symmetrical spectral clipping of a Gaussian profile; (j) blocking of the spectral center; (k) spectral interference of a temporal double pulse with a pulse separation of $\tau = 800$ fs; (l) two spectrally separated Gaussians (6nm FWHM located at $\lambda_1 = 787.0$ nm and $\lambda_2 = 807.6$ nm) leading to temporal interference.

Sect. 4.4.2. In contrast, two spectrally separated Gaussians in frequency domain cause temporal interferences, as illustrated in Fig. 2.3(l).

2.1.2 Joint Time–Frequency Descriptions

In the previous section, the Fourier description of femtosecond laser pulses was introduced. On this basis, arbitrary laser pulses can be described entirely either in time or frequency domain and both descriptions can be transformed into each other by Fourier transformation. Hence, both pictures are equivalent and complete from a mathematical point of view. The major drawback of the Fourier picture is that – at first glance – either only the spectral *or* the temporal nature of the laser pulse becomes apparent. For this reason, alternative descriptions termed joint time–frequency representations (JTFR), which are functions of time *and* frequency, were introduced.

In the long history of signal analysis, many different approaches were established in order to visualize the temporal evolution of the frequency content of a time-dependent signal $s(t)$. The most common approach is the use of the so-called *short-time Fourier transform* (STFT), alternatively termed *sliding window Fourier transform*. To analyze the signal at a given instant of time it is multiplied by a window function $h(t)$ which is centered at a given time t. By Fourier transformation of this gated signal, the STFT is obtained [61–64]:

$$S(t,\omega) = \frac{1}{\sqrt{2\pi}} \int s(\tau)h(\tau - t)\mathrm{e}^{-\mathrm{i}\omega\tau}\mathrm{d}\tau. \tag{2.27}$$

The squared absolute value of this term is referred to as the spectrogram of the signal. The choice of the window function is crucial for the resulting distribution function $S(t,\omega)$. This is demonstrated in Fig. 2.4 using the example of an oscillating waveform with random noise [Fig. 2.4(a), blue line] over a time range of 10 seconds and three different Hanning-type (raised cosine) windows of 0.4 s (red solid), 1.0 s (red dotted), and 4.0 s (red dashed) width. As shown in Fig. 2.4(b) the choice of a narrow temporal window leads to a broad frequency distribution and the noise-induced fluctuations dominate. This effect is reduced by using a longer window function [Fig. 2.4(c)]. If the temporal window is too long, as shown in Fig. 2.4(d), short time fluctuations are averaged out but the temporal resolution is substantially decreased. This is the reason why so-called *wavelet transforms* have been introduced in signal processing. The use of wavelets yield a high time resolution for high frequency contents and a high frequency resolution for lower frequencies and thus avoids the issue of a fixed window width. A more detailed discussion of wavelets can be found in Refs. [65–67].

The principle of gating an unknown signal with another signal plays also a role in the characterization (see Sect. 3.3) and visualization of femtosecond laser pulses, but also in time-resolved spectroscopy. The different techniques just differ in the choice of the window function (or gating signal). For the visualization of shaped femtosecond laser pulses the Wigner and the Husimi representation have become most widely used. Another JTFR, which has been established in our group, is the von Neumann representation [68–70]. This representation will be introduced and generalized for applications

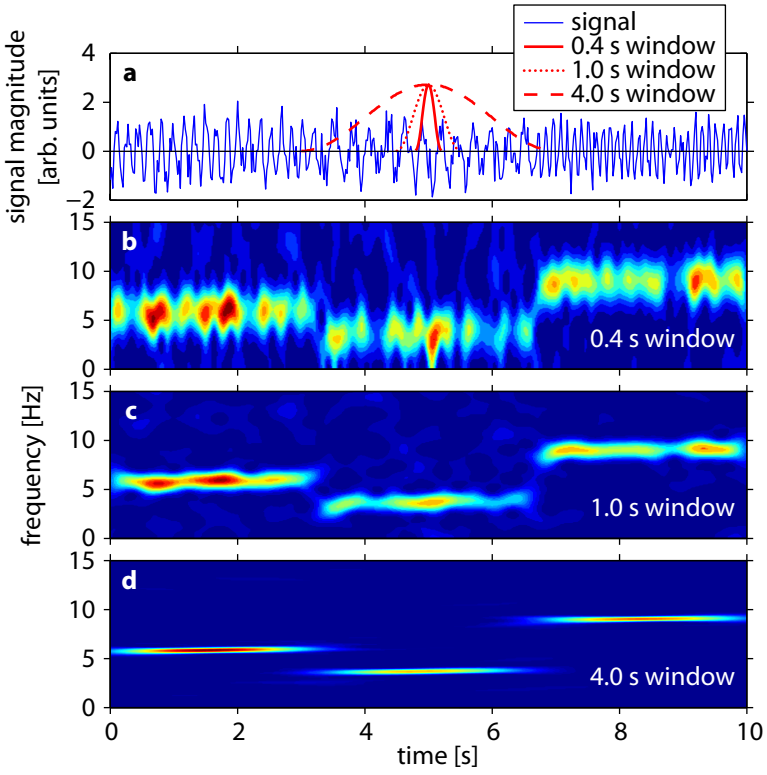

Figure 2.4 | Basic concept of the short-time Fourier transform (STFT). (a) For illustration the example of a noisy oscillating waveform (blue) over a time range of 10 seconds is considered. A Hanning window function with a width of 0.4 s (solid red), 1.0 s (red dotted), and 4.0 s (red dashed) is used to generate the STFTs shown below. (b) With the 0.4 s window the noise induced fluctuation of the frequency is strongly pronounced which is reduced using a window width of 1.0 s (c). (d) A 4.0 s window function averages over these short-time fluctuations but the temporal resolution is substantially reduced.

in polarization-sensitive multidimensional spectroscopy and quantum control in Chap. 6 of this thesis.

The Wigner representation

Many distribution functions have been established in quantum optics and quantum mechanics where they are also referred to as quasiprobability distributions. One of the most common distribution functions is the *Wigner representation* (also known as the Wigner function or the Wigner–Ville distribution), named after Eugene Paul Wigner who introduced it in 1932 in the context of quantum thermodynamics. It is based on a mixed description of states in the joint momentum–space phase space [71]. Later it was also established in quantum optics [72, 73] and in the early 1990s in the field of ultrashort laser pulses [74–77]. The Wigner representation $W(E^+,t,\omega)$ of the electric field $E^+(\omega)$ is given by

$$W(E^+,t,\omega) = \int E^+\left(\omega + \frac{\Omega}{2}\right) E^{+*}\left(\omega - \frac{\Omega}{2}\right) \mathrm{e}^{\mathrm{i}\Omega t}\mathrm{d}\Omega \tag{2.28}$$

and can also be derived from the temporal field via

$$W(E^+,t,\omega) = \int E^+\left(t + \frac{\tau}{2}\right) E^{+*}\left(t - \frac{\tau}{2}\right) \mathrm{e}^{-\mathrm{i}\omega\tau}\mathrm{d}\tau. \tag{2.29}$$

By considering the Wigner representation defined in Eq. (2.29) as a special form of an STFT it is extracted by using the temporally inverted field as a window function. This

already explains many basic properties of this representation. The Wigner representation is a real-valued but not a purely positive function and can exhibit non-zero amplitudes at time–frequency coordinates where no real content is found in the real electric field [62]. It was shown that the Wigner function is nonnegative only if the signal can be expressed as an exponential function of a quadratic polynomial [78], i.e., the laser pulse has a Gaussian profile with either a flat phase, linear phase, or linear chirp. Thus, the Wigner representation cannot be considered as a real probability distribution. However, it satisfies the marginals, which means that the frequency spectrum can be extracted by integration over $W(E^+,t,\omega)$ along the time axis:

$$I(\omega) = \frac{\epsilon_0 c_0 n}{\pi} \int W(E^+,t,\omega)\mathrm{d}t \tag{2.30}$$

$$= \frac{\epsilon_0 c_0 n}{\pi} \int\int E^+\left(\omega+\frac{\Omega}{2}\right) E^{+*}\left(\omega-\frac{\Omega}{2}\right) \mathrm{e}^{\mathrm{i}\Omega t}\mathrm{d}\Omega\mathrm{d}t \tag{2.31}$$

$$= \frac{\epsilon_0 c_0 n}{\pi} \int E^+\left(\omega+\frac{\Omega}{2}\right) E^{+*}\left(\omega-\frac{\Omega}{2}\right) \delta(\Omega)\mathrm{d}\Omega \tag{2.32}$$

$$= \frac{\epsilon_0 c_0 n}{\pi} |E^+(\omega)|^2 \tag{2.33}$$

where δ refers to the Dirac delta function [62]. A similar relationship can be found for the temporal intensity profile:

$$I(t) = 2\epsilon_0 c_0 n \int W(E^+,t,\omega)\mathrm{d}\omega. \tag{2.34}$$

The Wigner representation contains the complete information – apart from a constant prefactor – to recover the original field. This is easily proven as $W(E^+,t,\omega)$ is the Fourier transform of $E^+\left(\omega+\frac{\Omega}{2}\right) E^{+*}\left(\omega-\frac{\Omega}{2}\right)$. Hence, the inverse Fourier transform yields

$$E^+\left(\omega+\frac{\Omega}{2}\right) E^{+*}\left(\omega-\frac{\Omega}{2}\right) = \frac{1}{2\pi}\int W(E^+,t,\omega)\mathrm{e}^{-\mathrm{i}\Omega t}\mathrm{d}t \tag{2.35}$$

and by choosing the value $\omega = \Omega/2$ and replacing Ω by ω leads to [61, 62]

$$E^+(\omega) = \frac{1}{2\pi E^{+*}(\omega=0)} \int W(E^+,t,\frac{\omega}{2})\mathrm{e}^{-\mathrm{i}\omega t}\mathrm{d}t \tag{2.36}$$

and similarly for the temporal field to

$$E^+(t) = \frac{1}{2\pi E^{+*}(t=0)} \int W(E^+,\frac{t}{2},\omega)\mathrm{e}^{\mathrm{i}\omega t}\mathrm{d}\omega. \tag{2.37}$$

Thus, the Wigner transform allows for inversion from which the complete electric field (apart from the CEP) can be recovered.

Figure 2.5 shows the Wigner representation of a double pulse with a Gaussian spectrum generated by shifting the red half of the spectrum by 800 fs to negative and the blue parts to positive times and adding a linear chirp ($a_2 = 2\cdot10^4$ fs^2). The temporal and spectral intensity profiles are shown in the diagrams next to the corresponding axis of

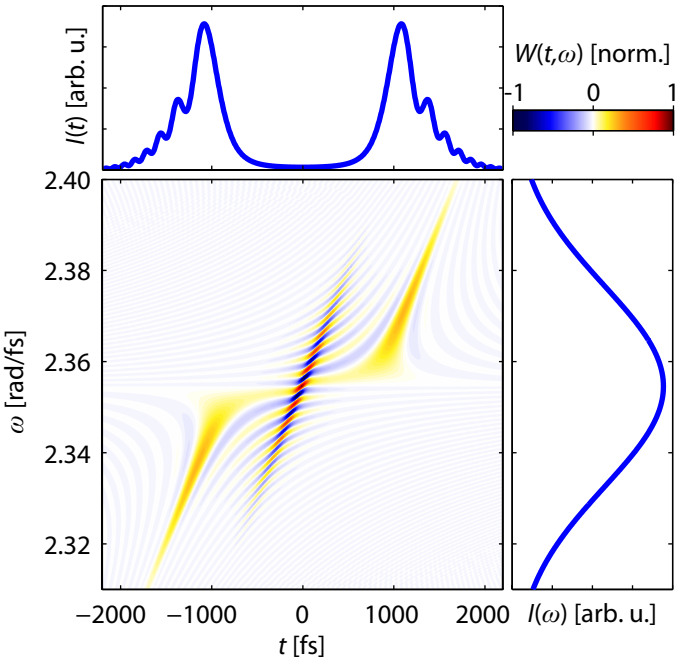

Figure 2.5 | Wigner representation of a chirped double pulse that is generated by shifting the red half of the spectrum to negative times and the blue half to positive ones and adding a linear chirp. The temporal and spectral intensity profiles are shown in the diagrams next to the corresponding axis of the Wigner representation. The pulse can be represented as a sum of two pulses and thus cross terms between the two parts lead to interferences around $t = 0$ that cause rapid signal oscillations where no amplitude is found in the original signal.

the Wigner representation. The laser pulse can be considered as the sum of two pulses. As a consequence, cross terms between the two subpulses arise and cause interferences around $t = 0$ where no amplitude is found in the original fields. It has to be noted that these cross-term interferences are no artifacts and are physically meaningful and contain relevant information about the encoded signal. However, the interpretation of such a distribution may be highly complicated in some cases due to the existence of such interference based oscillations which is the major downside of the Wigner representation.

The Husimi Representation

In order to suppress the oscillations that are observed in the Wigner representation it is possible to smooth it by a convolution of $W(E^+,t,\omega)$ with a suitable filter function. Thus a non-negative smoothed phase-space representation can be generated which is in many cases easier to interpret and more intuitive than the Wigner distribution [79]. If this is done using a 2D Gaussian as a filter function that satisfies the time-bandwidth product $\sigma_\omega\sigma_t = 4\ln 2$ [Eq. (2.25)], the so called Husimi representation is generated via

$$H(E^+,t,\omega) = \int\int W(E^+,\tau,\Omega)\mathrm{e}^{-\frac{4\ln 2}{\sigma_t^2}(t-\tau)^2-\frac{4\ln 2}{\sigma_\omega^2}(\omega-\Omega)^2}\mathrm{d}\tau\mathrm{d}\Omega. \tag{2.38}$$

The Husimi distribution resulting from the Wigner representation in Fig. 2.5 via convolution with the time–frequency distribution of the transform-limited pulse is shown in Fig. 2.6. The interference terms around $t = 0$ are averaged out and a purely positive time–frequency distribution is generated.

As only the product of σ_ω and σ_t is fixed, an infinite number of Husimi distributions exist for a given electric field. In contrast to the Wigner function, it can be shown that $H(E^+,t,\omega)$ can be interpreted in terms of a probability density for observing light intensity at a given coordinate in time–frequency phase space [80]. The Husimi distribution

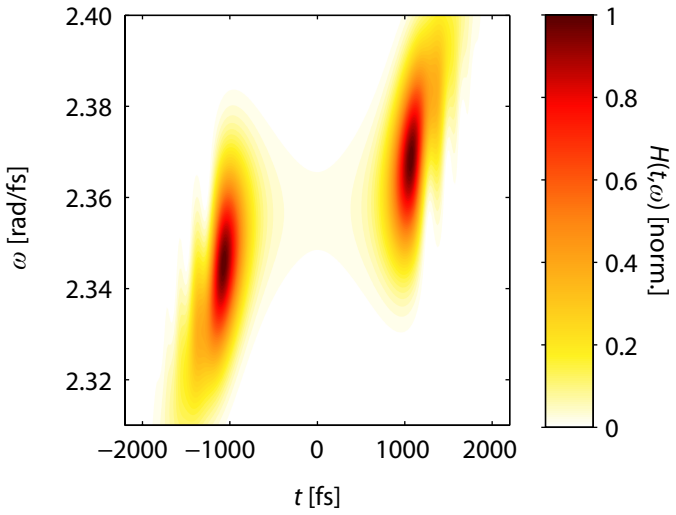

Figure 2.6 | Husimi representation of the same pulse as in Fig. 2.5. The resulting distribution function is positive and the interferences observed in the Wigner representation are smoothed out due to the two-dimensional convolution with a Gaussian phase-space function.

does not fulfill the marginal conditions of Eqs. (2.33) and (2.34) and the electric fields in pure time or frequency domain cannot be recovered analytically.

Originally, the Husimi distribution was introduced in 1940 by the Japanese physicist Kôdi Husimi who showed that *coherent states* can serve as a basis for a phase-space representation of quantum mechanical states [81]. Coherent states are Gaussian wave packets with a minimum amount of uncertainty in phase space [82–84]. In time–frequency phase space they can be considered in terms of bandwidth-limited Gaussian laser pulses centered at (ω,t). The Husimi representation is then given by the squared absolute value of the projection of E^+ onto the set of coherent state basis vectors $\alpha_{\omega t}$. Accordingly, in frequency space $H(E^+,t,\omega)$ can be derived via

$$H(E^+,t,\omega) = \left| \int E^{+*}(\omega')\alpha_{\omega t}(\omega')\mathrm{d}\omega' \right|^2 \tag{2.39}$$

$$\text{where} \qquad \alpha_{\omega t}(\omega') = \left(\frac{8\ln 2}{\pi\sigma_\omega^2}\right)^{\frac{1}{4}} \mathrm{e}^{-\frac{4\ln 2}{\sigma_\omega^2}(\omega'-\omega)^2 - \mathrm{i}t(\omega'-\omega)}. \tag{2.40}$$

Via Fourier transformation of $\alpha_{\omega t}(\omega')$ the electric field can also be expanded in time domain:

$$H(E^+,t,\omega) = \left| \int E^{+*}(t')\tilde{\alpha}_{\omega t}(t')\mathrm{d}t' \right|^2 \tag{2.41}$$

$$\text{where} \qquad \tilde{\alpha}_{\omega t}(t') = \left(\frac{8\ln 2}{\pi\sigma_t^2}\right)^{\frac{1}{4}} \mathrm{e}^{-\frac{4\ln 2}{\sigma_t^2}(t'-t)^2 + \mathrm{i}t'\omega}. \tag{2.42}$$

It can be shown that the coherent states form an overcomplete basis set [85], i.e., even subsets of coherent states may still be complete. One of these complete subsets of coherent states is the von Neumann basis which will be introduced in Chap. 6.

2.1.3 The Polarization State of Ultrashort Pulses

As discussed in previous sections, the electric field of light can (with few exceptions) be considered as a transversal electromagnetic wave. So far, only linearly polarized

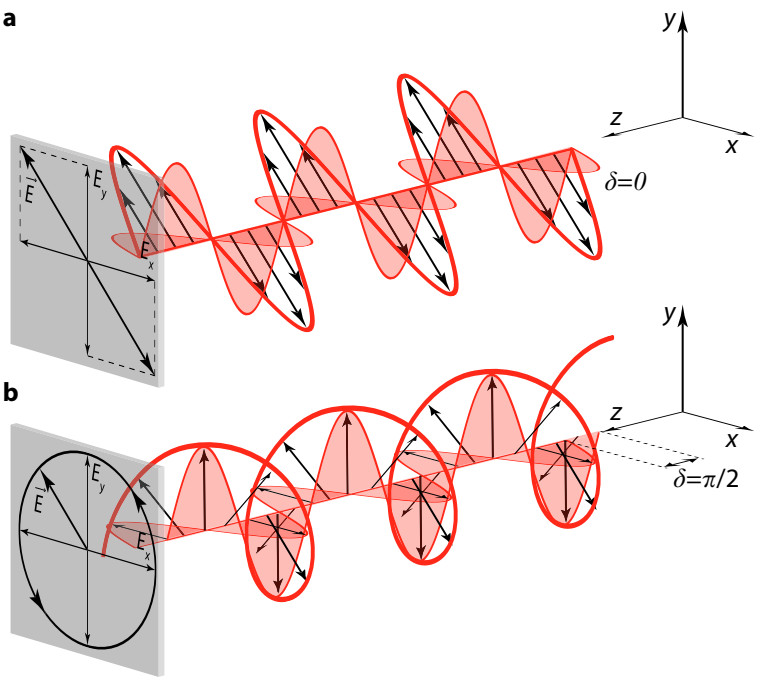

Figure 2.7 | The polarization state of a plane electromagnetic wave as a superposition of two waves with orthogonal polarization directions and specific phase difference. (a) For linear polarized light the phase difference between the two waves is zero and the two electric field vectors add up to a traveling wave with a fixed polarization direction. (b) Circular polarized light results from a phase difference of $\pi/2$ between the two components.

light was discussed, i.e., light where the electric field vector oscillates in a plane whose orientation is fixed in space. In this section, the vectorial character of ultrafast laser pulses will be discussed.

Since light is in general a transversal wave, every traveling electromagnetic wave can be considered as the vectorial sum of two linearly polarized orthogonal components [48, 86, 87]. The actual polarization state of the wave is then given by the ratio of the amplitudes of the two components and by their relative phase difference. This is illustrated in Fig. 2.7 by using the example of a continuous harmonic wave traveling in z-direction. The two orthogonal components are chosen here such that they point in x- and y- direction, respectively. In Fig. 2.7(a) the relative phase is zero resulting in a wave polarized linearly but tilted by -45° with respect to the x-direction. The convention used here is such that the polarization is defined by the view from the receiver along the negative z-direction. When the phase relation between the two waves is $\pi/2$ by shifting one of the components by $\delta z = \lambda/4$ compared to the other one, the two components add up to circularly polarized light which is characterized by the property that the electric field vector follows a helix in space along the direction of propagation. Consequently, the electric field does not change its strength but only its direction.

In general, i.e., for arbitrary amplitude ratios and phase relationships, the tip of the electric field vector describes an ellipse in space giving rise to elliptically polarized light. The same is true for ultrashort laser pulses where the polarization profile may change as a function of time. Thus, for a deeper mathematical understanding, we now consider

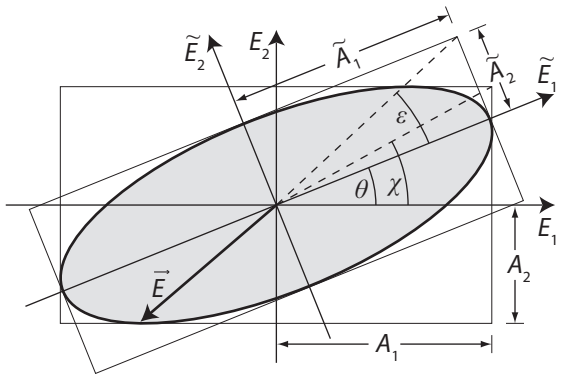

Figure 2.8 | Illustration of the elliptical pulse parameters. The orientation angle θ describes the inclination angle of the ellipse with respect to the laboratory frame, whereas ϵ defines its ellipticity angle. Both quantities are a function of the elliptical semi-major axis $\tilde{A}_1$ and semi-minor axis $\tilde{A}_2$. The magnitudes of the electric field vectors in polarization direction 1 and 2 are denoted by A_1 and A_2. The auxiliary angle χ is given by the A_2/A_1-ratio.

the electric field vector

$$\vec{E}(t) = \begin{pmatrix} E_1(t) \\ E_2(t) \end{pmatrix} = \begin{pmatrix} A_1(t)\cos[\omega_0 t + \varphi_1(t)] \\ A_2(t)\cos[\omega_0 t + \varphi_2(t)] \end{pmatrix} \tag{2.43}$$

of a laser pulse in time domain with center frequency ω_0 with its two linearly independent components $E_1(t)$ and $E_2(t)$ that can be described by the time dependent field amplitudes $A_1(t)$ and $A_2(t)$ as well as the associated temporal phases $\varphi_1(t)$ and $\varphi_2(t)$ [88, 89]. From a mathematical point of view, the parameter set $A_1(t)$, $A_2(t)$, $\varphi_1(t)$, and $\varphi_2(t)$ suffices to describe the polarization state of the laser pulse as a function of time, though it may not be very intuitive as the two polarization components interfere with each other such that the instantaneous polarization state cannot be extracted easily. Therefore, it is convenient to use the more descriptive "elliptical" representation as defined below. As mentioned above, for an arbitrary polarized stationary wave, the tip of the electric field vector follows an ellipse, as illustrated in Fig. 2.8. Assuming the SVEA (see Sect. 2.1.1), which is valid for all pulses employed in this thesis, this is still an excellent approximation for femtosecond laser pulses with a time-varying electric field and will only break down for extremely short (few-cycle) laser pulses [90]. In the following, the time dependence of all parameters is implicitly assumed, but for the sake of simplicity the time variable t is omitted.

The elliptical semi-major axis $\tilde{A}_1$ and semi-minor axis $\tilde{A}_2$ of the ellipse are tilted with respect to the laboratory frame defined by the angle θ that characterizes the orientation angle of the ellipse. The angle of ellipticity ϵ denotes the degree of which the ellipse is oval and is defined via

$$\tan\epsilon = \frac{\tilde{A}_2}{\tilde{A}_1}. \tag{2.44}$$

As shown in Fig. 2.8 the auxiliary angle

$$\chi = \arctan\frac{A_2}{A_1} \quad \in \left[0, \frac{\pi}{2}\right] \tag{2.45}$$

is introduced that describes the ratio of the two laboratory frame field amplitudes and helps to calculate ϵ and θ. In addition, we use the difference of the phase modulations

$$\delta = \varphi_2 - \varphi_1 \quad \in [-\pi, \pi] \tag{2.46}$$

between the two field components in the laboratory frame. Following Ref. [89] the elliptical pulse parameters are then given by

$$\epsilon = \frac{1}{2}\arcsin[\sin(2\chi)\sin\delta] \quad \in \left[-\frac{\pi}{4},\, \frac{\pi}{4}\right] \tag{2.47}$$

and

$$\theta = \begin{cases} \tilde{\theta} & \in [-\frac{\pi}{4},\, \frac{\pi}{4}] \quad \forall\chi \leq \frac{\pi}{4} \\ \tilde{\theta} + \frac{\pi}{2} & \in [\frac{\pi}{4},\, \frac{\pi}{2}] \quad \forall\chi > \frac{\pi}{4} \wedge \tilde{\theta} < 0 \\ \tilde{\theta} - \frac{\pi}{2} & \in [-\frac{\pi}{2},\, -\frac{\pi}{4}] \quad \forall\chi > \frac{\pi}{4} \wedge \tilde{\theta} \geq 0 \end{cases} \tag{2.48}$$

where

$$\tilde{\theta} = \frac{1}{2}\arctan[\tan(2\chi)\cos\delta] \quad \in \left[-\frac{\pi}{4},\, \frac{\pi}{4}\right]. \tag{2.49}$$

The domains of definition of the parameters are given in the square brackets in the equations above. In the used convention, the orientation angle θ is always defined in the first and fourth quadrant and thus takes values in the range $[-\pi/2,\, \pi/2]$. The ellipticity ϵ is given by the ratio of the semi-minor to the semi-major axis, i.e. $|\epsilon| \leq \pi/4$, and the sign of ϵ determines the sense of rotation where positive values correspond to left-handed and negative ones to right-handed elliptical polarization.

The total length of the instantaneous electric field vector is defined by the total intensity

$$I = \tilde{A_1}^{\,2} + \tilde{A_2}^{\,2} = A_1^2 + A_2^2. \tag{2.50}$$

Finally, a fourth parameter is necessary for a complete characterization of the electric field. This parameter will also be independent from the choice of the coordinate system (just as ϵ and I) and is termed the total phase φ. It is composed of the phase modulation φ_1 of component 1 corrected by a geometrical phase factor that adapts the phase of the field oscillations of component 1 to the ellipse-inherent coordinate system such that the reference point of phase zero is reached when the electric field vector reaches the perihelion of the light ellipse [88, 89]. It is defined by

$$\varphi = \varphi_1 + \mathrm{sign}\{\theta\epsilon\} \arccos\left[\sqrt{\frac{I}{I_1}}\cos\theta\cos\epsilon\right] \tag{2.51}$$

and still allows the definition of the instantaneous frequency by the derivative of the total phase with respect to time in analogy to the case of a linearly polarized field as introduced in Eq. (2.6). Furthermore, the total phase follows the phase of one component at times where the amplitude of the other component vanishes.

Thus instead of using $A_1(t)$, $A_2(t)$, $\varphi_1(t)$, and $\varphi_2(t)$, the parameter set consisting of $I(t)$, $\theta(t)$, $\epsilon(t)$, and $\varphi(t)$ can be used to completely specify the temporal evolution of the electric field vector as a function of time.

In some cases it is convenient to visualize the polarization state and its evolution with time in the so-called Poincaré plane which is spanned by the two θ and ϵ vectors as illustrated in Fig. 2.9(a) [91]. Points in the upper part represent left elliptically polarized light (solid ellipses), those in the lower part right elliptically polarized light (dashed ellipses). Another possibility is to project the two-dimensional (θ–ϵ) plane

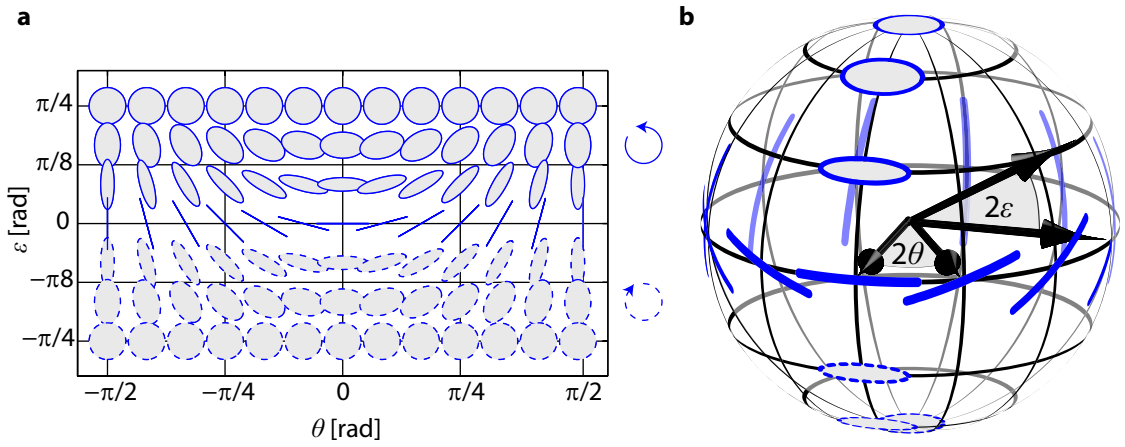

Figure 2.9 | Visualization of the polarization state of light in Poincaré phase space. (a) All possible polarization states can be described by plotting them in the two-dimensional (θ–ϵ) plane. The upper and lower parts describe left (solid ellipses) and right (dashed ellipses) elliptically polarized light. (b) For some applications it is convenient to project this plane onto a sphere, also termed the Poincaré sphere, where the azimuthal angle corresponds to 2θ and the polar angle to 2ϵ. Points on the equator describe linearly polarized light, whereas the upper and lower poles represent left-handed and right-handed circularly polarized light.

onto a sphere, called the Poincaré sphere, as it was originally introduced by the French mathematician and physicist Henri Poincaré in 1892 [92]. The spherical coordinates are mapped such that the azimuthal angle corresponds to 2θ and the polar angle to 2ϵ [Fig. 2.9(b)]. According to this, points on the equator of the sphere describe linearly polarized light whereas the upper and lower poles correspond to left-handed and right-handed circularly polarized light, respectively. The advantage of the Poincareé sphere is that it simplifies many calculations and provides an intuitive description of how polarized light behaves when it interacts with polarizing optical elements [93]. For example, the periodicity with respect to the orientation angle θ is inherently accounted for by the projection of the (θ–ϵ) plane onto a spherical surface.

2.1.4 Spatial Beam Propagation

As introduced in Sect. 2.1.1, the electric field was approximated by plane waves and the intensity distribution of the laser field orthogonal to the propagation direction was disregarded. This allowed us to describe the electric field as a function of just one spatial coordinate z associated with the propagation direction. This approximation is valid for example for point sources if the field is observed far from the origin. In contrast, lasers cannot be considered as such light sources because their light emission is highly confined in space. Most lasers are constructed such that they operate in the most fundamental transversal electromagnetic mode (TEM) of the optical laser resonator – the TEM_{00} mode. This mode is a solution to the paraxial Helmholtz equation with high axial symmetry. Thus, we can make use of cylindrical coordinates (ρ,z) and assume the paraxial approximation (i.e. $\rho \ll z$). Given these assumptions, the electric field

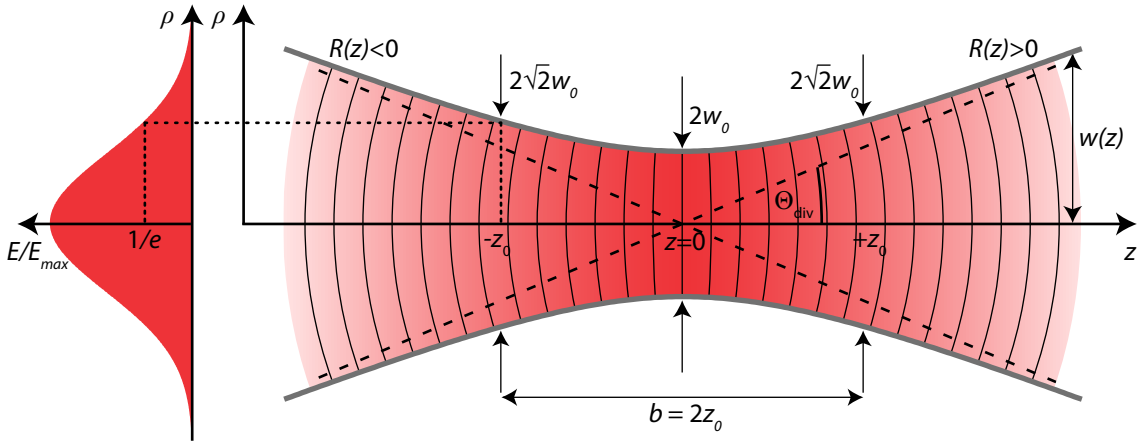

Figure 2.10 | A fundamental Gaussian mode near the beam waist. The spatial intensity in a plane orthogonal to the z-direction is given by a Gaussian distribution (left). The spot size $w(z)$, i.e., the $1/e$-radius of the electric field amplitude profile as a function of distance z is indicated by the red shaded area. The beam waist is located at $z = 0$ with the diameter $2w_0$ while at the Rayleigh length z_0 the diameter increases to $2\sqrt{2}w_0$. The radius of the wave front curvature at the focus is infinity whereas for larger z values the radius approaches z.

amplitude of the TEM_{00} mode in free space is proportional to [47, 94, 95]

$$u(\rho,z) = u_0 \frac{w_0}{w(z)} \mathrm{e}^{-\rho^2/w^2(z)} \mathrm{e}^{\mathrm{i}k\rho^2/2R(z)} \mathrm{e}^{\mathrm{i}[kz-\eta(z)]}. \tag{2.52}$$

In this equation, the first part describes the transversal field amplitude distribution where the beam diameter $w(z)$ is defined as the distance from the optical axis ($\rho = 0$) where the field amplitude has dropped to the factor $1/e$. The parameters used in Eq. (2.52) are illustrated in Fig. 2.10. Making use of the Rayleigh length z_0 and the beam waist w_0 (the beam radius at $z = 0$) $w(z)$ is given by

$$w^2(z) = w_0^2 \left[1 + \left(\frac{z}{z_0}\right)^2\right]. \tag{2.53}$$

Consequently, the beam diameter increases by a factor of $\sqrt{2}$ within the Rayleigh length. The beam waist and the Rayleigh length are connected via

$$w_0^2 = z_0 \lambda/\pi \tag{2.54}$$

from which it becomes obvious that beams with a smaller beam waist will exhibit a shorter Rayleigh length and thus will be more divergent. In this context, the so-called confocal parameter b, also called depth of focus, is introduced defined by $b = 2z_0$.

The second exponential term of Eq. (2.52) consists of a complex phase term describing the radius

$$R(z) = z \left[1 + \left(\frac{z_0}{z}\right)^2\right] \tag{2.55}$$

of the curvature of the wavefront, which is defined as the surface of points having the same phase. The radius diverges for $z \to 0$ and approaches z for larger distances.

The divergence angle Θ_{div} of the beam is given by

$$\Theta_{\mathrm{div}} = \frac{w_0}{z_0} \tag{2.56}$$

and can be approximated in the far field where $z \gg b$ by $\Theta_{\mathrm{div}} = w(z)/z$.

The last term of Eq. (2.52) contains the linear phase evolution of a plane wave but modified by the function

$$\eta(z) = \arctan\left(\frac{z}{z_0}\right), \tag{2.57}$$

termed the Gouy phase which describes an additional phase shift of π compared to a plane wave when the beam propagates through the focus.

In the later described experiments the Gaussian beam (Rayleigh length z_{01}, beam waist w_{01}) is focused with a lens or a spherical mirror into the sample. Assuming that the Rayleigh length of the incoming beam is much larger than the focal length f of the focusing element, it can be shown that the beam waist w_{02} in the focus can be estimated via [95]

$$w_{02} \approx \frac{\lambda f}{\pi \omega_{01}}. \tag{2.58}$$

Especially in such cases where non-linear processes take place in the focus of the beam or where the laser is used to obtain a high spatial resolution, the size and shape of the focus is a critical parameter. Also in cases where several beams are spatially overlapped in the focal region the parameters introduced above have to be carefully adjusted and deviations from the Gaussian beam profile should be avoided.

2.2 Nonlinear Processes in Ultrafast Optics

Ultrafast laser pulses possess the unique property that very high peak intensities can be reached. If such pulses propagate through a medium, the electric polarization $\vec{P}(\vec{r},t)$ may not respond linearly to the electric field of the light. This typically appears, if the value of the electric field is comparable to the interatomic field strength. An upper limit of this field strength can be estimated using Coulomb's law in the case of the hydrogen nucleus at a distance of the Bohr radius a_0 which results in $E_{\mathrm{atom}} = e/(4\pi\epsilon_0 a^2{}_0) = 5.1 \times 10^{11}$ V/m [96]. Electric field strengths on this order of magnitude are easily achievable with femtosecond laser pulses.

In such high intensity regimes, the conversion of the laser pulse frequency to other spectral regions is possible using particular nonlinear media. In this way, the fundamental wavelength of the laser system centered in the NIR can be converted to the visible or even to the UV spectral range, which is necessary for most experiments discussed in this work. In addition, also broader laser pulse spectra can be obtained enhancing the time resolution in spectroscopic studies. The underlying nonlinear optical processes are discussed in the following subsections.

2.2.1 Nonlinear Polarization

In the nonlinear regime, the electric polarization $\vec{P}(t)$ in a lossless and dispersionless medium can be described by a power series in terms of the electric field [47, 96, 97]:

$$\vec{P}(t) = \epsilon_0 \left(\chi^{(1)} \vec{E}(t) + \chi^{(2)} \vec{E}^2(t) + \chi^{(3)} \vec{E}^3(t) + ... \right) \tag{2.59}$$

with the $n-$th-order nonlinear optical susceptibility $\chi^{(n)}$ of the medium, which is a tensor of rank $n+1$. It can be shown that the second-order susceptibility $\chi^{(2)}$ vanishes in centrosymmetric media (i.e., isotropic materials such as glasses or crystals with inversion symmetry) and thus second-order nonlinear interactions, and also all other nonlinearities of even order, cannot occur in these materials. In contrast, third-order phenomena associated with $\chi^{(3)}$ can be observed for materials with and without inversion symmetry. Thus, in many cases the third-order polarization gives rise to the lowest nonlinear term in Eq. (2.59). Most time-resolved spectroscopic techniques such as transient absorption and coherent two-dimensional spectroscopy are also based on $\chi^{(3)}$ processes.

2.2.2 Frequency Conversion

In the following, a number of nonlinear processes such as second-harmonic generation and optical parametric amplification, which are essential for this work, are briefly discussed. An overview over these processes is given in Fig. 2.11.

Sum- and Difference Frequency Generation

We now consider the case where two laser pulses with frequencies ω_1 and ω_2 pass an optical material whose response to the applied electric field is nonlinear. The total electric field is given by

$$E_{tot}(t) = \frac{1}{2} A_1(t) \mathrm{e}^{\mathrm{i}\omega_1 t} + \frac{1}{2} A_2(t) \mathrm{e}^{\mathrm{i}\omega_2 t} + \text{c.c.}. \tag{2.60}$$

In the following we omit the vectorial character of Eq. (2.59) and assume a non-vanishing second-order nonlinear polarization (i.e. $\chi^{(2)} \neq 0$) with an instantaneous response given by

$$P^{(2)}(t) = \epsilon_0 \chi^{(2)} E_{tot}^2(t) \tag{2.61}$$

which gives rise to a signal field

$$\begin{aligned} E_s(t) \propto E_{tot}^2(t) \;\propto\; & A_1^2(t)\mathrm{e}^{2\mathrm{i}\omega_1 t} + A_1^{*2}(t)\mathrm{e}^{-2\mathrm{i}\omega_1 t} && \text{SHG } 2\omega_1 \\ & + A_2^2(t)\mathrm{e}^{2\mathrm{i}\omega_2 t} + A_2^{*2}(t)\mathrm{e}^{-2\mathrm{i}\omega_2 t} && \text{SHG } 2\omega_2 \\ & + 2A_1(t)A_2(t)\mathrm{e}^{\mathrm{i}(\omega_1+\omega_2)t} + 2A_1^*(t)A_2^*(t)\mathrm{e}^{-\mathrm{i}(\omega_1+\omega_2)t} && \text{SFG } \omega_1+\omega_2 \\ & + 2A_1(t)A_2^*(t)\mathrm{e}^{\mathrm{i}(\omega_1-\omega_2)t} + 2A_1^*(t)A_2(t)\mathrm{e}^{-\mathrm{i}(\omega_1-\omega_2)t} && \text{DFG } \omega_1-\omega_2 \\ & + 2|A_1(t)|^2 + 2|A_2^*(t)|^2. && \text{OR } \omega \approx 0 \end{aligned} \tag{2.62}$$

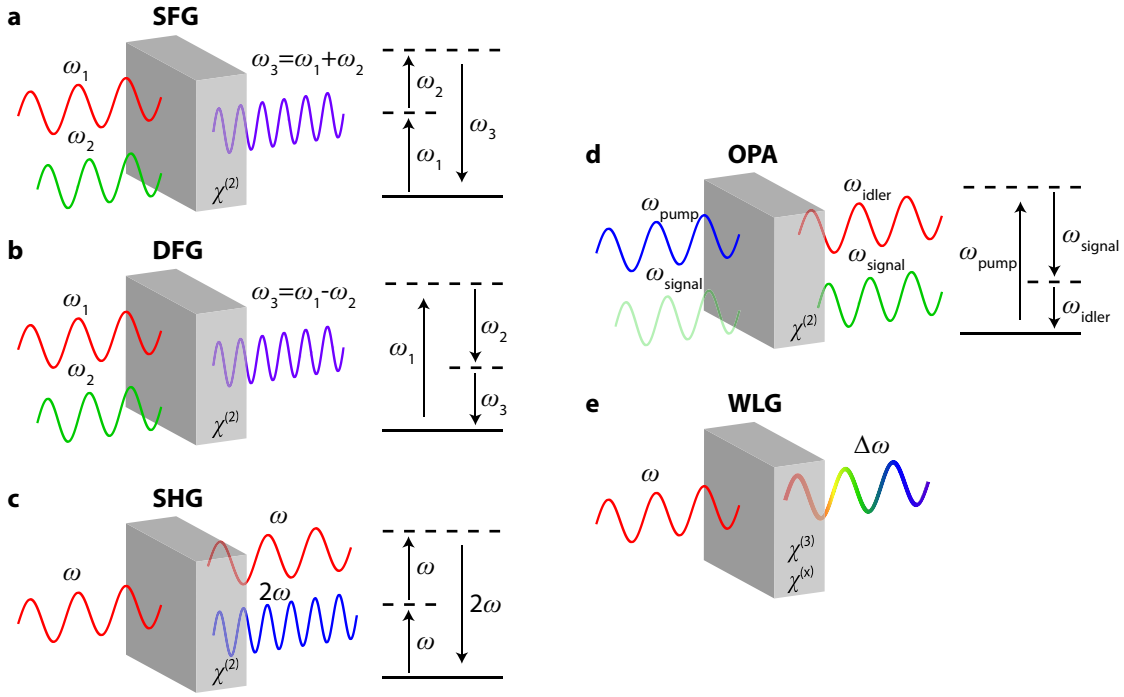

Figure 2.11 | Illustration of basic nonlinear processes and their energy-level descriptions. (a) In the process of sum-frequency generation (SFG), two input waves of different frequencies are mixed giving rise to an output field of which the frequency is given by the sum of the frequencies of the input fields. In contrast, for difference-frequency generation (DFG) (b) the frequency of the output field is given by the difference of the input fields. (c) Second-harmonic generation (SHG) can be considered as the SFG process for two input fields with the same frequency. (d) The process of optical parametric amplification (OPA) is based on DFG generation of a pump and a signal field giving rise to an idler and an amplified signal field. (e) Focusing a femtosecond laser pulse into a nonlinear optical medium can lead to white-light generation (WLG) where self-phase modulation is assumed to play a dominant role.

According to the first and second term of Eq. (2.62) a second-order polarization causes new frequencies at $2\omega_1$ and $2\omega_2$, which are the second-harmonic of the two fundamental frequencies. This process is called second-harmonic generation [SHG, Fig. 2.11(c)] which was observed for the first time in 1961 by Franken *et al.* [98]. In addition, the sum [third term in Eq. (2.62)] and the difference (fourth term) of the two frequencies can also be observed, called sum-frequency generation [SFG, Fig. 2.11(a)] and difference-frequency generation [DFG, Fig. 2.11(b)]. The SHG process can principally be considered as the SFG process for the special case $\omega_1 = \omega_2$. Additionally, the last term of Eq. (2.62) predicts the presence of a non-oscillating (DC) component, also known as optical rectification (OR).

On the right-hand side of Figs. 2.11(a)-(d) the energy-level descriptions of the processes are depicted. Being generally based on nonresonant interactions, only the atomic ground state (solid line) is an energy eigenlevel. In contrast, the dashed lines represent virtual levels that are not eigenlevels of the system but can be considered as the combined energy of the ground state and of one or more photons of the radiation field [96].

Optical Parametric Amplification

As shown in Fig. 2.11(d), a photon of frequency ω_{pump} can interact with a photon of frequency ω_{signal} giving rise to $\omega_{idler} = \omega_{pump} - \omega_{signal}$ via DFG and to an amplified signal field because the emission of additional photons at ω_{signal} can be stimulated by the existence of photons at these frequencies [96]. This process is called optical parametric amplification (OPA) and can be employed to efficiently generate broadband laser pulses over a wide spectral range, as will be shown in Sect. 3.1.2.

Phasematching

In above descriptions of second-order optical nonlinearities, we ignored the spatial dependence of the electric fields. However, to ensure that the new frequencies generated in the nonlinear material will add up constructively, it is necessary that the second-order polarization oscillates in phase with the signal field at each position in space.

For example for sum frequency generation [third term of Eq. (2.62)] the signal field at frequency ω_3 with the wave vector $\vec{k}_3$ is given by

$$E_s(\vec{r},t) = A_3(t)\mathrm{e}^{\mathrm{i}(\omega_3 t - \vec{k}_3\vec{r})} + \text{c.c.} \tag{2.63}$$

$$= 2A_1(t)A_2(t)\mathrm{e}^{\mathrm{i}\left[(\omega_1+\omega_2)t - (\vec{k}_1+\vec{k}_2)\vec{r}\right]} + \text{c.c.} \tag{2.64}$$

where $\vec{k}_1$ and $\vec{k}_2$ are the wave vectors of the incoming waves. It follows that effective frequency conversion requires

$$\vec{k}_3 = \vec{k}_1 + \vec{k}_2 \tag{2.65}$$

known as the phase matching condition. If beam 1 and 2 travel collinearly, this condition also holds for the absolute values $|\vec{k}_n| = n(\omega_n)\omega_n/c_0$ and we obtain

$$n(\omega_3)\omega_3 = n(\omega_1)\omega_1 + n(\omega_2)\omega_2. \tag{2.66}$$

With $\omega_3 = \omega_1 + \omega_2$ this condition can only be met if

$$n(\omega_3) = n(\omega_1) = n(\omega_2). \tag{2.67}$$

Yet, the refractive index is in general not constant as a function of frequency and therefore Eq. (2.67) can not be satisfied. This can be circumvented by using uniaxial birefringent nonlinear crystals where the refractive index depends on the polarization direction of the beams with respect to the optic axis of the crystal. For light with polarization parallel to the optic axis, the refractive index n_e is different from the refractive index n_o for light perpendicularly polarized to the optic axis. The subscripts e and o refer to *extraordinary* and *ordinary*. For collinear phase matching in SHG ($\omega_1 = \omega_2 = \omega$), Eq. (2.67) leads to the condition $n(\omega) = n(2\omega)$, which can be satisfied for negative uniaxial crystals (i.e., $n_e < n_o$) if the beam of the fundamental is polarized in the ordinary direction. Then phase-matching can be realized by adjusting the angle θ between the wave vector and the optic axis because the extraordinary index n_e is a function of θ and $n_o(\omega) = n_e(2\omega)$ can be achieved.

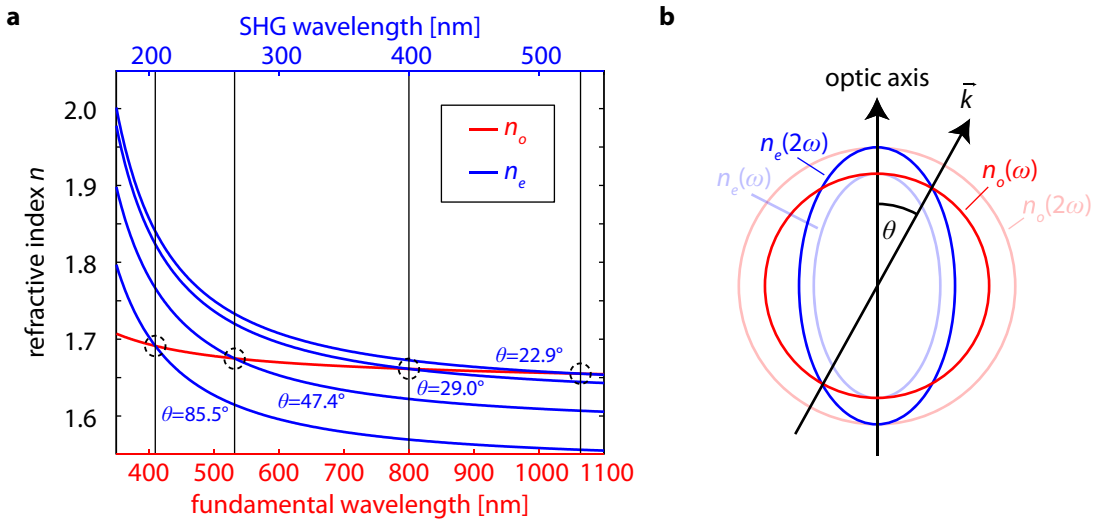

Figure 2.12 | Phase matching by angle adjustment for second-harmonic generation employing the negative uniaxial crystal BBO. (a) The ordinary index of diffraction n_o (red) as a function of the fundamental laser wavelength does not depend on the angle θ between the optic axis and $\vec{k}$. In contrast, the extraordinary index n_e (blue) varies with θ and phase matching can be achieved by adjusting θ such that $n_e(2\omega) = n_o(\omega)$ (dashed circles). This is shown here for four selected fundamental wavelengths of 410, 532, 800, and 1064 nm in which cases the phase matching angles are 85.5°, 47.4°, 29.0°, and 22.9°, respectively. (b) To achieve phase matching an intersection must exist between the index ellipsoid $n_e(\theta)$ of the extraordinary direction and the circle representing the angle-independent ordinary index n_o [95].

This principle is illustrated in Fig. 2.12 for the case of SHG using the nonlinear crystal β-barium borate (BBO). Figure 2.12(a) shows the index of refraction for ordinary (red) and extraordinary (blue) polarization directions as a function of wavelength for different angles θ. The curves were calculated using the Sellmeier equation (see e.g. Refs. [47, 99, 100]) with coefficients given in Ref. [101] and the well-known angular dependency as for example treated in Ref. [96]. The ordinary index n_o does not depend on θ and decreases for higher wavelengths. The extraordinary index shows the same trend as a function of wavelength and additionally depends on θ. Thus the fundamental wavelength for which phase matching is achieved can be adjusted by choosing the correct angle as shown here for fundamental wavelengths of 410, 532, 800, and 1064 nm (dashed circles), in which cases the phase matching angles are 85.5°, 47.4°, 29.0°, and 22.9°, respectively. As shown in Fig. 2.12(b), the extraordinary index in negative uniaxial crystals is given by an ellipsoid with $n_e(90°) = n_o$ and $n_e(\omega) < n_o(\omega)$ for all other angles θ. The ordinary index is angle independent and can thus be represented by a circle. By adjusting θ the wave vector $\vec{k}_{2\omega}$ of the second-harmonic points to the direction of the intersection of the circle and the ellipsoid where $n_e(2\omega) = n_o(\omega)$ and therefore phase matching is achieved [95].

If wave 1 and 2 (signal and idler) are polarized parallelly, this is called "type-I phase-matching" whereas in "type-II phase-matching" the two waves are polarized perpendicularly to each other.

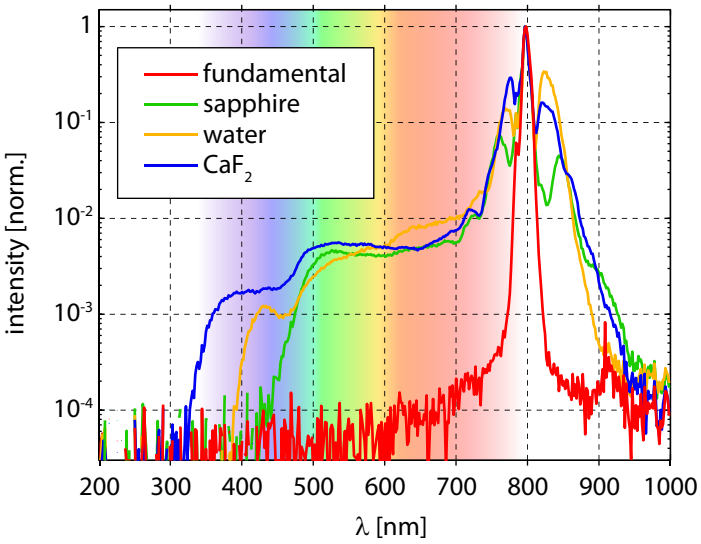

Figure 2.13 | White-light continua generated in different materials. The supercontinua are generated by focusing 100 fs pulses with about 1 μJ pulse energy centered at 800 nm (red) with an $f = 75$ mm lens into different transparent materials (semi-log scale). The supercontinuum generated in a sapphire plate (green) ranges down to 425 nm while the use of water (orange) extends the lower spectral limit below 400 nm. The material used in this work is CaF_2 (blue) yielding a white-light spectrum that exceeds the visible spectral range (indicated by the background color gradient).

White-Light Generation

Another frequently utilized nonlinear effect in ultrafast optics is the generation of a white-light supercontinuum [Fig. 2.11(e)] [47, 96, 102]. White-light generation (WLG) can in general be observed when laser pulses are focused into transparent media and was first reported by Alfano and Shapiro with picosecond pulses in 1970 [103]. Later, supercontinua ranging from 0.3 ω_0 to 2.4 ω_0 were reported [104] and theoretical models were introduced to describe this phenomenon properly.

Typical white-light spectra generated in different materials are shown in Fig. 2.13. For this purpose, the pulses at the fundamental wavelength (red) centered at 800 nm with a pulse energy of 1 μJ and 100 fs duration were focused with a lens (focal length of 75 mm) into different transparent media. The spectrum generated in sapphire (green) ranges from 450 nm up to the near IR. Also liquids like water (orange) can be used leading to a blue-edge spectral limit slightly below 400 nm. One of the most effective solid-state media for white-light generation for spectroscopic purposes is CaF_2 (blue) which allows the generation of white-light supercontinua exceeding the visible spectral range [105–107]. Yet, the major drawback of Caf_2 as a source for supercontinua lies in the fact that the material gets irreversibly damaged if it is not constantly moved during illumination.

As the nonlinear effect of white-light generation can be observed in isotropic materials with inversion symmetry in which the second-order susceptibility $\chi^{(2)}$ vanishes it can be concluded that this effect is caused by the third-order susceptibility $\chi^{(3)}$. Considering only contributions oscillating at the same frequency as the incoming field, the dielectric

polarization is given under these circumstances by

$$P(t) = \epsilon_0\chi^{(1)}\left[E^+(t) + \text{c.c.}\right] + \epsilon_0\chi^{(3)}\left[E^+(t) + \text{c.c.}\right]^3 \tag{2.68}$$

$$= \epsilon_0\left[\chi^{(1)} + \frac{3\chi^{(3)}}{4}|A(t)|^2\right]E^+(t) + \text{c.c.} \tag{2.69}$$

$$= \epsilon_0\left[\chi^{(1)} + \frac{3\chi^{(3)}}{2\epsilon_0 c_0 n_0}I(t)\right]E^+(t) + \text{c.c.} \tag{2.70}$$

$$=: \epsilon_0\chi_{\text{eff}}E^+(t) + \text{c.c.}. \tag{2.71}$$

Thus, the total effective susceptibility χ_{eff} can be expressed in terms of the sum of the linear term and the intensity dependent nonlinear susceptibility.

In the linear regime the refractive index of the medium is given by $n_0 = \sqrt{1+\chi^{(1)}}$, but in the nonlinear case $\chi^{(1)}$ has to replaced by χ_{eff} as defined in Eqs. (2.70) and (2.71) leading to

$$n(t) = \sqrt{1+\chi_{\text{eff}}(t)} = \sqrt{1+\chi^{(1)} + \frac{3\chi^{(3)}}{2\epsilon_0 c_0 n_0}I(t)} \tag{2.72}$$

$$= n_0\sqrt{1 + \frac{3\chi^{(3)}}{2\epsilon_0 c_0 n_0^3}I(t)} \approx n_0\left[1 + \frac{3\chi^{(3)}}{4\epsilon_0 c_0 n_0^3}I(t)\right] \tag{2.73}$$

$$=: n_0 + n_2 I(t) \tag{2.74}$$

resulting in the intensity-dependent refractive index where $n_2 = 3\chi^{(3)}/4\epsilon_0 c_0 n_0^3$ is the nonlinear index coefficient [47].[1] This process is known as the *optical Kerr effect*. The consequence of the Kerr effect is on the one hand that the transversal beam profile of the laser pulse with its varying transversal intensity leads to a spatial modulation of the refraction index causing lensing effects, also called self-focusing or Kerr lensing [47, 96]. On the other hand, the temporal intensity variation of the laser pulse leads to a temporal phase modulation giving rise to what is known as *self-phase modulation* (SPM). This effect can be explained considering the temporal phase as introduced in Eq. (2.5) (with $\Phi_0 = 0$) explicitly at a given z-position:

$$\Phi(t,z) = \omega_0 t + \varphi(t) - kz = \omega_0 t + \varphi(t) - \frac{n(t)\omega_0}{c_0}z$$

$$= \omega_0 t + \varphi(t) - \frac{z\omega_0}{c_0}\left[n_0 + n_2 I(t)\right] \tag{2.75}$$

where the time dependent refractive index as given in Eq. (2.74) was used. The instantaneous frequency as the time derivative of $\Phi(t,z)$ [Eq. (2.6)] is hence given by

$$\omega(t,z) = \frac{\mathrm{d}\Phi(t,z)}{\mathrm{d}t} = \omega_0 + \frac{\mathrm{d}\varphi(t)}{\mathrm{d}t} - \frac{z\omega_0 n_2}{c_0}\frac{\mathrm{d}I(t)}{\mathrm{d}t}. \tag{2.76}$$

[1] In Eq. (2.73) we made the approximation $\sqrt{1+x} \approx 1 + x/2$ for $x \ll 1$, which is valid because $n_2 I \ll n_0$.

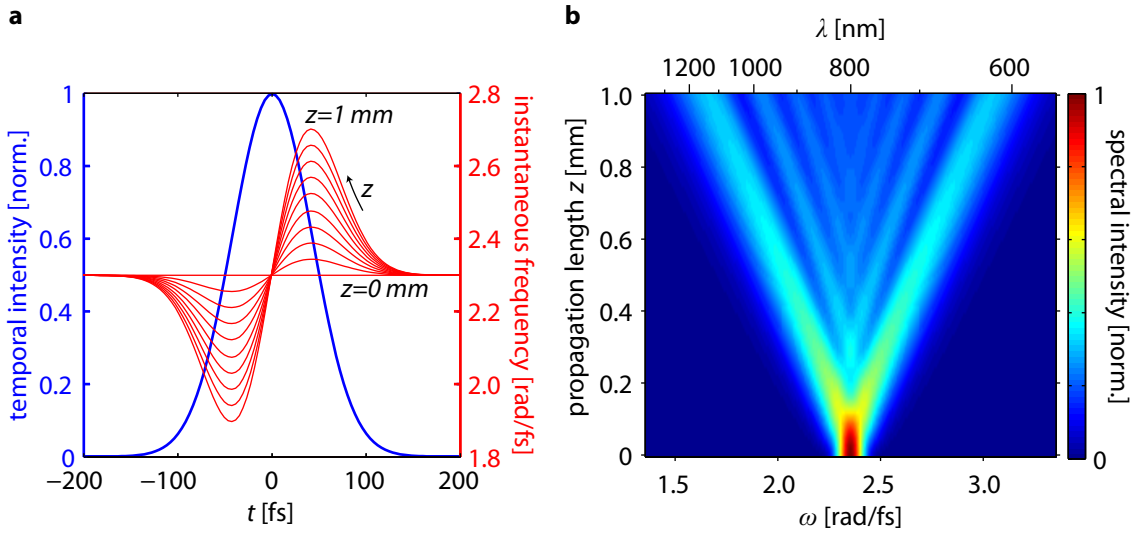

Figure 2.14 | Principle of self-phase modulation. Pulse broadening by SPM is simulated with an initially bandwidth-limited 100 fs Gaussian pulse centered at 800 nm traveling through 1 mm of sapphire with a peak intensity of $1.2 \cdot 10^{11}$ W/cm^2. (a) The temporal intensity profile (blue) leads to a temporal phase modulation that causes a decrease of the instantaneous frequency (red) at the leading edge of the pulse and an increases of the frequency at the trailing edge. (b) The frequency broadening becomes apparent in the spectral evolution as a function of the propagation length z, which is linear in z and symmetric with respect to ω_0 if only SPM is considered.

This means that the phase modulation in Eq. (2.75) leads to the generation of new frequencies during pulse propagation because the temporal intensity profile causes a shift of the instantaneous frequency. This is illustrated in Fig. 2.14 where the self-phase modulation of a 100 fs pulse centered at 800 nm with a Gaussian temporal intensity profile (9.4 nm bandwidth) traveling through 1 mm of sapphire ($n_2 \approx 3 \cdot 10^{-16}$ cm^2/W [108]) is simulated. As shown in Fig. 2.14(a) the leading edge of the temporal profile (blue line), where $\mathrm{d}I(t)/\mathrm{d}t > 0$, leads to a spectral red-shift whereas the trailing edge with $\mathrm{d}I(t)/\mathrm{d}t < 0$ causes a blue-shift of the instantaneous frequency (red lines for different propagation lengths z). In Fig. 2.14(b) the evolution of the pulse spectrum is depicted as a function of the propagation length z. The maximum of the spectrum of the incoming pulse at 800 nm is strongly reduced while new frequencies at the blue- and red-edge are generated during the propagation along z. While in the simulation the material dispersion and the transversal beam profile (and thus spatial effects like self-focusing) were neglected, both processes will have a strong effect in a real medium.

Self-phase modulation is considered as the dominant starting mechanism behind white-light generation, but this effect alone is not sufficient to explain the broad and asymmetric spectra as observed in experiments, which becomes obvious when Fig. 2.13 is compared to Fig. 2.14(b). It is now widely accepted that other (predominantly nonlinear) effects like self-steepening, Kerr lensing, material dispersion, and plasma formation have to be taken into account as well [109–112].

2.3 Photochemical Processes

Many fundamental processes in our daily life are based on photochemical processes. In this work, different organic photoreactive compounds are employed serving as model systems for various ultrafast time-resolved spectroscopy methods. In order to understand the underlying photochemical processes a short introduction to this topic is given in the following sections.

2.3.1 Electronic States and Transitions

As molecules are microscopically small objects on the order of a few angstroms that are composed of electrons and atomic nuclei, a quantum mechanical treatment is necessary to describe and understand their properties entirely. In order to evaluate the stationary states of a molecule with discrete energy levels E, we have to solve the Schrödinger equation

$$\hat{H}|\Psi(\vec{r},\vec{R})\rangle = E|\Psi(\vec{r},\vec{R})\rangle \tag{2.77}$$

where $\hat{H}$ is the Hamilton operator and $|\Psi(\vec{r},\vec{R})\rangle$ the associated wave function which is a function of the coordinates of the electrons $\vec{r}$ and the nuclei $\vec{R}$ [84, 113, 114]. The Hamilton operator can be expressed in terms of a sum

$$\hat{H} = T_\mathrm{e} + T_\mathrm{N} + V_\mathrm{ee} + V_\mathrm{eN} + V_\mathrm{NN} \tag{2.78}$$

of the kinetic energies of the electrons (T_e) and nuclei (T_N), and the electron–electron (V_ee), electron–nuclear (V_eN), and nuclear–nuclear (V_NN) potential energies. As even for the simplest molecule – the H_2^+ ion – no exact analytical solution is possible, certain approximations need to be introduced. As electrons are much lighter than the nuclei, it can be assumed that electrons will follow the motion of the nuclei quasi instantaneously. For this reason, the *Born–Oppenheimer approximation* was introduced [115], neglecting the electron–nuclear correlation of motion, which is why it is sometimes also called the *adiabatic approximation*. Disregarding spin contributions and rotational states, the total wavefunction can thus be factorized into a product

$$|\Psi(\vec{r},\vec{R})\rangle = |\Psi^e(\vec{r},\vec{R})\rangle|\chi(\vec{R})\rangle \tag{2.79}$$

of an electronic wavefunction $|\Psi^e(\vec{r},\vec{R})\rangle$ for fixed nuclear coordinates and a vibrational wavefunction $|\chi(\vec{R})\rangle$. As a consequence, electronic *potential energy surfaces* (PES) can be calculated point–by–point, by fixing the nuclear positions at different molecular geometries because the electronic term only depends on the nuclear coordinates and not on their motions.

In order to describe the transition probabilities between different molecular eigenstates, we consider the coupling of the classically treated electric field $E(t)$ with the dipole moment of the molecule. Using the elementary charge e and the charges of the nuclei Z_k, we define the dipole moment operator

$$\hat{M} = -e\left(\sum_j \vec{r}_j - \sum_k Z_k\vec{R}_k\right), \tag{2.80}$$

which can be used to calculate the transition probability between an initial state i to a final state f. This probability is determined by the square of the absolute value of the transition moment $\mu_{i\to f}$ given by

$$\begin{aligned}\mu_{i\to f} =&\langle\Psi_f(\vec{r},\vec{R})|\hat{M}|\Psi_i(\vec{r},\vec{R})\rangle = \\ =&-e\sum_j\langle\Psi_f^e(\vec{r}_j,\vec{R})|\vec{r}_j|\Psi_i^e(\vec{r},\vec{R})\rangle\langle\chi_f(\vec{R})|\chi_i(\vec{R})\rangle \\ &+\sum_k eZ_k\langle\Psi_f^e(\vec{r}_j,\vec{R})|\Psi_i^e(\vec{r},\vec{R})\rangle\langle\chi_f(\vec{R})|\vec{R}_k|\chi_i(\vec{R})\rangle.\end{aligned} \tag{2.81}$$

In contrast to pure vibrational transitions where no change of the electronic wavefunction occurs (i.e., $|\Psi_i^e\rangle = |\Psi_f^e\rangle$), for electronic transitions the second term of Eq. (2.81) vanishes since different electronic eigenstates are orthogonal (i.e., $\langle\Psi_f^e(\vec{r}_j,\vec{R})|\Psi_i^e(\vec{r},\vec{R})\rangle = 0$ for $i \neq f$). Consequently, the expression for the transition dipole moment can be simplified to [114]

$$\mu_{i\to f} = \left[-e\sum_j\langle\Psi_f^e(\vec{r}_j,\vec{R})|\vec{r}_j|\Psi_i^e(\vec{r},\vec{R})\rangle\right] \times \langle\chi_f(\vec{R})|\chi_i(\vec{R})\rangle. \tag{2.82}$$

According to this equation, the transition probability is determined by two terms. The first term of Eq. (2.82) is called the *electric-dipole transition moment*, which describes the electronic redistribution associated with the photoexcitation. The second term is the overlap integral of the nuclear wave functions, i.e., of the vibrational levels of initial and final vibrational state. The squared value $|\langle\chi_f(\vec{R})|\chi_i(\vec{R})\rangle|^2$ is called the *Franck–Condon factor*. From this it follows that a larger overlap between the initial and final vibrational wave functions leads to an increased transition probability between the two vibrational states.

Another frequently used physical quantity used in this context is the oscillator strength $f_{i\to f}$. The oscillator strength is a dimensionless parameter that can be calculated using $\mu_{i\to f}$ via

$$f_{i\to f} = \frac{2m_e\omega_{i\to f}}{3\hbar e^2}|\mu_{i\to f}|^2 \tag{2.83}$$

where m_e is the electron mass and $\omega_{i\to f}$ the frequency of the radiation field necessary for a transition from the initial to the final state. The oscillator strength is well suited for comparing the relative transition probabilities between different electronic states or molecular configurations. For forbidden electronic transitions f approaches zero, whereas for very strong electronic transitions it reaches values close to 1. The oscillator strength can be determined experimentally by integration over the absorption band [114].

Different molecular state representations to visualize electronic and vibrational levels are used in the literature. The *Jablonski diagram* depicts electronic levels as a function of energy. It also visualizes transitions between states and is especially useful for that class of molecules that do not undergo substantial configurational changes upon photoexcitation. An exemplary Jablonski diagram is shown in Fig. 2.15(a) including the

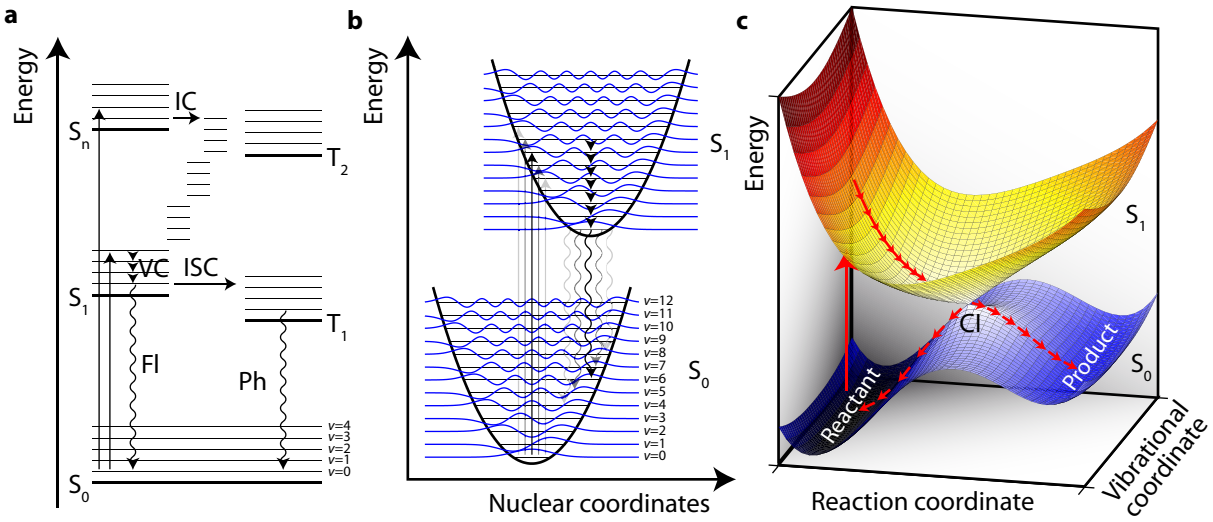

Figure 2.15 | Molecular electronic state representations. (a) The Jablonski diagram can be used to visualize involved electronic eigenstates and transition between them which is shown here exemplary for a system with several singlet (S_0, S_1, S_n) and triplet states (T_1, T_2). (b) To illustrate the Franck–Condon principle and the red shift of the fluorescence (Kasha's rule), the dependency of the potential energy on the nuclear coordinates has to be considered, as done here for the case of harmonic S_0 and S_1 potentials with their associated (analytical) vibrational wave functions (blue curves). (c) The concept of potential energy surfaces is commonly used in photochemistry. The reaction from the reactant to the product can then be considered as the motion of a wave packet on a high-dimensional hypersurface.

lowest electronic singlet state S_0, the first excited state S_1, another higher lying singlet state S_n, and two triplet states T_1 and T_2 (thick horizontal lines). The vibrational states can be considered as additional levels on top of each electronic level characterized by a vibrational quantum number v (thin horizontal lines). Absorption of a photon of proper energy excites the molecule from the ground state to an excited state (vertical straight arrows). Since in general this process involves also a vibrational excitation, higher vibrational levels will be populated after excitation and thus the molecule will undergo *vibrational cooling* (VC, small arrowheads), also called vibrational relaxation, to the lowest vibrational state of the corresponding electronic level. As radiative processes typically have a much larger time constant, they cannot compete with VC, which is the basis for *Kasha's rule*, stating that polyatomic molecules luminesce predominantly from the lowest vibrational state of a given electronic level [114, 116]. Once the molecule reaches the lowest vibrational level different radiative and nonradiative deexcitation processes may take place. *Fluorescence* (Fl) is observed for radiative transitions between states of the same spin multiplicity while *phosphorescence* (Ph) occurs when the involved states possess different multiplicities (usually triplet → singlet transitions). Nonradiative transitions between different electronic states of the same spin multiplicity are called *internal conversion* (IC), the same process for states of different multiplicity is referred to as *intersystem crossing* (ISC).

The potential energy can also be visualized as a function of one (or several) of the nuclear coordinates, as shown exemplary in Fig. 2.15(b) for a harmonic potential. The

transition probability (straight arrows for absorption, undulated arrows for fluorescence) is given by the Franck–Condon factors determined by the square of the integrated overlap between the vibrational states (blue curves). The onset of the S_1 state with respect to S_0 and the fact that fluorescence originates (as a direct consequence of Kasha's rule) from the lowest vibrational S_1 state generally leads to a spectrally red-shifted fluorescence.

2.3.2 Photochemical Reactions

As already indicated in Fig. 2.15(b), the vibrationally relaxed electronic excited state molecular configuration differs for most photosystems from the ground state configuration. As a consequence, photoexcitation is in many cases accompanied by a structural rearrangement of the molecule which is caused by the spatial redistribution of the electronic probability density. Nevertheless, in most cases the molecule returns to its original structure upon relaxation to the electronic ground state.

In contrast, *photoreactive* molecules can undergo major structural changes after photoexcitation. In this context, the concept of potential energy surfaces has to be introduced. It allows us to describe the molecular motion as a propagation of a wave packet (see Sect. 2.3.3) in an $n = (3N - 6)$-dimensional phase space, where N is the number of atoms in the molecule [114].[2] The PES then describes the molecule's potential energy as a function of the molecular coordinates. These are typically atomic Cartesian coordinates, but in many cases it is more intuitive to employ a transformation of coordinates to internal molecular coordinates such as bond lengths, bond angles, or torsional angles. For photoreactive systems, the PES is constituted in such a way that a structural change is possible (or even favored) after excitation to an excited electronic state and the molecule may thereupon reach another local minimum of the PES. Such a process is visualized in Fig. 2.15(c) where a fictitious PES is plotted as a function of two independent molecular coordinates. One of them is associated with the reaction coordinate, a second one with another vibrational coordinate of the molecule. The reactant is located in the global minimum of the S_0-state, which means that this point is a minimum with respect to all internal degrees of freedom. By excitation to S_1 the molecule is transferred to an elevated point and the molecule then follows the gradient of the PES. For this reason the shape of the PES is the decisive parameter for the outcome of the photoreaction. In the depicted example, there is no local maximum along the reaction coordinate, but in the S_0-state a local maximum is found preventing the thermal reaction in the electronic ground state. Such local maxima are called *transition states* (TS) and are involved in many (photo)reactions [114, 117].

Another important concept in photochemistry is also shown in Fig. 2.15(c). The depicted energy profiles share a single point where the two surfaces are degenerate and an intersection between ground and excited state is formed. It can be shown that PESs are allowed to cross in an $(n - 2) = (3N - 8)$-dimensional subspace [114]. If the two PESs are plotted as a function of the two remaining coordinates (also called branching plane), they form the shape of a cone centered at the degeneracy, which is the reason why such points are called *conical intersections* (CI) [118–121]. At a conical intersection

[2] The number $n = (3N - 6)$ only strictly holds for non-linear molecules where 3 translational and 3 rotational degrees of freedom have to be accounted for.

the Born–Oppenheimer approximation fails and the non-adiabatic coupling between the two states has to be taken into account. Conical intersections play a major role in many photochemical processes because their existence permits ultrafast and therefore highly-effective transitions between electronic states. As a result of the conical intersection in Fig. 2.15(c), the molecule may either react radiationless towards the product side or relax back to the reactants region of the PES.

The physical parameter which is commonly used to quantify the efficiency of a photochemical process $A \rightarrow B$ is the *quantum yield* $\Phi_{A\rightarrow B}$ [114]. It is defined as the ratio of the number n_B of product molecules formed to the amount of photons n_p absorbed by the reactant at a specific wavelength:

$$\Phi_{A\rightarrow B} = \frac{n_B}{n_p} \tag{2.84}$$

It follows from this definition that the quantum yield of a process like $A \rightarrow B$ is always in the range $0\ \% \leq \Phi_{A\rightarrow B} \leq 100\ \%$.

2.3.3 Molecular Wave-Packet Dynamics

Femtosecond lasers are light sources that emit spectrally broad and highly coherent electromagnetic waves in the form of ultrashort laser pulses. With such laser pulses it is not only possible to transfer energy to a photosystem via photoexcitation, but also the coherent character of the light field can be transferred to matter.

We now assume that a laser pulse is used to excite a molecule from an electronic ground state to some excited electronic state. Typically, the laser bandwidth of a femtosecond laser pulse covers several vibrational levels of the molecule. In order to understand the nature of molecular wave packets the time evolution $\mathrm{e}^{-\frac{\mathrm{i}}{\hbar}E_v t}$ of the quantum states with energies E_v ($v = 0,\ 1,\ 2,\ 3,...$) has to be included explicitly. The coherent excitation of several vibrational states can be expressed in terms of a linear combination of the vibrational levels yielding the total vibrational wave function [84]

$$|\chi(\vec{R},t)\rangle = \sum_v a_v |\chi_v(\vec{R})\rangle \mathrm{e}^{-\frac{\mathrm{i}}{\hbar}E_v t} \tag{2.85}$$

where a_v stands for the amplitude of each vibrational level given by the laser spectrum and the corresponding transition dipole moment. If only a single vibrational level is excited (for instance by a narrowband continuous wave laser), the squared absolute value of the wave function is time independent as the time evolution operators cancel. The result is a stationary probability distribution. However, for a coherent superposition of different vibrational states, cross-terms of the form $\mathrm{e}^{-\frac{\mathrm{i}}{\hbar}(E_v - E_{v+1})t} = \mathrm{e}^{\mathrm{i}\hbar w_{\mathrm{vib}} t}$, $\mathrm{e}^{-\frac{\mathrm{i}}{\hbar}(E_v - E_{v+2})t} = \mathrm{e}^{\mathrm{i}\hbar 2 w_{\mathrm{vib}} t}$, etc. arise resulting in an oscillating probability distribution as a function of time with the classical vibrational frequency $w_{\mathrm{vib}} = (E_{v+1} - E_v)/\hbar$.

The phenomenon of a molecular vibrational wave packet in a harmonic potential with a periodic time of $T = 100$ fs is illustrated in Fig. 2.16. To illustrate the transition from a stationary state to the quasi-classical limit, different numbers of eigenstates are superposed by varying the width of a Gaussian amplitude function centered at $v = 5$. In Fig. 2.16(a) the Gaussian FWHM is set to 0.5 $\hbar\omega_{vib}$ such that virtually only the

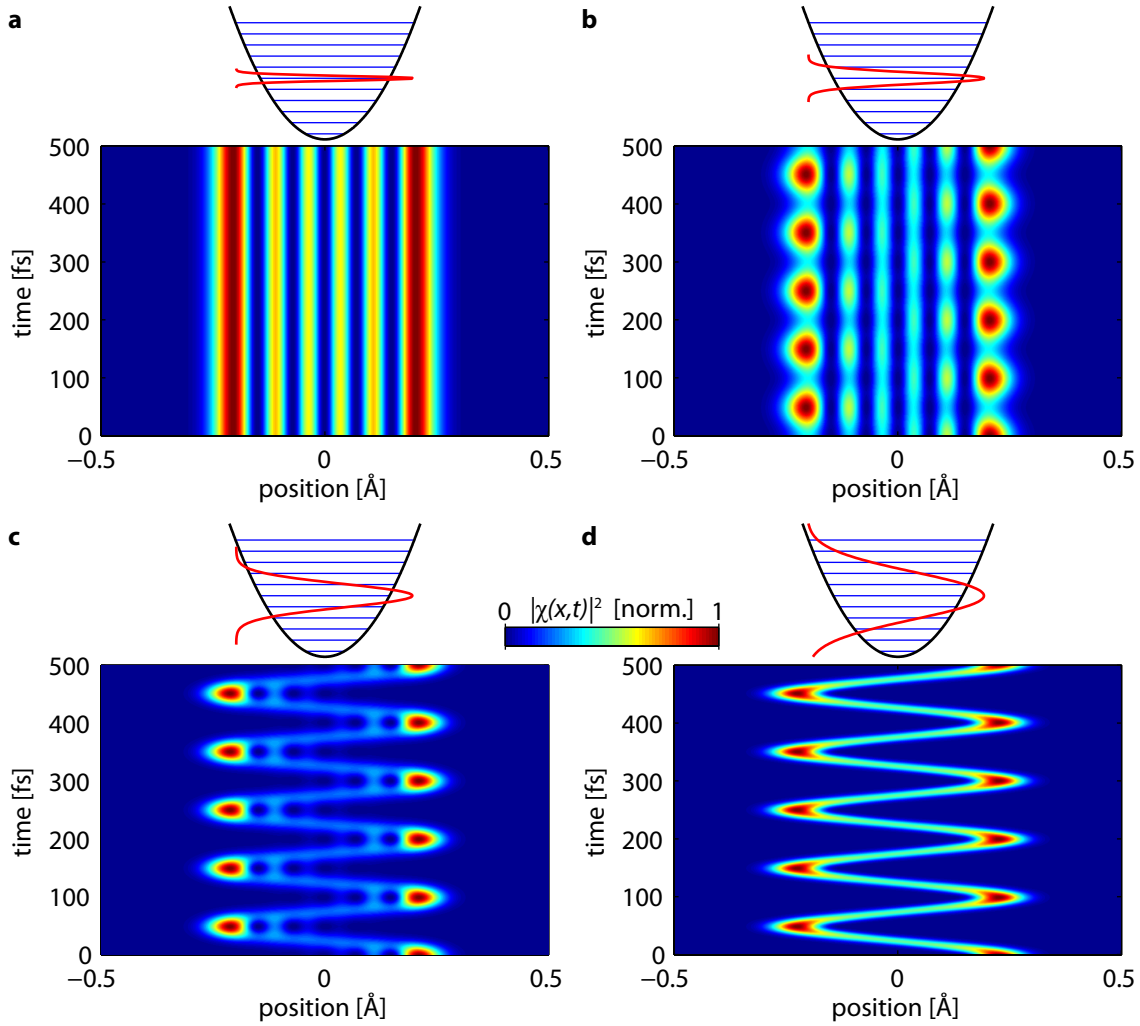

Figure 2.16 | Simulation of the temporal evolution of the probability distribution $|\chi(\vec{R},t)|^2$ of a Gaussian vibrational wave packet in a harmonic potential with T = 100 fs. The amplitudes of the vibrational states contributing to the wave packet are indicated above each panel by the Gaussian amplitude profiles (red) centered at $\nu = 5$ for different FWHM widths of (a) 0.5 $\hbar\omega_{vib}$, (b) 1.2 $\hbar\omega_{vib}$, (c) 2.5 $\hbar\omega_{vib}$, and (d) 5 $\hbar\omega_{vib}$.

$v = 5$ state is excited resulting in a stationary distribution. In Figs. 2.16(b)–(d), the Gaussian width was set to 1.2 $\hbar\omega_{vib}$, 2.5 $\hbar\omega_{vib}$, and 5 $\hbar\omega_{vib}$, respectively, resulting in temporally oscillating probability distributions with increasing localization with respect to the nuclear coordinates. This demonstrates that the more eigenstates are excited simultaneously, the more localized the wave packet gets. For large amounts of excited vibrational eigenstates [Fig. 2.16(d)] the dynamics are comparable to the classical sinusoidal motion of the harmonic oscillator, which is the reason why this is called the *quasi-classical limit*.

Coherent vibrational wave packets were already observed in the early days of femtosecond spectroscopy in many different molecular systems such as liquids [122, 123], dyes in solution [124, 125], small molecules in the gas phase [126], unimolecular reactions [127–129], and even in biological systems [130–132], which demonstrates that such

vibrationally coherent phenomena can be induced in a large variety of molecular systems. In principle molecular wave packets are not limited to vibrational states. Also coherent rotational wave packets [133–136] exploited in molecular alignment techniques [137] and coherences between electronic states [138–141] can be induced and analyzed by femtosecond laser pulses.

3 Experimental Techniques

In this chapter the main techniques relevant for the realization of the experiments discussed in this thesis will be briefly explained. A schematic overview of the experimental setup, which is placed on a damped optical table, is shown in Fig. 3.1. In essence, it consists of a commercial Ti:Sa oscillator and amplifier system followed by elements for frequency conversion necessary for obtaining broadband tunable pump laser spectra in regions ranging from 250 nm up to 1000 nm. A home-built pulse shaper is used to manipulate those laser pulses for pulse characterization, pulse compression, and for spectroscopic purposes. For most applications, a simple SHG-crystal was employed for collinear pulse characterization. A variable temporal delay can be introduced using a mechanical translation stage allowing for a maximum delay of the pump pulses of roughly 4 ns. For transient absorption, every second pump pulse needs to be blocked, which was done using a phase-locked optical chopper. The actual experiments were performed in a home-built transient absorption setup where the pump and probe beams were spatially and temporally overlapped by focusing them into a quartz flow cell. A spectrometer, consisting of a spectrograph with two separated entrance slits and a two-dimensional CCD chip, was used to determine the spectra of the employed laser pulses. Most of these elements and their functional principles will be discussed in more detail in the following section. First, the laser system and necessary elements for frequency conversion are explained (Sect. 3.1). Then, the technique of LCD-based frequency-domain pulse shaping is briefly reviewed (Sect. 3.2). This is followed by a short introduction to the utilized methods for femtosecond pulse characterization and compression (Sect. 3.3). In the end, a short overview over transient absorption (Sect. 3.4) and coherent two-dimensional spectroscopy (Sect. 3.5) is given.

3.1 Femtosecond Laser Pulse Generation

3.1.1 Ti:Sapphire Lasers and Chirped Pulse Amplification

The centerpiece of a state-of-the-art femtosecond laser is a so-called oscillator consisting of a pump laser, a gain medium, and an optical resonator of length L. The longitudinal modes are standing waves of the resonator cavity equally spaced in frequency domain at

$$\omega_m = \frac{2\pi m c}{2 n_{\text{eff}} L} \tag{3.1}$$

where m is a positive integer and n_{eff} the effective average refractive index of the cavity [47]. Thus, the mode spacing is given by

$$\Delta = \omega_{m+1}/(2\pi) - \omega_m/(2\pi) = c/(2 n_{\text{eff}} L). \tag{3.2}$$

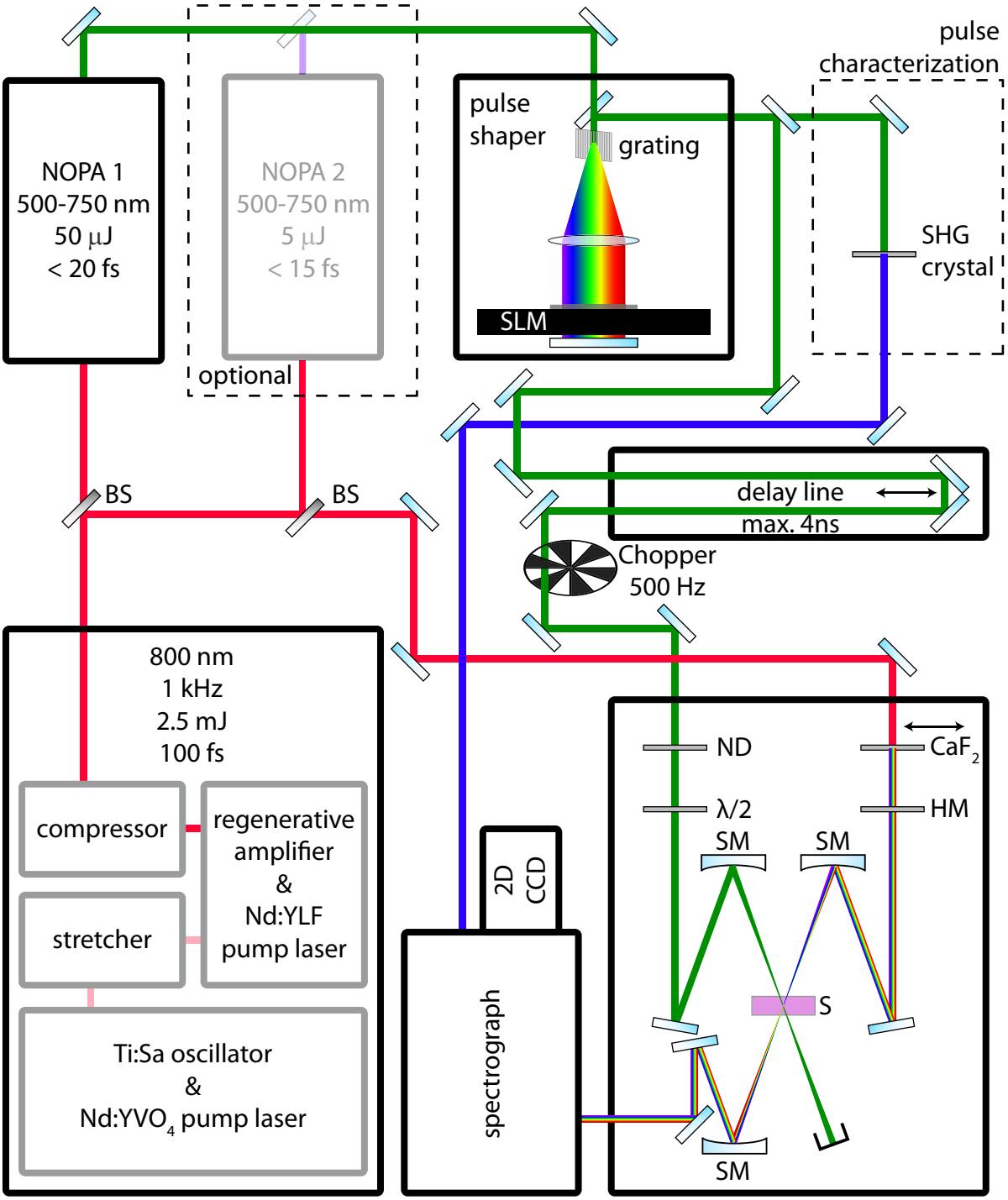

Figure 3.1 | Schematic overview of the setup used for most experiments presented in this thesis. All components are placed on a damped optical table, including the Ti:Sa amplifier as the light source, elements for frequency conversion, pulse shaping, pulse characterization, temporal pulse delay, transient absorption measurements, and spectral pulse characterization. Some of the employed optical elements are beam splitters (BS), a neutral density filter (ND), a half-wave plate ($\lambda/2$), a hot mirror (HM), the sample inside a flow cell (S), and spherical mirrors (SM). The Ti:Sa oscillator and amplifier system, NOPA 1, SLM, delay line, Spectrograph, and the CCD are computer-controllable.

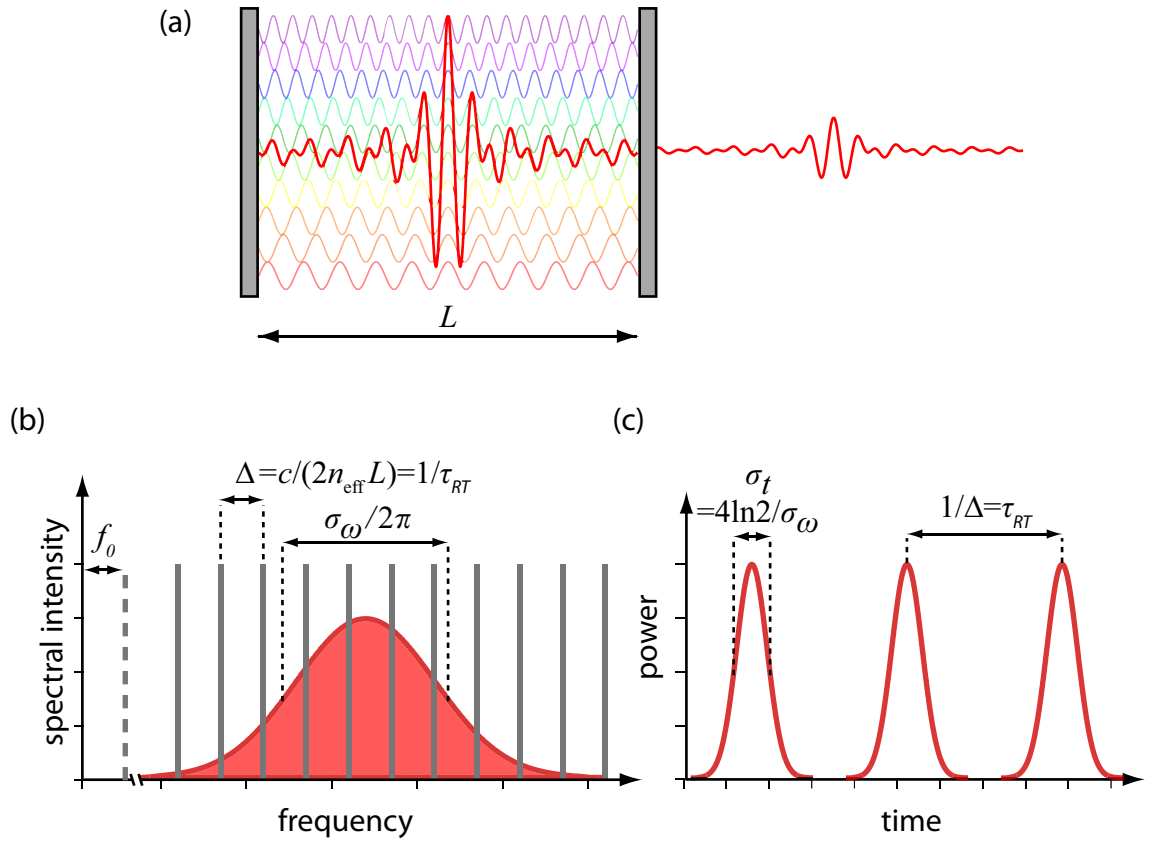

Figure 3.2 | Ultrashort laser pulse generation via mode locking. (a) By superposing many longitudinal resonator modes of the laser cavity of length L, an ultrashort laser pulse is generated by forcing the modes to share the same phase. (b) The longitudinal modes (grey vertical lines) are equally spaced in frequency domain forming a frequency comb with a frequency spacing of Δ and an offset f_0. Only those modes located within the amplification profile of the gain medium (red curve) will be emitted leading (c) in time domain to a sequence of laser pulses with a temporal separation of τ_{RT}.

In order to enable a laser to operate in a pulsed mode, the basic idea is to force those longitudinal cavity modes to share the same phase offset such that they add up at a specific instant of time resulting in an ultrashort 'burst' of light as illustrated schematically in Fig. 3.2(a). As shown in Fig. 3.2(b) only those modes (vertical gray lines) that are located within the amplification profile of the gain medium (red) are amplified and can contribute to the laser emission. The laser pulse travels through the cavity with a roundtrip time $\tau_{RT} = n_{\text{eff}}L/c$ and a small portion of it is transmitted by one of the cavity mirrors (output coupler) resulting in a sequence of femtosecond laser pulses at a repetition rate of $1/\tau_{RT} = \Delta$, as depicted in Fig. 3.2(c). Hence the oscillator's repetition rate is given by the optical path length of the resonator, whereas the pulse duration is limited by the spectral amplification bandwidth of the gain medium.

In Eqs. (3.1) and (3.2) the refractive index is assumed to be constant as a function of frequency. This approximation is not true for real laser cavities where material dispersion, e.g., in the gain medium, has to be taken into account. For this reason, the following essential conditions must be met for a working femtosecond laser: firstly, a mechanism

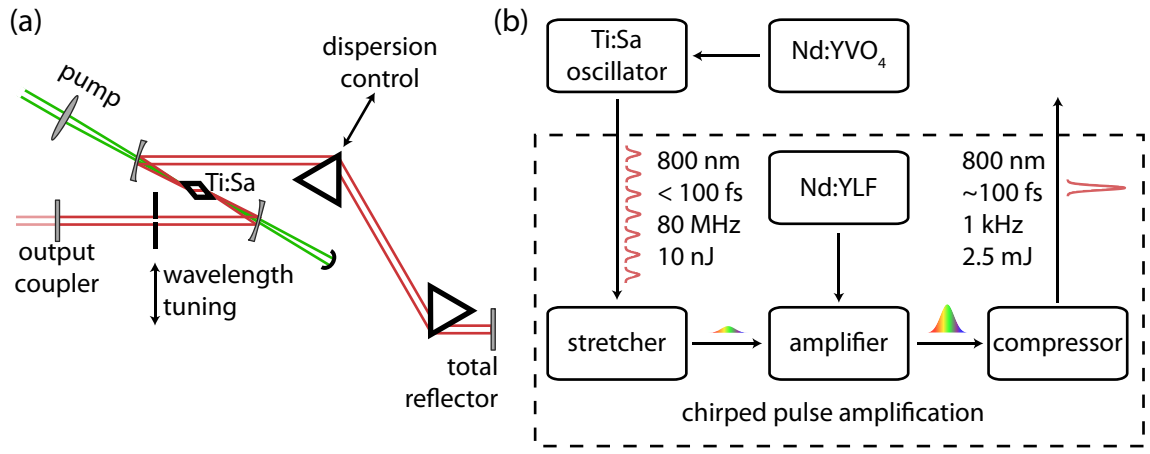

Figure 3.3 | Femtosecond laser pulse generation and amplification in a Ti:Sapphire oscillator and CPA system. (a) A typical a Ti:Sapphire oscillator consists of two end mirrors (output coupler and total reflector), the Ti:Sapphire crystal pumped by a green cw laser, a prism compressor for dispersion compensation, and an aperture for blocking of the cw mode and wavelength tuning. (b) The principle of chirped pulse amplification used to generate pulses with very high peak intensities; the depicted pulse parameters are taken from the laser system used in this work (*Solstice*, Spectra Physics);

for mode-locking of the (longitudinal) laser-cavity modes has to be employed; secondly, a broadband gain medium is necessary; thirdly, an element for dispersion compensation needs to be inserted into the resonator.

For several years, mostly passively mode-locked dye laser were employed which were able to produce sub-100 fs pulses in the visible regime [142] employing prism pairs for dispersion compensation within the resonator cavity. While pulse durations below 30 fs were reported, the average output power was typically limited to about 100 mW [143, 144].

However, in the early 1990s, the self-mode locked Ti:sapphire laser was established [145], which is still the most popular source of femtosecond laser pulses and was also used in this work. Utilizing optimized techniques for intracavity dispersion compensation, pulse durations below 12 fs were possible [146, 147]. Later, by using chirped mirrors, even the single pulse regime with octave-spanning spectra was reached [148, 149]. Ti:sapphire crystals, i.e., Al_2O_3 substrate that is highly doped with titanium, possess a very broad gain bandwidth, a high nonlinear index, outstanding mechanical, optical, and thermal properties, and provide a wide spectral tuning range in the near infrared spectral region peaking at 795 nm [47]. The large nonlinear index n_2 leads to a strong intensity dependent refractive index $n(I)$ resulting in a pronounced electrooptical Kerr effect (see Sect. 2.2.2). Due to the Kerr effect, pulsed cavity modes are – under certain circumstances – more stable than continuous wave (cw) modes. This is due to the fact that pulsed modes have higher peak intensities leading to a tighter focus in the gain medium because of Kerr lensing. By adjusting the pump laser focus such that the pulsed mode has a better overlap with the pump beam and by introducing an aperture inside the laser cavity, the gain of the pulsed mode is increased while the cw mode experiences more intracavity losses. Hence, the mode-locking process may start spontaneously or

can be initiated by applying moderate external perturbations, for instance, at the prisms or cavity mirrors [145].

A typical Ti:sapphire oscillator layout is illustrated in Fig. 3.3. The Ti:sapphire crystal is pumped by a frequency doubled Nd:YVO_4 cw laser at 532 nm (green). The cavity consists of an output coupler at one end and a highly reflective mirror at the other end. Dispersion compensation is achieved by employing a prism compressor within the laser cavity, but also chirped mirrors can be used. An aperture is used to block the cw cavity mode and for wavelength selection and control of the spectral bandwidth. The beam (red) hits the Ti:sapphire crystal under Brewster's angle in order to minimize losses due to reflection on the crystal surface.

For many applications such as material processing, frequency conversion, and nonlinear spectroscopy, the pulse energy provided by typical Ti:sapphire oscillators is not sufficient. Therefore, amplification of the pulses can be carried out using the chirped pulse amplification (CPA) technique [150–152], where due to the risk of damaging the amplifier and for the suppression of nonlinear effects, the low power input pulses are stretched by gratings [153]. The block diagram in Fig. 3.3(b) shows the principle of the CPA technique, where the depicted pulse parameters are taken from the laser system used in this work (*Solstice*, Spectra Physics). The oscillator (*Mai Tai*, Spectra Physics) delivers pulses with a typical pulse duration below 100 fs at 80 MHz repetition rate with about 10 nJ of pulse energy. Before amplification, a Pockels cell is used to select from this sequence the laser pulses to be amplified at a repetition rate of 1 kHz. These pulses are strongly stretched in time to typically more than 100 ps. Afterwards, these pulses are amplified in another Ti:sapphire crystal pumped by a pulsed nanosecond Nd:YLF laser at 527 nm. Here, two important requirements have to met. The amplification bandwidth has to be broader than that of the pulses to be amplified and the amplifier should not be saturated [47]. Only under these circumstances the pulse spectrum is not substantially affected by the amplification process. After a small number of round trips in the regenerative amplifier cavity, the pulses are coupled out and recompressed again by a grating compressor resulting in pulses with a duration of about 100 fs at 1 kHz repetition rate and 2.5 mJ pulse energy. As a result the CPA system increases the pulse energy by a factor of $2.5{\cdot}10^5$ on the expense of reducing the repetition rate. It should be noted that an increased number of round trips in the amplifier cavity leads to an increase in pulse energy, but the pulse will also accumulate more third-order dispersion (TOD). However, the grating compressor can only compensate second order dispersion and consequently uncompensated TOD leads to a slight temporal pulse broadening compared to the seed pulses. In addition, even if the two above mentioned requirements are met, the amplification process is not perfectly linear and thus the laser pulse spectrum is usually slightly narrowed during amplification which also leads to a minor increase in pulse duration.

3.1.2 Noncollinear Optical Parametric Amplification

The laser system described in the previous section delivers laser pulses of 100 fs pulse duration centered at 800 nm. Yet, most molecules absorb at other wavelengths in the visible or even in the UV. In addition, for very fast processes on the order of tens of

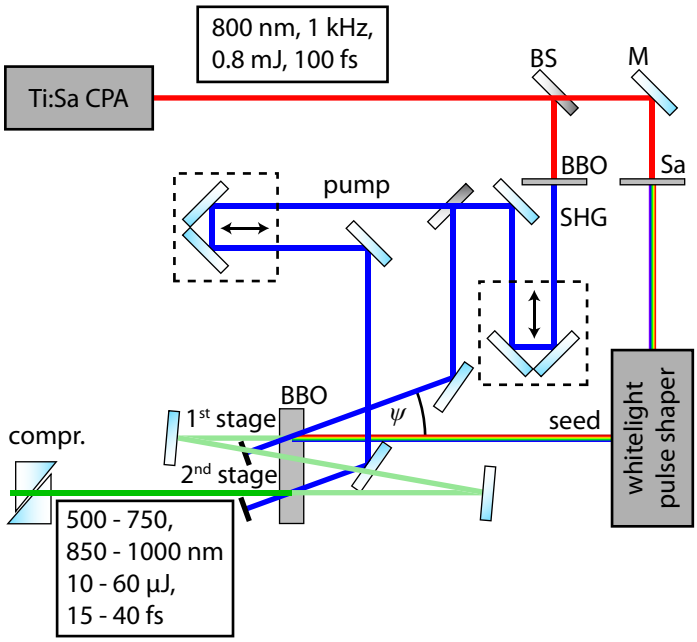

Figure 3.4 | Schematic layout of the used NOPA (*TOPAS White*, *Light Conversion*). A small portion of the incoming beam is used to generate the white light seed pulses in a sapphire plate (Sa) which are modified using a simple static frequency domain pulse shaper construction. The remaining part is frequency-doubled (SHG) and split in two parts pumping the first and second amplification stage. Amplification is achieved by overlapping pump and seed/signal in a BBO crystal under a certain angle of noncollinearity Ψ. Finally the output pulses are compressed using an adjustable pair of fused silica wedges (compr.).

femtoseconds, an improved time resolution would be desirable, which is only possible by employing even shorter laser pulses. For these reasons, techniques for frequency conversion of the 800 nm pulses are required.

The presently most versatile and efficient method for frequency conversion of femtosecond laser pulses is a technique termed *noncollinear optical parametric amplification* (NOPA) making use of the OPA effect explained in Sect. 2.2 by mixing the SHG signal of the CPA system at 400 nm (pump) with a whitelight continuum as seed [signal, compare also Fig. 2.11(d)] under a certain angle of noncollinearity [154]. In conventional OPA systems with collinearly propagating pump, signal, and idler pulses, phase matching is achieved by adjusting the crystal angle. However, the three group velocities cannot be matched properly resulting in narrowband pulses with typical pulse duration not below 100 fs. In contrast, if pump and signal propagate under a certain angle of noncollinearity, the signal group velocity can be matched to the idler group velocity projected onto the signal direction which means that the pump, signal, and idler pulses overlap over the complete crystal length. Using this principle it was shown that pulses with durations below 20 fs which are tunable over almost the complete visible regime can be generated [155, 156] and pulse durations even below 10 fs are possible by proper compression [157] and adjustment of the pulse fronts [158, 159].

The schematic layout of the NOPA used for all experiments in this thesis (*TOPAS White*, *Light Conversion*) is shown in Fig. 3.4 consisting of two amplification stages. A small portion of the fundamental (800 nm, 1 kHz, 0.8 mJ, 100 fs) is used to generate a whitelight continuum as seed which is negatively chirped by a static double-pass pulse shaper both for precompression and for preparing the seed pulses such that the desired seed bandwidth can be amplified by the pump pulses. Thus the NOPA bandwidth is easily adjustable and the output pulses can be compressed by material dispersion. The remaining fundamental is frequency doubled, split in two parts for the two amplification

stages, and focused into a BBO crystal where it is overlapped with the seed (first stage) and the signal (second stage). For the used combination (BBO, type-I phase-matching, pump at 400 nm, signal at 600 nm), the optimum angle of noncollinearity between pump and signal is $\Psi = 3.7°$ [154]. For tuning of the NOPA wavelength, the delay between the two pump pulses and the seed/signal pulses as well as the crystal angle can be adjusted using computer-controlled stepping motors. Finally, the output pulses (500–750 or 850–1000 nm, 10–60 μJ, 15–40 fs) are compressed using an adjustable amount of material dispersion provided by a pair of fused silica wedges.

3.2 Ultrafast Pulse Shaping

Femtosecond laser pulse shaping has become a key technology in almost all areas employing ultrashort laser pulses which is why it is an indispensable element in present-day femtosecond laser laboratories [160–163]. Manipulating the temporal and spectral properties of the light field via pulse shaping has applications in areas like pulse characterization and compression (see Sect. 3.3), time-resolved spectroscopy (Sect. 4.4.2), microscopy, coherent control, material processing, optical communications, and many more. As femtosecond pulse shaping also plays a major role in the experiments and formalisms presented in this thesis, a brief overview over this technique is provided in the following.

Considering Eq. (2.7) it becomes obvious that the electric field of a laser pulse can in principle be manipulated in a similar way both in time or frequency because both domains are unambiguously linked via Fourier transformation. However, frequency-domain shaping was introduced over a decade before first techniques working in time domain were established. This is due to the fact that for frequency domain pulse shaping a static spatial modulation can be employed while in time domain a temporally varying filter is necessary which requires fast electronic control units.

The field of laser pulse shaping was established in the late 1980s by Weiner *et al.* who used static phase masks to modulate the properties of femtosecond pulses [164, 165]. But broad application was not possible until computer-controllable spatial-light modulators (SLMs) based on liquid-crystal displays (LCDs) were available several years later [166].

In the most common experimental implementation an SLM is placed in the Fourier plane of a zero-dispersion compressor, as illustrated in Fig. 3.5. The pulse shaper consists of a diffraction grating that splits the beam into its spectral components, a focusing element such as a lens or focusing mirror with a focal length f placed at a distance f behind the grating in order to focus each spectral component into the Fourier plane, another focusing element separated by f from the Fourier plane, and a second grating that recombines the spectral components to a collimated beam. As the light passes four times the distance f, this kind of setup is also called a $4f$-configuration. Depending on the type of the employed SLM, which is placed in the Fourier plane, the spectral phase, the spectral amplitude, and the polarization profile of the laser pulse can be manipulated.

In this thesis, a two-layer LCD mask (*SLM-640, CRI*) with 640 pixels was used as SLM. The advantage of LCDs is that they can be used with almost arbitrary repetition

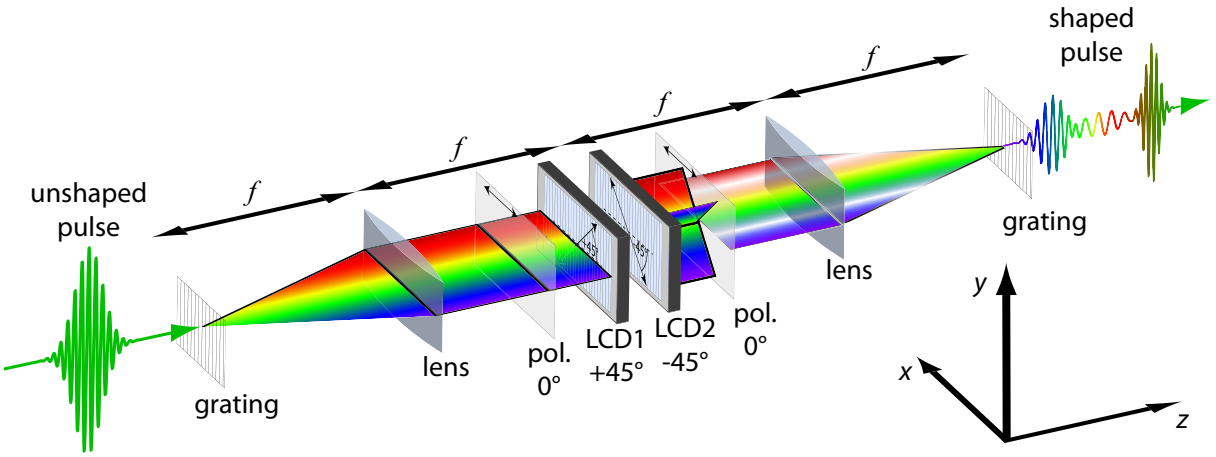

Figure 3.5 | Working principle of an LCD-based frequency-domain femtosecond pulse shaper in a $4f$-configuration capable of phase and amplitude shaping. The laser pulse is split into its spectral components by a diffraction grating. A focusing element with focal length f focuses each spectral component into the Fourier plane. A spatial-light modulator is placed into the Fourier plane consisting of an entrance polarizer at 0°, two LCD layers with optical axes tilted by ±45°, and an exit polarizer at 0°. Another focusing element and a second grating recombine all spectral components to a shaped laser pulse.

rates of the laser system and high pulse energies as they possess a high damage threshold. Moreover, they are capable of generating highly complex phase functions which can also feature discontinuities. Yet, the update rate of such pulse shapers is limited by the comparatively slow speed of operation of liquid-crystal displays on the order of several tens of milliseconds up to seconds. Other disadvantages of LCD-based pulse shaping are the limited spectral range given by the restricted transparency of LCDs (only VIS to NIR), the sensitivity to the alignment, and pulse shaping artifacts caused by the pixelation of the phase mask [167, 168]. Independent of the type of SLM used in a $4f$-configuration, it was further shown that frequency domain pulse shaping can result in a spatio–temporal coupling [169–171], leading to a spatial displacement of different spectral or temporal components of the shaped laser pulse.

The working principle of an LCD mask used for pulse shaping is as follows: two parallel glass plates coated with indium tin oxide (ITO) at the inner surface, which serve as an electrode film, are separated by a distance d. A nematic liquid crystal compound is inserted between the two electrodes whose preferential orientation direction, associated with the SLM modulation axis, is determined by a specific coating of the glass substrate. If no voltage is applied to the electrodes, the liquid crystals orient along this axis which is orthogonal to the direction the light travels through the LCD pixel [chosen here as the $z-$direction as in Fig. 3.5]. If a voltage U is applied between the two electrodes in $z-$direction, the crystals will twist in the plane spanned by the $z-$axis and the modulation axis. As a result, the dipole moment of the crystals projected on the modulation axis and thus the refractive index $n_{\mathrm{mod}}(U)$ for light polarized along the modulation axis (mod) is changed. In this way the optical path length and thereby the phase retardance $\Delta\Phi_{\mathrm{mod}}(U,\omega)$ of the light travelling through the LCD pixel and polarized

along the modulation axis can be manipulated by changing the voltage. Taking zero voltage as reference, the phase retardance of light at frequency ω is given by

$$\Delta\Phi_{\mathrm{mod}}(U,\omega) = \frac{\omega d}{c}[n_{\mathrm{mod}}(U) - n_{\mathrm{mod}}(0V)]. \tag{3.3}$$

For typical LCDs the maximum phase retardance is about 6π for light in the visible spectral range. The voltage–phase relationship is typically not linear which is the reason why the LCD mask has to be calibrated carefully. In addition, a wavelength calibration is necessary to assign the correct wavelength value to each LCD pixel.

Pure phase shaping can then be achieved by using a single-mask LCD SLM with the modulation axis oriented along the polarization direction of the incoming light. In contrast, for independent phase *and* amplitude shaping, a two-mask LCD is necessary with the modulation axes tilted by $+45°$ and $-45°$ with respect to the polarization direction of the incoming light combined with linear polarizers before and after the LCD arrays, as also shown in Fig. 3.5. As linearly polarized light can be considered as a superposition of two orthogonal linearly polarized components, the two layers will affect these two components independently. For arbitrary phase retardance of the two components, this will result in elliptically polarized and phase-shaped pulses after the two LCD layers. This light can be converted back to linearly polarized phase- and amplitude-shaped pulses by a linear polarizer. The complex-valued modulation function $M(\omega)$ describes the resulting phase and amplitude mask [48]. In the considered case of a dual-layer LCD used in amplitude and phase shaping mode, it can be shown that $M(\omega)$ is given by

$$M(\omega) = \mathrm{e}^{-\mathrm{i}\frac{\Delta\Phi_1(\omega)+\Delta\Phi_2(\omega)}{2}} \cos\left(\frac{\Delta\Phi_1(\omega) - \Delta\Phi_2(\omega)}{2}\right) \tag{3.4}$$

where $\Delta\Phi_{1,2}(\omega)$ is the phase retardance in polarization direction 1 and 2 at $\pm 45°$. It follows from this equation that the phase retardance of a single spectral component is determined by the sum of the phases of the two layers while the amplitude can be controlled by the argument of a cosine function consisting of the difference of the two phases.

The linearly polarized spectral output field of the pulse shaper can be derived by multiplying the incoming field with the modulation function:

$$E^{+}_{\mathrm{out}}(\omega) = M(\omega)E^{+}_{\mathrm{in}}(\omega). \tag{3.5}$$

The temporal output field is given by the convolution of the incoming temporal field with the Fourier transform $M(t)$ of the spectral mask:

$$E^{+}_{\mathrm{out}}(t) = M(t) \otimes E^{+}_{\mathrm{in}}(t). \tag{3.6}$$

3.3 Pulse Characterization and Compression

Characterizing and compressing the laser pulses that are provided by the laser system is an essential procedure before spectroscopy measurements can be carried out with these

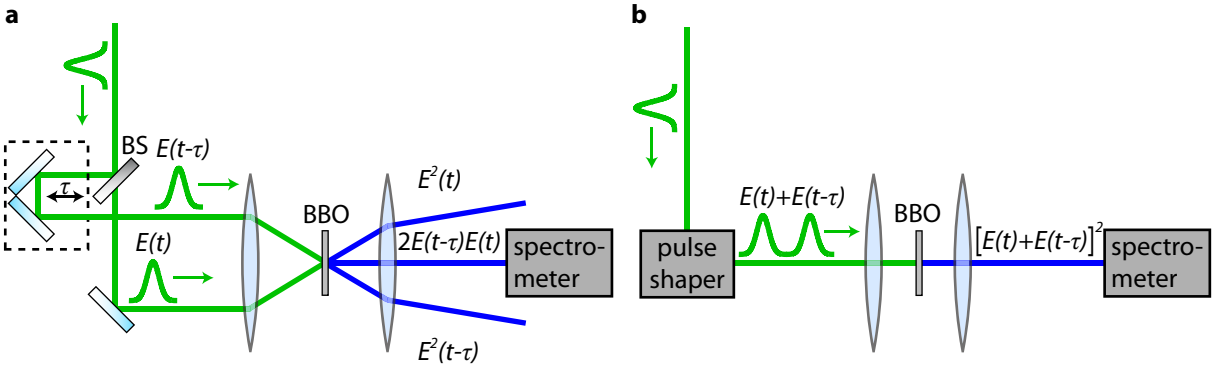

Figure 3.6 | Conventional SHG FROG setup and pulse-shaper assisted collinear SHG FROG. (a) In conventional noncollinear SHG FROG, a copy of the pulse to be characterized is generated by a beam splitter (BS), delayed, and focused together with the undelayed pulse in a noncollinear fashion into a nonlinear crystal for SHG generation. The SHG FROG trace is achieved by measuring the SHG signal originating from the interaction of both pulses spectrally resolved as a function of delay time τ. (b) In pulse shaper assisted collinear SHG FROG, the pulse copy is generated with a variable delay using a femtosecond pulse shaper and both pulses are focused collinearly into the crystal. The conventional SHG FROG trace can be isolated from the cFROG trace using a specific Fourier filter as described in the text.

pulses. The reason for this is that the outcome of nonlinear time-resolved experiments is highly sensitive to the degree to which the laser pulse is compressed to its bandwidth limit and it is obvious that the time resolution of the experiment is directly connected to the laser pulse duration.

As there exist no electronic detectors with response times fast enough to follow the temporal evolution of the electric field on a femtosecond time scale, the only way to characterize a laser pulse is to measure its interaction with another femtosecond laser pulse. One of the most reliable and robust methods is the technique termed *frequency-resolved optical gating* (FROG) [172–174]. In its simplest version, the SHG FROG technique depicted in Fig. 3.6(a), a copy of the laser pulse is generated with a beam splitter and temporally delayed with respect to the other pulse with an interferometer [175]. Both pulses are focused in a noncollinear beam geometry into a nonlinear crystal (typically BBO) and the SHG signal (see Sect. 2.2) originating from the interaction of both pulses is detected spectrally resolved as a function of delay time τ. The resulting SHG-FROG trace

$$S_{\mathrm{FROG}}^{\mathrm{SHG}}(\omega,\tau) = \left|E_{\mathrm{FROG}}^{\mathrm{SHG}}(\omega,\tau)\right|^2 \propto \left|\int_{-\infty}^{\infty} E^+(t)E^+(t-\tau)\mathrm{e}^{-\mathrm{i}\omega t}\mathrm{d}t\right|^2 \tag{3.7}$$

is symmetric with respect to $\tau = 0$ and can be considered as a spectrally resolved autocorrelation. The corresponding spectral and temporal intensities and phases can be retrieved iteratively on the basis of the FROG trace utilizing the method of generalized projections with the software package *FROG* (*Femtosoft Technologies*) which minimizes the deviation between the experimental trace and a calculated trace [176].

In this work another variation of the SHG FROG technique was implemented, using

the pulse shaper instead of an interferometer setup to create a copy of the pulse with variable delay, as shown in Fig. 3.6(b). As a result, the two pulses travel along the same path and a collinear SHG FROG (cFROG) is measured [177, 178], which is the same as a spectrally resolved interferometric autocorrelation. The use of a pulse shaper further simplifies the alignment, the measurement process, and the analysis of the resulting FROG trace (pulse-shaper assisted cFROG) [179, 180]. It can be shown [177, 178] that the expression for the cFROG trace

$$S^{\mathrm{SHG}}_{\mathrm{cFROG}}(\omega,\tau) \propto \left| \int_{-\infty}^{\infty} \left[E^{+}(t) + E^{+}(t-\tau)\right]^2 \mathrm{e}^{-\mathrm{i}\omega t} \mathrm{d}t \right|^2 \tag{3.8}$$

can be simplified to

$$\begin{aligned} S^{\mathrm{SHG}}_{\mathrm{cFROG}}(\omega,\tau) = {} & 2\left|E_{\mathrm{SHG}}(\omega)\right|^2 \\ & + 4S^{\mathrm{SHG}}_{\mathrm{FROG}}(\omega,\tau) \\ & + 8\cos\left[(\omega_0+\omega/2)\,\tau\right] \mathrm{Re}\left[E^{\mathrm{SHG}}_{\mathrm{FROG}}(\omega,\tau) E^{*}_{\mathrm{SHG}}(\omega) \mathrm{e}^{\mathrm{i}\frac{\omega}{2}\tau}\right] \\ & + 2\left|E_{\mathrm{SHG}}(\omega)\right|^2 \cos\left[(2\omega_0+\omega)\,\tau\right] \end{aligned} \tag{3.9}$$

where ω_0 is the fundamental carrier frequency of the laser pulses. Thus the cFROG trace $S^{\mathrm{SHG}}_{\mathrm{cFROG}}(\omega,\tau)$ contains four different contributions of which one [second term of Eq. (3.9)] is the desired conventional SHG FROG trace (DC term). As the third and fourth term of Eq. (3.9) are modulated by the frequencies ω_0 and $2\omega_0$ (AC cross-terms) they can be removed by applying a suited Fourier filter. The time independent offset in the first term of Eq. (3.9) is simply the SHG spectrum of the laser pulse and can be removed by subtracting the background for long delay times.

The pulse shaper modulation function for creating two replica of the incoming pulse separated by the time delay τ is

$$M(\omega) = \frac{1}{2}\left[1 + \mathrm{e}^{-\mathrm{i}[\omega-(1-\gamma)\omega_0]\tau}\right] \tag{3.10}$$

where one pulse is fixed at $t = 0$ and only the second pulse can be scanned which has the advantage that the fixed pulse suppresses the $t = 0$ replica caused by the pixel gaps of the LCD mask [168] which may perturb the measured FROG trace. The parameter γ determines whether the carrier envelope phase is shifted together with the envelope of the pulse ($\gamma = 1$) as would be the case in a real interferometer or whether only the envelope is shifted while the carrier phase remains unchanged ($\gamma = 0$) [179]. The resulting spectrally integrated cFROG signal will only accord with the interferometric autocorrelation for $\gamma = 1$, whereas for $\gamma = 0$ no modulations occur as the two pulses always interfere constructively. Choosing $\gamma = 0$ results in an effective measured carrier frequency of 0 and the measured signal is the envelope of the interferometric autocorrelation. For $0 < \gamma < 1$ the carrier phase is adjusted in such a way that the measured modulation frequencies are reduced depending on the chosen γ value, e.g., for $\gamma = 0.5$ the oscillation frequency is reduced by a factor of two. In this way, the amount of sampling points (and thus the time) necessary for measuring the complete cFROG trace can be substantially reduced

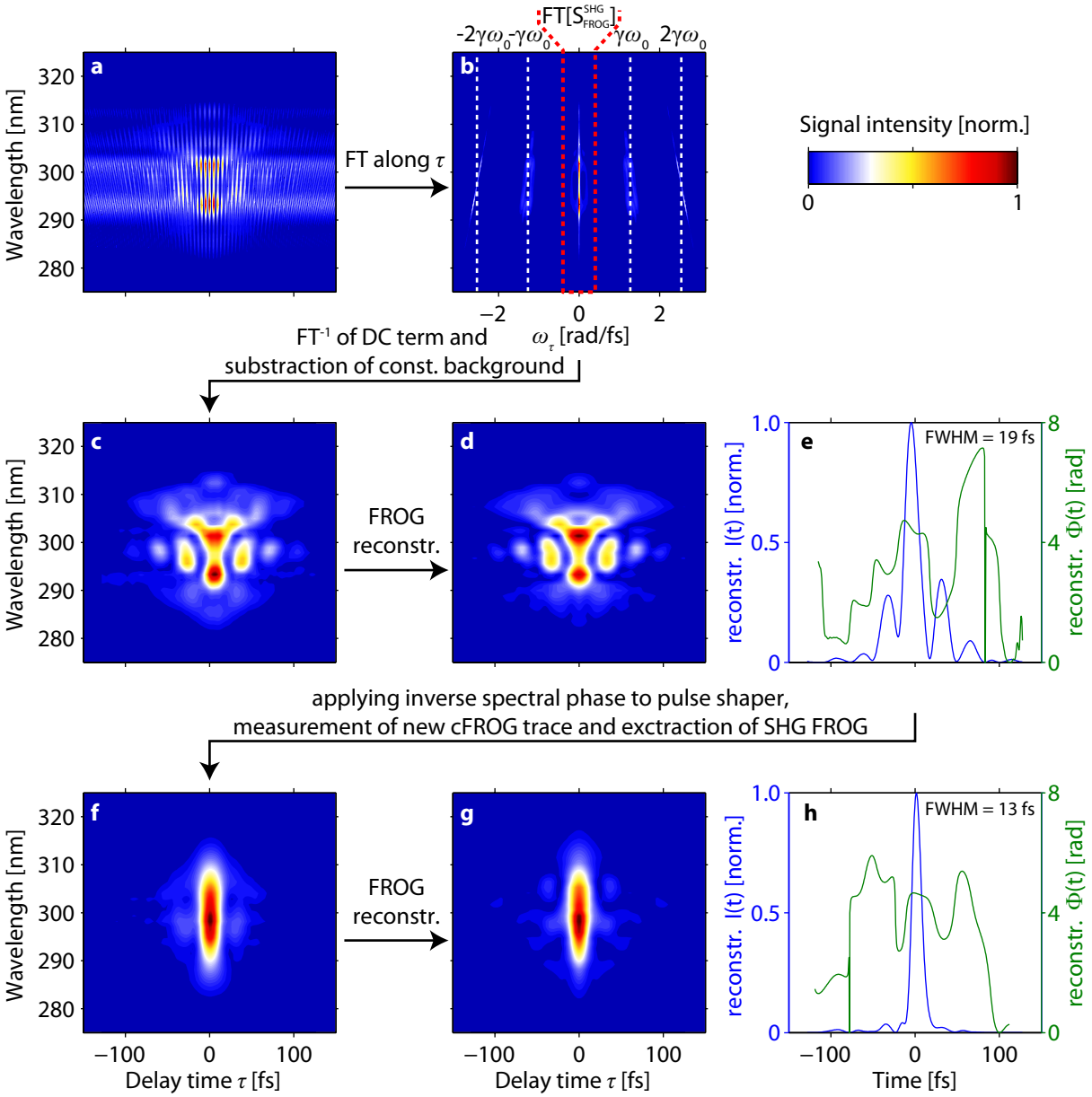

Figure 3.7 | Procedure of laser pulse characterization and compression via pulse-shaper assisted collinear SHG FROG. (a) An exemplary cFROG trace is shown measured with $\gamma = 0.4$ and $\omega_0 = 3.17333$ rad/fs. To extract the desired SHG FROG trace, the cFROG trace is Fourier transformed along τ (b) (absolute value shown). Four different AC terms at $\omega_\tau = -2\gamma\omega_0$, $-\gamma\omega_0$, $+\gamma\omega_0$, and $+2\gamma\omega_0$ (vertical dashed lines) are observed that can be separated from the unmodulated term (red dashed lines) containing the conventional SHG FROG (c) using a suitable filter function. Afterwards, the FROG trace is reconstructed (d) using a commercially available software package from which the temporal (e) and spectral field (not shown) is retrieved. By applying the inverse spectral phase to the pulse shaper, the laser pulse is compressed and another FROG trace of the compressed pulse is measured (f) and again the corresponding field is retrieved (g) confirming successful compression of the pulse to a temporal FWHM of 13 fs (h). This procedure may be repeated if the laser pulse is not entirely compressed to its bandwidth limit in the first iteration.

because the Nyquist limit (which holds strictly for such interferometric measurements) can be expanded. This demonstrates very nicely the advantages of pulse shaping for interferometric measurements as it allows control over the carrier envelope phase in a very simple fashion. The minimum possible γ value is given by the spectral bandwidth of the laser pulse because for Fourier filtering the contributions at ω_0 and $2\omega_0$ which shift towards zero frequency for lower γ values have still to be separable from the desired unmodulated SHG FROG trace.

The complete procedure of pulse shaper assisted laser pulse characterization and compression is demonstrated in Fig. 3.7. An exemplary collinear FROG trace measured with $\gamma = 0.4$ and $\omega_0 = 3.17333$ rad/fs is shown in Fig. 3.7(a). The absolute value of the Fourier transformed data set [Fig. 3.7(b)] contains four AC terms at $\omega_\tau = -2\gamma\omega_0$, $-\gamma\omega_0$, $+\gamma\omega_0$, and $+2\gamma\omega_0$ (vertical dashed lines) and the conventional SHG FROG trace as unmodulated DC term (red dashed box), which can be extracted by applying an inverse Fourier transform after filtering of the AC terms and subtraction of the constant SHG background [Fig. 3.7(c)]. Figure 3.7(d) shows the retrieved FROG trace obtained with a commercially available software package. The corresponding temporal electric field [Fig. 3.7(e)] features several pre- and post-pulses, the temporal FWHM of 19 fs is in this case an unsuitable parameter for the characterization of the pulse structure. In the next step the inverse spectral phase is applied to the pulse shaper and another SHG FROG is measured [Fig. 3.7(f)]. The retrieved FROG trace [Fig. 3.7(g)] confirms the successful compression of the laser pulse with a temporal FWHM of 13 fs. This procedure can be repeated several times for compensation of the remaining phase distortions.

3.4 Transient Absorption Spectroscopy

The concept of detecting extremely fast photophysical or photochemical processes with very short pulses of light was introduced in the late 1940s under the name *flash photolysis* by Ronald G.W. Norrish, and George Porter providing time resolutions on the order of milliseconds to microseconds [181, 182]. In 1967 they were awarded with the Nobel Prize in Chemistry for this groundbreaking development together with Manfred Eigen. In the late 1980s, researchers – among them the Nobel prize winner Ahmed H. Zewail – succeeded in pushing the time resolution towards the femtosecond regime based on the development of new ultrafast laser sources thereby establishing the field of *femtochemistry* [12] while the basic idea behind the technique remained the same. Transient time-resolved absorption measurements also form the basic technical concept of most experiments performed in the course of this thesis. In the following, the main principles of the femtosecond transient absorption technique, the used experimental setup, typical observed signal contributions, and data analysis are discussed.

3.4.1 Basic Principle

Transient absorption is a special subtype of the pump–probe technique and designed for the investigation of ultrafast photodynamics in the condensed phase [183–186]. As illustrated in Fig. 3.8(a), an excitation pulse ('pump') in the visible regime, provided

by the NOPA as discussed in Sect. 3.1.2, is used to induce an electronic transition in the system under investigation. The photodynamics triggered by this transition are detected by measuring the evolution of the sample's change of absorption as a function of wavelength λ and time T elapsed since the pump pulse has excited the sample. This is done by using another laser pulse ('probe') sent through the sample volume after a well known pump–probe delay time T. In order to investigate a broad spectral range, a whitelight supercontinuum covering the complete visible spectral range [see Sect. 2.2.2] is used. To extract the change of absorption, every second pump pulse is blocked such that the change of absorption between the pumped and unpumped probe volume can be measured for consecutive laser shots by sending the part of the probe that is transmitted by the sample into a spectrometer.

In general, the intensity $I_{\mathrm{PPr}}(d,\lambda,T)$ of the probe light at a specific wavelength λ travelling through the absorbing sample of path length d at the pump–probe delay T and in presence of the pump pulse is described by the Lambert–Beer law

$$I_{\mathrm{PPr}}(\lambda,T) = I_0(\lambda)\mathrm{e}^{-\sigma(\lambda)N(T)d} \tag{3.11}$$

where $\sigma(\lambda)$ is the (wavelength dependent) absorption cross section and $N(T)$ the density of molecules absorbing at this wavelength at the time delay T after the pump pulse. In practice it is convenient to describe the probe transmission in terms of the logarithmic quantity *absorbance*, also called *optical density* (OD), which is defined via

$$OD(\lambda,T) = -\log_{10}\left[\frac{I_{\mathrm{PPr}}(\lambda,T)}{I_0(\lambda)}\right] = \frac{1}{\ln 10}\sigma(\lambda)N(T)d \tag{3.12}$$

and thus depends linearly on the density of absorbing molecules, their absorption cross section and the path length. Alternatively, the above relationship between the optical density and the path length can also be described using the molar decadic extinction coefficient $\epsilon(\lambda)$ and the molar concentration $c(T)$ instead of the cross section and the density of molecules:

$$OD(\lambda,T) = \epsilon(\lambda)c(T)d \tag{3.13}$$

If the pump pulse is blocked and only the probe with intensity $I_{\mathrm{Pr}}(\lambda)$ is present, Eq. (3.11) takes the form

$$I_{\mathrm{Pr}}(\lambda) = I_0(\lambda)\mathrm{e}^{-\sigma(\lambda)N_0 d}. \tag{3.14}$$

In transient absorption the difference of optical density between the pumped (probe intensity I_{PPr}) and unpumped sample volume (probe intensity I_{Pr}) is evaluated as a function of pump–probe delay

$$\Delta OD(\lambda,T) = -\log_{10}\left[\frac{I_{\mathrm{PPr}}(\lambda,T)}{I_0(\lambda)}\right] + \log_{10}\left[\frac{I_{\mathrm{Pr}}(\lambda)}{I_0(\lambda)}\right] = -\log_{10}\left[\frac{I_{\mathrm{PPr}}(\lambda,T)}{I_{\mathrm{Pr}}(\lambda)}\right] \tag{3.15}$$

$$= \frac{1}{\ln 10}\sigma(\lambda)\left[N(T) - N_0\right]d \tag{3.16}$$

$$= \epsilon(\lambda)\left[c(T) - c_0\right]d \tag{3.17}$$

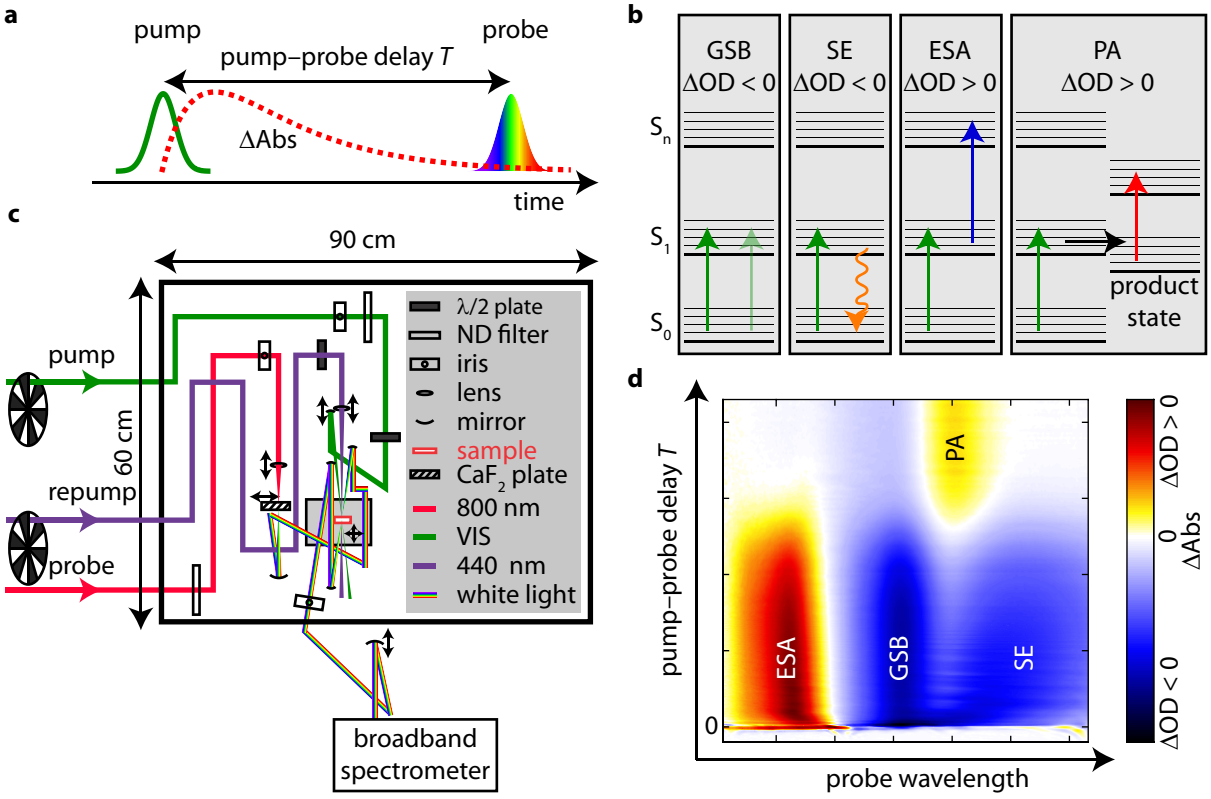

Figure 3.8 | Principle of transient absorption experiments. (a) In the used implementation a visible pump pulse for excitation and a whitelight continuum with a variable delay T is used as probe. (b) A schematic representation illustrates typical signal contributions observed in transient absorption. While ground-state bleaching (GSB) and stimulated emission (SE) lead to a negative change of optical density, excited-state absorption (ESA) and photoproduct absorption (PA) are characterized by an increase of the optical density. (c) Layout of the used optical setup for transient absorption measurements. The setup is designed such that three different beams (pump, repump, probe) can be employed. A white light probe continuum is generated by focusing a small amount of the 800 nm pulses into a linearly moving CaF_2 plate. Attenuator wheels are used to regulate the pump and repump pulse energies and $\lambda/2$ plates are inserted to adjust their polarization angles. All three beams are focused and spatially overlapped in a flow cell with a path length of 200 μm. The transmitted white light beam is then sent into a broadband spectrometer with a cooled CCD camera capable of shot-to-shot detection (figure adapted from Ref. [187]). (d) Exemplary transient absorption data (6-nitro BIPS in acetonitrile) as a function of pump–probe delay T and probe wavelength. Typical signal contributions are marked at the corresponding regions. Bluish colors represent negative ΔOD values while yellow/red indicate regions of positive changes of the optical density.

which reflects the temporal evolution of the population change [Eq. (3.16)] of the absorbing molecules and accordingly also of the molecular concentration [Eq. (3.17)].

From Eq. (3.15), it follows that within this sign convention positive changes of the optical density result from an increase of absorption with respect to the reference signal without preceding pump pulse whereas negative changes follow from a decreased transient sample absorption caused by the pump pulse. The main signal contributions that

are typically observed in transient absorption spectroscopy are summarized in Fig. 3.8(b) and explained in the following:

- *Ground-state bleaching* (GSB): molecules are excited by the pump pulses to a higher-lying electronic state. As a consequence, the number of molecules in the ground state is reduced. This depopulation of the ground state results in a decreased ground state absorption band (bleach). This signal contribution is negative ($\Delta OD < 0$) and the spectral shape matches the inverted steady-state absorption spectrum of the excited species.

- *Stimulated emission* (SE): stimulated emission is observed when the excitation step leads to the population of an emissive state from which fluorescence can be observed. In this case emission of photons can be stimulated by the photons of the probe light. The direction of the emitted photons is the same as the direction of the incoming probe photons, whereby both signals will be detected. As this results in an increase of probe light intensity these signal contributions are negative ($\Delta OD < 0$). Moreover, the SE signal is typically red-shifted with respect to the GSB due to the Stokes-shift.

- *Excited-state absorption* (ESA): Molecular excited states exhibit – just as the electronic ground state – a typical absorption band. This additional absorption can only appear if excited-state population is generated which might be reexcited by the probe to higher-lying states. The probe pulse is thus attenuated by this absorption of the excited-state population resulting in a positive change of optical density ($\Delta OD > 0$).

- *Photoproduct absorption* (PA): Photochemical reactions result in the formation of photoproducts either in their ground states or in some other long-living intermediate states. Photoproduct formation is accompanied by an emerging positive absorption band characteristic for the type of product such as, e.g., an isomerized species, radicals, or charge-separated states. Photoproduct absorption gives rise to a positive change of optical density ($\Delta OD > 0$).

The setup used for all measurements discussed in this thesis was designed by J. Buback and is explained in detail in Ref. [187]. The layout is illustrated in Fig. 3.8(c). According to the experimental requirements three beams – pump, repump, and probe – can be employed. The pump pulses (green) as well as the (optional) repump pulses (purple) are independently delayed with respect to the probe using motorized delay stages (not shown) with a maximum temporal delay of about 4 ns. Before entering the optical setup, choppers are used to block a certain amount of the pump and repump pulses at variable frequencies and phases determined by the type of experiment. The pulse energies can be adjusted with continuous attenuator wheels. Typical pump/repump pulse energies are on the order of 5-200 nJ while for whitelight generation seed pulse energies below 1 μJ have been proven to result in the most stable continuum pulses. Silver-coated planar mirrors are used to guide the pump beam to the sample position and allow for a spectrally broad tuning range of the pump pulses over almost the complete visible spectral range. For the repump beam aluminum coated mirrors are utilized which extend

the usable spectral range for this beam line into the UV regime at the cost of a slightly lower efficiency in the visible. High-reflective dielectric mirrors are used for the 800 nm seed pulses (red), while silver mirrors guide the probe continuum to the sample and into the spectrometer. To generate the probe pulses, the 800 nm pulses are sent through an iris for improving the spatial beam profile of the seed pulses and focused into a 5 mm thick linearly moving CaF_2 plate. The fundamental was filtered using a custom made dielectric hot mirror. The relative polarization directions of the pump and repump beams can be adjusted by $\lambda/2$ plates. For all transient absorption measurements the pump polarization was set to the so-called magic angle of 54.7° in order to eliminate orientational effects [188]. All beams are focused into a flow cell with a path length of 200 μm where they are spatially overlapped. The transmitted probe beam is sent into a broadband spectrometer (*SpectraPro-2500i, Acton*) with a cooled CCD camera (*Pixis 2k, Princeton Instruments*) with a resolution of 2048×512 pixels capable of a multichannel shot-to-shot detection of the probe continuum. The major advantage of the shot-to-shot readout lies in the fact that consecutive laser shots are highly correlated which is the reason why experimental noise caused by long term laser drifts is reduced to a great extent. To refresh the sample volume between consecutive laser shots a micro annular gear pump (*mzr-4605, HNP Mikrosysteme*) is used to pump the sample from the reservoir to the flow cell and back through flexible tubings.

Exemplary transient-absorption data (merocyanine form of 6-nitro BIPS dissolved in acetonitrile, see Sect. 4.2) is shown in Fig. 3.8(d) as a function of pump–probe delay time and probe wavelength in terms of a two-dimensional contour plot. Bluish colors represent a pump induced decrease of sample absorption (GSB, SE), whereas yellow and red colors indicate an increase of the optical density (ESA, PA). In this case all possible contributions as illustrated in Fig. 3.8(b) can be observed and are marked at the corresponding region of the transient map. GSB contributions arise instantaneously after excitation. ESA at shorter wavelengths and SE signals in the red part of the probe axis are also detected which decay exponentially as a function of time with characteristic decay times. The spectral signatures of an absorbing photoproduct emerge after longer delay times. As this photoproduct originates from excited molecules that do not react back to the original ground state a remaining GSB – slightly red-shifted to the PA – is also observed.

In order to better visualize the temporal evolution at a certain probe wavelength, it is convenient to display slices of the data along the pump–probe delay time T, called *single transients*. In contrast, whenever the spectral shape at a fixed delay time is of major interest, cuts along the probe wavelength axis – also referred to as *difference spectra* – might be helpful.

3.4.2 Data Evaluation

In multichannel time-resolved measurements like broadband transient absorption one faces the challenge that large amounts of data spreading over several dimensions (time *and* frequency) are obtained, containing rich information about the investigated photoprocesses. In many cases, spectral signatures of different states overlap and competing processes may make a straightforward interpretation of the data impossible. In order to

gain an exhaustive picture of the system, such as the states involved in the dynamics, their time scales and spectra, a global model-based data fitting method is desired. Such a model should properly account for all spectral signatures that may be observed over a broad spectral range as well as on many different time scales [189].

In order to correctly model the spectral evolution as a function of delay time T we have to extend the Lambert–Beer law as given in Eq. (3.13) because in general a molecular sample may contain a mixture of components, e.g., different populated states, several isomers, solvent and molecular contributions, various photoproducts and so on. The concentration c_l of the component l, characterized by its spectral profile $\epsilon_l(\lambda)$, may vary as a function of time T. The difference spectrum $\Delta OD(\lambda,T)$ of the sum of n_{comp} components can then be described as a superposition

$$\Delta OD(\lambda,T) = \sum_{l=1}^{n_{\mathrm{comp}}} c_l(T)\epsilon_l(\lambda)d - c^0\epsilon^0(\lambda)d \tag{3.18}$$

$$= \sum_{l=1}^{n_{\mathrm{comp}}} c_l(T)\Delta\epsilon_l(\lambda)d \tag{3.19}$$

where c^0 represents the total initial concentration of molecules before delay time zero and $\epsilon^0(\lambda)$ the corresponding absorption spectrum. Assuming that the number of molecules is conserved, the total initial concentration equals the sum over all components, i.e., $c^0 = \sum_{l=1}^{n_{\mathrm{comp}}} c_l(T)$.

In order to extract the properties of each component from the measured spectra either a parameterized kinetic model for the temporal evolution of the concentrations $c_l(T)$ or a spectral model describing the spectral profiles $\epsilon_l(\lambda)$ of the compounds can be used. In this thesis kinetic modelling is preferred over the spectral model which means that the temporal dynamics are modelled with a predefined analytical function whose parameters are part of the fitting process, while the spectral profile is fitted without further restrictions. On the basis of a simple rate equation of first order (i.e., the concentrations can be described by linear differential equations) the concentration of each component can be parameterized by a monoexponential decay

$$c_l(T) = \mathrm{e}^{-k_l T} \tag{3.20}$$

with the rate constant k_l. The wavelength dependent amplitudes of the single decay components are called *decay-associated difference spectra* (DADS) describing the spectral difference profiles $\Delta\epsilon_l(\lambda)$ of each component. Thus, using the wavelength-dependent DADS profiles, the data set can be modelled via

$$\Delta OD(\lambda,T) = \sum_{l=1}^{n_{\mathrm{comp}}} DADS_l(\lambda)\,[c_l(T) \otimes IRF(\lambda,T)] \tag{3.21}$$

where each decay function is convoluted with the instrument response function $IRF(\lambda,T)$ which is assumed to be a Gaussian function with variable width and position. The chirp of the whitelight probe continuum is accounted for by fitting time zero as a function of wavelength with a polynomial function such that time zero (i.e. $T = 0$) can be assigned independently for every single transient.

Thus, with the formalism described by Eq. (3.21) the contributions of all states and associated processes are disentangled using a sum over independent monoexponential decay functions whose wavelength dependent amplitudes reflect the spectral profiles of all excited, intermediate, and product states. This type of data analysis is called *global fitting* because the complete spectroscopic data set is modelled with the same fixed set of rate constants. In this thesis the open-source software program *Glotaran* [190], a graphical interface to the R-package *TIMP* [191], was utilized for global data fitting, allowing for the determination of the DADS under consideration of the IRF and the probe chirp.

One of the drawbacks of global data fitting with a kinetic model might be that different processes that possess (within the experimental uncertainties) similar rate constants will be combined into a single DADS and are consequently not distinguishable on the basis of a global fitting routine.

3.4.3 Correction of Probe Chirp

As described in Sect. 3.4.1, a whitelight continuum generated in a moving CaF_2 plate is used as a probe which allows us to follow the photoinduced dynamics in the spectral range between 370 and 720 nm. Self-phase modulation is the dominant mechanism in the generation of supercontinua, as was discussed in Sect. 2.2.2, and it was also shown [Fig. 2.13(a)] that this effect leads to a varying instantaneous frequency with time and the resulting spectrally broadened laser pulses are not bandwidth-limited. In addition, material dispersion of the used optical devices such as filters and the flow cell inevitably leads to a positively chirped continuum with a typical pulse duration on the order of several hundreds of femtoseconds at the sample position. This already takes effect in transient absorption measurements where it results in a probe-wavelength dependent time zero where pump and probe pulses overlap. In the global fitting procedure this effect can easily be accounted for by assigning every single transient a specific time-corrected pump–probe axis $T(\lambda)$, as mentioned in Sect. 3.4.2. Nevertheless, in order to extract single difference spectra at the correct delay time and for reasons of illustration, it is useful to correct the data for the probe chirp.

The chirp of the probe continuum is easily characterized by recording transient absorption data in the pure solvent. When the pump and probe pulses overlap coherent non-resonant processes are observed that are in general summarized under the expression *coherent artifact* though it is very useful for the time correction of the raw data [184, 185, 192]. The dominant process leading to this effect is cross-phase modulation [193–195] resulting from the variation of the refractive index of the solvent under the influence of the strong pump pulse. But also two-photon absorption [192, 194] and stimulated Raman processes are assumed to play a major role in the formation of the coherent artifact [184]. Exemplary transient absorption raw data of pure acetonitrile with a pump center wavelength of 595 nm and a pump pulse duration of 15 fs is shown in Fig. 3.9(a). The probe chirp results in an elongated and distorted coherent artifact signal extending over a temporal range of about 600 fs between 370 and 720 nm. To correct for the chirp of the probe, the temporal center of the coherent artifact is extracted at several points in the raw data (red squares) and fitted with a low-order polynomial

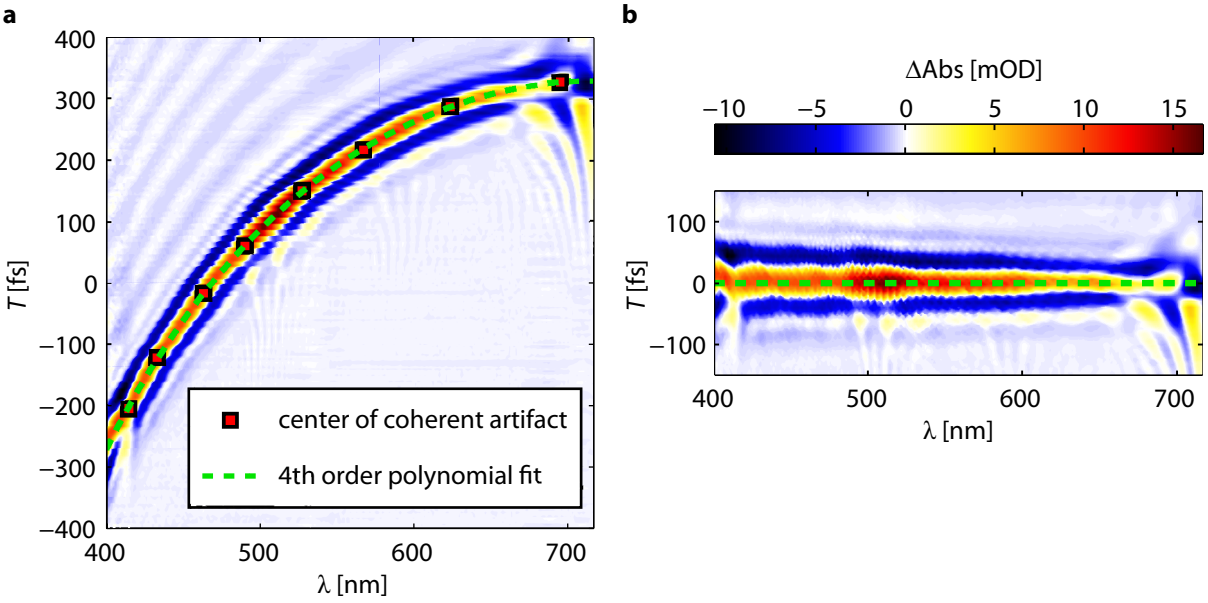

Figure 3.9 | Correction of chirp in transient absorption with a continuum probe. (a) The raw transient absorption data of pure acetonitrile shows an elongated probe pulse extending a temporal range of about 600 fs between 400 and 720 nm. Time zero is assigned with the help of the center of the coherent artifact at several selected data points (red squares) and fitted with a 4th order polynomial function (green dashed). (b) After shifting and interpolating every single transient, the corrected transient absorption data map is generated.

(green dashed line). Afterwards, every single transient is shifted by interpolating the data along slices through the transient map parallel to the fitted polynomial [185]. Using this method the maxima of the coherent artifact coincide at all wavelengths at time zero, as shown for the same data set in Fig. 3.9(b). This procedure requires that the data is recorded over a sufficient temporal range before *and* after time zero for all probed wavelengths.

3.4.4 Temporal Resolution

A key point in time-resolved ultrafast spectroscopy is the time resolution achieved with the employed apparatus. A rough estimation of the upper limit in transient absorption is received on the basis of the coherent artifact in the pure solvent [192]. Assuming a Gaussian profile of the cross-correlation of pump and probe, the coherent artifact can be modelled with the sum of a Gaussian and its first and second time derivative [184, 185].

This is demonstrated in Fig. 3.10 on the basis of the data shown in Fig. 3.9(a). The measured data is fitted with a sum of a Gaussian and its first and second derivatives, as shown in Fig. 3.10(a) exemplarily at a probe wavelength of 600 nm. An evaluation of the FWHM of the fitted Gaussian [Fig. 3.10(b)] yields an average temporal resolution of 47 fs (horizontal black line), but a pronounced variation as a function of the probe wavelength is observed. The FWHM curve decreases from around 70 fs around 400 nm to below 30 fs at 670 nm and a temporal resolution below 50 fs is achieved in a spectral window ranging from 510 nm to 690 nm. It can be assumed that the effective temporal

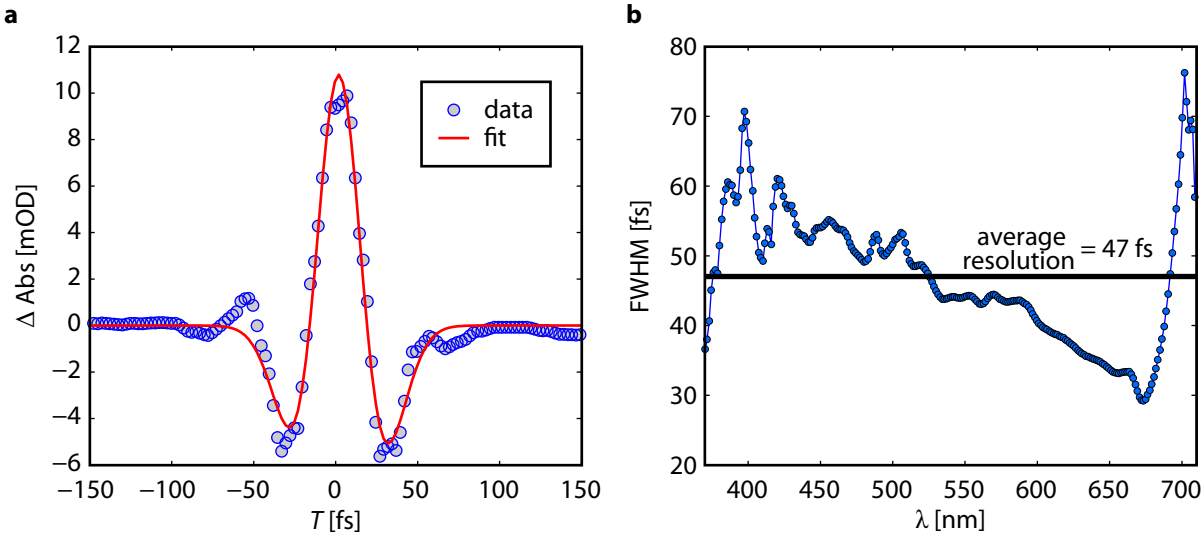

Figure 3.10 | Estimation of the temporal resolution of the used transient absorption setup on the basis of the coherent artifact measured in acetonitrile with a pump pulse centered at 595 nm with 15 fs duration [same data as in Fig. 3.9]. (a) The data of the coherent artifact (blue circles) is fitted with the sum of a Gaussian function and its first and second time derivative (red line) as shown here exemplarily for a single probe wavelength of 600 nm. (b) The fitted Gaussian FWHM as a function of probe wavelength gives a rough estimation of the temporal resolution which is in the range between 29 fs at 670 nm and 76 fs at 700 nm. The spectrally averaged temporal resolution is 47 fs (black horizontal line).

resolution is below these estimated values as real cross-correlation measurements, as for example by analyzing the sum frequency of pump and probe, typically yields values lower than that achieved with the coherent artifact [185].

3.5 Coherent Two-Dimensional Spectroscopy

3.5.1 Motivation

Deciphering the complex nature of photophysical and photochemical molecular processes in condensed phase is a fundamental research objective that necessitates spectroscopic information on ultrashort time scales. Third-order techniques like femtosecond pump–probe spectroscopy are capable of providing these valuable pieces of information in various spectral regions from the Terahertz down to the X-ray regime. However, most of these well-established techniques are not capable of characterizing the complete third-order response leading to ambiguities in the detected signals. Capturing as much of spectroscopic information about the processes as possible while maintaining the highest possible temporal resolution is therefore an essential requirement for all newly-developed time-resolved methods. In this context coherent multidimensional spectroscopy is – with all its variations – one of the most promising techniques that is capable of clearing up many of the still unanswered questions in physics, chemistry, and biology and resolves several drawbacks of conventional pump–probe spectroscopy.

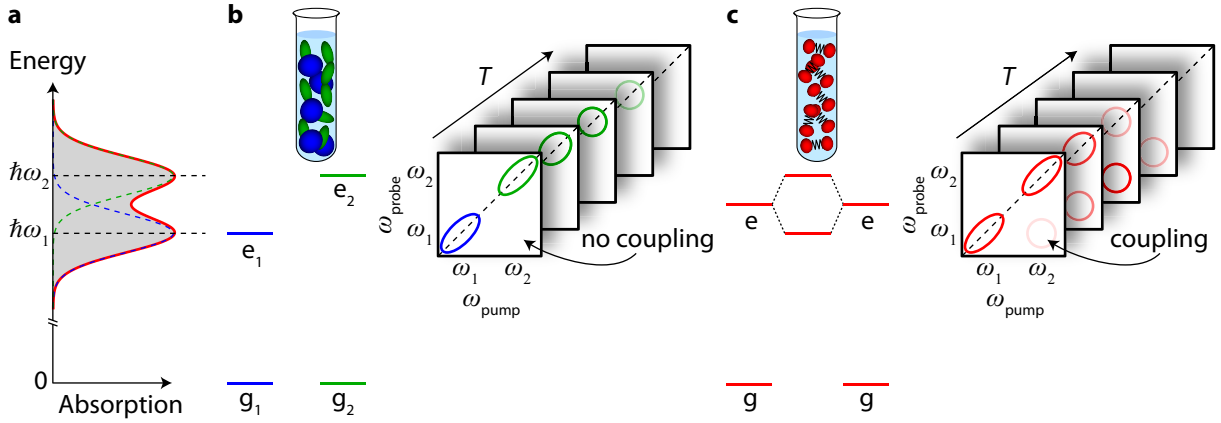

Figure 3.11 | Motivating example illustrating the benefit of coherent two-dimensional electronic spectroscopy. (a) A fictitious absorption spectrum consists of two overlapping but well-separated peaks centered at frequencies ω_1 and ω_2. (b) On the one hand, the origin of this absorption spectrum could be a mixture of two independent molecular species absorbing at ω_1 (blue) and ω_2 (green), respectively. (c) On the other hand, a strongly coupled molecular homodimer could possess the same absorption spectrum (red) emanating from the excited-state level-splitting. In transient absorption spectroscopy, the two cases are almost indistinguishable because the coupling between states is not directly accessible with this technique. Coherent two-dimensional spectroscopy extends the measured data into a second frequency dimension and detects the correlation between pump (excitation) and probe (emission) frequencies. Thus the couplings between states appear as off-diagonal contributions in the 2D spectra and their temporal evolution is easily monitored.

One potential issue of conventional pump–probe techniques such as transient absorption is illustrated in Fig. 3.11 demonstrating the need for the introduction of multidimensional electronic spectroscopy. We consider a photoactive molecular system whose absorption spectrum is illustrated in Fig. 3.11(a) comprising two separated peaks located at frequencies ω_1 and ω_2. The origin of such an absorption spectrum can not be resolved on the basis of linear absorption spectroscopy because fundamentally different molecular systems may possess one and the same spectral profile. On the one hand a mixture of two independent molecular species (ground states g_1 and g_2, excited states e_1 and e_2), or a system with two excited states that are virtually uncoupled, may be the reason for the two peaks [Fig. 3.11(b)]. On the other hand, a strongly coupled molecular dimer with identical monomer units (ground state g and excited states e) could possess an excited-state energy splitting which would also lead to the illustrated absorption band [Fig. 3.11(c)]. Conventional time-resolved techniques are not capable of measuring the coupling between the two components directly because they are limited to the time evolution of the populations without detecting the correlation between the states. Thus the two illustrated scenarios can probably not be discriminated with transient absorption spectroscopy as there only a projection of the full third-order response is detected. To overcome this issue, two-dimensional (2D) electronic spectroscopy was established providing spectroscopic data in two independent dimensions by resolving not only the emission frequency but also the excitation frequency as a function of time. In this way correlations and couplings between different states can easily be visualized

combining the benefits of the high time resolution of pump–probe spectroscopy with the rich information about the system's absorption–emission frequency correlation. In the given example the coupling between the two excited states resulting in off-diagonal peaks could not only be exposed, but also its temporal evolution would be observable using two-dimensional electronic spectroscopy resolving pump (excitation) *and* probe (emission) frequencies independently.

The concept of ultrafast two-dimensional spectroscopy was adapted from two-dimensional nuclear magnetic resonance (2D-NMR) [196–198] and was first realized in the NIR [14, 15] and the IR (2D-IR) region [199–201] for electronic and vibrational transitions in the late 1990s. A few years later coherent 2D spectroscopy was also established in the visible spectral range [202–204] opening up this field for a much larger number of potential applications such as the investigation of photosynthesis [21]. An in-depth treatment of the theoretical background of femtosecond multidimensional spectroscopy is given in a number of books [205–207] and review articles [16–20] while in the following only a brief overview over the main theoretical concepts is given.

3.5.2 Theoretical Concepts

Most established time-resolved spectroscopy methods are third-order techniques which means that the detected signal arises from three interactions between the electric field of the laser pulse and the sample. Hence the detected signal emanates from the third order nonlinear polarization $P^{(3)}(\vec{r},t)$ induced by the light field. The existence of three light matter interactions implies that the emitted signal is determined by three temporal variables: the time interval between interaction 1 and 2, the interval between interaction 2 and 3, and the time variable describing the evolution of the emitted signal itself. Consequently, third-order techniques are capable of inducing signals that depend on three independent variables. In contrast, for example in transient absorption (see Sect. 3.4), the signal is measured only as a function of two variables, namely the pump–probe delay T and the emission wavelength λ. This means that a simple pump–probe experiment is not capable of capturing the complete third-order response but only a subset of it.

Characterizing the complete third-order response as done in two-dimensional spectroscopy requires that the three interaction times are adjustable independently from each other. This is done by employing three laser pulses interacting with the system at interaction times τ_1, τ_2, and τ_3 followed by the emitted signal at the emission time τ_s, as illustrated in Fig. 3.12(a).

On the basis of time-dependent perturbation theory combined with the quantum mechanical density matrix formalism [205, 206] the third-order polarization is given by

$$P^{(3)}(\vec{r},t) = \int_0^\infty \mathrm{d}t_3 \int_0^\infty \mathrm{d}t_2 \int_0^\infty \mathrm{d}t_1 R^{(3)}(t_3,t_2,t_1) E(\vec{r},t-t_3) E(\vec{r},t-t_3-t_2) E(\vec{r},t-t_3-t_2-t_1) \quad (3.22)$$

where $R^{(3)}(t_3,t_2,t_1)$ is the real-valued third-order nonlinear response function in time domain containing all information about the system responding to an external field E

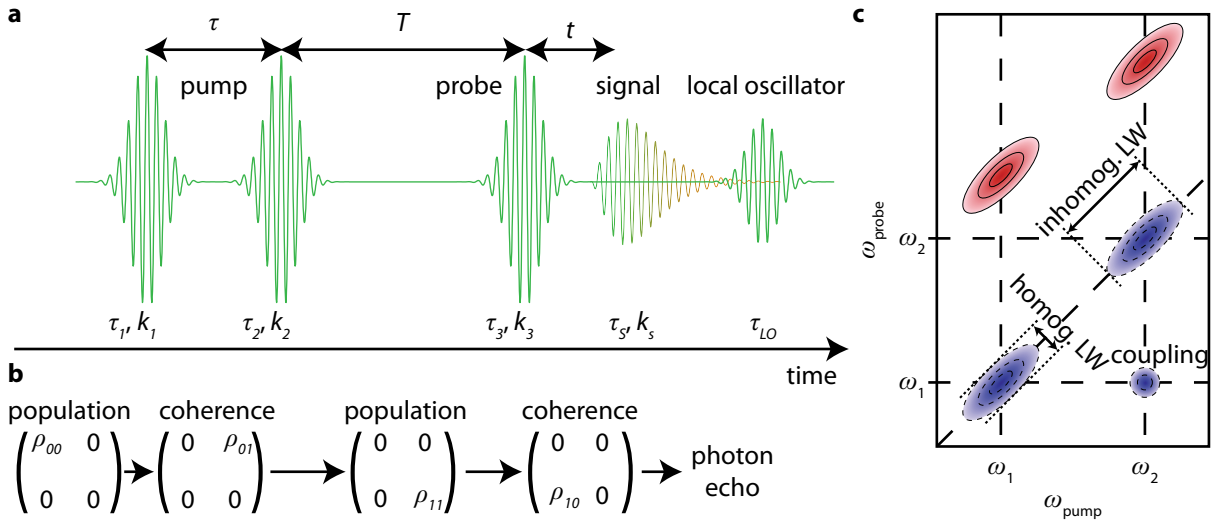

Figure 3.12 | Basic principle of coherent two-dimensional spectroscopy. (a) Three laser pulses with wave vectors $\vec{k}_1$, $\vec{k}_2$, and $\vec{k}_3$, separated by coherence time τ and waiting time T are used to interact with the sample. The first two pulses may be considered as the pump sequence while the third pulse acts as a probe. The signal is emitted at time t after the third pulse in the phase-matched direction $\vec{k}_s$. (b) Exemplary temporal evolution of the density matrix of a two-level system during the laser pulse sequence. The first interaction creates a coherence between ground and excited state while the second pulse after time τ projects the coherence to a population either in the ground or in the excited state. A third interaction induces another coherence. A photon echo is emitted after the detection time t. It has to be noted that in reality only a small number of molecules interacts with the light field while the major part of molecules remains in the ground state (matrix entry 00). (c) Illustration of a possible two-dimensional spectrum of a multilevel system consisting of two diagonal contributions with $\omega_{pump} = \omega_{probe}$ for the two states absorbing at ω_1 and ω_2 and a cross peak indicating coupling between these two states at $\omega_{pump} = \omega_2$ and $\omega_{probe} = \omega_1$. The peak width along the diagonal is given by the inhomogeneous linewidth while the peak width along the anti-diagonal reflects the homogeneous linewidth.

after three light–matter interactions. The variables of integration in Eq. (3.22) are the relative time intervals between successive interactions, i.e., $t_1 = \tau_2 - \tau_1$, $t_2 = \tau_3 - \tau_2$, and $t_3 = \tau_s - \tau_2$. For reasons of causality the response function is non-zero only for t_3, t_2, and $t_1 > 0$.

In two-dimensional spectroscopy three laser beams with wave vectors $\vec{k}_1$, $\vec{k}_2$, and $\vec{k}_3$ irradiate the sample while a fourth one with the wave vector $\vec{k}_s$ is emitted by the sample which is the reason why this technique is assigned to the class of *four-wave mixing* (FWM) experiments. The direction of the emitted signal field is (as in all FWM processes) determined by the phase-matching condition. The signal emitted in the direction $\vec{k}_s = -\vec{k}_1 + \vec{k}_2 + \vec{k}_3$ is called the rephasing part, while the role of the first two interactions is switched for the non-rephasing part emitted in the direction $\vec{k}_s = \vec{k}_1 - \vec{k}_2 + \vec{k}_3$.

In the context of two-dimensional spectroscopy and assuming that the pulse envelopes can be approximated by δ-functions, the time interval between interaction 1 and 2 is called *coherence time* $\tau = t_1$, while the interval between the second and third interaction

is referred to as the *population* or *waiting time* $T = t_2$ in accordance with the pump–probe delay in conventional pump–probe spectroscopy. The signal detection time is $t = t_3 = \tau_s$ assuming that the absolute time origin is at $\tau_3 = 0$.

Different experimental methods have been introduced to characterize the emitted signal. In heterodyned 2D spectroscopy a fourth laser pulse – the local oscillator (LO) – propagates in the signal direction as a reference beam at time t_{LO} and the signal is characterized in amplitude and phase using the technique of spectral interferometry [208, 209]. The use of a fourth pulse can be circumvented using specific beam geometries as will be explained in Sect. 4.4.2.

An intuitive description of nonlinear spectroscopy techniques is obtained with the density matrix representation. The density matrix ρ of a quantum system with several states describes the probability of the system to be found in one of these states. The possible time evolution of a (2×2)-density matrix of a two-level system (ground state 0 and excited state 1) during the 2D pulse sequence is given in Fig. 3.12(b). In the beginning, the system is in the ground state (ρ_{00}). This condition is called a population. Each light–matter interaction results in a step in the density matrix either in vertical or horizontal direction. The first light–matter interaction leads to the coherent superposition of ground and excited state, the system is thus prepared in a coherence (either ρ_{01} or ρ_{10}) in which it evolves during the coherence time τ. The second interaction projects the coherence back to a population in the ground (ρ_{00}) or in the excited state (ρ_{11}). After the population time T, the third laser pulse induces a second coherence which leads to the emission of the signal in terms of a photon echo in the phase-matched direction $\vec{k}_s$. The reason for the echo is the phase inversion between the two coherence times resulting in a constructive interference of all individual polarizations of the molecules at time τ_s. All typical signal contributions that can be observed in transient absorption spectroscopy like GSB, SE, and ESA can also be resolved with coherent two-dimensional spectroscopy and can be described with the density matrix representation where they correspond to different quantum pathways.

In order to extract the two-dimensional spectrum, a Fourier-transform of $P^{(3)}(\tau,T,t)$ with respect to τ and t has to be performed for each population time T resulting in the frequency axes $\omega_\tau = \omega_{pump}$ and $\omega_t = \omega_{probe}$. However, in most experimental implementations the signal field E_s is detected spectrally resolved with a spectrometer as a function of ω_t and the second Fourier transform is not necessary. It can be shown that this signal field is connected to the third-order polarization under ideal conditions via

$$E_s(\tau,T,\omega_t) \propto \frac{\mathrm{i}\omega_t}{n(\omega_t)} P^{(3)}(\tau,T,\omega_t) \tag{3.23}$$

where $n(\omega_t)$ is the linear refractive index of the sample [202]. A Fourier transformation along the coherence time then leads to the desired two-dimensional spectrum

$$S_{2D}(\omega_\tau,T,\omega_t) = \int_{-\infty}^{\infty} \frac{E_s(\tau,T,\omega_t)}{\omega_\tau} \mathrm{e}^{\mathrm{i}\omega_\tau\tau} \mathrm{d}\tau \tag{3.24}$$

where the frequency dependence of the refractive index is neglected. The two-dimensional spectrum $S_{2D}(\omega_\tau,T,\omega_t)$ is in general a complex-valued quantity which is why it can be

separated into its real part – the absorptive contribution – and imaginary part – the refractive contribution. It should also be noted that the two-dimensional spectrum only covers the frequency range provided by the used laser pulses. If pulse 3 (the probe) covers a broader spectral range than pulses 1 and 2 (the pump), this will also be the case for the exploitable range of the ω_t-axis of $S_{2D}(\omega_\tau,T,\omega_t)$.

Figure 3.12(c) displays an exemplary cartoon-like two-dimensional spectrum illustrating typical signal contributions of a system with several energy levels. Emission of the two levels absorbing at frequencies ω_1 and ω_2 leads to the two diagonal contributions (blue ellipses) with $\omega_{pump} = \omega_{probe}$. A coupling between the two states results in a cross-peak at off-diagonal regions (blue circle) at the excitation frequency $\omega_{pump} = \omega_2$ whereas the emission frequency is $\omega_{probe} = \omega_1$, which would not be observable with transient absorption spectroscopy where only the integral over ω_{pump} is measured. Signals arising from excited-state absorption (red ellipses) might also be detected. Another benefit of two-dimensional spectroscopy is that homogeneous and inhomogeneous contributions can be separated. The peak width along the diagonal reflects the inhomogeneous linewidth while the peak width along the anti-diagonal is connected to the homogeneous linewidth.

3.5.3 Beam Geometries for 2D Spectroscopy

Since the first experimental implementation of femtosecond two-dimensional spectroscopy, a large variety of different methods has been introduced to perform such experiments, each of them possessing certain advantages over other approaches. All methods have in common that at least three light-matter interactions lead to the detection of a signal from which a spectrum extending over two frequency dimensions is extracted. However, not all methods provide this signal background-free and therefore specific procedures may be necessary to extract the desired contributions resulting from the interaction with all involved pulses. Furthermore, phase-stability is required between interaction 1 and 2 and between pulse 3 and the local oscillator. An overview over the principles of the four most common methods for collecting 2D spectra is presented in Fig. 3.13.

One possible method is to use an entirely collinear sequence of laser pulses [Fig. 3.13(a)]. The fully **collinear arrangement** impairs the detection of a photon echo which is emitted in the direction of the incoming beams. For this reason typically four pulses are employed that create a second population and consequently an incoherent signal such as fluorescence [210, 211] or photoelectrons [212, 213] is detected. The signal is measured in time domain as a function of τ and t and a two-dimensional Fourier transform along these variables is used to generate the 2D spectrum.

One of the most popular methods is the **fully non-collinear box geometry**, depicted in Fig. 3.13(b), which has been successfully implemented for electronic 2D spectroscopy [14, 15, 202–204] as well as in 2D-IR [200, 214]. Four laser pulses are used propagating at different angles. The photon echo is emitted spatially separated from the incoming beams in the phase-matching direction and heterodyned with a local oscillator. The signal is usually detected with a spectrometer and the 2D spectrum is obtained via a single Fourier transform along τ. This scheme is on the one hand very sensitive due to the background-free signal detection. On the other hand, this technique

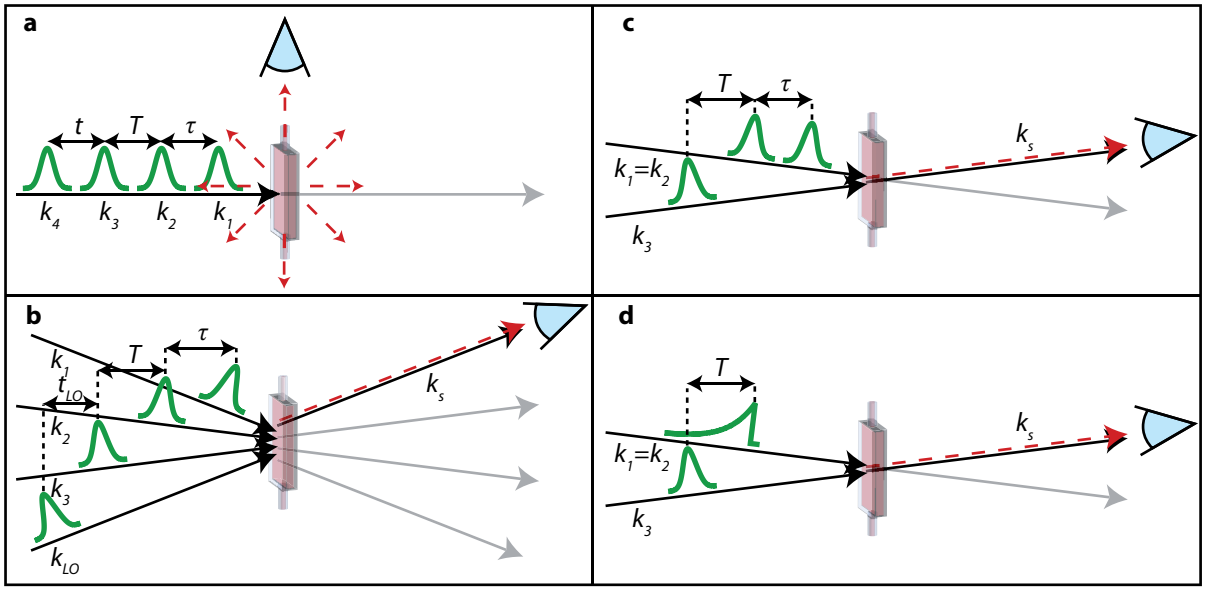

Figure 3.13 | Different possible methods and beam geometries for two-dimensional spectroscopy experiments. (a) In the completely collinear arrangement with four pulses travelling along a common path an incoherent signal such as fluorescence is detected orthogonal to the direction of the laser beam. (b) In the box geometry the four pulses propagate at different angles and the signal is emitted spatially separated from the incoming beams in the phase-matching direction. A local oscillator is used to characterize the signal in amplitude and phase. (c) In the pump–probe geometry a pump pulse is split into a double-pulse sequence with time delay τ either with a pulse shaper or an interferometer. The probe beam gives rise to the third interaction and serves as the local oscillator at the same time. The signal is automatically phase matched. (d) In the hole-burning approach the center wavelength of a narrowband pump pulse, created for example with an etalon, is scanned, generating a two-dimensional spectrum directly in frequency domain at the expense of a decreased temporal and spectral resolution [216–218].

intrinsically provides the real and imaginary part of the spectrum and the rephasing and nonrephasing contributions are separable through proper pulse ordering. Despite these advantages, the use of four different beams makes this approach very sensitive to mechanical perturbations and the spatial position of all four beams has to be adjusted carefully such that they overlap at the sample position. Another downside is the uncertainty in the pulse timings and relative phases which necessitates an elaborate phasing procedure [202, 215].

The method employed in this work is shown in Fig. 3.13(c). In this arrangement a **partly collinear pump–probe geometry**, consisting of two separated beams is employed and the pump pulse is split up into a double pulse sequence separated by coherence time τ. The signal is detected just as in transient absorption spectroscopy in frequency domain with a spectrometer and the ω_{pump}-axis is generated by measuring the signal as a function of τ. The real part of the Fourier transform along τ yields the purely absorptive 2D spectrum. This possibility was first discussed theoretically by Gallagher Faeder and Jonas in 1999 [219] and has later been implemented for 2D-IR [216, 218, 220],

in the near-IR [217], in the visible [8, 24, 221, 222], and even for 2D experiments in the ultraviolet spectral region [223, 224]. The pump–probe geometry has several major advantages over all other methods: first, just one single modification is required to convert a pump–probe setup into a two-dimensional spectrometer, which is a device that is capable of splitting up a single pulse into a phase-locked double pulse sequence. Second, a pulse shaper has turned out to be best suited for this task as it permits the generation of common path and thus intrinsically phase-stable pulse sequences. For this reason interferometric stability is not an issue if a pulse shaper is used to create pulses 1 and 2. Third, the probe beam serves both as pulse 3 and as the local oscillator (with $t_{LO} = 0$), which makes the phasing procedure necessary in the box geometry redundant. Fourth, the use of a pulse shaper also allows the manipulation of the carrier phases of pulses 1 and 2 which opens up a multitude of new options such as the mitigation of the Nyquist limit and signal-to-noise improvements by making use of the so-called rotating frame or of phase-cycling schemes to extract different contributions while at the same time undesirable scattering can be suppressed [210, 218, 225, 226]. In this way purely absorptive and inherently properly phased 2D spectra can be collected in a very simple fashion. The pump–probe geometry hence represents the best compromise between intricacy and simplicity as it provides an experimentally easy implementation of coherent 2D spectroscopy with the highest achievable time and frequency resolution while the complexity of the measurement procedure and the amount of data post-processing is kept to a minimum. A detailed description of the experimental implementation of coherent electronic 2D spectroscopy in the pump–probe geometry with a femtosecond pulse shaper is given in Sect. 4.4.2 of this work.

Also methods that are not based on explicit Fourier transformations have been implemented. In the so-called **hole burning approach** [Fig. 3.13(d)], primarily established for 2D-IR spectroscopy [199, 227], a spectrally narrow pump beam is created, for example with the use of an etalon. To ensure spectral selectivity, the spectral bandwidth of the pump has to be smaller than the homogeneous linewidth of the investigated sample. The 2D spectrum is measured by scanning the center wavelength of the pump pulse. Since spectral narrowing with an etalon results in pulses with durations in the picosecond regime and an exponential-like pulse envelope, the time and pump-frequency resolution is substantially reduced in this approach [228]. The hole-burning technique is certainly the most facile method to implement because only two laser pulses are used without any need for interferometric stability making it a very simple, robust, and reliable option for collecting 2D spectra.

4 Exposing Reactive Modes in Ultrafast Photochemistry by Third-Order Three-Dimensional Electronic Spectroscopy

Elucidating the nature of a chemical reaction on its fundamental time scale with all its microscopic aspects requires ultrafast temporal resolution. In this chapter, it is demonstrated that third-order time-resolved spectroscopy techniques can be exploited for clearing up a highly-complex photochemical reaction that includes multiple reaction paths with a large variety of rate constants. As a model reaction, the *cis–trans* photoisomerization of a merocyanine isomer is investigated. In order to resolve the dynamics associated with the photoreaction itself a third-order three-dimensional electronic spectroscopy technique is implemented. Such a technique is applied here for the first time to analyze a chemical reaction network. It is demonstrated that this novel approach is capable of uncovering partly concealed reaction products which would not be possible with conventional third-order techniques like transient absorption or even coherent 2D spectroscopy.

This chapter is organized as follows: The spiropyran/merocyanine photosystem is briefly introduced in Sect. 4.1. Then broadband femtosecond transient absorption data of the model system is discussed and analyzed in detail in Sect. 4.2. On this basis a reaction scheme of the investigated system is inferred in Sect. 4.3. The experimental implementation of 2D spectroscopy in the pump–probe geometry and the 2D spectra of 6-nitro BIPS are explained in Sect. 4.4. The third-order three-dimensional spectrum is subject of Sect. 4.5 and parts of the results of quantum chemical calculations performed by our collaborators in the theoretical chemistry group of Prof. B. Engels are presented in Sect. 4.6.

Parts of this chapter have been submitted for publication in Ref. [2] or already been published in Ref. [4], as detailed in the table on page v.

4.1 The Spiropyran–Merocyanine Photosystem

Two slightly different representatives of the spiropyran/merocyanine family are explored in this thesis. Spiropyrans are photochromic compounds that can exist in two different molecular configurations with differing colors which are (partly) interconvertible by light irradiation [229–231]. The compounds investigated in this work are nitro-substituted indolinobenzopyrans. The spiropyran form (SP) consists of two perpendicular heterocyclic

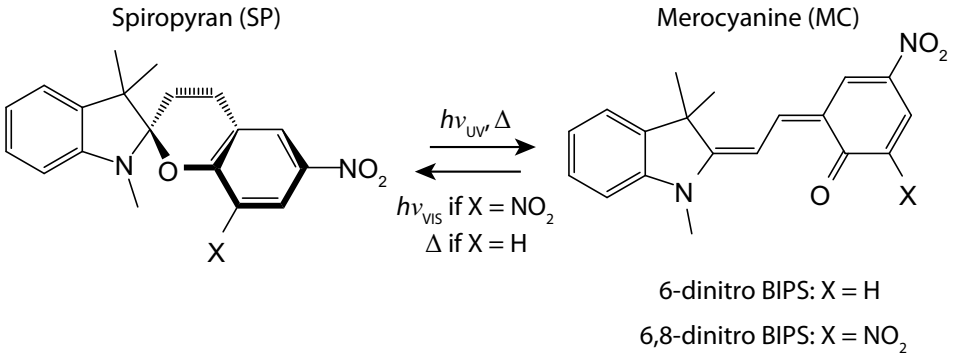

Figure 4.1 | The photochromic spiropyran/merocyanine compounds investigated in this thesis. While for both compounds the ring-opening reaction from SP to MC can be induced by absorption of a UV photon, the photoinduced ring-closure reaction by illumination of visible light is only possible for 6,8-dinitro BIPS (X = NO_2) while for 6-nitro BIPS (X = H) the ring-closure reaction proceeds exclusively thermally.

ring systems – a pyran moiety and an indole moiety – linked by a single spiro carbon atom. Due to the orthogonality of the two ring systems, their $\pi-$systems do not interact and, as a result, the spiropyran electronic absorption is located in the ultraviolet spectral region. Upon UV light irradiation the SP form undergoes an electrocyclic ring-opening reaction to the merocyanine form (MC), which exhibits an extended conjugation because the two ring systems form a planar structure. Consequently, the ring-open MC form possesses an electronic absorption band in the visible. In some cases several MC isomers can be formed, as will be discussed in more detail in Sect. 4.1.1. The ring closure reaction proceeds either thermally [229, 232] or photochemically [233–237] depending on the substituents of the SP/MC systems and the solvent. The two molecular structures relevant for this thesis are illustrated in Fig. 4.1. The spiropyran compound with a single nitro substituent (X = H), 6-nitro-1',3',3'-trimethylspiro[2*H*-1-benzopyran-2,2'-indoline], commonly referred to as 6-nitro BIPS, is studied in this chapter, while the photochemistry of 6,8-dinitro BIPS (X = NO_2) is analyzed in Chap. 5.

The photochromic properties of spiropyrans allow numerous potential applications in the fields of molecular electronics, material sciences, and biology, such as optical storage [238], surface coatings [239], or DNA photoswitching [240].

4.1.1 Isomerism of the Merocyanine Form

Already in the 1960s it was conjectured that, due to different configurations of the polymethine chain, the open-ring merocyanine might form different stereoisomers [241]. The methine bridge of 6-nitro BIPS is characterized by three dihedral angles α, β, and γ of the three adjacent C–C bonds [upper left corner of Fig. 4.2]. While the *cis* (C) configuration corresponds to an angle of 0°, the *trans* (T) configuration is characterized by a dihedral angle of 180°. Consequently, in principle $2^3 = 8$ possible MC isomers may be formed, which are located at the corners of an isomer cube in the three-dimensional space spanned by the three dihedral angles [242, 243], as depicted in Fig. 4.2. From the corresponding molecular structures, also shown in Fig. 4.2, it can be inferred that

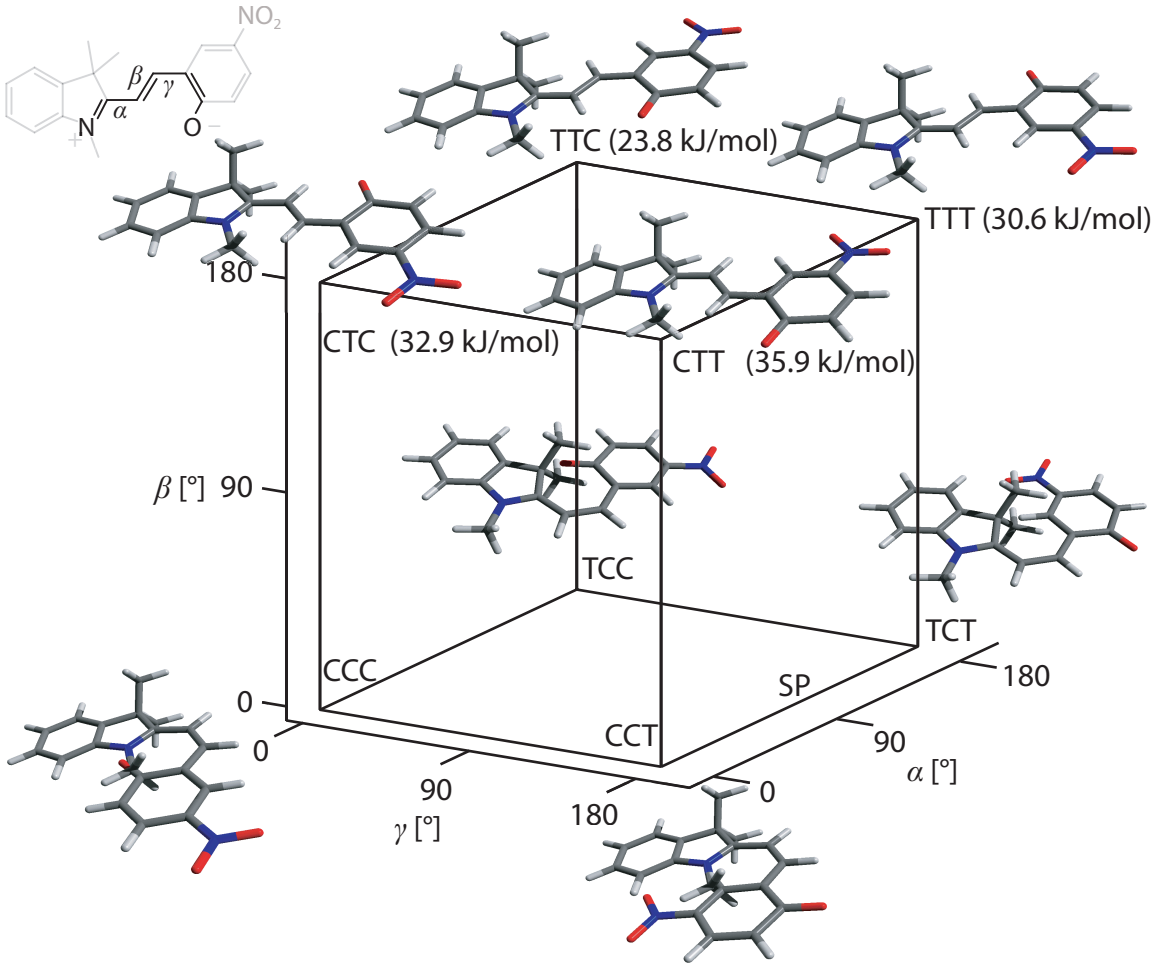

Figure 4.2 | Isomerism of the merocyanine form of 6-nitro BIPS. The structure of the polymethine chain is determined by the three dihedral angles α, β, and γ that describe the *cis* (0°) or *trans* (180°) configuration of the three C–C bonds. In a three-dimensional space spanned by the three dihedral angles all $2^3 = 8$ resulting stereoisomers are located at the corners of an isomer cube [242, 243]. Isomers with a *cis* configurations in the central C–C bond are less stable due to steric hindrance, as can be inferred from the depicted molecular structures. The most stable isomer is TTC followed by TTT, CTC, and CTT. Depicted relative isomer energies are scaled to the SP energy and taken from Ref. [246].

isomers with a *cis* configuration in the central C–C bond (CCC, CCT, TCT, TCC) are not stable due to steric hindrance between the methyl groups of the indol moiety and the ring system where the nitro group is attached. Calculation and experimental data published in the literature have shown that the most stable MC configuration is the TTC isomer, followed by TTT, CTC, and CTT (relative energies scaled to the SP energy are given in Fig. 4.2) [242, 244–247]. The reason why the *trans* configuration of α as in TTC and TTT is favored over the *cis* structure of CTC and CTT is that for $\alpha = 0°$ the distance between the in-plane methyl group and the hydrogen atoms of the methine chain is shorter, resulting in a slight deformation of the molecular backbone due to steric strain [246].

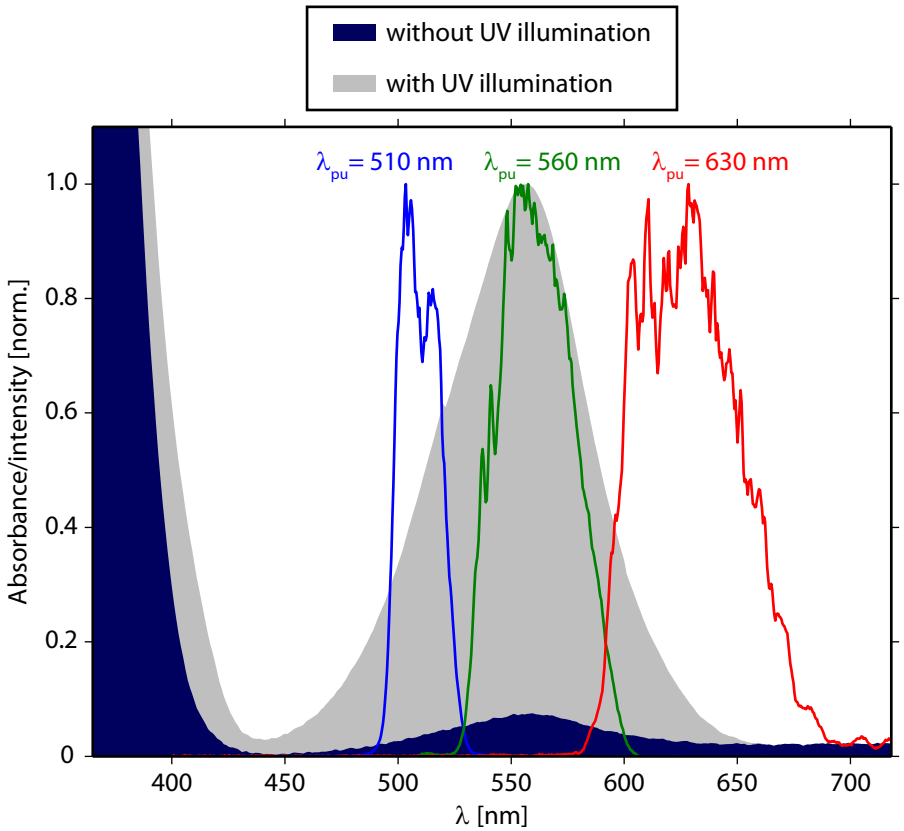

Figure 4.3 | Absorption spectrum of 6-nitro BIPS in acetonitrile. Without UV illumination (dark blue area) the spiropyran form dominates in solution exhibiting a pronounced absorption in the UV around 340 nm and a second band below 300 nm (not shown). Upon UV illumination (gray area), the merocyanine is formed as is evidenced by its strong absorption in the visible spectral range centered at 560 nm. Three different excitation wavelengths of 510 nm (blue), 560 nm (green), and 630 nm (red) are used for the transient absorption studies discussed in Sect. 4.2. Figure adapted from Ref. [2].

4.1.2 Steady-State Properties of Ring-Open 6-nitro BIPS

The steady-state absorption spectrum of commercially available 6-nitro BIPS (*ABCR GmbH*, Karlsruhe) dissolved in acetonitrile measured with a *Jasco V-670* UV-Vis spectrometer is shown in Fig. 4.3 (dark blue shaded area). For 6-nitro BIPS, the ring-closed spiropyran form is dominant in solution, which possesses its main absorption bands in the UV spectral region around 340 nm and below 300 nm (not shown in Fig. 4.3). In order to increase the ratio of ring-open merocyanine molecules the solution is illuminated with UV light-emitting diodes at 365 nm (*LZ100U600, LED Engin*, San Jose, USA). The formation of the merocyanine is accompanied by the emergence of a broad absorption band in the visible centered around 560 nm (gray shaded area). The absorbance increase after UV illumination in the range below 430 nm indicates that the merocyanine form also exhibits absorption bands in the UV region with a slightly higher extinction coefficient than the spiropyran form.

While on the basis of the steady-state absorption spectrum no indication of multiple

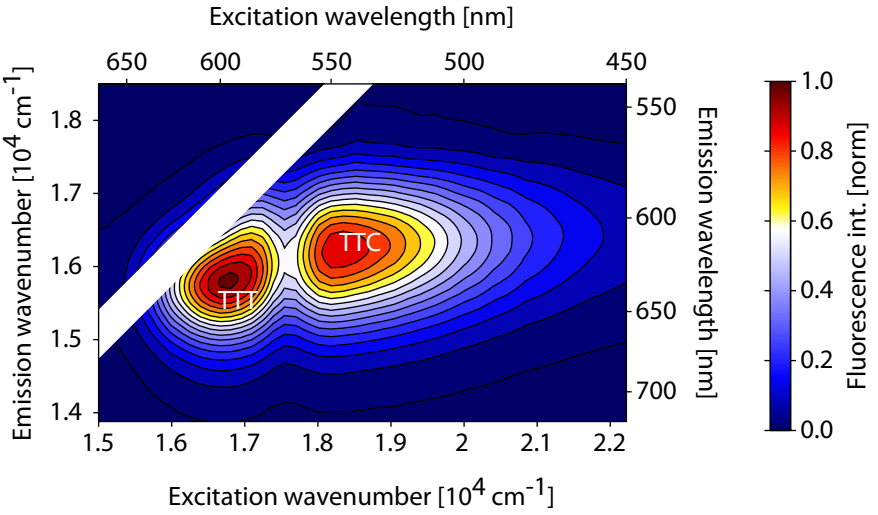

Figure 4.4 | Fluorescence spectrum of 6-nitro BIPS in acetonitrile under continuous UV illumination as a function of the excitation wavenumber. The existence of two ring-open isomers is proven by the observation of two distinct and separated fluorescence peaks that are assigned to the TTC and TTT isomers as labeled. Contributions on the diagonal originating from stray light have been masked. Figure adapted from Ref. [4].

ring-open conformers is found, the emission spectrum clearly evidences the existence of different MC isomers with slightly differing absorption and emission properties. The fluorescence spectrum of 6-nitro BIPS in acetonitrile under continuous UV illumination of the sample reservoir is shown in Fig. 4.4 as a function of the excitation wavenumber. Two clearly separated and distinct emission maxima are observed. One of the peaks is assigned to the TTC isomer peaking at an excitation wavelength of 550 nm with a central emission wavelength of 618 nm. The second peak is attributed to TTT isomers, whose absorption (around 600 nm) is red-shifted with respect to TTC and with an emission wavelength of about 630 nm. Since the MC steady-state absorption spectrum has its maximum around 560 nm, we can conclude that the TTC isomer is dominant in solution assuming comparable extinction coefficients for both isomers. However, the excitation–emission spectrum shows two contributions of almost the same magnitude indicating that the fluorescence quantum yield of TTT is considerably higher than that of TTC which in turn might indicate a longer excited-state lifetime of the TTT isomer.

4.1.3 Current State of research

6-nitro BIPS has been object of numerous experimental and theoretical studies and is probably one of the most popular compounds of the BIPS family. Since the discovery of the photochromic properties of spiropyrans by Hirshberg and coworkers in the 1950s [248, 249], a vast amount of scientific studies about their structures, as well as photochromic and thermochromic properties, has been reported. In the 1990s, first subpicosecond transient absorption measurements were conducted on the photoinduced ring-opening reaction of 6-nitro BIPS, from which it was concluded that the SP form is formed with a rise time of about 20 ps [243] and a biexponential behavior of the characteristic bands

was attributed to the emergence of two different MC isomers [250, 251].

In contrast to other SP/MC systems where the MC is the more stable form – as for instance for the related 6,8-dinitro BIPS [5, 8, 235, 236] which will be discussed in Chap. 5 – the photochemical properties of the 6-nitro BIPS MC remained almost unexplored. For 6-nitro BIPS, the MC/SP equilibrium distribution depends on the polarity of the solvent and is below 10 % for most solvents [252]. Therefore, the sample has to be continuously irradiated with UV light before any kind of experiment on the ring-open form may be performed. The results of nanosecond laser photolysis experiments published by Görner *et al.* suggested that another MC isomer may be formed after S_1 excitation of the TTC isomer with a pronounced solvent-dependent quantum yield (< 10 % in ethanol, about 90 % in toluene) and a thermal lifetime of several tens of microseconds [252, 253]. Wohl and Kuciauskas employed single-channel femtosecond transient absorption spectroscopy to investigate the excited-state dynamics of the MC form in toluene solution [254]. They identified different photoisomerization channels that were assigned to the TTC→CTC or TTC→CTT reactions while the emerging signatures after TTT excitation were ascribed to the formation of TTC and CTC/CTT.

Various studies published in the literature explored this class of compounds from a theoretical point of view by means of quantum chemical calculations. Density functional theory was used by several groups to determine the geometries and ground-state energies of spiropyran and its merocyanine isomers. Futami *et al.* [246] and Cottone *et al.* [255] calculated the vibrational frequencies while other groups focused on the ring-opening pathways and associated activation energies, suggesting that the ring-opening reaction probably proceeds over several reaction intermediates involving a cisoid structure and the CTC isomer before mainly TTC is formed [247, 256]. Considerably fewer quantum chemical studies about interconversion processes between different MC isomers were conducted, mostly using simplified model merocyanines. Baraldi and coworkers for example analyzed the energy profiles as a function of various dihedral angles of polymethinemerocyanines [257] and Cottone *et al.* calculated the thermal isomerization barrier between TTC and TTT of 8-Br-6-nitro BIPS [258]. Sanchez-Lozano *et al.* found several S_1-S_0 conical intersections in a highly simplified model of the BIPS molecule [259]. In a very recent publication the authors report the existence of a conical intersection connecting the first excited singlet state of TTC with the TTT ground state in 6,8-dinitro BIPS [260] which is, however, contrary to experimental results for the same system by our group (see also Chap. 5) [235, 236].

Since many aspects of the photochemistry of the MC form of 6-nitro BIPS are still unclear, and several states are expected to contribute to the relaxation processes, this system represents a promising model compound to test the potential of novel and innovative time-resolved techniques. In a first step, transient absorption measurements were conducted in order to identify the dominant pathways after photoexcitation together with the associated lifetimes and quantum yields. Moreover, evidences of isomerization processes among different MC isomers are also obtained with transient absorption measurements which can be investigated in much more detail by means of third-order multidimensional spectroscopy.

4.2 Femtosecond Transient Absorption Spectroscopy

4.2.1 Dynamics After Excitation at Various Wavelengths

The transient absorption data as a function of pump–probe delay T and probe wavelength λ of the MC form of 6-nitro BIPS in acetonitrile is shown in Fig. 4.5 for three different central pump wavelengths [261]. The excitation laser spectrum was adjusted to the blue edge (510 nm, blue line in Fig. 4.3), to the maximum (560 nm, green), and the red-edge (630 nm, red) of the steady-state absorption spectrum of the MC form in order to excite a variable isomer ratio. In the depicted ΔOD map positive changes of absorbance (e.g., ESA, PA) are indicated by red and yellow colors, while bluish colors denote a pump induced decrease of absorbance (e.g., GSB, SE).

Fig. 4.5(a) shows the transient absorption data after excitation at 510 nm, in which case the TTC isomer is predominantly excited. The ground-state bleach around 560 nm emerges quasi instantaneously after excitation. Below 500 nm a positive signal arises, assigned to excited-state absorption peaking around 460 nm. Above 600 nm stimulated emission is observed, centered around 650 nm for longer pump–probe delays. A rise time for both SE and ESA signals on a subpicosecond time scale is evident. As indicated in Fig. 4.5(a) (white arrows), both bands feature a pronounced spectral shift during the first picosecond (blue-shift of ESA contributions, red-shift of SE), probably due to vibrational cooling of the excited-state population. SE and ESA signals decay on a time scale of tens of picoseconds and practically disappear after about 100 ps whereas in the GSB region a constant negative signal persists for more than 2 ns. A similarly long-lived positive feature, centered around 600 nm and red-shifted to the TTC bleach, emerges after about 50 ps. This signal can be assigned to a photoproduct absorption and is attributed to a TTT isomer formation. This assignment is made here purely on the spectral position of the PA band around 600 nm, which agrees very well with the excitation wavelength of the TTT fluorescence peak in Fig. 4.4, but will be substantiated in the following. Thus TTT isomers are formed after TTC photoexcitation, accounting for the remaining TTC bleach caused by a decrease of the TTC concentration and an associated increase of TTT concentration in the pumped sample volume.

By tuning the pump laser spectrum to 560 nm [Fig. 4.5(b)] also TTT isomers are excited. In the measured data, all the signatures previously mentioned are again observed and, due to the higher absorbance of the sample at these wavelengths, the total signal magnitude is increased by a factor of 3 (see color bar on the right hand side). The most prominent change with respect to the data shown in Fig. 4.5(a) is the slightly less pronounced PA band, probably caused by the slightly reduced ratio of excited TTC molecules.

It can be assumed that pumping at the red edge of the absorption spectrum [around 630 nm, Fig. 4.5(c)] results predominantly in TTT excitation. In this case several prominent differences can be noticed if compared to the data of Figs. 4.5(a) and (b). Firstly, all three bands – ESA, GSB, and SE – are slightly red-shifted from those after blue-edge excitation. While the maximum of the ESA contributions differs only by a few nanometers, being now at 470 nm, GSB and SE are considerably red-shifted (595 nm and 660 nm, respectively). This is in good agreement with the fluorescence

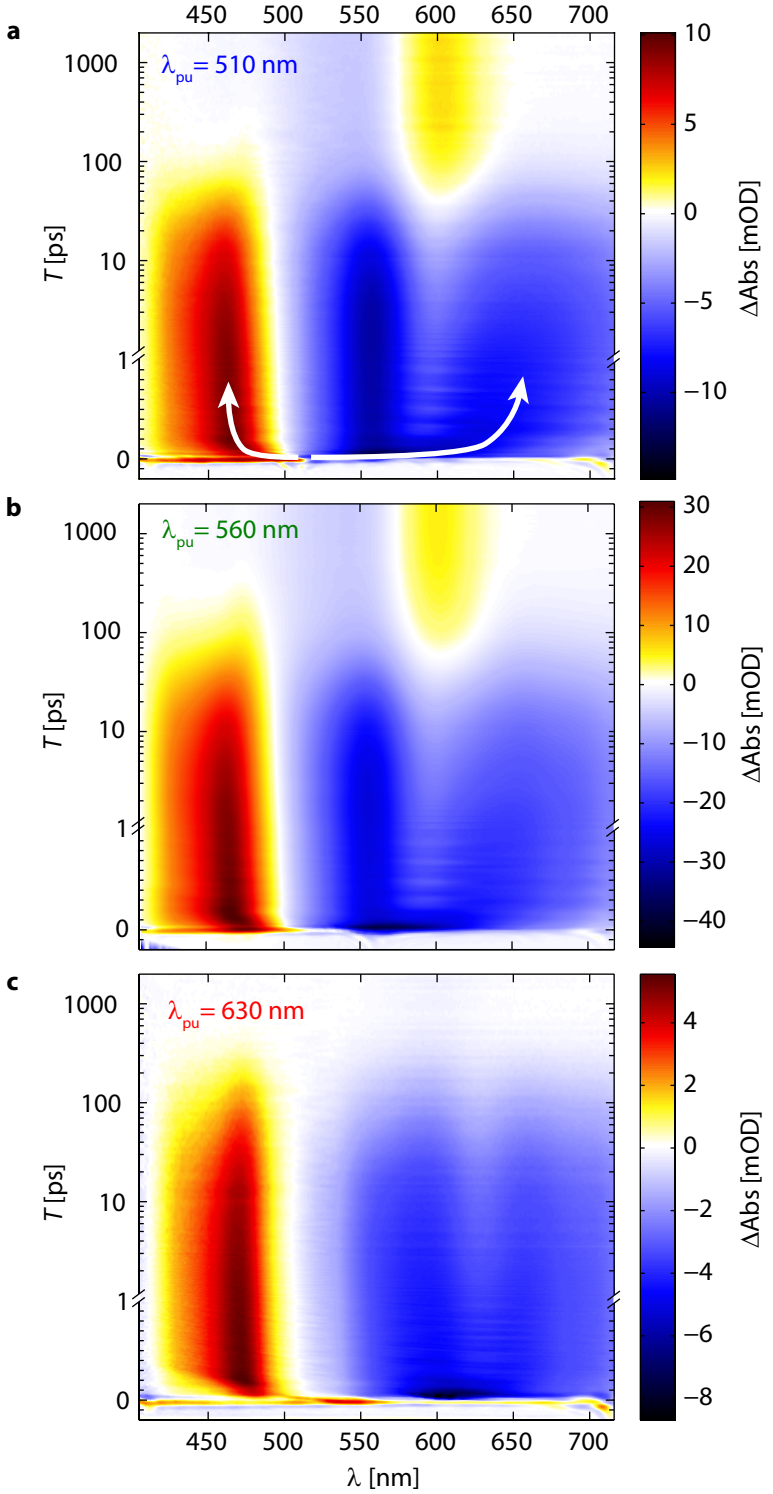

Figure 4.5 | Transient absorption maps of the merocyanine form of 6-nitro BIPS dissolved in acetonitrile. Various excitation wavelengths of (a) 510 nm, (b) 560 nm and (c) 630 nm were employed. Positive changes in absorption are indicated by yellow and red colors, negative contributions by bluish ones. Note that the time axis is plotted linear in the range $-0.2 < T < 1$ ps and logarithmic from there on. The data was corrected for probe chirp (see Sect. 3.4.3) only for visualization purposes. Figure adapted from Ref. [2].

data in Fig. 4.4. Secondly, the observed decay times are clearly longer than after TTC excitation, indicating a longer excited-state lifetime of the TTT isomer. Thirdly, all signal contributions decay to zero after several hundreds of picoseconds and no PA band is observed, evidencing that all excited TTT isomers return to the TTT ground state without forming any long-living intermediates or photoproducts. Therefore, while TTC→TTT isomerization can be photoinduced, signatures of the reverse process do not appear in our data.

4.2.2 Global Data Analysis

In order to extract a comprehensive picture of the relaxation of all involved species and the corresponding spectral signatures and lifetimes, each data set was modelled with a global multiexponential fit as described in Sect. 3.4.2. To completely describe the temporal behavior of the data over the monitored spectral range, five rate constants were necessary. In order to model the constant contributions related to the photoproduct formation one of the time constants was fixed to $\tau = \infty$. The remaining four contributions can be described by time constants of (100 ± 30) fs, (1.2 ± 0.2) ps, (35 ± 4) ps, and (160 ± 40) ps. The associated DADS for 560 nm excitation are shown in Fig. 4.6.

The 100 fs DADS (black) describes the second strongest component and exhibits strong negative (460 and 580 nm) as well as positive (490 and above 630 nm) features with distinct changes of sign in between. Such an antisymmetric derivative-like peak shape typically describes the spectral shift of bands and is in our case associated with a fast blue-shift of the ESA and a simultaneous red-shift of SE contributions. Based on this observation and on the short time constant, we can conclude that this DADS describes an ultrafast inertial motion of the created wave packet from the Franck–Condon point of the S_1 potential towards lower-energy regions of the PES. However, also fast solvent reorganization processes could play a role on this time scale [262, 263].

The 1.2 ps component is considerably lower in amplitude but its spectral profile is partly comparable to the 100 fs DADS, although slightly blue shifted in the ESA region and slightly red-shifted in the SE band. For this reason, this DADS is assigned to vibrational cooling which is associated with a characteristic Stokes shift of ESA and SE signatures.

The dominating component of the global fit corresponds to a decay constant of 35 ps (green) which is assigned to the S_1 lifetime of the TTC isomer in good agreement with the results of Wohl *et al.* for the same compound in toluene, who found a 36 ps decay time after excitation at 490 nm [254]. The assignment to the S_1 state of the TTC isomer is based on the fact that this component possesses strong ESA (400–500 nm) and SE (> 600 nm) signatures and a GSB band centered around 560 nm.

In analogy to the 35 ps component we can assign the 160 ps DADS (red) to the S_1 lifetime of TTT with the GSB at 595 nm and SE around 660 nm as this spectral profile is slightly red-shifted with respect to the TTC DADS (GSB at 560 nm, SE at 625nm). Due to the lower equilibrium TTT concentration it is considerably lower in amplitude, but very similar in shape to the 35 ps TTC component. Thus the excited-state lifetime of the TTT isomer extends the TTC lifetime by a factor of 4.5 which nicely resembles the observation of a higher fluorescence quantum yield for TTT (Fig. 4.4) which can

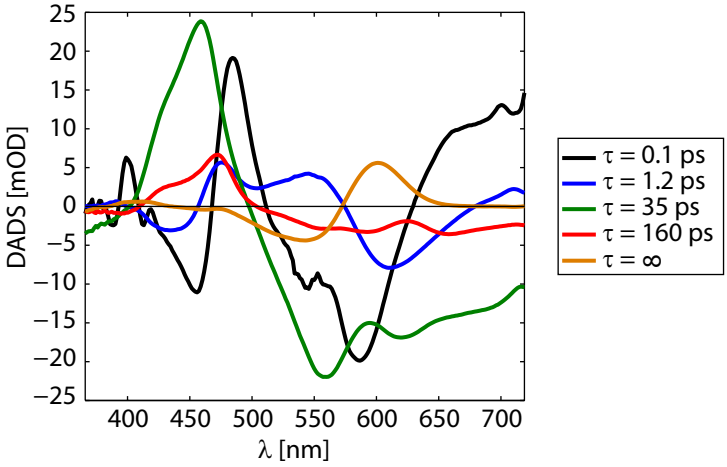

Figure 4.6 | Results of the global fitting routine. Decay-associated difference spectrum of the MC form of 6-nitro BIPS in acetonitrile after excitation with 560 nm pulses extracted by a global fitting routine with four different time constants and a constant ($\tau = \infty$) contribution. Figure adapted from Ref. [2].

also be deduced from the SE/GSB ratio in the DADS profiles of the two isomers.

The constant $\tau = \infty$ component (orange) resembles the remaining negative TTC bleach around 557 nm and the corresponding TTT absorption band in the form of a positive PA contribution centered at 600 nm. Since both signatures are located in the region of the steady-state MC absorption ranging from 450 to 650 nm (see Fig. 4.3) this DADS further confirms the observation of two unidirectionally interconvertible MC isomers. Moreover, negative and positive contributions share almost the same absolute amplitudes, which means that the spectrally integrated $\tau = \infty$ signal almost vanishes. Accordingly, provided that both isomers have roughly the same S_0–S_1 oscillator strength (which will be discussed in more detail in Sect. 4.6), it can further be deduced that all TTC molecules that do not return to the TTC ground state react to the TTT ground state without the presence of loss channels as, for instance, triplet states or the ring-closed SP form, which would result in a more pronounced TTC bleach. Thus, the ring-closure reaction, as well as long-lived triplet states, can be excluded as dominant reaction pathways for the two observed MC isomers, which is in strong contrast to other compounds of the BIPS family.

From the constant remaining bleach and the PA signal it can be concluded that the thermal back reaction from TTT to TTC does not take place within our experimentally accessible time window of about 3 ns. Thus the isomerization barrier in the ground state is too high to influence the isomer distribution in the ground state on a nanosecond time scale, which is also in agreement with the studies of Görner *et al.*, who found a thermal lifetime of 16 μs for the TTT isomer in acetonitrile and estimated the activation energy for the thermal back reaction to be 39 kJ/mol [252, 253].

The isolated TTC and TTT steady-state absorption spectra can be estimated with the aid of the $\tau = \infty$ DADS and the measured steady-state absorption spectrum of the isomer mixture as described in the following. The isolated TTC absorption spectrum is extracted by subtracting the $\tau = \infty$ DADS, multiplied by a scaling factor, from

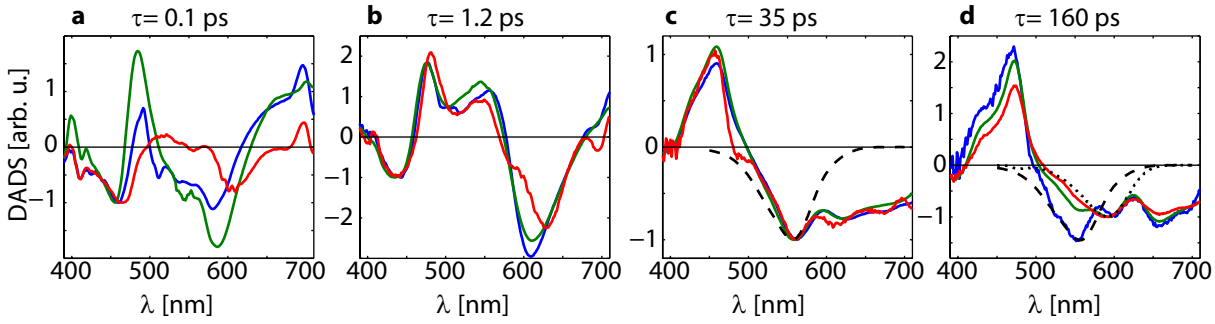

Figure 4.7 | Change of the DADS spectra with the excitation wavelength. DADS of the MC form of 6-nitro BIPS in acetonitrile are compared for different excitation wavelengths of 510 nm (blue), 560 nm (green), and 630 nm (red) of the $\tau = 0.1$ (a), 1.2 (b), 35 (c), and 160 ps (d) components. The inverse of the isolated isomer absorption spectra (TTC: dashed, TTT: dotted) were estimated on the basis of the $\tau = \infty$ component and the steady-state absorption spectrum. All spectra are normalized at spectral regions where they exhibit similar spectral profiles. Figure adapted from Ref. [2].

the measured MC absorption spectrum. The scaling factor accounts for the number of excited molecules undergoing isomerization and is adjusted such that the resulting absorption spectrum fits the inversed GSB profile of the 35 ps DADS. The procedure for the TTT isomer is similar with the difference that in this case the measured MC absorption spectrum is subtracted from the $\tau = \infty$ DADS with another scaling factor chosen in a way that the resulting spectrum fits the inverse GSB profile of the 160 ps DADS. Assuming again the same S_0–S_1 oscillator strength for both isomers, the ratio of the scaling factors then acts as an indicator for the equilibrium TTT:TTC isomer ratio at room temperature which is found to be about 1:10.

As mentioned above, all data sets have been modelled with a global fit. The excitation-wavelength dependence of the resulting DADS is illustrated in Fig. 4.7, comparing the DADS profiles of (within the experimental accuracy) the same time constants for excitation wavelengths of 510 nm (blue), 560 nm (green), and 630 nm (red). To facilitate their comparison, all spectra were normalized to the amplitudes in regions where they share a similar spectral profile.

The most pronounced variation with the excitation wavelength is found for the 100 fs DADS shown in Fig. 4.7(a). While this component seems to play a role in both isomers, it exhibits a substantially different spectral shape depending on the excitation wavelength. Since this component is attributed to the primary photodynamics initiated at the Franck–Condon region, it is very sensitive to the amount of excess energy transferred to the system. A higher amount of excess energy leads to the creation of a wave packet at higher energy regions of the PES. Hence, the ESA and SE bands are observed at different spectral regions during the first 100 fs in comparison with excitation with a lower amount of excess energy. The variation of the 100 fs DADS seems to resemble this as, for instance, the positive peak at the blue edge of the ESA is most pronounced for the data with 510 nm excitation, while after 630 nm excitation this feature is almost absent. Moreover, the negative SE part of this component is considerably red-shifted for 630 nm excitation (ca. 610 nm) compared to the case of excitation at 560 nm and

510 nm (ca. 590 nm).

We assigned the 1.2 ps DADS to vibrational cooling in the first-excited state. For this component only minor spectral variations with the excitation wavelength are found as shown in Fig. 4.7(b) indicating that vibrational cooling occurs for both isomers. The most noticeable feature is the red-shift of the negative peak in the SE regions by roughly 20 nm, which is probably caused by the fact that the stimulated emission of the TTT isomer is also red-shifted with respect to the TTC SE.

Only marginal variations of the spectral profile are found for the 35 ps component [Fig. 4.7(c)], confirming that this spectrum has to be attributed to the vibrationally relaxed S_1 state of the TTC isomer. The assignment of this component to the TTC isomer is also verified by the observation that its amplitude is substantially reduced with respect to the amplitude of the 160 ps DADS when the sample is excited at 630 nm, where mainly TTT absorbs. The inverse of the extracted TTC absorption spectrum is shown in the same graph as a black dashed curve. It nicely reproduces the GSB part of this DADS and overlaps with ESA signatures at shorter wavelengths and parts of the SE at the red edge.

The 160 ps DADS is attributed to the emissive S_1 state of the TTT isomer which is why no substantial change of its spectral shape is expected. Nonetheless, as shown in Fig. 4.7(d), a significant variation of this DADS is observed in the region between 500 and 600 nm. While upon 630 nm excitation a single GSB contribution around 600 nm is observed, which matches the inverse of the estimated TTT absorption (black dotted line), a second GSB band emerges at TTC wavelengths (black dashed line) when the sample is excited at the blue edge of the MC absorption. It can be concluded that this DADS resembles the spectral signatures of at least two different excited states that relax with very similar time constants of about 160 ps and thus cannot be distinguished with our analysis. From this observation it is inferred that after TTC excitation two different radiative states – a dominant state with $\tau = 35$ ps and a second one with $\tau = 160$ – might be reached, which are followed by emission of a photon and the relaxation to the TTC ground state. In contrast, after TTT excitation all molecules return to the ground state via the TTT S_1 state with $\tau = 160$ ps.

4.2.3 Isomerization Quantum Yield

The quantum yield of the photoinduced TTC→TTT isomerization is given by the ratio of molecules that undergo *cis-trans* isomerization to the total amount of excited TTC molecules (see also definition in Sect. 2.3.2). On the basis of our data, this quantity can be determined by analyzing the quotient of the amplitude of the remaining TTC bleach in the $\tau = \infty$ DADS to the sum of all components containing the TTC bleach. Thus, the three DADS characterized by τ =35 ps, 160 ps, and ∞ are included for the computation of $\Phi_{\mathrm{TTC}\to\mathrm{TTT}}$ and a probe wavelength of $\lambda_{\mathrm{GSB}}^{\mathrm{TTC}} = 540$ nm is chosen. Accordingly, the quantum yield is given for each data set by

$$\Phi_{\mathrm{TTC}\to\mathrm{TTT}} = \frac{\mathrm{DADS}_{\infty}\left(\lambda_{\mathrm{GSB}}^{\mathrm{TTC}}\right)}{\mathrm{DADS}_{35\,\mathrm{ps}}\left(\lambda_{\mathrm{GSB}}^{\mathrm{TTC}}\right) + \mathrm{DADS}_{160\,\mathrm{ps}}\left(\lambda_{\mathrm{GSB}}^{\mathrm{TTC}}\right) + \mathrm{DADS}_{\infty}\left(\lambda_{\mathrm{GSB}}^{\mathrm{TTC}}\right)}. \tag{4.1}$$

A major issue in this approach is the overlap of the TTC GSB with ESA contributions

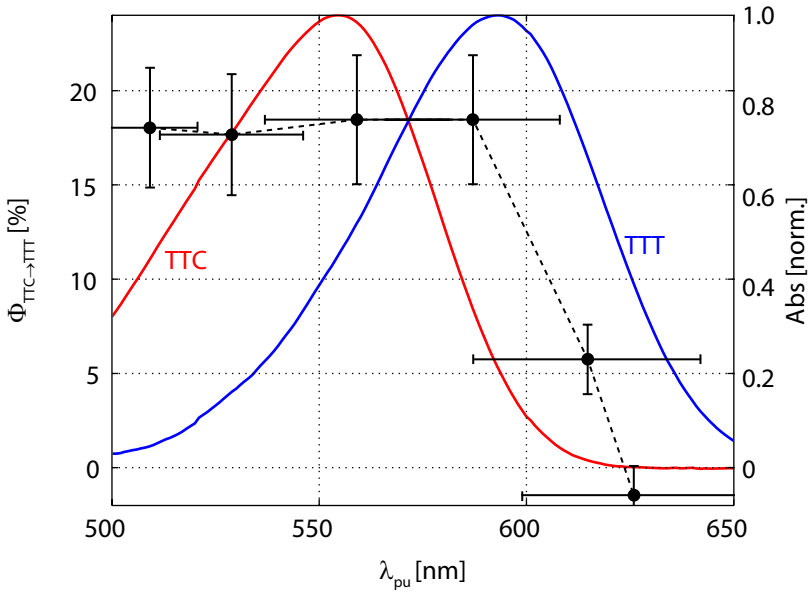

Figure 4.8 | Quantum yield of the TTC→TTT photoisomerization reaction as a function of pump wavelength λ_{pu} calculated at a probe wavelength of λ_{GSB}^{TTC} = 540 nm. The horizontal error bars indicate the spectral FWHM of the pump laser spectra while vertical error bars denote the maximum quantum yield variation in the probe wavelength window of $\lambda_{GSB}^{TTC} = (540 \pm 10)$ nm used to determine the quantum yield using Eq. 4.1. The estimated absorption spectra of the isolated isomers are shown in red for TTC and blue for TTT. Figure adapted from Ref. [2].

at shorter wavelengths in the 35 ps and the 160 ps components and with the TTT PA and SE bands above 560 nm. This results in a strong systematic variation of the calculated quantum yield with the probe wavelength used to calculate it which means that these values are subject to relatively large experimental uncertainty.

The quantum yield was calculated for six different excitation wavelengths between 510 and 630 nm, as shown in Fig. 4.8. The horizontal error bars represent the FWHM of the employed pump pulses and therefore give a rough indication of the corresponding spectral window associated with the specified value of the quantum yield. The vertical error bars reflect the uncertainty due to the variation of Eq. 4.1 with the probe wavelength. This error was calculated by taking the maximum deviation of the quantum yield within the probe wavelength range of $\lambda_{GSB}^{TTC} = (540 \pm 10)$ nm.

The reaction quantum yield is virtually constant in the excitation wavelength regime between 510 and 590 nm with a value of $\Phi_{TTC\rightarrow TTT} = (18 \pm 4)$ %. For excitation wavelengths above 600 nm, the quantum yield drops to values around 5 % around 610 nm and finally to zero for 630 nm excitation. This likely indicates that the isomerization proceeds over a small barrier in the first excited state of TTC. Consequently, a certain amount of vibrational excess energy is required for the isomerization reaction. Once enough excess energy is available for the reaction to occur, the quantum yield is almost independent of the excitation energy, as observed for wavelengths below 590 nm. The quantum yield of (18 ± 4) % is by a factor of 2 smaller than the value of about 40 % estimated by Görner *et al.* for the same solvent [252]. However, their value of 90 % in

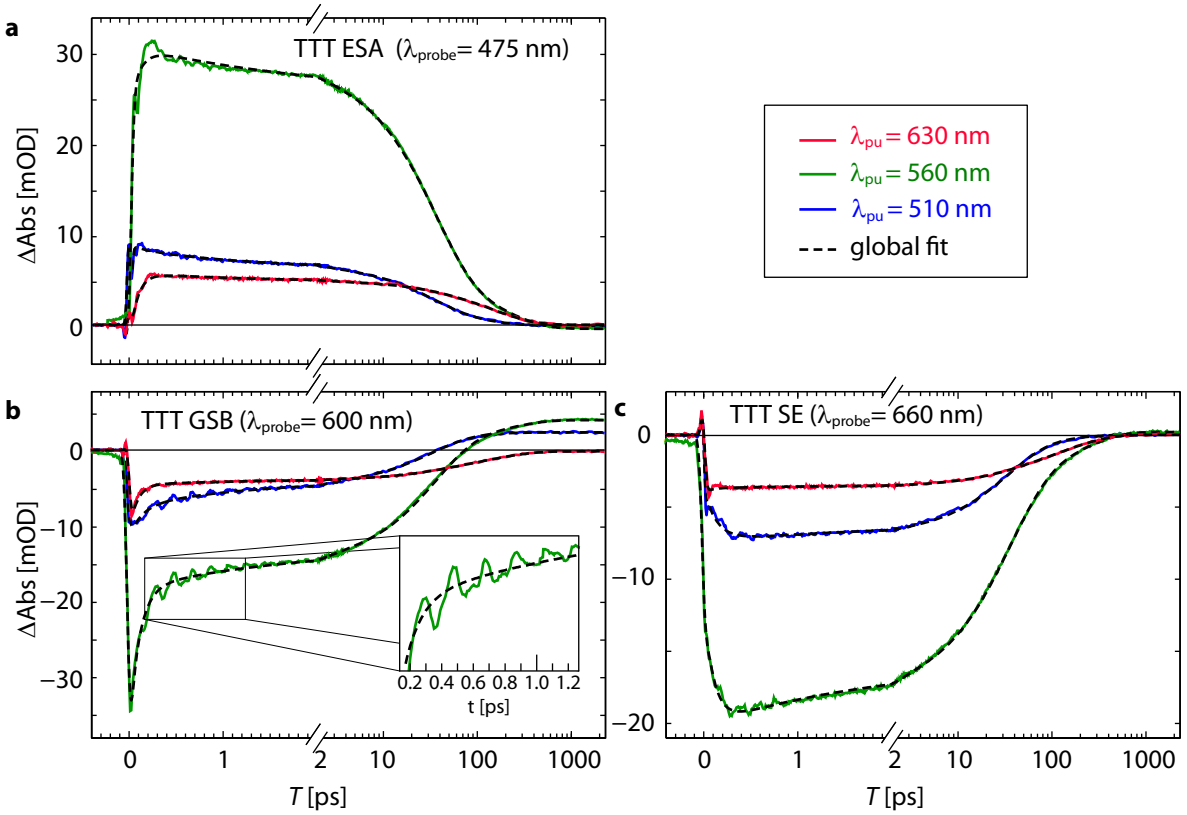

Figure 4.9 | Single transients of 6-nitro BIPS. Selected single transients of the data shown in Fig. 4.5 are shown together with the global fit (black dashed line) at a probe wavelength of (a) 475 nm, (b) 600 nm, and (c) 660 nm for excitation wavelengths of 510 nm (blue), 560 nm (green), and 630 nm (red). Note that the time axis is linear up to 2 ps and logarithmic from there on. Figure adapted from Ref. [2].

toluene also differs substantially from the quantum yield of 10 % as derived by Wohl *et al.* [254].

4.2.4 Analysis of Wave-Packet Dynamics

We now continue with the detailed analysis of the ultrafast primary photodynamics of the MC form of 6-nitro BIPS. Coherent processes often play a dominant role in photoreactions during the first hundreds of femtoseconds after photoexcitation leading to a non-exponential behavior which cannot be modelled properly with a global multiexponential fitting routine.

Single transients at selected probe wavelengths for the ESA, GSB, and SE bands are shown in Fig. 4.9 for the three different excitation wavelengths of 510 (blue), 560 (green), and 630 nm (red) together with the global fit at these wavelengths (black dashed line). The global fit reproduces the exponential decay in all spectral regions for delay times larger than 2 ps very well. But for shorter pump–probe delays significant deviations from a purely multiexponential decay become obvious.

In the ESA region at a probe wavelength of 475 nm [Fig. 4.9(a)] a short positive

spike is observed between 50 and 150 fs after excitation, most pronounced at a pump wavelength of 560 nm, which is not properly modelled by the global fit. This feature is most probably caused by a coherent vibrational wave packet moving away from the Franck–Condon region towards lower lying regions of the PES. During this movement the wave packet passes this ESA probe window during a short period of time until it reaches the bottom of the excited state potential from where ESA around 440 nm occurs. Since after excitation with less amount of vibrational excess energy the excited-state population is already formed in the lowest vibrational states of the potential, this feature is not observed in the data set with 630 nm excitation.

Much more striking is the observation of pronounced oscillations observed in the GSB region of the TTT isomer at a probe wavelength of 600 nm [Fig. 4.9(b)]. These oscillations are most pronounced after excitation at 560 and 510 nm and indicate the existence of coherent vibrational motions. After a rise time of roughly 200 fs these oscillations decay on a time scale between 1.5 and 2 ps with a major vibrational period of about 200 fs [inset of Fig. 4.9(b)]. The relative amplitude of the signal oscillations seems to be slightly higher after 510 nm excitation. In contrast, no oscillations are observed in the data set with 630 nm excitation wavelength where almost exclusively TTT molecules are excited.

Similar oscillations are observed in the SE region at a probe wavelength of 660 nm [Fig. 4.9(c)]. They are also most pronounced for shorter excitation wavelengths and again vanish when the sample is excited in the red edge of the absorption band. The oscillation period seems consistent with the period observed in the GSB band although the oscillations are not as distinct in this probe region.

The coherent contributions of the data were extracted by taking the residuals of the global fit for the data set with 560 nm excitation, as shown in Fig. 4.10(a), as a function of pump–probe delay T and the probe wavelength λ. Signatures of a vibrational wave packet are observed in various spectral ranges between 450 nm and above 700 nm. The most distinct oscillations are observed around 600 nm, matching the maximum of the TTT GSB band, and remain visible up to over 2.0 ps after excitation. A second oscillating contribution emerges red-shifted above 630 nm. These oscillations are out of phase with those observed around 600 nm with a distinct phase change of π around 630 nm. In the region of the TTC GSB the oscillations vanish while in the ESA region oscillations are again observed with much lower amplitude than at 600nm but also with a phase change of π at 460 nm.

To extract the involved vibrational frequencies, the data of Fig. 4.10(a) was Fourier transformed along T in the range $0 < T < 2.5$ ps. The absolute value of this data is depicted in Fig. 4.10(b) as a function of the vibrational wavenumber and the probe wavelength. We yield two major modes at $\overline{\nu}$ =170 cm^{-1}, reflecting a vibrational period of about 190 fs, in the following referred to as the low-frequency mode (LFM), and at 360 cm^{-1}, corresponding to a 90 fs oscillation period, referred to as the high-frequency mode (HFM). Some low-frequency contributions below 100 cm^{-1} are also observed, which are most probably caused by minor imperfections of the global fit. Both, the LFM and the HFM, are most pronounced at the TTT GSB region at 600 nm and in the red-edge of the SE band. For both modes minor contributions are also found in the ESA region. The same analysis for 510 nm excitation yields practically the same vibrational modes

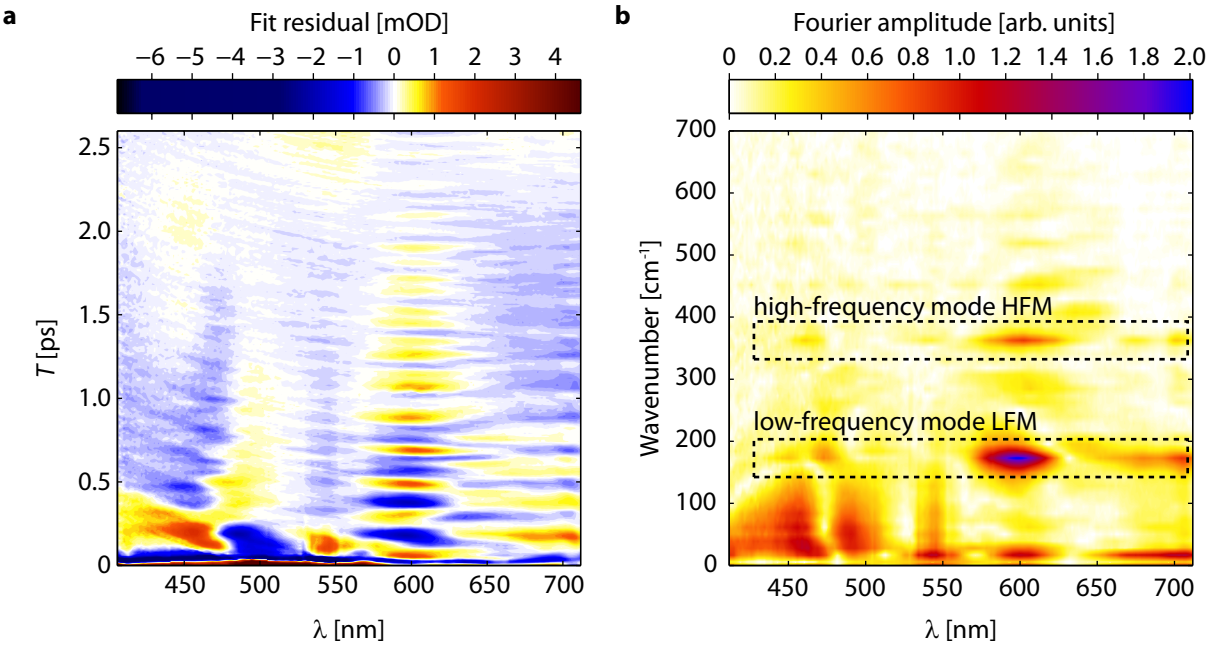

Figure 4.10 | Coherent wave packet dynamics of the MC form of 6-nitro BIPS in acetonitrile after 560 nm excitation analyzed on the basis of the global fit residuals. (a) Fit residuals as a function of probe wavelength λ and the delay time T during the first 2.5 ps. Signatures of a coherent vibrational wave packet are clearly visible in the TTT GSB, TTT SE as well as in the ESA region which are damped on a time scale of about 1.5 to 2.0 ps. The data indicates a fixed phase relationship between oscillations around 600 nm and those in the red edge of the SE above 650 nm. (b) Absolute values of the Fourier transformation of the residuals along T as a function of λ. Figure adapted from Ref. [2].

with almost identical oscillation frequencies while after 630 nm excitation no signatures of vibrational coherences are observed (data not shown), suggesting that the wave-packet dynamics might be related to the observed *cis-trans* isomerization.

More insight is gained by considering slices through the Fourier transformed data map of Fig. 4.10(b) along the probe wavelength. One such slice at $\overline{\nu}$ =170 cm^{-1} is shown in Fig. 4.11 depicting the normalized FFT amplitude (black line) and FFT phase (green circles) as a function of the probe wavelength for the dominant LFM together with the estimated TTT absorption spectrum (dashed blue line). The spectral location of the maximum of the FFT amplitude coincides with the maximum of the TTT steady-state absorption, suggesting that the observed wave-packet dynamics occur in the TTT region of the PES. Minor contributions are again observed in the red edge of the SE band above 650 nm and in the ESA region centered around 470 nm. The Fourier phase reflects the phase relationship between the oscillations at different probe wavelengths. It exhibits a steep phase step of π at 630 nm at the minium of the FFT amplitude between the TTT GSB and the red edge of the SE band. Another phase change of π is observed in the ESA region where a double peak is also observed in the FFT amplitude. Furthermore, by comparing the phase at ESA, GSB, and SE regions, it can be seen that the red part of the ESA oscillations are in phase with the oscillations in the TTT GSB region while the blue ESA parts oscillate in phase with contributions in the SE band. From this it

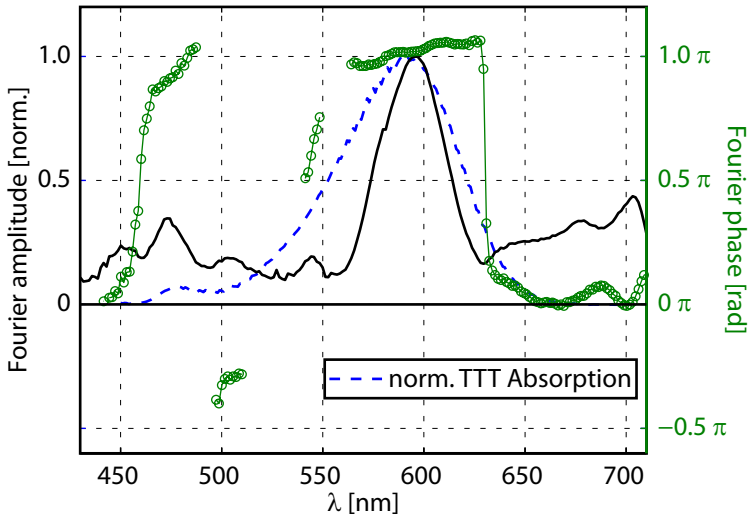

Figure 4.11 | Analysis of coherent wave-packet dynamics of excited 6-nitro BIPS. Slices through the data of Fig. 4.10 along the probe wavelength at $\overline{\nu}$ =170 cm^{-1} show the normalized Fourier transform amplitude (black line) and the Fourier phase (green circles) of the dominant LFM. The maximum of the normalized FFT amplitude coincides very well with the maximum of the normalized TTT absorption (blue) and phase steps of π are observed between this maximum and contributions in the SE band and in the center of the ESA. Figure adapted from Ref. [2].

can be concluded that the oscillations, which are observed over almost the entire probed wavelength range, are most probably caused by one and the same wave packet located in a region of the potential energy surface associated with the TTT isomer. In addition, the fact that the observed oscillations are most pronounced when mainly TTC isomers are excited (see Fig. 4.9) while exhibiting most dominant signature at TTT absorption and emission wavelengths is a strong indicator that the observed coherent wave-packet dynamics are connected to the TTC→TTT isomerization reaction.

The data of Figs. 4.10 and 4.11 contain typical signatures of a vibrational wave packet oscillating periodically in a local minimum of one of the involved PESs. These oscillations can be considered as periodic fluctuations of the spatial probability distribution of the molecular wave function also causing periodic modulations of the transient absorption signal. Whenever the wave packet is located at one of its reversal points at one side of the potential the probe pulse interacts with an increased transient population at those probe wavelengths where photoinduced transitions from this region of the PES may occur resulting in an increased transient signal amplitude. At the same time the transient signal at the probe window emanating from the opposite side of the minimum of the PES is minimal because the amplitude of the molecular wave function is also minimal there. The reason for this was already demonstrated in Fig. 2.16 in Sect. 2.3.3 for the case of a harmonic potential illustrating that the wave packet is strongly localized at the two turning points while in between, i.e, at the bottom of the potential, the wave packet is strongly delocalized with respect to the spatial coordinate. In addition, signatures from the two opposite reversal points should be out of phase with a phase difference of π in between, as also observed in other molecular systems [131, 132]. Thus, both the phase jump of π and the spectral profile of the amplitude of the oscillations proof that the wave packet is probed in its entirety between the two turning points allowing us to

nonambiguously assign the electronic state on which the wave packet propagates.

Since the wave-packet dynamics is observed solely in the course of the TTC→TTT isomerization, its signatures yield rich information about the isomerization process such as its time scale, the reaction coordinate, involved electronic states, and the corresponding molecular normal modes. Upon photoexcitation of the TTC isomer a vibrational wave packet is prepared in a highly vibrationally excited configuration at the Franck–Condon point. Afterwards, this wave packet propagates on the excited-state PES towards a TTT-like configuration and two different scenarios of the photoisomerization are possible. On the one hand, the wave packet could reach a lower-lying region of the PES followed by an ultrafast nonradiative transition, e.g., via a conical intersection, to an elevated point of the electronic ground state from where the TTT ground-state configuration can be reached. This kind of ultrafast nonradiative mechanism was found in many different classes of organic molecules such as retinal in rhodopsin [130, 132, 264] and a large number of other compounds including cyanine dyes [265–270] and biomimetic molecules [271] demonstrating the high efficiency of this mechanism in the context of isomerization reactions [272]. On the other hand, another possible scenario would be that the vibrational wave packet propagates on the excited-state towards the excited-state molecular configuration of the product and remains there until it undergoes a radiative decay to the ground state of the product. This kind of process was found for example in the photochemical interconversion of the photosensory protein phytochrome [273].

For both scenarios the wave packet may retain its vibrational coherence and oscillate in a local minimum of the PES, either in the electronic ground or the excited state of the TTT isomer. If the wave packet is located in the ground state of TTT, the TTT PA band is modulated accordingly; if it remains in the excited state, periodic oscillations of the stimulated emission or excited-state absorption signal occur. In both cases it can be assumed that the molecule is still in a vibrationally hot state and thus GSB, SE, and PA bands may strongly overlap.

In our case the profiles shown in Fig. 4.11 can be used to distinguish between the two scenarios explained above [131, 132, 274–276] on the basis of the following considerations:

i) As evidenced in Figs. 4.9–4.11 signal oscillations are observed in the ESA region (430-480 nm) as well as in spectral regions where SE is observed (> 650 nm). Since these signals originate from population in the excited state it is very likely that the wave packet is also located in one of the first excited states of the merocyanine.

ii) As already mentioned, the maximum of the signal oscillations typically occur at the spectral regions associated with the two turning points of the wave packet because there the wave packet is strongly localized. In the data presented here maximal signal oscillations are observed at 600 nm and at 700 nm with a distinct dip around 630 nm. This profile suggests that the wave packet is located in the first excited singlet state of the TTT isomer as illustrated schematically in Fig. 4.12. From the estimated isomer absorption spectrum it is known that the TTT ground state absorption is maximal at 600 nm, corresponding to a transition from the S_0 minimum to an elevated point of the S_1 potential. According to the above arguments, vanishing oscillations would be observed there if the wave packet was located in the ground state since at the minimum of the S_0 potential it would

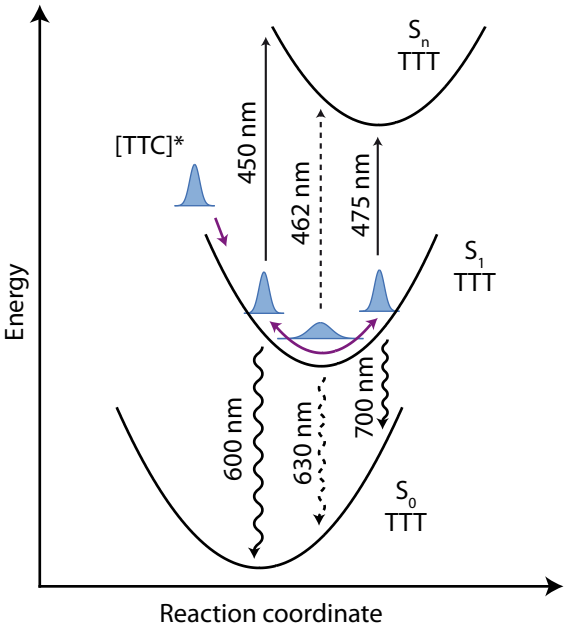

Figure 4.12 | Signatures of a vibrational wave packet oscillating in the first excited singlet state of TTT upon photoisomerization of excited TTC isomers. In the SE bands maximum oscillation amplitudes are observed blue- and red-shifted from the vibrationally relaxed SE maximum around 600 and 700 nm (undulated arrows) while at the bottom of the potential the oscillation exhibits a minimum and a phase step of π (dashed undulated arrow). The same happens in the ESA band with maximum amplitudes red- and blue-shifted (straight arrows) from the vibrationally relaxed ESA where again a minimum and phase step of π is observed (dashed straight arrow). Figure adapted from Ref. [2].

be strongly delocalized and oscillations would be observed blue- and red-shifted from the GSB band. However, for an S_1 wave packet it seems very plausible that the 600 nm transition corresponds to the inner turning point of the wave packet while the outer turning point is reached red-shifted from the maximum of the vibrationally relaxed SE band above 650 nm (undulated continuous arrows in Fig. 4.12). The same two turning points are probed in the ESA region at 450 and 457 nm (straight continuous arrows). Consequently, minima of the oscillations are located in between in regions where the wave packet is most delocalized, which is typically near the maximum of the vibrationally relaxed $S_1 \rightarrow S_0$ emission and $S_1 \rightarrow S_n$ absorption observed in our data at the dips at 630 and 462 nm, respectively (dashed arrows).

iii) Since the two turning points oscillate out of phase a phase step of $\Delta\Phi = \pi$ is observed in between at the bottom of the potential. This is in line with the phase jumps observed in the data of Fig. 4.11 at 630 and 462 nm, both matching the locations of the minima of the oscillations. In addition, taking into account that ESA and SE signals have opposite signs, it can be deduced from the Fourier phase that red-edge ESA and red-edge SE signals oscillate in phase. Therefore, it can be concluded that the minimum of the S_n potential is shifted in the same direction with respect to the S_1 state as the S_1 state is shifted compared to the electronic ground state, as also illustrated in Fig. 4.12.

All these considerations nonambiguously lead to the conclusion that the wave packet is localized in the S_1 state of the TTT isomer formed upon ultrafast isomerization of photoexcited TTC isomers. The *cis–trans* isomerization occurs in the excited state where vibrational coherence is preserved during the complete duration of the structural rearrangements. It can further be stated that photoisomerization is accompanied by at

least two independent molecular normal modes at 170 (LFM) and 360 cm^{-1} (HFM). It can also be ruled out that the HFM is just the doubled frequency of the LFM which would be observed at the bottom of the potential where the wave packet passes twice per vibrational period [131, 277] since in this case its amplitude would also be maximal at spectral regions where the bottom of the S_1 potential is probed.

Recently, Kumar *et al.* reported very similar oscillating signatures in a closely related spirooxazine compound. However, the authors did not attribute these features to vibrational wave-packet motions in the excited state but to the non-adiabatic formation of a hot ground state in the reactant [278].

4.3 Reaction Scheme

The reaction scheme illustrated in Fig. 4.13 summarizes the results of our femtosecond transient absorption studies on the merocyanine form of 6-nitro BIPS dissolved in acetonitrile. The scheme contains all observed lifetimes and states as obtained from the global analysis of the time resolved data. Photoexcitation into the S_1 state of both, the TTC and the TTT isomer, is followed by very fast primary dynamics on the order of 100 fs associated with the inertial motion of the wave packet away from the Franck-Condon region and possibly fast solvent reorganization. Vibrational cooling in the S_1 state is observed for both isomers on a 1.2 ps decay component accompanied by a pronounced spectral shift of ESA and SE bands. The TTC→TTT photoisomerization pathway was identified with a quantum yield of about 18 % for excitation wavelengths below 600 nm. Upon the isomerization process pronounced coherent oscillations caused by a vibrational wave-packet with two independent modes at 170 cm^{-1} and 360 cm^{-1} were observed in the S_1 state of the product. Since these oscillations rise on a time scale of 100–200 fs it is concluded that isomerization happens on a similar time scale after TTC excitation. The major part of excited TTC molecules not undergoing *cis–trans* isomerization relaxes to the ground state under emission of a photon at a wavelength of 625 nm with an excited-state lifetime of 35 ps. A small fraction of TTC molecules reaches another minimum on the excited state potential, from which emission at 655 nm with $\tau = 160$ ps is observed. In contrast, all excited TTT molecules relax back to the TTT ground state via emission of a photon with a wavelength of 655 nm and a characteristic time constant of 160 ps. Thus, no reverse reaction pathway from TTT to TTC was detected. Excited-state absorption occurs for both isomers at 458 nm (TTC) and 470 nm (TTT). No evidences for a photoinduced ring-closure reaction back to the SP form of 6-nitro BIPS were found in the used solvent.

The discussed *cis–trans* photoisomerization demonstrates that vibrational coherence induced into a reactive molecular species can be maintained during the reaction and can in this way be transferred from the reactant to the product. Since the creation of femtochemistry as a new area of research in the 1980s, there have been numerous examples published in the literature where coherent wave packets were observed in chemical reactions, for instance on transition states in dissociation reactions of isolated molecules in the gas phase [126, 127, 279–281], or in liquid phase dissociation reactions [282, 283]. Concerning more complex and larger reactive molecular species, coherent vibrational

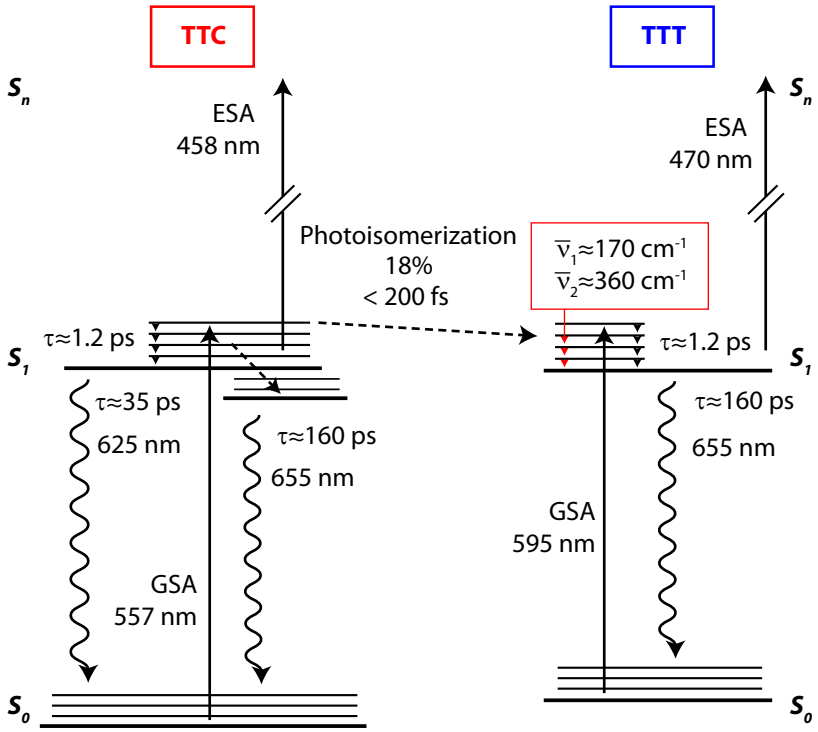

Figure 4.13 | Extracted reaction scheme of the MC form of 6-nitro BIPS dissolved in acetonitrile. After excitation of TTC, most molecules return back to the TTC ground state after emission of a photon with an S_1 lifetime of about 35 ps. A second emissive state might be reached by a much smaller ratio of excited TTC molecules with a lifetime of 160 ps. About 18 % of excited TTC molecules undergo a *cis–trans* isomerization in the excited state on a time scale below 200 fs accompanied by pronounced coherent wave-packet dynamics. All excited TTT molecules return to their ground state by fluorescence with an S_1 lifetime of 160 ps. Vibrational cooling in the excited state, excited-state absorption, and stimulated emission is observed for both isomers. Figure adapted from Ref. [2].

wave-packet dynamics were frequently detected in ultrafast *cis–trans* photoisomerization reactions [132, 271, 284–291], as is the case in our studies. However, in most cases the wave packet passes a conical intersection and is observed afterwards in the electronic ground state of the product. In our case, there is no evidence of a conical intersection and the wave packet is located on the excited state of the reaction product. In all cases an ultrafast dissipation of excess energy, which was transferred to the system by the photoexcitation, is necessary for the reaction to proceed. As stated by the so-called *loose bolt theory* by Lewis and Calvin [292], energy dissipation in molecular systems will be most efficient in the presence of vibrational degrees of freedom capable of 'absorbing' this excess energy, comparable with some loose bolts in the moving parts of a machine. Thus, the fact that in many cases very pronounced wave-packet dynamics are observed in the course of ultrafast isomerization reactions might be the result of the loose bolt effect in which a strong coupling between the electronic transition and the vibrational degrees of freedom exists. Consequently, the observed modes might not necessarily be connected to the reaction coordinate itself but mainly serve as dissipative molecular

modes allowing for an efficient non-radiative transition from the educt to the product. However, the role of the normal modes in the observed isomerization reaction of 6-nitro BIPS will be investigated and discussed in more detail in Sects. 4.5 and 4.6.

4.4 Coherent Two-Dimensional Electronic Spectroscopy

In the previous section an ultrafast photochemical interconversion between different merocyanine isomers in solution was investigated with the help of femtosecond transient absorption spectroscopy. The main challenge was the identification of the isolated signatures of reactants, intermediates, and products. Though the PA band in the transient data unambiguously proves the formation of TTT isomers after long pump–probe delay times, no direct photochemical correlation between TTC and TTT is detectable in transient absorption. Moreover, as in many other cases, spectroscopic product bands overlap with signals of the reactants or intermediate species, which further complicates the analysis of such photochemical reactions. A technological advancement to circumvent this issue is coherent multidimensional electronic spectroscopy, where the correlation of a system's excitation and emission frequencies is measured and as a result features that would overlap in transient absorption schemes can be separated. Though 2D electronic spectroscopy was primarily implemented for studying photophysical coherent phenomena, the principle of spreading the spectral signatures along several frequency axes makes this technique an ideal candidate also for the investigation of *photochemical* reactions, i.e., when the investigated system is permanently changed during the reaction.

As an extension of 2D spectroscopy, three-dimensional (3D) representations may provide an even more detailed picture. Coherent 3D spectroscopy has been introduced in infrared spectroscopy [38–40] and has recently been transferred to electronic spectroscopy for isolating excitonic coherences [41, 43], for liquid- and gas-phase model systems [42, 45, 46], and for the analysis of coherent oscillations in photosynthetic light-harvesting systems [44, 293]. Regarding these approaches, one has to differentiate between fifth-order experiments [38–40, 45, 294–296] which allow for the observation of signals that necessitate a higher nonlinearity (e.g., three-point frequency-fluctuation correlation functions [38, 40]) and studies exploiting the third-order susceptibility [44, 46, 293, 297, 298], as done in Sect. 4.5 to unravel a photochemical reaction.

4.4.1 Detection of Photochemical Exchange in Multidimensional Electronic Spectroscopy

The principal idea of coherent multidimensional spectroscopy for photoreactive processes as employed in the following sections is sketched in Fig. 4.14. We consider a fictitious "photoreactive network" [Fig. 4.14(a)] where the molecular species $\boldsymbol{A}$ can be converted into $\boldsymbol{C}$ by illumination of light either directly via reaction channel ③ or via an intermediate $\boldsymbol{B}$ involving channels ① and ②. Species $\boldsymbol{C}$ in turn will react to $\boldsymbol{A}$ after photoexcitation only via reaction channel ③. In practice, the spectral signatures of reactants and products may strongly overlap in a solvent environment. Hence, the assignment of reaction channels on the basis of linear spectroscopy or conventional transient absorption

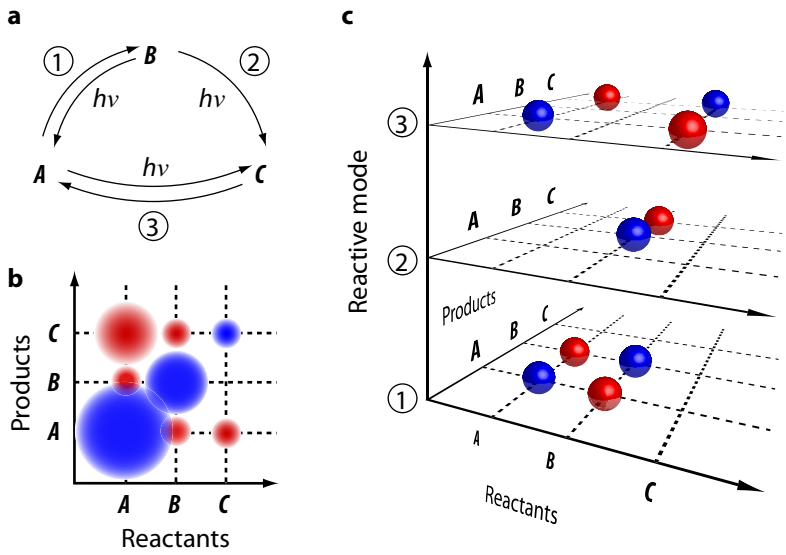

Figure 4.14 | Principle of coherent multidimensional spectroscopy of photoreactive species. (a) For illustration, we assume a "photoreactive network" composed of three chemical species connected by different reaction channels. (b) 2D frequency spectra of this network visualize the correlations of reactants and products. (c) The introduction of a third frequency dimension exposes involved reactive modes and associated reaction pathways. Channels overlapping in the 2D spectrum might be resolved in the 3D spectrum. Figure adapted from Ref. [4].

is unfeasible in many cases.

A 2D spectrum [Fig. 4.14(b)] can visualize the correlations between products and reactants as a function of population time T. Negative diagonal peaks (blue) occur upon excitation and describe at long times T population loss due to the photoreaction. Positive cross peaks (red) emerge at points connecting the ground states of reactants and photochemical products and are caused by an increase of the product concentration, disclosing correlations between different reactive species.

However, a single 2D spectrum provides only a temporal snapshot, while dynamics related to T and associated reaction channels and involved modes are not directly accessible. By introducing an additional frequency axis the various reaction channels may be separated depending on the associated reactive modes (e.g., vibrations), as illustrated in Fig. 4.14(c). Therefore, also photoreactions with a very low quantum yield could be detectable without being obscured by competing signals located in the same excitation frequency regime. In the proposed approach, these reaction channels are isolate by measuring a large set of 2D spectra for different values of T followed by a Fourier transformation of the 2D signal along T. This results in a third-order three-dimensional (3D) electronic spectrum [297].

To demonstrate this concept, the coherent vibrational dynamics in the course of the *cis–trans* photoisomerization reaction of the merocyanine form of 6-nitro BIPS in acetonitrile, already analyzed with transient absorption measurements in Sect. 4.2, is investigated. Specific cross peaks associated with the ultrafast photoreaction will be isolated by analyzing the global response in terms of vibrational modes.

4.4.2 Experimental Implementation of 2D Spectroscopy in the Pump–Probe Beam Geometry

Phase Cycling and the Rotating Frame

In two-dimensional spectroscopy in the pump–probe geometry, three laser pulses interact with the sample. The electric field can thus be expressed as

$$\begin{aligned} E^{+}(\vec{r},t) =& A_1(t+\tau+T)\mathrm{e}^{-\mathrm{i}\left[\omega_1 t-\vec{k}_1\vec{r}+\phi_1\right]} \\ &+A_2(t+T)\mathrm{e}^{-\mathrm{i}\left[\omega_2 t-\vec{k}_2\vec{r}+\phi_2\right]} \\ &+A_3(t)\mathrm{e}^{-\mathrm{i}\left[\omega_3 t-\vec{k}_3\vec{r}+\phi_3\right]} + \text{ c.c.} \end{aligned} \tag{4.2}$$

where $\phi_i = \Phi_0 + \varphi(t)$ is the temporal phase of the i-th laser pulse. It can be shown that the third-order response consists of $2^{(3-1)} = 4$ terms. Therefore, by combining Eq. (3.22) with Eq. (4.2) we obtain $4 \cdot 6 \cdot 6 \cdot 6 = 864$ terms that describe all possible temporal combinations of the three interactions between the light field and the system. This number is highly reduced considering the *rotating-wave approximation* (RWA). In the near-resonance condition – i.e., the electric field carrier frequency ω_0 is close to the transitions frequency ω_{eg} – an evaluation of the resulting $\vec{P}^{(3)}$ with the electric field given in Eq. (4.2) yields dominant terms that are modulated with the temporal electric-field envelope function at frequencies $\omega_0 - \omega_{\mathrm{eg}}$ while terms that oscillate at frequencies $\omega_0 + \omega_{\mathrm{eg}}$ are neglected in the integral [205]. In this way the number of terms is reduced by a factor of 8 to $4 \cdot 3 \cdot 3 \cdot 3 = 108$.

Taking the experimental conditions such as beam geometry and pulse ordering into account, the number of remaining terms is further reduced. In the box geometry, the wave vectors of the three beams differ ($\vec{k}_1 \neq \vec{k}_2 \neq \vec{k}_3$). Provided that the RWA is valid and that strict time ordering is given, only four-wave mixing contributions propagating in the two phase-matched signal directions $\vec{k}_s = \pm(\vec{k}_2 - \vec{k}_1) + \vec{k}_3$ are emitted, corresponding to the rephasing (+) and non-rephasing (−) components. Thus, by detecting only the signal at one fixed phase-matched direction the desired signal can be observed background-free.

This is not the case in a pump–probe geometry because the wave vectors of pulse 1 and 2 are identical and only the wave vector of the probe differs ($\vec{k}_1 = \vec{k}_2 \neq \vec{k}_3$). As a consequence, also transient-absorption contributions where either pulse 1 or pulse 2 interacts twice with the sample are emitted in the same direction $\vec{k}_{\mathrm{TA}} = \vec{k}_1 - \vec{k}_1 + \vec{k}_3 = \vec{k}_2 - \vec{k}_2 + \vec{k}_3 = \vec{k}_3$ as the desired four-wave mixing signal. Moreover, the rephasing and non-rephasing contributions are emitted simultaneously in the same signal direction $\vec{k}_s = \vec{k}_1 - \vec{k}_2 + \vec{k}_3 = -\vec{k}_1 + \vec{k}_2 + \vec{k}_3 = \vec{k}_3$.

To eliminate transient absorption contributions another degree of freedom can be exploited, based on the phases of pulses 1 and 2, which are easily controllable with a pulse shaper. In the procedure termed *phase-cycling*, which is adopted from NMR techniques [196, 198], one varies the interpulse phase $\phi_{12} = \phi_1 - \phi_2$ and exploits the fact that the transient absorption background is independent of ϕ_{12}, while the contributions resulting from the single interaction with pulse 1 and 2 change their sign upon a phase change of $\Delta\phi_{12} = \pi$ [210, 218, 225, 299, 300]. Accordingly, each 2D data set in the pump-probe

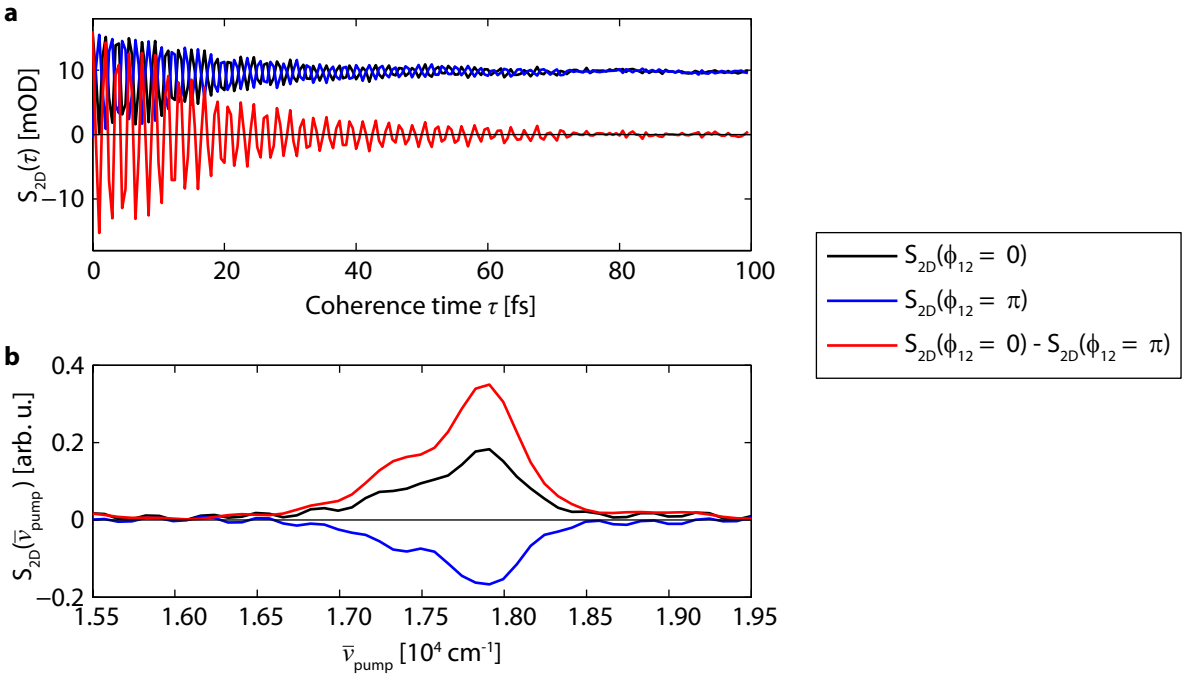

Figure 4.15 | Principle of 2D signal extraction by phase cycling in the pump–probe beam geometry. (a) The time domain data as a function of coherence time of the merocyanine form of 6-nitro BIPS in acetonitrile at a single selected probe frequency ($\overline{\nu}_{\text{probe}} = 1.655{\times}10^4$ cm^{-1}) is measured with $\phi_1 = 0$, $\phi_2 = 0$ (black) and with $\phi_1 = 0$, $\phi_2 = \pi$ (blue). Both data sets contain transient absorption contributions which can be inferred from the fact that both curves possess a remaining positive signal offset for long coherence times. While in frequency domain (b) the transient absorption contribution has the same sign for both measurements, the 2D signal changes its sign upon a phase change of $\Delta\phi_{12} = \pi$. Thus the subtraction of both curves yields the background free photon echo signal (red) [207, 218].

geometry is collected for a fixed population time T as a function of τ for two different settings of ϕ_{12}: $\phi_{12} = 0$, and $\phi_{12} = \pi$. Since the desired signal changes its sign when the relative phase is changed by π, which is not the case for the transient absorption contributions, a subtraction of the two data sets yields the background free, purely absorptive, and properly phased 2D time domain data. This procedure is illustrated in Fig. 4.15. The time domain raw data is shown in Fig. 4.15(a) as a function of the coherence time at a single selected probe frequency for $\phi_1 = \phi_2 = 0$ (black) and $\phi_1 = 0$, $\phi_2 = \pi$ (blue). The presence of the transient absorption background can be inferred from the fact that both curves possess a remaining positive signal offset for long coherence times. While this background is insensitive to the interpulse phase $\Delta\phi_{12}$ the desired 2D signal changes its sign if the relative phase is changed by $\Delta\phi_{12} = \pi$, as shown in Fig. 4.15(b). Thus the subtraction of both raw data sets extracts the desired background free signal $S_{2D} = S(\phi_1 = \phi_2 = 0) - (\phi_1 = 0, \phi_2 = \pi)$ (red). In addition, the signal to noise ratio is significantly increased as random noise is averaged out while the third-order signal amplitude is doubled.

For strongly scattering samples this two-step phase-cycling scheme can be extended to four-step phase cycling by an additional incrementation of the total pump pulse phase

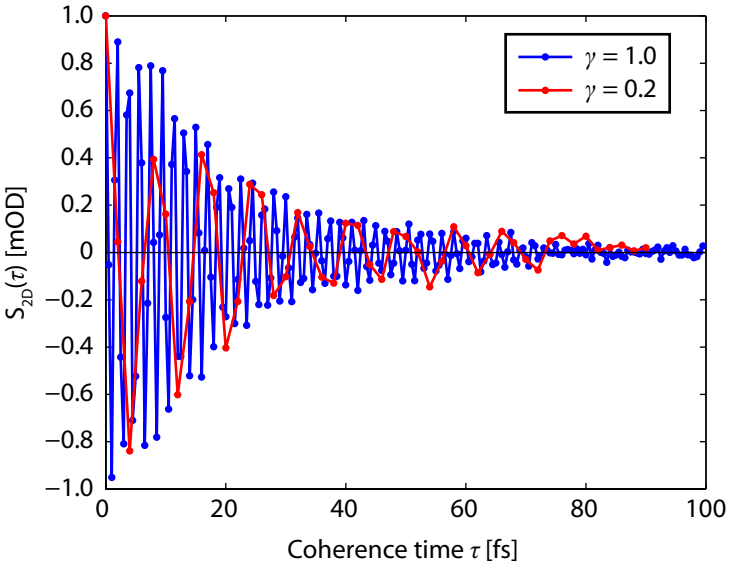

Figure 4.16 | Principle of 2D data collection in the rotating frame. The comparison of the phase-cycled time-domain raw data at a selected probe frequency ($\overline{\nu}_{\text{probe}} = 1.655{\times}10^4$ cm^{-1}) measured in the laboratory frame (blue) with $\gamma = 1.0$ and the data with $\gamma = 0.2$ (red), achieved by adding a delay dependent phase offset $\Delta\phi = -(1-\gamma)\omega_0\tau$ to the phase of pulse 1, demonstrates the effect of the partially rotating-frame. While the time domain data oscillates at the carrier frequency in the laboratory frame the effective oscillation frequency is reduced in the partially rotating frame by a factor of $1/\gamma = 5$ allowing for a much more rapid data acquisition.

by π and by combining $S(\phi_1 = \phi_2 = 0)$, $S(\phi_1 = 0,\phi_2 = \pi)$, $S(\phi_1 = \phi_2 = \pi)$, and $S(\phi_1 = \pi,\phi_2 = 0)$. In this way, additionally to transient absorption contributions, also scattered light can be eliminated to a high degree [207, 218, 223, 301].

The control over the carrier phases of pulses 1 and 2 with a pulse shaper offers several further advantages over approaches where the relative phase is not adjustable. In Sect. 3.3 the pulse shaper modulation function for creating double pulses was introduced [see Eq. (3.10)]. For pulse-shaper assisted two-dimensional spectroscopy in the pump–probe geometry we make use of the same modulation function

$$M(\omega) = \frac{1}{2}\left[\mathrm{e}^{-\mathrm{i}[\omega-(1-\gamma)\omega_0]\tau}\mathrm{e}^{\mathrm{i}\phi_1} + \mathrm{e}^{\mathrm{i}\phi_2}\right] \tag{4.3}$$

where now in addition the phases ϕ_1 and ϕ_2 of pulses 1 and 2 can be varied separately. The parameter γ can now be used (similar to pulse-shaper assisted cFROG) to shift the experiment into the rotating frame. By doing so, the effective signal field oscillation as a function of coherence time is reduced by a factor of $1/\gamma$ and consequently also the number of necessary data points to achieve the Nyquist limit is reduced by the same amount.

This principle is demonstrated in Fig. 4.16. The phase-cycled time-domain raw data measured in the laboratory frame (blue) with $\gamma = 1.0$ oscillates at the carrier frequency of the laser. Due to the stringent Nyquist limit the data is collected with coherence time steps of $\delta\tau = 0.5$ fs. In the partially rotating frame (red) with $\gamma = 0.2$, achieved by adding a delay dependent phase offset $\Delta\phi = -(1-\gamma)\omega_0\tau$ to the phase of pulse 1, the effective oscillation frequency is reduced substantially by a factor of $1/0.2 = 5$. Consequently, the Nyquist limit is extended considerably and the data can be collected

with time steps of $\delta\tau = 2$ fs. As a consequence, the data acquisition time is reduced by the same amount. Another advantage of shifting the experiment into a partially rotating frame is that the 2D signal can be shifted to $\omega_{pump}-$frequency regions that are less affected by experimental noise caused for example by inevitable laser instabilities, fluctuations of the laboratory climate, and so forth.

Correction of Chirp in 2D Spectroscopy

The use of a whitelight probe continuum for two-dimensional spectroscopy in the pump–probe geometry offers the great opportunity to probe contributions far-off the diagonal. This makes the technique even more valuable especially for spectroscopic applications in the visible [222] and the ultraviolet spectral region [224], since electronic transitions typically possess much broader absorption bands than vibrational transitions in the infrared. However, several challenges are associated with the use of a probe continuum. In analogy to transient absorption, the chirp of the probe pulse results in a probe-frequency dependent waiting time T leading to spectral distortions of peak shapes [302]. Chirp-correction is therefore crucial, especially when fast contributions at short population times are observed. Hence, it is essential to correct for the probe chirp if population times on the order of the probe pulse duration (≈ 600 fs) are considered. The procedure, which will be explained in the following, is very similar to the method explained in Sect. 3.4.3 for transient absorption and was demonstrated in the literature for the first time by Tekavec *et al.* [303].

The principle of the probe-chirp correction in 2D spectroscopy with a continuum probe is illustrated in Fig. 4.17(a). For the implementation of this method a three-dimensional data set as a function of ω_{pump}, ω_{probe}, and T is necessary. Population time steps below 30 fs in a temporal range of several hundreds of femtoseconds are required, covering a sufficient temporal range before and after time zero for all probe frequencies. In the first instance, the chirp of the probe pulse is characterized by analyzing the temporal location of the coherent artifact, which is then fitted with a low-order polynomial (compare Sect. 3.4.3). This low order polynomial describes the correct population time zero as a function of the probe frequency and is independent of ω_{pump} if bandwidth-limited pump pulses are employed. Afterwards, the three-dimensional data set is interpolated along slices parallel to the fitted polynomial. In principle, the method is identical to the procedure used for transient absorption data, as slices through the three-dimensional data set along the population time and at a fixed ω_{pump}-frequency can be considered as transient absorption maps.

In order to prove the feasibility of this method the 2D spectrum of 6-nitro BIPS in acetonitrile is considered depicted in Fig. 4.17(b) for $T = 1$ ps (the data is discussed in detail in the next section). As shown in Fig. 4.17(c), before the chirp-correction contributions at different probe frequencies [colored circles as marked in Fig. 4.17(b)] appear at different population times T and time zero deviates by about 500 fs between the blue probe edge of the spectrum (black circles) and the red edge at lower probe frequencies (white circles). After the chirp correction [Fig. 4.17(d)] all data curves are shifted by their proper population time mismatch and time zero is observed for all contributions at the same T.

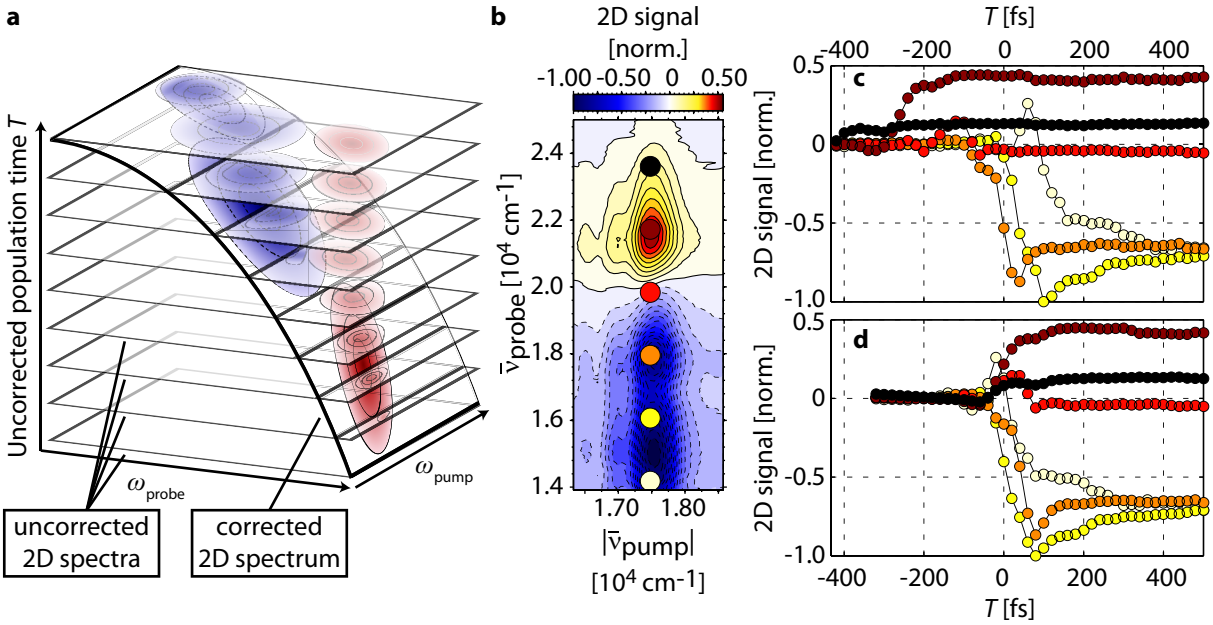

Figure 4.17 | Probe-chirp correction in 2D spectroscopy with a continuum probe. (a) In analogy to the procedure used in transient absorption spectroscopy (see Sect. 3.4.3), the chirp of the probe is corrected by interpolating the three-dimensional data set as a function of ω_{pump}, ω_{probe}, and T along slices parallel to a low order polynomial fitted to the coherent artifact [303]. (b) 2D spectrum of the merocyanine form of 6-nitro BIPS in acetonitrile at $T = 1$ ps (chirp-corrected). To visualize the correction procedure the 2D signal is analyzed at different (ω_{pump}, ω_{probe})-coordinates equally spaced along the probe axis (colored circles) and plotted as a function of T before (c) and after (d) the chirp-correction. In the raw data time zero is observed for different probe frequencies at different population times in a temporal range of about 500 fs while this effect is eliminated in the corrected data set.

4.4.3 Two-Dimensional Spectroscopy – Long-Time Dynamics

In this section, the long-time dynamics observed in the coherent 2D spectra of the MC form of 6-nitro BIPS in acetonitrile are discussed. The data collection and analysis was conducted as explained in the previous section. As shown in Fig. 4.18, the employed pump laser spectrum (green) was centered at 585 nm (green line) such that it overlaps with the absorption bands of both, the TTC isomer (red dotted line) and the TTT isomer (blue dashed line).

For collecting the 2D data, the transient signal of 6-nitro BIPS in acetonitrile was measured as a function of the coherence time τ for every population time T in the partially rotating frame ($\gamma = 0.2$). A two-step phase-cycling scheme was used to eliminate the contributions arising from transient absorption. The short-time 2D spectra, presented in Sect. 4.4.4, were corrected for chirp of the continuum probe as described in Sect. 4.4.2 [261].

A subset of absorptive electronic 2D spectra for $T \geq 2$ ps is shown in Fig. 4.19. The frequencies of the ESA, SE, and ground-state absorption (GSA) bands of the two isomers as retrieved from the global fitting routine of the transient absorption data (Sect. 4.2.2) are marked in all 2D spectra by red (TTC) and blue (TTT) horizontal dashed lines. In

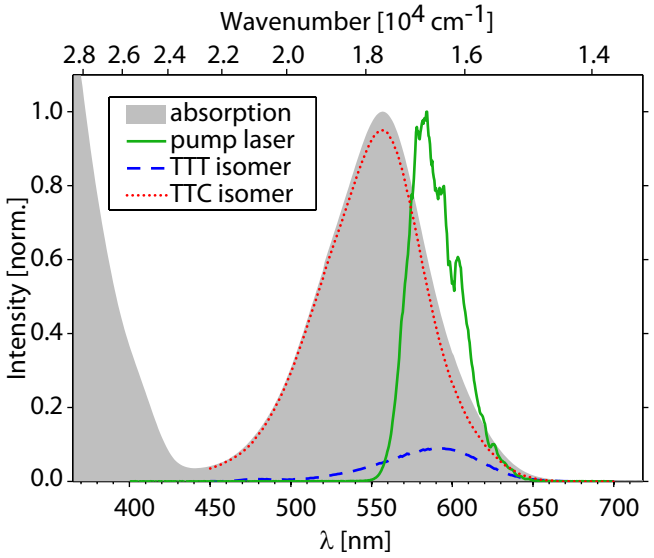

Figure 4.18 | Absorption spectrum (gray) of ring-open 6-nitro BIPS in acetonitrile together with the pump laser spectrum used for the 2D measurements. The spectrum is the sum of the (estimated) absorption spectra of the two isomers (TTC: red dotted line, TTT: blue dashed line). The pump laser spectrum of pulses 1 and 2 used for the 2D/3D measurements (green line) was adjusted such that both isomers can be excited. Figure adapted from Ref. [4].

analogy to the transient absorption data, bluish colors and dashed contour lines denote a decrease of absorption (GSB, SE) whereas an increase of absorption (ESA, PA) is represented by yellow and red colors and solid contour lines.

As it can be seen in Fig. 4.18, the spectral bandwidth of the pump laser is narrower than the absorption bands of the molecule, whereas the probe continuum (not shown in Fig. 4.18) covers the complete visible spectral range. The signal is measured in the same way as in transient absorption by chopping the pump-pulse sequence at half the repetition rate of the laser, and a shot-to-shot detection of the probe. Thus, as the difference in the absorption of the probe is measured, the spectral shape of the 2D signal is independent of the spectral amplitude of the probe pulse. In contrast, the spectral shape along the pump axis is determined by the product between the spectrum of the excitation pulse and the absorption of the sample. As a result, contributions which would appear on the diagonal (e.g., bleaching of the GSA) are shifted along the $\overline{\nu}_{\mathrm{pump}}$ axis. The signal maxima for each isomer along $\overline{\nu}_{\mathrm{pump}}$, given by the maximum of the product of the pump pulse spectrum and the corresponding isomer absorption spectrum, are indicated by the vertical dashed lines in the depicted 2D spectra.

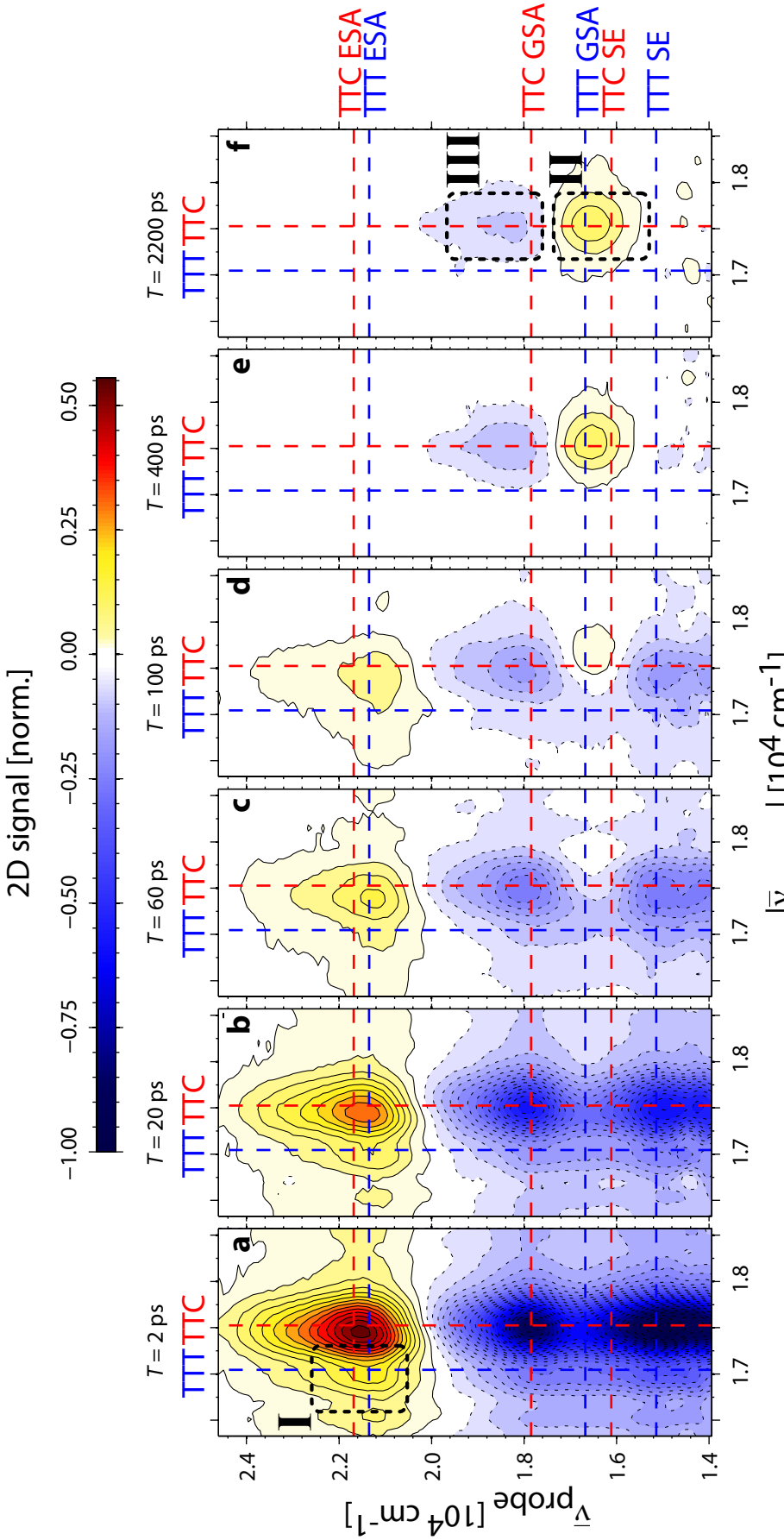

Figure 4.19 | Long-time evolution of absorptive electronic 2D spectra of 6-nitro BIPS in acetonitrile for various population times T between 2 ps and 2.2 ns. All spectra are normalized to the minimum of the $T = 2$ ps spectrum. Negative values (blue) correspond to a decrease of the sample absorption, positive ones (yellow/red) to an increase. Contour lines (dashed for negative, solid for positive values) are drawn in intervals of 4 % of the maximum amplitude. Maxima of the TTC contributions are indicated by red dashed lines, those of the TTT isomer by blue dashed lines. Figure adapted from Ref. [4].

For $T \leq 100$ ps [Figs. 4.19(a)–(d)], strong excited-state absorption is observed for $\overline{\nu}_{\mathrm{probe}} > 2 \times 10^4$ cm^{-1}, while bleaching of the GSA and stimulated emission (SE) are detected between $\overline{\nu}_{\mathrm{probe}} = 1.4$ and 2.0×10^4 cm^{-1}. As shown in Fig. 4.18, the equilibrium isomer ratio is strongly shifted towards TTC for which reason its absorption is considerably stronger than that of TTT. The 2D signal is therefore dominated by TTC contributions located along the vertical red line. Nevertheless, also TTT contributions can be identified, e.g., TTT ESA causing a pronounced distortion of the contour lines towards lower pump wavenumbers [mark I in Fig. 4.19(a)].

While ESA and SE contributions decrease with T, a positive cross peak emerges at TTC excitation and TTT GSA probe wavenumbers (mark II) for $T \geq 100$ ps [Figs. 4.18(d)–(f)]. A corresponding negative contribution appears blue-shifted at TTC GSA probe wavenumbers (mark III). These signals corroborate a decreased TTC amount (III) and an associated TTT increase after photoexcitation of TTC (II), explicitly proving *cis–trans* photoisomerization. The occurrence of the reversed isomerization reaction (TTT→TTC) can be excluded as no cross peaks remain on the blue vertical line that would correspond to TTT excitation and reaction. In transient absorption, such conclusions cannot be obtained directly as only the integral over the 2D spectrum along $\overline{\nu}_{\mathrm{pump}}$ is measured. Thus the measured 2D spectra directly reveal the photochemical relationship between the TTC isomer as the reactant and TTT as the reaction product in a very intuitive manner just as proposed in Fig. 4.14(b).

4.4.4 Two-Dimensional Spectroscopy – Ultrafast Primary Photodynamics

We now proceed to extract the details on the primary isomerization dynamics as, for instance, their time scale, the associated reaction path, and the involved states. As already discussed in Sect. 4.2.4, either an excited-state isomerization followed by photoemission from the photoproduct's region of the electronic potential energy surface or ultrafast radiationless isomerization to the electronic ground state (e.g., via a conical intersection) is consistent with the data of Fig. 4.19. In Sect. 4.2.4 it was concluded that an excited-state isomerization reaction is the most probable explanation for the observed signatures. Yet, no direct photochemical correlation between the two isomers could be detected there.

In both scenarios, .i.e., excited-state reaction and ultrafast non-radiative transition to the ground state, cross peaks indicative of photoproduct formation at early population times would be buried under much larger negative contributions such as stimulated emission or bleaching of the GSA of the majority of molecules not undergoing photoisomerization. To overcome this problem, the structural rearrangements by analyzing characteristic molecular vibrations observed during the first picoseconds are monitored, leading to the identification of the photoproduct and the relevant electronic state.

Multiple 2D spectra for population times between $T = 0$ and 2.2 ps have been recorded and corrected for probe-pulse chirp. The chirp-corrected spectrum for $T = 1$ ps is shown exemplarily in Fig. 4.20(a). Specific points in ($\overline{\nu}_{\mathrm{pump}}$,$\overline{\nu}_{\mathrm{probe}}$) space can be associated with different reaction paths. The corresponding temporal evolutions as a function of T are shown in Fig. 4.20(b) for contributions arising from ESA (circles), in Fig. 4.20(c) for

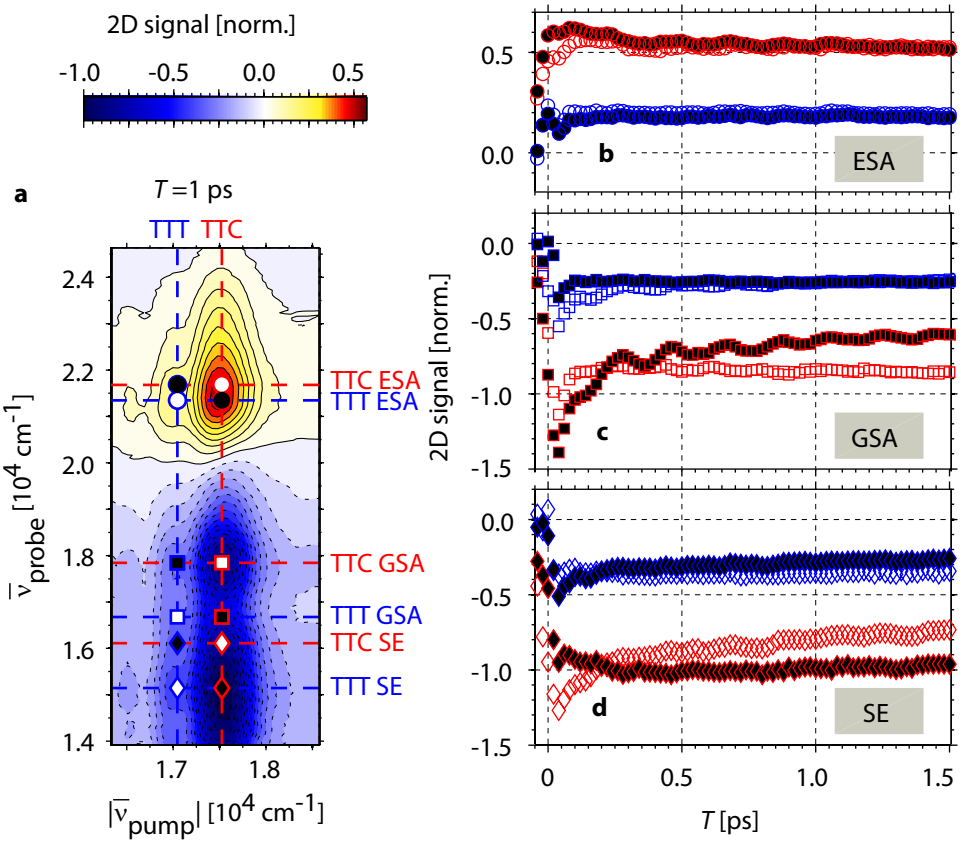

Figure 4.20 | Evolution of the 2D signal up to 1.5 ps after photoexcitation. (a), Exemplary 2D spectrum for $T = 1$ ps; The temporal evolution as a function of population time is shown (b) for ESA (circles), (c) GSA (squares), and (d) SE signals (diamonds). Corresponding $(\bar{\nu}_{\mathrm{pump}}, \bar{\nu}_{\mathrm{probe}})$ coordinates are indicated in (a) by their associated markers. Red markers represent contributions after TTC excitation, blue ones those after mostly TTT excitation. White filling corresponds to excitation and probing of the same isomer, black filling to different isomers, respectively. Figure adapted from Ref. [4].

signals at GSA wavenumbers (squares), and in Fig. 4.20(d) for SE signatures (diamonds). Red markers indicate signals after TTC excitation, those in blue after mainly TTT excitation. White markers correspond to excitation and emission frequencies of one and the same isomer whereas at black filled markers mainly the emission of the isomer is monitored, which is not directly photoexcited.

Discriminating between the two isomers solely from ESA signals [circles, Fig. 4.20(b)] is not possible as the spectral separation of the two ESA bands is too small. However, a pronounced Stokes shift of the ESA band towards higher probe wavenumbers is observed as the slightly higher-energetic part (white-filled red circles) takes longer to reach its maximum compared to the lower-energetic part (black-filled red circles) during the first 200 fs. The same characteristic Stokes shift was already observed in the transient absorption measurements [see Fig. 4.5(a)] and was discussed in more detail in Sects. 4.2.1 and 4.2.2.

In the components at GSA wavenumbers [squares, Fig. 4.20(c)] an oscillatory behavior

is found, most pronounced for the data plotted in black-filled red squares, corresponding to TTC excitation and TTT GSA probing. The dominant contribution of these oscillations has a period of 190 fs and is observed up to roughly 1.5 ps after excitation. These beatings are absent at TTC GSA probe wavenumbers (white-filled red and black-filled blue squares) and are also substantially decreased when mainly TTT is excited (white-filled blue squares). These oscillations are assigned to the same coherent vibrational wave-packet motions also detected in the transient absorption data presented in Sect. 4.2.4.

Concerning the SE region [diamonds, Fig. 4.20(d)], the Stokes shift is observed again as the low-energy signal (black-filled red diamonds) reaches its minimum temporally delayed by a few hundreds of femtoseconds compared to the blue edge of the emission band (white-filled red diamonds).

4.5 Third-Order Three-Dimensional Electronic Spectroscopy

Following the idea of coherent third-order three-dimensional spectroscopy of photochemical processes, as proposed in Fig. 4.14(c), the first experimental realization of this method is now described, using the *cis–trans* isomerization of the MC form of 6-nitro BIPS as a model system. From the previous section, we can deduce that the coherent 2D data of the primary photodynamics may contain very rich and detailed information about the photoprocess of interest, but single 2D spectra as a function of T can not expose the ultrafast reaction dynamics due to the large amount of different overlapping contributions not connected to the isomerization reaction itself obscuring potential signatures of the reaction. In contrast, by utilizing third-order three-dimensional spectroscopy, isolating specific contributions also at early waiting times is achieved, uncovering the photoreaction and associated molecular reactive modes.

The 2D data set for short population times was recorded with population-time steps of $\delta T = 20$ fs over a ΔT range of more than 2.2 ps. In order to generate the third-order three-dimensional spectrum, an additional Fourier transformation along the population time axis between 160 fs $< T <$ 2200 fs transfers the (complex-valued) ($\overline{\nu}_{\mathrm{pump}}$,$T$,$\overline{\nu}_{\mathrm{probe}}$) data set into ($\overline{\nu}_{\mathrm{pump}}$,$\overline{\nu}_T$,$\overline{\nu}_{\mathrm{probe}}$) space with a frequency increment along the $\overline{\nu}_T$-axis of $\delta\overline{\nu}_T = 1/(c\Delta T) \approx 15$ cm^{-1}. The $\overline{\nu}_T$-axis thus contains information about coherent vibrational signatures in the 2D signal during the population time.

The absolute value of the 3D spectrum extracted by this procedure is shown in Fig. 4.21 as an isosurface graph. For visualizing cross peaks, semitransparent surfaces with isovalues of 0.65 %, 0.9 %, 1.15 %, and 1.40 % of the maximum amplitude were chosen. As the 3D data was received by Fourier transformation over the unprocessed 2D data, which also contains incoherent non-oscillating signatures from the relaxed S_1 population, the main contribution of the 3D spectrum is found at very low $\overline{\nu}_T$ wavenumbers. In addition, two pillar-shaped structures are found for wavenumbers below $\overline{\nu}_T = 100$ cm^{-1} in the region of TTT GSA and TTT ESA probe wavenumbers which are not isolated from the $\overline{\nu}_T = 0$ cm^{-1} contributions. They might be related to vibrational cooling and the associated Stokes shift occurring within the first picosecond after

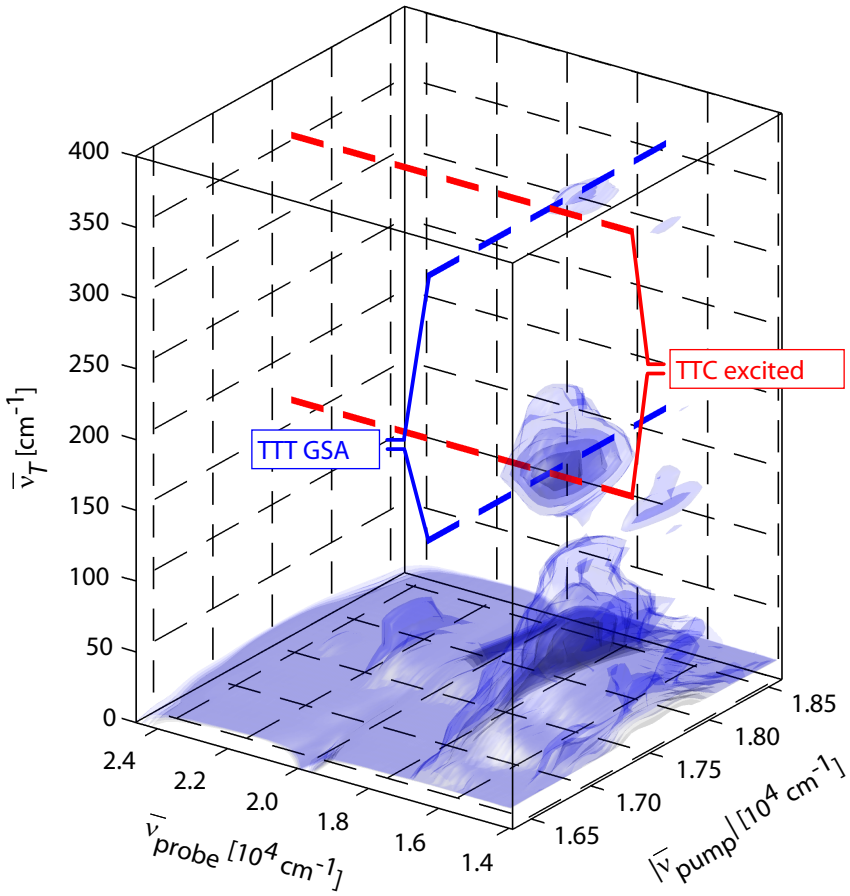

Figure 4.21 | Third-order 3D spectrum of the MC form of 6-nitro BIPS in acetonitrile. A three-dimensional isosurface representation is used to visualize the absolute value of the 3D spectrum. Isovalues of 0.65 %, 0.9 %, 1.15 %, and 1.40 % of the maximum amplitude were chosen. Red dashed lines indicate TTC excitation, blue dashed lines the TTT GSA probe wavenumber. Figure adapted from Ref. [4].

excitation. As (incoherent) populations with an exponential decay lead to Lorentzian line shapes in the 3D spectrum centered at $\overline{\nu}_T = 0$ cm^{-1}, vibrational cooling results in broadened Lorentzians showing up as broad unstructured contributions at these low values of $\overline{\nu}_T$.

By contrast, the observed vibrational motion leads to separated cross peaks in the 3D spectrum. One such isolated cross peak around $\overline{\nu}_T = 176$ cm^{-1} reflects the 190 fs vibrational period evident in Fig. 4.20 and is consistent with the frequency of the LFM as assigned in Sect. 4.2.4. This cross peak is centered at the crossing of TTC excitation (red dashed line) and TTT GSA probe wavenumbers (blue dashed line). A second isolated cross peak – albeit lower in amplitude – shows up around $\overline{\nu}_T = 363$ cm^{-1}, corresponding to a vibrational period of 90 fs and thus matching the vibrational period of the HFM. This cross peak is slightly shifted away from the crossing point towards higher electronic excitation frequencies, which may be explained by more excess energy required for this vibrational mode. The location in the 3D spectrum reveals that oscillations of cross peaks connecting the two isomers give rise to these signatures.

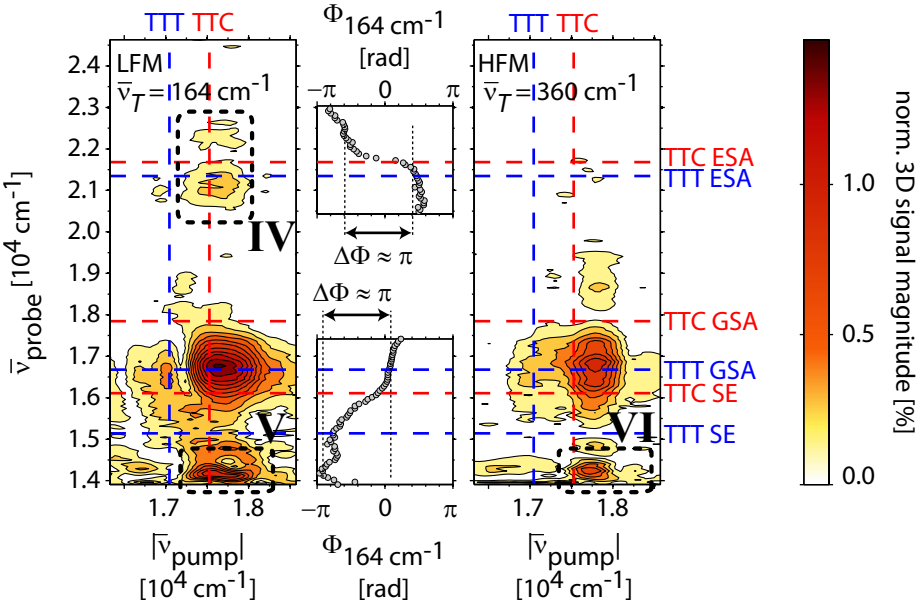

Figure 4.22 | Slices through the 3D spectrum in the ($\bar{\nu}_{\mathbf{pump}}$,$\bar{\nu}_{\mathbf{probe}}$) plane. For both $\bar{\nu}_T = 164$ cm^{-1} (left) and $\bar{\nu}_T = 360$ cm^{-1} (right), typical signatures of an excited-state wave packet are observed. The phase for $\bar{\nu}_T = 164$ cm^{-1} at a vertical cut at the TTC excitation wavenumber is shown in the center. Figure adapted from Ref. [4].

Slices through the 3D spectrum in the ($\bar{\nu}_{\mathrm{pump}}$,$\bar{\nu}_{\mathrm{probe}}$) plane are shown in Fig. 4.22 for the two dominating vibrational modes – at $\bar{\nu}_T = 164$ cm^{-1} for the LFM (left), and at 360 cm^{-1} for the HFM (right) – together with the 3D phase for the LFM along the TTC excitation wavenumber (center). For both modes the main contributions are located at TTC excitation and TTT GSA probe wavenumbers. These modes are a result of an impulsively driven photoreaction where vibrational coherence is maintained during the isomerization process.

The data confirms the results of the transient absorption measurements and again proves that the formation of the TTT photoproduct occurs in the first excited singlet state S_1 accompanied by wave-packet motions on the potential energy surface. The line of argument is similar to that in Sect. 4.2.4 but is now reaffirmed by the data shown in Fig. 4.22 as follows:

i) Signatures of the vibrational wave packet can again be found in the ESA region of TTT (mark IV in Fig. 4.22). In addition, both modes are observable at the red-edge of the stimulated emission (marks V and VI). As ESA and SE signals originate from the excited-state, oscillatory signatures observed at both spectral regions have to be associated to excited-state vibrations.

ii) Signals of an oscillating wave packet are typically most pronounced at the inner and outer turning points, where the wave packet's position is strongly localized, whereas the lowest oscillation amplitudes occur at the minimum of the potential energy surface [131, 132]. In the case of an excited-state wave packet, a distinct minimum of the modulations is therefore expected at the maximum of the (vibrationally

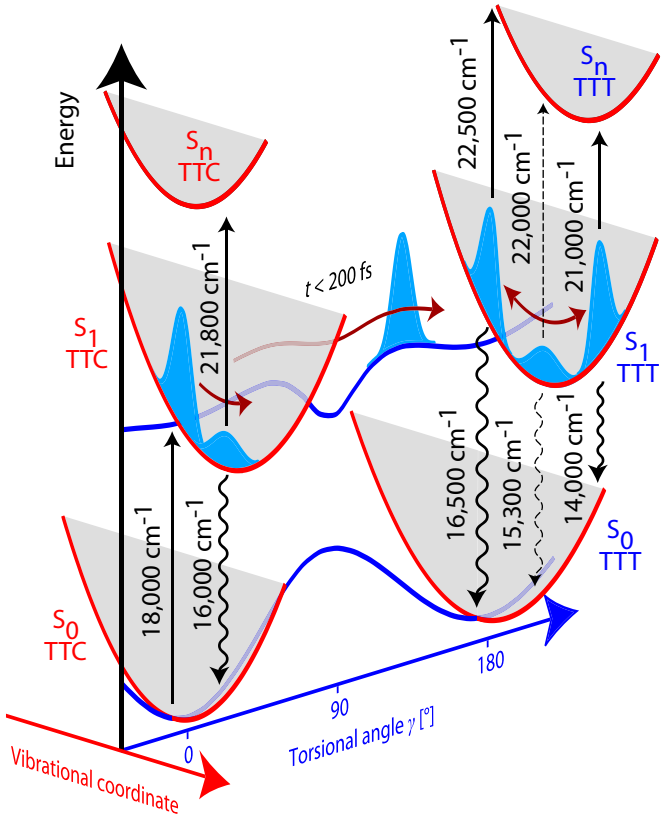

Figure 4.23 | Simplified picture of signatures arising from a vibrational wave packet in the S_1 state of TTT after *cis-trans* isomerization. The wave packet is created at the Franck–Condon region of TTC and propagates on the PES along the reaction coordinate given by the torsional angle γ. Signatures of the wave packet rise on a time scale below 200 fs in the photoproduct region where periodic modulations of the 2D signal are observed. These signal oscillations are most pronounced at the inner and outer turning points (solid arrows). In between, a phase change of π and a minium of the signal oscillations is observed (dashed arrows). The wavenumbers of the transitions were extracted from the 3D spectrum. Vibrations that are not directly connected to the isomerization coordinate are approximated by parabolas. Figure adapted from Ref. [4].

relaxed) TTT SE signal and the most pronounced signature will emerge red- and blue-shifted, as sketched in Fig. 4.23. This is in agreement with the data shown in Fig. 4.22.

iii) A phase change of π is observed for the oscillations as a function of probe wavenumbers [131] reflecting the phase difference of π between the inner and outer turning point. In our case, the two turning points are probed at the spectral edges of the TTT ESA and TTT SE band with the blue- and red-edge signals oscillating out of phase and a distinct phase change of π in between (center of Fig. 4.22). Please note that minor deviations in the 3D phase may result from experimental uncertainties of $T = 0$ due to imperfections of the probe chirp correction.

All these arguments substantiate that the photoproduct is formed on the time scale of a few vibrational periods in its first excited electronic state. This is unambiguously proven by the third-order 3D spectrum, which isolates characteristic 3D cross peaks indicative for the photoreaction also for short population times.

The use of third-order 3D spectroscopy leads to a comprehensive picture of the ultrafast photoisomerization dynamics visualized in Fig. 4.23, where the molecular potential energy is sketched as a function of the main reaction coordinate, i.e., the torsional angle γ (blue), and a second not further specified vibrational coordinate (red). The curves along the torsional angle are based on theoretical calculations (which will be discussed in more detail in Sect. 4.6), whereas the curves along the vibrational coordinates are

approximated by parabolas (harmonic approximation). After TTC excitation, most molecules return to the TTC ground state. However, a smaller portion undergoes *cis* → *trans* isomerization in the excited state, upon which pronounced wave-packet dynamics are observed. Several internal molecular coordinates are involved in this reaction based on the observation of two independent vibrational modes.

Moreover, the phase of the vibrational motion corroborates that an excited-state vibrational wave packet is induced and that the S_n potential is displaced in the same direction relative to the S_1 potential as the S_1 is displaced compared to S_0. Thus, low-energy ESA transitions occur from the same position on S_1 from which low-energy SE originates (and vice versa for the high-energy contributions), as also sketched in Fig. 4.23.

4.6 Quantum Chemical Calculations

In order to assign the observed vibrational modes to specific excited-state molecular normal modes of ring-open 6-nitro BIPS and to gain a detailed picture about the mechanism of the photoreaction on a microscopic level, quantum chemical calculations were carried out on the investigated system. These calculations were performed by C. Walter in the theoretical chemistry group of Prof. B. Engels and parts of the results are discussed in the following sections.

4.6.1 Potential Energy Surfaces

Density functional theory was used to compute the potential energy profiles of the electronic ground state and the first excited state along the TTC→TTT reaction coordinate, which is parameterized by the torsional angle γ of the last C–C bond of the methine bridge around which isomerization is observed (see also Fig. 4.2 for the definition of the torsional angles that characterize the merocyanine isomers).

The potential energy profiles of the electronic ground (red) and first excited state (blue) of ring-open 6-nitro BIPS are shown in Fig. 4.24(a). The ground state curves were calculated on the B3LYP/cc-pVDZ level of theory [304] while the CAM-B3LYP approach [305] was used for the excited state profiles. In both cases the software package gaussian09 [306] was employed. Since strong solvent effects were observed in the photochemistry of merocyanines the solvent was accounted for employing a polarizable continuum model (acetonitrile, $\epsilon = 35.688$). The curves in Fig. 4.24(a) were scaled in such a way that the ground state of TTC [S_0(GS) at 0°] is set to zero energy serving as a reference. Solid lines and circles represent the curves at the optimized ground-state geometry, dashed lines and squares describe the potential at the relaxed excited-state molecular configuration. The solvent was adapted to the corresponding molecular geometry and, accordingly, the energy gap between solid lines describes the S_0–S_1 excitation condition while transitions between dashed lines characterize the S_1–S_0 emission energy. In contrast, the red dotted line represents the ground state energy at the S_1 geometry but with ground-state solvation.

To investigate the potential along the reaction coordinate the torsional angle γ was

fixed at predefined values while at the same time all other internal nuclear coordinates were optimized to minimize the total potential energy. By doing so, a rotational barrier of about 0.7 eV (68 kJ/mol) is found at $\gamma = 80°$ in the ground state which explains why the thermal back reaction is not observed on a nanosecond time scale. In the excited state the rotational barrier is reduced significantly to below 0.1 eV (10 kJ/mol). In addition, when the solvent and the molecular geometry are optimized with respect to the excited-state electron density, the rotational barrier vanishes completely and a distinct minimum in the excited state at $\gamma = 90°$ is found while the ground-state energy is increased substantially at this twisted geometry. Though the S_1 and S_0 potentials approach each other at this point no indication for a conical intersection is found.

The calculated $S_0 \leftrightarrow S_1$ oscillator strength is shown in Fig. 4.24(b) for both the ground-state (red line) and the excited-state configuration (blue dashed line). While for the two isomers at $\gamma = 0°$ and 180° very similar values between 0.7 and 0.9 are found, the oscillator strength approaches zero at the twisted configuration, which is due to the fact that in this case the conjugation is interrupted at the last carbon atom of the methine bridge. Hence, no radiative transition and also no spectroscopic signatures from S_1 can be observed at this configuration. It seems very likely that parts of the excited-state population propagate in the direction of a twisted geometry, where it may traverse the 90° configuration in the excited state and end up in the energetically slightly lower 180° geometry of the excited TTT isomer. In addition, since the barrier in the ground state is slightly shifted to lower values of γ, a radiative transition to the TTT ground state could be slightly favored over the transition to TTC as soon as a twisted configuration with $\gamma > 80°$ is reached in the excited state. The low barrier in the S_1 (GS) curve also matches the experimental observation that a minimum amount of excess energy is required for the reaction (compare Fig. 4.8).

Two-dimensional PESs were approximated based on the energy profiles shown in Fig. 4.24(a) by combining all internal coordinates to an effective mode whose amplitude is given by the root mean square (RMS) deviation of all bond lengths from the S_0 condition, as illustrated in Fig. 4.24(c). A harmonic behavior of the PES along this effective mode was assumed, thus the red solid line and the blue dashed lines form the apex of a parabola. For the S_0 PES ground-state solvation was assumed also at the excited-state geometry (red dotted line). The S_1 Franck–Condon points are indicated by blue (TTT) and red (TTC) colored circles. A distinct depression located at $\gamma = 90°$ in the excited state results from the decrease of the excited-state energy after a full solvent relaxation. Since this process occurs on a time scale of several hundreds of femtoseconds it can be assumed that the excited state PES is considerably smoother directly after photoexcitation. Taking this and the shape of the PES into consideration it seems likely that the wave packet is created at the Franck–Condon region of TTC isomers where vibrations with respect to the effective mode orthogonal to the reaction coordinates are initiated. The wave packet will therefore initially follow the steepest gradient of the PES by which the observed vibrational modes are induced. At the same time the excited-state TTC→TTT barrier is reduced during solvent and internal reorganization and parts of the excited molecules undergo the photoisomerization by passing the twisted molecular configuration and finally product vibrations can occur in the excited state of TTT.

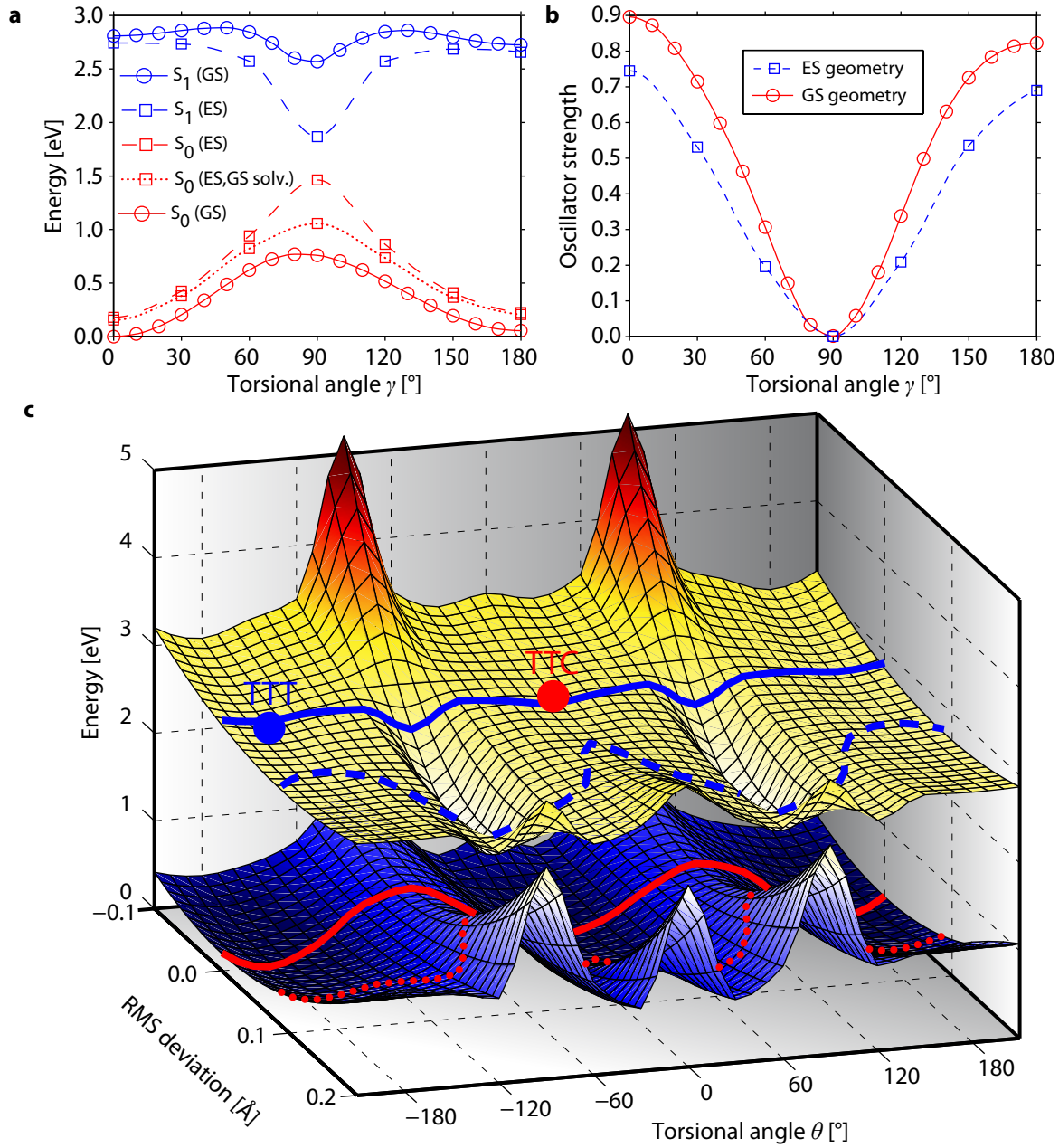

Figure 4.24 | Computed potential energy profile and oscillator strength along the torsional angle γ of the last C–C bond of the methine bridge. (a) The energy profiles are shown for the electronic ground state S_0 (red) and first excited state S_1 (blue). The labels in brackets denote the corresponding molecular geometry (ground state: GS, circles; excited state: ES, squares). The red dotted curve shows the ground-state energy at the optimized excited-state geometry but with ground-state solvation. (b) The oscillator strength for $S_0 \leftrightarrow S_1$ transitions approaches zero at the 90° transition state both for the ground-state (red) and for the excited-state geometry (blue). (c) Approximated S_0- and S_1-PES as a function of γ and the generalized effective mode given by the root-mean-square bond-length variation with respect to the optimized ground-state geometry. The surfaces were obtained assuming a harmonic behavior of the effective mode and on the basis of the energy profiles of (a).

4.6.2 Normal Mode Analysis

Since in the experimental data signatures of excited-state vibrational wave packets were observed it was necessary to calculate the excited-state normal modes. These calculations were performed at the twisted excited-state configuration at $\gamma = 90°$ in the gas phase. The corresponding molecular geometry is given in Table A.1 of Appendix A.1 where all nuclear Cartesian coordinates are listed. All 120 normal modes, corresponding vibrational wavenumbers, reduced masses, and IR intensities are listed in Table A.2 in Appendix A.2.

Several vibrational normal modes (# 11,12, and 22–24, marked by red font color in Table A.2) with (unscaled) wavenumbers of $\overline{\nu} = 177$, 185, 361, 362, and 376 cm^{-1} are found within the two experimentally observed wavenumber ranges [LFM: (176 ± 23) cm^{-1}, HFM: (363 ± 7) cm^{-1}].

To extract from all modes the ones which might play a dominant role in the isomerization process, the values of different geometrical parameters, e.g., bond lengths, bond angles, torsional angles, etc., were analyzed as a function of the torsional angle γ. The most prominent variation as a function of γ is found for the C–C bond around which the isomerization occurs, as shown in Fig. 4.25(a). A pronounced C–C bond elongation at $\gamma = 90°$ and subsequent shortening is found both in the excited state (red) and in the ground state (blue). This indicates that C–C stretching modes of this bond could play a major role during the photoisomerization.

This assumption is confirmed by the data depicted in Fig. 4.25(b), which shows the calculated C–C bond stretching amplitude for all normal modes up to 500 cm^{-1} as a function of their vibrational wavenumbers. Modes # 11,12, and 22–24 are marked by red color. Very pronounced C–C bond stretching amplitudes are found for modes 12 and 22–24 in the experimentally observed frequency range which substantiates that the observed vibrations are directly connected to the isomerization process during which the carbon bond is strongly modulated. The 185 cm^{-1} mode – possessing the strongest C–C bond stretching amplitude for all low frequency vibrations below 500 cm^{-1} – can thus be assigned to the observed LFM and is visualized in Fig. 4.25(c) by the two overlaid reversal-point molecular geometries. Apart from the C–C stretching, this mode also involves tilting of the benzene ring at which the nitro group is attached. This further suggests that this mode plays a major role in the photoisomerization upon which the ring is rotated by 180°.

An analysis of the role of further geometry parameters for the low frequency normal modes is described in Appendix A.3. The data suggests that the photoreaction is also accompanied by a slight bending of the rotating benzene ring [Fig. A.2(a–b)] and the methine chain [Fig. A.2(c–d)] and possibly by a twisting of the two out-of-plane methyl groups [Fig. A.3(a–b)]. In contrast, no major contributions of the torsional angle γ [Fig. A.3(c–d)] are found in the low-frequency range which evidences that the vibrations are not directly connected to the reaction coordinate.

Thus, the quantum chemical calculations provide a mechanistic picture of the investigated photoreaction. The calculated potential energy profiles prove that an excited-state *cis-trans* isomerization reaction is the most probable scenario for 6-nitro BIPS and demonstrate that the solvent environment could be a crucial parameter for the dy-

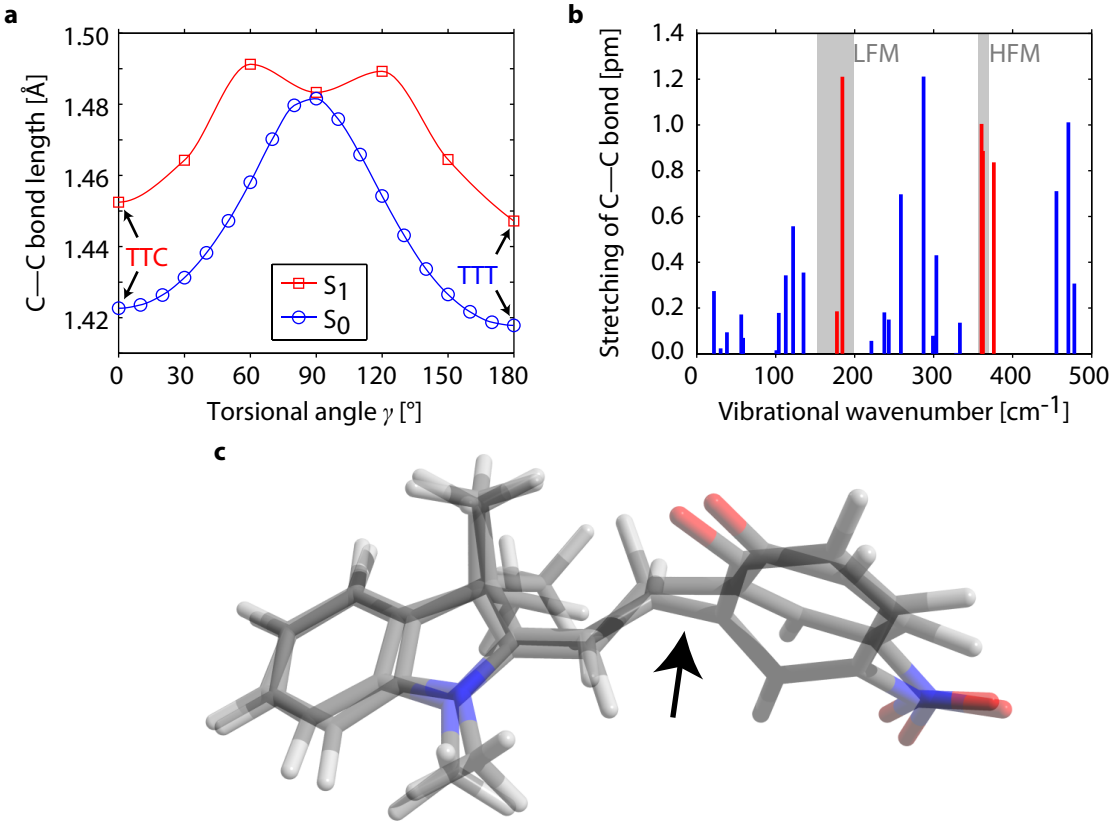

Figure 4.25 | Quantum-chemical analysis of the reaction mechanism and involved vibrational normal modes. (a), The C–C bond around which the *cis–trans* isomerization occurs [arrow in (c)] is substantially stretched during the bond rotation both for ground (blue) and first excited state (red). (b), The calculated stretching amplitudes of the C–C bond for all low-frequency normal modes (see Table A.2 for all normal modes) show pronounced contributions at those modes (red) located in the two experimentally observed frequency ranges of the LFM and the HFM (gray). (c), The dominant 185 cm^{-1} mode (normal mode # 12) assigned to the LFM is visualized by overlaying the two reversal point geometries (dark gray: C, light gray: H, red: O, blue: N; corresponding molecular geometry given in Table A.1). Figure adapted from Ref. [4].

namics since both ground- and excited-state energies are substantially affected at the twisted transition-state configuration. Finally, specific molecular normal modes could be assigned to the cross peaks extracted in the third-order 3D spectrum. The experimentally observed vibrational wavenumbers were reproduced by the calculations and it was shown that C–C stretching modes of the carbon bond around which the isomerization is observed plays a dominant role in the photoreaction.

4.7 Conclusion

Our results lead to a comprehensive picture of the ultrafast *cis-trans* photoisomerization dynamics of ring-open 6-nitro BIPS in acetonitrile. Using broadband transient absorp-

tion spectroscopy with sub-50 fs temporal resolution in combination with global data analysis several photophysical and photochemical channels of merocyanine in solution were detected. Two different MC isomers were observed and assigned to the TTC and TTT configurations. On the basis of the global fit the corresponding excited-state lifetimes of $\tau_{\mathrm{TTC}} = (35 \pm 4)$ ps and $\tau_{\mathrm{TTT}} = (160 \pm 40)$ ps and associated spectral profiles were extracted. A product absorption emerging after about 100 ps was attributed to the TTT isomer formed after TTC excitation with a quantum yield of $\Phi_{\mathrm{TTC}\rightarrow\mathrm{TTT}} = (18 \pm 4)$ %. In addition, pronounced signatures of coherent vibrational motions were detected and attributed to product vibrations initiated upon the isomerization reaction.

Coherent 2D spectroscopy in a pump–probe beam geometry employing femtosecond pulse shaping was implemented successfully and the experimental procedures of phase cycling, the rotating frame, and probe-chirp correction were discussed.

It was further demonstrated for the first time that coherent multidimensional electronic spectroscopy can be used for analyzing the dynamics of an ultrafast photochemical process and the involved molecular reactive modes. Through the emergence of the TTC $\rightarrow$ TTT cross peak in the 2D spectra, the existence of the unidirectional *cis–trans* photoisomerization was explicitly proven. An even deeper understanding of the reaction dynamics was gained by probing the short-time dynamics with high temporal resolution and by evaluating the molecular response via a third-order three-dimensional electronic spectrum. Such a spectrum correlates the signatures of reactants with those of the photoproducts and additionally exposes the involved reactive modes connecting them. Employing this technique, it has been shown that the photoproduct is impulsively formed in its first excited singlet state, maintaining vibrational coherence during the complete process of structural rearrangement. Molecular normal modes in the experimentally detected frequency range have been identified by quantum chemical calculations and could be associated with the observed photoreaction. Thus, third-order 3D spectroscopy offers great potential for the real-time analysis of complex chemical reaction networks involving a multitude of reactants and products with a variety of reaction quantum yields.

5 Experimental Implementation of Fifth-Order Triggered-Exchange Two-Dimensional Electronic Spectroscopy

In the previous chapter an ultrafast photoreaction was studied by means of third-order spectroscopy techniques which in most cases provide sufficient information about the system under investigation. Even though third-order techniques, i.e., approaches employing laser pulse sequences with exactly three light–matter interactions, yield spectroscopic information in up to three temporal or spectral dimensions in (τ,T,t)- or (ω_{pump},ω_T,ω_{probe})-space, in some cases signals based on higher-order nonlinearities may be desired. A typical example for such a scenario would be multiphoton ionization or dissociation processes that compete with other photophysical or photochemical reaction channels as for instance photoemission or internal conversion. In order to determine the role of all involved electronic states, higher-order electronic spectroscopy techniques will be necessary.

In this part of this thesis, one of these higher-order nonlinear spectroscopy techniques, which has so far only been available in the IR regime with vibrational transitions, will be implemented for the first time in the visible spectral region for exploring the role of higher-lying electronic states in the photochemistry of an organic model compound. This approach, termed coherent electronic triggered-exchange 2D (TE2D) spectroscopy, provides the correlations between a reactant's excitation and the emission frequency of a product which is formed by the absorption of an additional photon during the population time T.

This chapter opens with a brief overview of typical laser-pulse sequences used in ultrafast time-resolved spectroscopy (Sect. 5.1). Then, the photophysical and -chemical properties of the system analyzed in the following – the molecular switch 6,8-dinitro BIPS – is summarized (Sect. 5.2). As a first experiment, pulse-shaper assisted coherent 2D spectroscopy of 6,8-dinitro BIPS is performed in order to resolve the photochemistry after S_1 excitation (Sect. 5.3). As a next step towards electronic TE2D spectroscopy, pump–repump–probe experiments are used to identify potential reaction paths after S_1-S_n transitions (Sect. 5.4). Finally, by combining the pump–repump–probe pulse sequence with our coherent 2D setup, electronic TE2D spectroscopy is established (Sect. 5.5). The results of all experiments are combined and illustrated in a reaction scheme at the end of this chapter (Sect. 5.6).

Parts of this chapter have been published in Refs. [5][1], [6], and [8][2], as listed in the table on page v.

5.1 Pulse Sequences in Ultrafast Spectroscopy

A brief overview of some of the most popular laser pulse sequences typically used for nonlinear time-resolved spectroscopy is given in Fig. 5.1. These techniques mainly differ in the number of employed laser pulses and their temporal (and possibly also spatial) arrangement and, hence, in the degree of nonlinearity. While in most approaches third-order signals are detected, also methods that make use of fifth-order light–matter interactions have been established successfully in the field of time-resolved spectroscopy and will be of relevance in the following.

By far the most popular approach is pump–probe spectroscopy [Fig. 5.1(a)] where a pump laser pulse (green) excites the sample while a probe pulse (gradient color) is employed to monitor the pump induced photodynamics as a function of the varied pump–probe delay T. One of the most versatile types of this third-order technique is transient absorption spectroscopy (see also Sect. 3.4) commonly used for time-resolved studies in the liquid phase.

In those cases in which it is desired to manipulate the pump-induced excited population, an additional repump or dump pulse (blue) may be employed, which interacts with the sample after the pump–repump delay t_{PR} but before the probe process. Accordingly, population can be transferred either to higher-lying states [307–310] or to lower intermediate or product states [311–316] [Fig. 5.1(b)]. Since both the pump and the repump pulse interact with the sample twice, a fifth-order signal is created by the subsequent probe pulse.

In coherent 2D spectroscopy [Fig. 5.1(c), see also Sect. 3.5] a variable time delay between the first and second light–matter interaction is introduced by splitting up the pump pulse into a phase-stable double pulse sequence separated by coherence time τ. The third interaction with the system is provided by the probe pulse, which may in addition serve as a local oscillator that heterodynes the third-order signal emitted by the sample as a photon echo. In 2D experiments using a pump–probe geometry phase cycling is necessary to isolate the photon echo from the undesired transient absorption background (see also Sect. 4.4.2).

In transient 2D spectroscopy [Fig. 5.1(d)] an additional pulse preceding all other pulses creates a transient species, for instance, by inducing certain vibrations or a temperature jump. The time evolution of the non-equilibrium ensemble is then monitored with a conventional 2D pulse sequence resulting in a fifth-order signal emitted in the probe direction [317–322].

In contrast, in coherent triggered-exchange 2D (TE2D) spectroscopy [Fig. 5.1(e)], which has so far been limited to 2D experiments in the IR regime, a repump pulse

[1]Reproduced and adapted with permission from Physical Review Letters **110**, 148305 (2013). © (2013) by the American Physical Society

[2]Reproduced and adapted with permission from Journal of the American Chemical Society **133**, 13074–13080 (2011). © (2011) by the American Chemical Society.

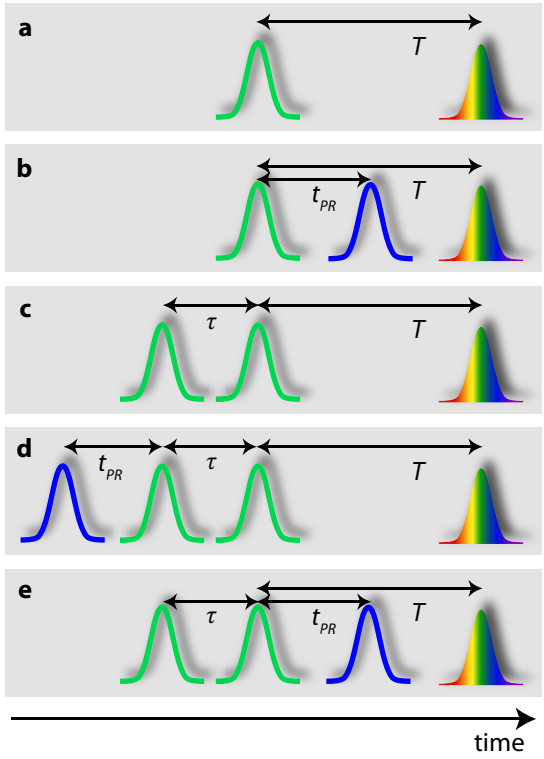

Figure 5.1 | Pulse sequences for time-resolved spectroscopy. (a) pump–probe: A pump pulse (green) excites the sample while a probe pulse (colored) monitors the pump induced dynamics as a function of pump–probe delay T. (b) pump–repump–probe: An additional repump or dump pulse (blue) manipulates the excited population at the pump–repump delay t_{PR}. (c) Coherent 2D: A pump pulse is split up into a phase-stable double pulse separated by the coherence time τ. The probe interacts a third time with the sample and serves as a local oscillator. (d) Transient 2D: An additional pulse creates a transient species and a conventional 2D pulse sequence detects its temporal evolution resulting in a fifth-order signal emitted in the probe direction. (e) Triggered-exchange 2D: A combination of pump–repump–probe and coherent 2D spectroscopy permits the manipulation of the sample during the population time. Figure adapted (and modified) from Ref. [5]. © (2013) by the American Physical Society.

interacts with the system after the pump-pulse sequence but before the probe event [323–325]. In this way the spectral correlation between the system's excitation frequency and the emission frequency of the species formed by the repump pulse is detected. Depending on the beam geometry the fifth-order signal emanating from the interaction with all four pulses can be extracted either by phase matching or by a combination of phase cycling and mechanical pulse chopping.

In this chapter three out of the five techniques discussed above, namely coherent 2D (Sect. 5.3), pump–repump–probe (Sect. 5.4), and coherent electronic TE2D spectroscopy (Sect. 5.5) will be implemented experimentally for a comprehensive study of the photochemistry of 6,8-dinitro BIPS initiated upon excitation to its first excited state as well as to higher-lying electronic states.

5.2 6,8-dinitro BIPS

5.2.1 Steady-State Properties

The second compound investigated in this thesis is the dinitro substituted BIPS, namely 6,8-dinitro-1',3',3'-trimethylspiro[2*H*-1-benzopyran-2,2'-indoline] (6,8-dinitro BIPS), also shown in Fig. 4.1 in Sect. 4.1 with X=NO_2. Similar to 6-nitro BIPS, this molecule has

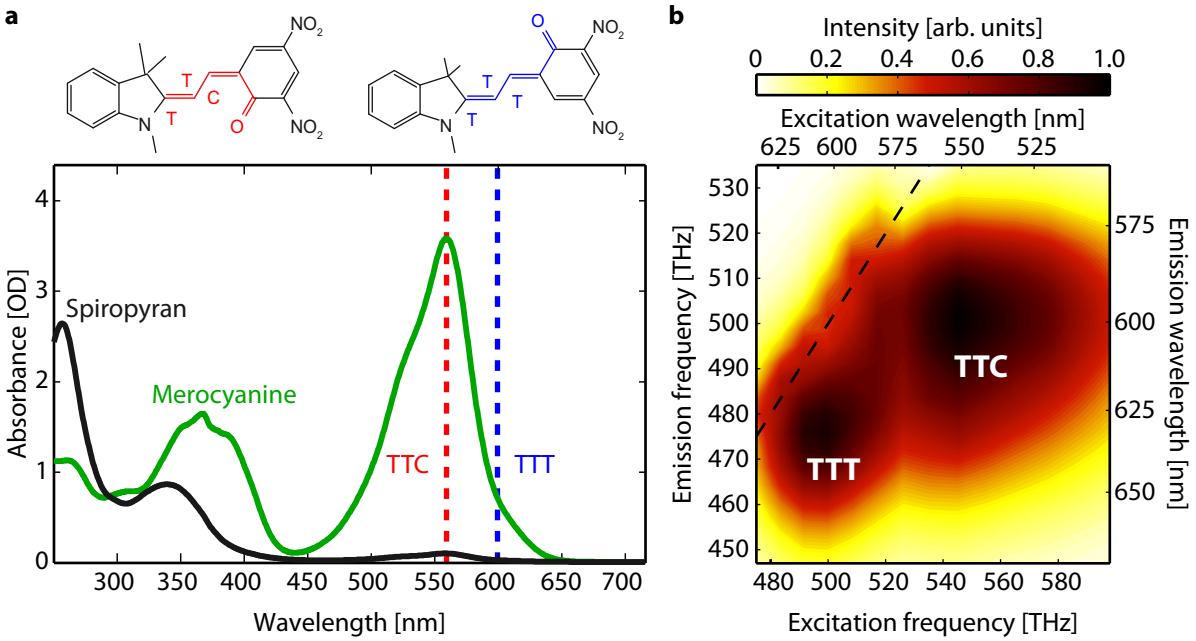

Figure 5.2 | Steady-state absorption and emission properties of 6,8-dinitro BIPS in chloroform. (a) Without illumination (green) the merocyanine form dominates (in the used solvent) with a broad absorption band in the visible peaking around 560 nm. After irradiation of light in the visible range, the ring-closed spiropyran (black) is formed with absorption bands in the UV regime around 340 and 260 nm. Similar to 6-nitro BIPS, the MC form exists as a mixture of TTC (top left) and TTT (top right) isomers with strongly overlapping absorption bands centered at 560 (TTC, vertical red dashed line) and 600 nm (TTT, vertical blue dashed line). Figure adapted from Ref. [5]. © (2013) by the American Physical Society. (b) In the fluorescence spectrum as a function of excitation frequency the existence of the two isomers leads to two clearly separated emission maxima as labeled. Figure adapted from Ref. [8]. © (2011) by the American Chemical Society.

numerous potential applications due to its photochromic properties ranging from three-dimensional optical data storage to light-adaptive sunglasses and molecular electronics [229, 230, 326]. The synthesis and NMR characterization of this compound was performed by R. Schmidt in the organic chemistry group of Prof. F. Würthner and is described in Ref. [235] in detail.

The second nitro group attached to the benzene ring acts as an electron withdrawing substituent and therefore significantly modifies the photophysical and photochemical properties of the dinitro-substituted BIPS with respect to 6-nitro BIPS, which was studied in Chap. 4. Therefore, when dissolved in organic solvents, the merocyanine form of 6,8-dinitro BIPS is more stable than the spiropyran form, which is in strong contrast to 6-nitro BIPS, where the ring-closed form is energetically favored in organic solvents. The absorption spectrum of 6,8-dinitro BIPS in chloroform is shown in Fig. 5.2(a) (green), which is dominated by the merocyanine form absorbing in the visible region with a maximum around 560 nm. Thus, the 6,8-dinitro BIPS solution has a dark purple color. Upon irradiation of visible light the solution is decolorized as the ring-open merocyanine is switched to the transparent ring-closed spiropyran form (black) with absorptions in

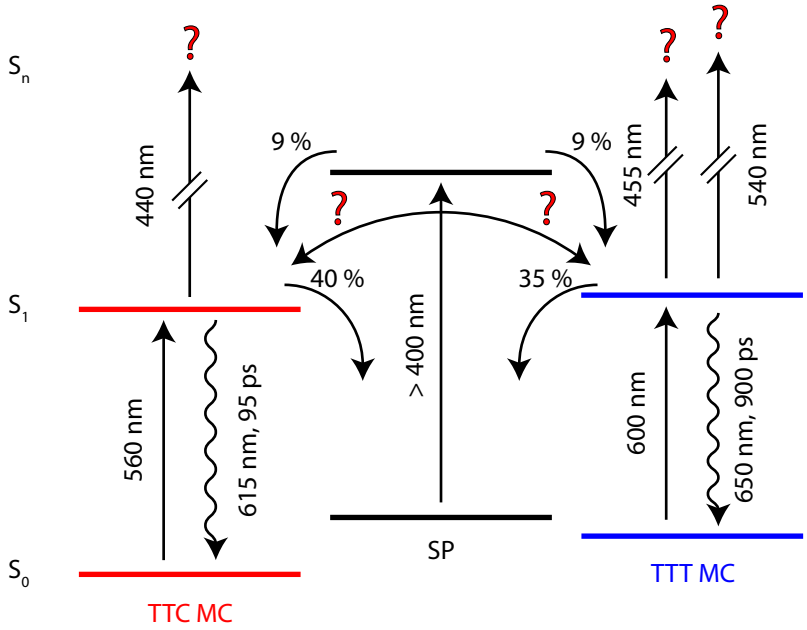

Figure 5.3 | Energy level diagram and reaction paths of 6,8-dinitro BIPS in chloroform as determined by ultrafast time-resolved measurements by Buback *et al.* with S_1 excitation. After photoexcitation at 560 nm 40 % of the TTC molecules undergo the ring-closure reaction to SP. SE is observed for TTC at 615 nm with an S_1 lifetime of $\tau_{TTC} = 95$ ps, ESA appears around 440 nm. The TTT isomer absorbs at 600 nm, leading to SP formation with a quantum yield of about 35 %, SE at 650 nm with $\tau_{TTT} = 900$ ps, and two separated ESAs at 455 and 540 nm. The quantum yield of the ring-opening reaction was found to be 9 %. The existence of $cis - trans$ photoisomerization between TTC and TTT is discussed in detail in Sect. 5.3 while reaction paths emerging after S_1-S_n transitions are determined in Sects. 5.4 and 5.5. Data taken from Refs. [235] and [236].

the UV spectral regions around 340 and 260 nm, which is also contrary to 6-nitro BIPS where the MC form undergoes a *cis-trans* isomerization reaction but no photoinduced ring closure, as was shown in Chap. 4. The ring-closed spiropyran form reacts back to the merocyanine form either by absorption of a UV photon below 400 nm or thermically on a time scale of several minutes. Consequently, no additional illumination of light is necessary for preparing the sample for the experiment if the MC form of 6,8-dinitro BIPS is investigated.

NMR studies by Hobley *et al.* revealed that also for 6,8-dinitro BIPS the two dominating isomers are the TTC and TTT configurations [245], the corresponding structures are depicted on top of Fig. 5.2(a). Transient absorption studies performed in our research group have shown that the TTC isomer absorption is centered at 560 nm (vertical red dashed line) while the TTT absorption band is located red-shifted at 600 nm (vertical blue dashed line) [236]. The equilibrium TTT/TTC concentration ratio was estimated in this study to be on the order of 0.3.

5.2.2 Photophysical and Photochemical Properties

The existence of the two MC isomers of 6,8-dinitro BIPS in chloroform is confirmed by the fluorescence spectrum as a function of the excitation frequency [Fig. 5.2(b)], where two well-separated peaks are detected. While TTC fluorescence is observed at an emission wavelength of 600 nm after 550 nm excitation, the TTT signal is red-shifted to an emission wavelength of 635 nm and 600 nm excitation (see labels). This data suggests that the two isomers are also distinguishable in time-resolved measurements on the basis of their excitation frequencies, which will be exploited in coherent 2D spectroscopy (Sect. 5.3) to disentangle the photochemical connectivity between the two isomers.

The photochemistry of 6,8-dinitro BIPS in chloroform solution was analyzed in previous work by Buback *et al.* by means of transient absorption and ultrafast three-pulse experiments [235, 236]. The results of these studies are summarized in Fig. 5.3. Using variable excitation energies and a global fitting model, it was found that after S_1 excitation at 560 nm about 40 % of all excited TTC isomers undergo the ring-closure reaction to the SP form. For TTC, SE is observed at 615 nm with a characteristic S_1 lifetime of $\tau_{TTC} = 95$ ps. A single ESA band is detected for this isomer around 440 nm. In the case of TTT, which absorbs at 600 nm, the SE signal is also red-shifted to 650 nm with a lifetime of $\tau_{TTT} = 900$ ps. In contrast to TTC, two separated ESA bands are observed at 455 and 540 nm, respectively. The quantum yield of the ring-opening reaction was estimated to be 9 %. Likewise, it was shown that a complete opening–closure–opening switching cycle can be conducted within 40 ps while the reversed ring closure–opening–closure cycle is even faster and can be completed within 6 ps in chloroform [235]. Thus, 6,8-dinitro BIPS is a promising candidate as a molecular "bit" in future applications due to its capability of ultrafast and bidirectional switching with comparatively high switching quantum yields.

The *cis-trans* photoisomerization reaction among the two ring-open merocyanine isomers could not be excluded for this compound, but an upper limit for the quantum yield of 1–2 % was given. In order to address the question regarding the photoisomerization between the MC isomers of 6,8-dinitro BIPS, coherent 2D measurements will be the method of choice in the following section.

Furthermore, to probe the photochemistry of higher-lying electronic states S_n, pump–repump–probe spectroscopy and electronic TE2D spectroscopy will be implemented in Sects. 5.4 and 5.5, as previously discussed.

5.3 Two-Dimensional Electronic Spectroscopy of 6,8-dinitro BIPS

To clarify the question whether *cis–trans* isomerization is also one of the possible reactions paths among the MC isomers of 6,8-dinitro BIPS, coherent two-dimensional electronic spectroscopy experiments in the pump probe geometry with a femtosecond pulse shaper as described in Sect. 4.4.2 were performed. As was demonstrated in Sect. 4.4, third-order 2D spectroscopy is capable of elucidating whether photochemical exchange between different molecular species is part of their photochemistry. However, for

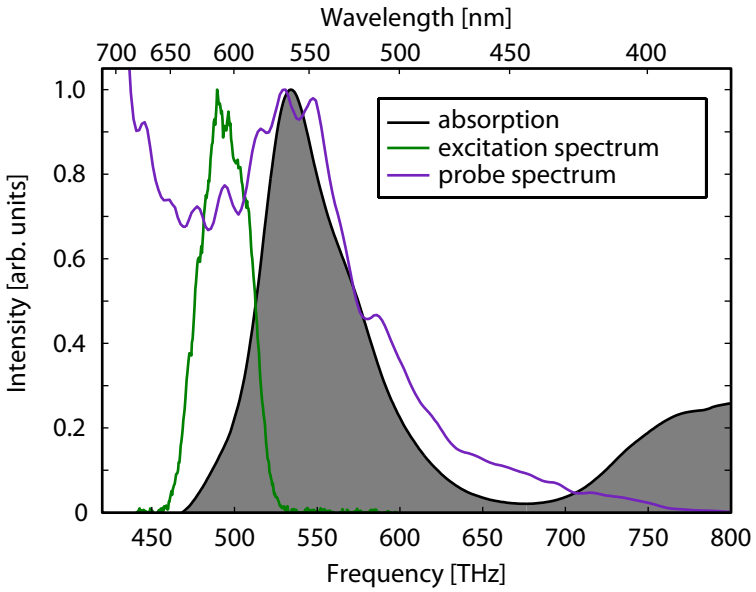

Figure 5.4 | Absorption spectrum of 6,8-dinitro BIPS in chloroform (gray), probe (purple), and pump laser spectrum (green) used for the 2D measurement. The employed broadband white light probe continuum covers the complete visible range. In contrast, the pump-laser spectrum is much narrower and tuned to the red edge of the absorption band in the visible around 605 nm such that both isomers can be excited. Figure adapted from Ref. [8]. © (2011) by the American Chemical Society.

6,8-dinitro BIPS, previous studies already showed that the ring-closure reaction dominates, but *cis–trans* isomerization between the TTC and the TTT isomer could not be excluded entirely [236].

To collect 2D electronic spectra of both isomers of 6,8-dinitro BIPS within a single measurement, the pump pulses were tuned towards the red-edge of the absorption band, as shown in Fig. 5.4 (green line). Therefore, the pump pulses are centered around 605 nm (495 THz) where the TTT isomers absorption is located peaking at 600 nm (490 THz), since the equilibrium TTT isomer concentration is considerably lower than the TTC concentration. Hence, a comparable signal strength is expected for the two isomers. The spectrum of the white-light probe continuum (purple line) covers almost the complete visible range, which allows us to probe contributions far off the diagonal. The pump pulses were compressed to pulse durations below 20 fs using pulse-shaper assisted cFROG (Sect. 3.3).

5.3.1 Isomerization Scenarios for Ring-Open 6,8-dinitro BIPS

In the following, different potential TTC–TTT photoisomerization scenarios and their corresponding expected 2D spectrum will be discussed. An overview over these processes is given in Fig. 5.5 with the reaction schemes on the left-hand side and their associated cartoon-like 2D spectra for short ($T > 0$, left) as well as for longer population times ($T \gg 0$) on the right.

Expected signal contributions are numbered (signals 1–7) in Fig. 5.5(a) in the $T >$

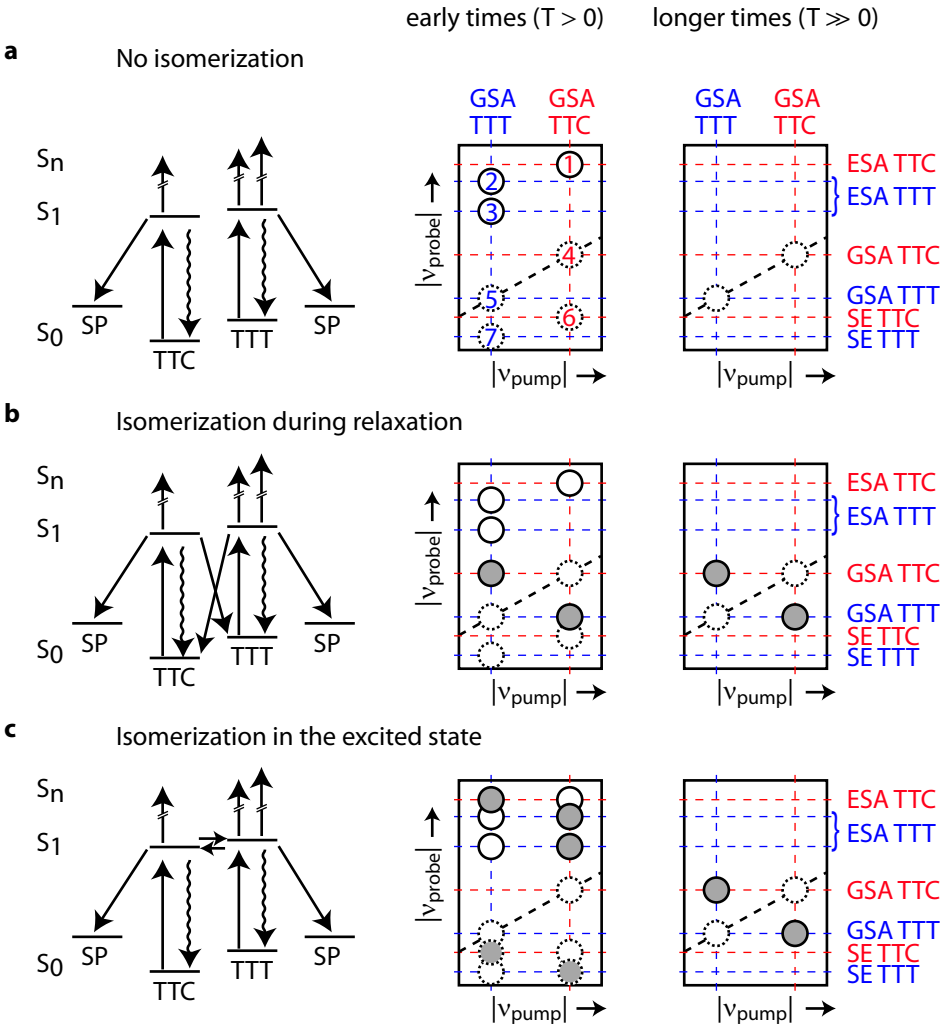

Figure 5.5 | Potential isomerization scenarios (left) and corresponding 2D spectra (right) of the two MC isomers of 6,8-dinitro BIPS. Red-dashed lines represent TTC signals while TTT contributions are marked by blue-dashed lines. Positive signals (ESA, PA) are marked by solid circles, those with negative amplitudes (GSB, SE) by dashed circles. Off-diagonal peaks indicative for *cis–trans* isomerization are filled with gray color and located at points where blue and red lines intersect. (a) In the absence of TTC–TTT isomerization, no isomerization cross peaks will emerge at early waiting times ($T > 0$, left) or on longer time scales ($T \gg 0$, right). (b) For the scenario with ultrafast isomerization with a non-radiative transition to the ground state additional cross peaks will emerge at the GSA frequencies of the respective other isomer on all time scales. (c) If isomerization occurs in the S_1 state, isomerization cross peaks will be observed in ESA and SE regions at early times and at GSA region for longer waiting times. Figure adapted from Ref. [8]. © (2011) by the American Chemical Society.

0 spectrum, the numbers will be used later for discussion of the experimental data. Negative peaks (GSB, SE) are indicated by dashed circles, positive ones (ESA, PA) by solid circles. Additional off-diagonal peaks that are associated with the isomerization reaction are marked by gray color. Both isomers undergo the ring-closure reaction with a

quantum yield of about 40 % [235, 236]. In addition, both molecules exhibit ESA signals in the higher-frequency probe region (signal 1 for TTC, signals 2 and 3 for TTT). The bleaching of the ground state results in negative diagonal (black dashed line) peaks (4,5), while SE leads to negative contributions below the diagonal for both isomers (6,7). As in the case of the related 6-nitro BIPS, all signals are slightly red-shifted for TTT compared to TTC.

In the absence of TTC–TTT *cis–trans* photoisomerization [Fig. 5.5(a)], neither isomerization cross peaks at early waiting times ($T > 0$, left) nor on longer time scales ($T \gg 0$, right) will emerge. Since the ring-closure reaction leads to the formation of the spiropyran form without any absorption bands in the visible spectral range, the associated reduced MC concentration will be reflected by constant negative GSB peaks on the diagonal at longer waiting times. Since no photochemical exchange is assumed in this case, all peaks are observed at crossings of lines with the same color.

The scenario with ultrafast isomerization via a non-radiative transition to the ground state [Fig. 5.5(b)] would be possible in the presence of an S_1-S_0 conical intersection. In this case, additional cross peaks will emerge shortly after photoexcitation at the GSA frequencies of the respective other isomer and will remain there for longer times since the thermal back reaction is expected to be slower than the experimentally accessible time scales.

In case of an isomerization in the first excited electronic state S_1 [Fig. 5.5(c)], isomerization cross peaks will be observable in the ESA and SE regions at early times and at GSA probe frequencies for longer waiting times after which relaxation to the ground state has occurred.

In this context it should be noted that in the 2D electronic spectra, contributions of the two isomers will most probably strongly overlap such that cross peaks might not be resolved at first glance, as was discussed in Sect. 4.4.1. Moreover, the peak shapes along the ν_{pump}-axis are dominated by the pump laser spectrum which is considerably narrower than the MC absorption band (see Fig. 5.4), whereas the 2D spectrum is automatically normalized to the probe pulse spectrum along the ν_{probe}-axis. This can lead to spectral shifts of the measured 2D peaks such that contributions that are expected on the diagonal (such as GSB) might be slightly shifted away from it.

5.3.2 2D Electronic Spectra

The measured absorptive 2D electronic spectra of ring-open 6,8-dinitro BIPS in chloroform are shown in Fig. 5.6 for various population times between 3 and 3000 ps. The measurements were performed with the same setup as discussed in Sect. 4.4.2 and the signal was detected in the laboratory frame with $\gamma = 1$. Blue/purple colors and solid contour lines again denote a decrease of transient absorption whereas at yellow/red regions with dashed contour lines an increased absorption is detected. The vertical dashed blue and red colors indicate the TTT and TTC contributions as labeled on the right side which were determined by global fitting of transient absorption data by Buback *et al.* [236]. The vertical blue and red dashed lines indicate the maximum of the overlap between the corresponding isomer absorption spectrum, which were also determined with a global fit, and the pump laser spectrum [shown above Fig. 5.6(a) together with the

measured absorption spectrum of the sample]. Due to the detuning of the pump laser, especially TTC contributions are shifted away from the maximum of the MC absorption spectrum towards lower pump frequencies ($\approx$ 515 THz). TTT contributions are expected to peak around $\nu_{pump} \approx 495$ THz. After 3 ps [Fig. 5.6(a)], the 2D spectra are dominated by TTC ESA (signal 1) for $\nu_{pump} > 600$ THz and by TTC SE contributions (signal 6) for lower probe frequencies. Nevertheless, contributions of the TTT isomer are clearly identified, for example, in the ESA region where the lower-frequency ESA of TTT leads to the positive tongue-shaped signal for lower pump frequencies [signal 3 in Fig. 5.6(d)] reaching from $\nu_{probe} \approx 600$ THz down to $\nu_{probe} \approx 530$ THz. The higher-frequency ESA of TTT is best visible for longer delay times above 300 ps [signal 2 in Fig. 5.6(d)]. This is due to the fact that TTC signals decay much faster than TTT contributions (95 ps for TTC compared to 900 ps for TTT) with the result that the TTT ESA is uncovered at times when most TTC molecules have already relaxed to their ground state.

Moderate oscillations of the contour lines along the probe-frequency axis are observed at the low pump-frequency edge of the 3 ps spectrum in the ESA. This effect is most probably caused by Raman active modes of chloroform. These modes become visible for short population times due to the chirp of the continuum probe which results in a probe frequency dependent waiting time (as discussed in Sect. 4.4.2) such that temporal oscillations lead to spectral modulations as well [184, 185, 327]. Since the excited-state lifetimes of both MC isomers are much longer than the decay time of the Raman modes, these modes are no longer observed for longer population times.

The strongly differing excited-state lifetimes of the isomers also lead to a shift of the ESA signal towards lower pump and probe frequencies in the first few hundreds of picoseconds [Figs. 5.6(a)–(d)] and even after 3000 ps a low TTT ESA signal remains. The stimulated-emission signals of the two isomers are most clearly discriminated at $T = 100$ ps [Fig. 5.6(c)] and 300 ps [Fig. 5.6(d)]. The TTT SE signal (7) is marked in the $T = 100$ ps spectrum.

All S_1 contributions (ESA, SE) decay on their characteristic timescales. Finally, the presence of the ring-closure reaction and the associated decrease of the MC ground-state concentration for both isomers is reflected by the remaining bleach at TTC GSA (signal 4, at $\nu_{probe} \approx 535$ THz) and TTT GSA (signal 5, at $\nu_{probe} \approx 500$ THz) probe frequencies.

Another low-amplitude negative signal is observed for high probe frequencies above 750 THz best resolved in the $T = 300$ ps [Fig. 5.6(d)] and 1000 ps [Fig. 5.6(e)] spectra. This feature is due to the bleaching of the second MC absorption above 700 THz extending into the UV spectral region which is not covered by the probe continuum. For comparison, the measured MC absorption is also plotted on the right side of Fig. 5.6(f) along the probe axis.

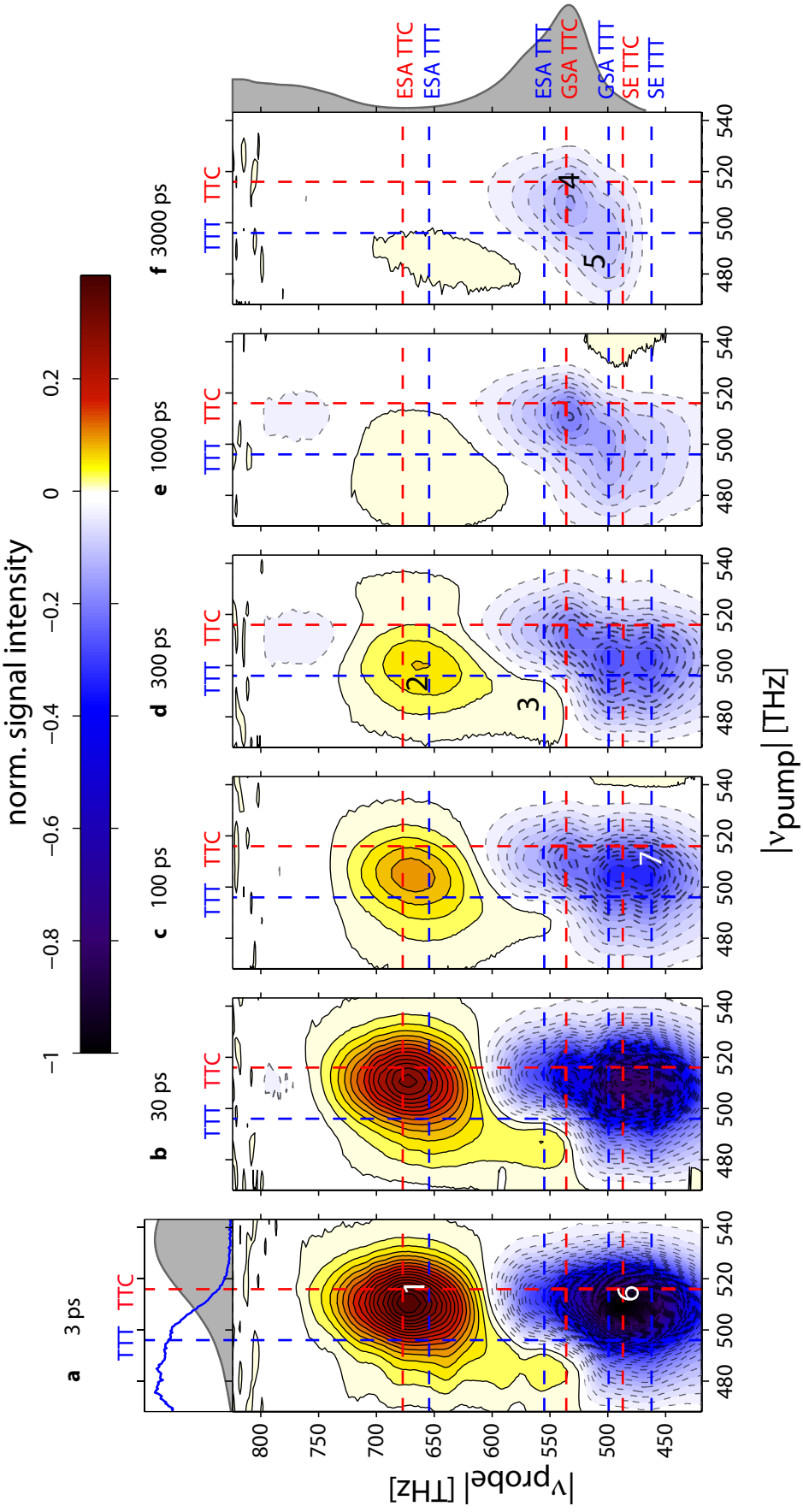

Figure 5.6 | Absorptive electronic 2D spectra of 6,8-nitro BIPS in chloroform for population times between 3 ps and 3000 ps. All spectra are normalized to the minimum of the $T = 3$ ps spectrum. Figure adapted from Ref. [8]. © (2011) by the American Chemical Society.

5.3.3 Discussion of the 2D Spectra

After the in-depth description of the measured 2D electronic spectra of ring-open 6,8-dinitro BIPS, the isomerization scenarios discussed in Sect. 5.3.1 can now be reconsidered and evaluated on the basis of the measurements.

In the case of an excited-state isomerization, one or more additional off-diagonal contributions in the ESA and in the SE region are expected for short population times. For low-quantum yield excited-state reactions, at least minor distortions of the contour lines would be observed. However, in addition to signals 1–7 no cross peaks indicative for excited-state isomerization are detected, neither at ESA nor at SE frequencies. Thus, it is very likely that, in contrast to 6-nitro BIPS, the region of the S_1 PES associated to the TTC isomer is separated from the TTT region of the potential by an energy barrier precluding the direct excited-state transformation.

Furthermore, *cis–trans* isomerization upon relaxation to the ground state can be ruled out. Though it is very likely that for short population times positive cross peaks in the GSA region, as drawn in Fig. 5.5(b), would be concealed by the much stronger GSB signals, such a reaction path seems highly unlikely on the basis of the 2D spectra for longer population times where no positive off-diagonal contributions are detected in the GSA region. Thus, our measurements unambiguously prove that the two isomers are not interconvertible via a conical intersection connecting the excited state of one isomer with the electronic ground state of the other isomer, as was found in a very recent theoretical study by Kobayashi and Amos [260].

Hence, *cis–trans* isomerization can be excluded as a dominant reaction path and the most likely scenario for the MC form of 6,8-dinitro BIPS after S_1 excitation is the one of Fig. 5.5(a) without any TTC↔TTT isomerization. Therefore, we can conclude that the second nitro group at position 8 drastically affects the photochemical properties of this BIPS compound since for 6-nitro BIPS the unidirectional TTC→TTT isomerization reaction was identified in Chap. 4 with a quantum yield of 18 % in acetonitrile and calculations (Sect. 4.6) predicted a very low excited-state barrier of about 0.1 eV or even lower when solvent effects are taken into account. However, for 6,8-dinitro BIPS, it seems that after S_1 excitation the ring-closure reaction, which is reflected by the two negative diagonal contributions for longer population times (signals 4 and 5), is dominant with a quantum yield of about 40 %, which is most likely too efficient for any competing photochemical reaction channel.

All in all, the results of the coherent 2D studies on the merocyanine isomers of 6,8-dinitro BIPS in chloroform can be summarized as illustrated in Fig. 5.7. After S_1 excitation, both isomers undergo the ring-closure reaction within 6 ps after excitation with a quantum yield of 35–40 %, presumably via a conical intersection. Most MC molecules relax back to their ground state via fluorescence within 95 ps (TTC) and 900 ps (TTT). Our data clearly proves that neither excited-state isomerization nor isomerization during relaxation to the ground state are dominant reaction channels for the ring-open merocyanine of 6,8-dinitro BIPS (red crosses). Besides, these results are also of significance for potential future applications of this compound, for example as a molecular “bit” or in optical data storage, where the isomerization process would be an undesirable loss channel lowering the efficiency of such devices.

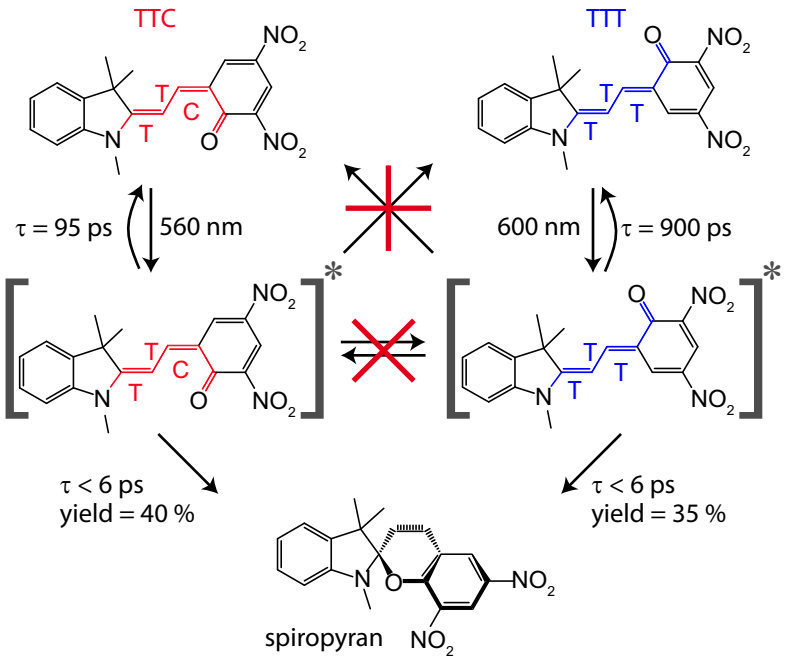

Figure 5.7 | Reaction scheme of 6,8-dinitro BIPS in chloroform as deduced from the 2D measurements. Both MC isomers of 6,8-dinitro BIPS are excited in the visible spectral range and undergo the ring-closure reaction to the spiropyran form with a quantum yield of 35-40 %. On the basis of our studies both *cis–trans* isomerization in the excited state as well as during relaxation to the ground state can be excluded (red crosses). Figure adapted from Ref. [8]. © (2011) by the American Chemical Society.

5.4 Pump–Repump–Probe Spectroscopy

With the experiments discussed in the previous section the photochemical reaction paths of 6,8-dinitro BIPS after excitation to the first-excited electronic state were explored and photoisomerization between the two MC isomers was excluded for both species. However, the role of higher-lying electronic states in the photochemistry of the molecule can not be elucidated with these third-order experiments since only processes initiated by optical S_0-S_1 transitions are probed there. Nonetheless, it seems plausible that further reaction channels might be revealed if the molecule is reexcited after a first excitation step to another higher-lying electronic state. By doing so additional energy is absorbed by the molecule which could lead to the formation of new reaction products, e.g., via photoisomerization or photodissociation, which are not observed after excitation to S_1.

5.4.1 Experimental Implementation

To realize this concept, we implement pump–repump–probe spectroscopy by employing an additional repump pulse, resonant to the excited-state absorption of 6,8-dinitro BIPS around 440 nm, which induces the S_1-S_n transition of already excited merocyanine molecules. The signal emerging of the reexcited molecules is thus based on a fifth-order non-linear light–matter interaction since the repump pulse ("R") creates the S_n popula-

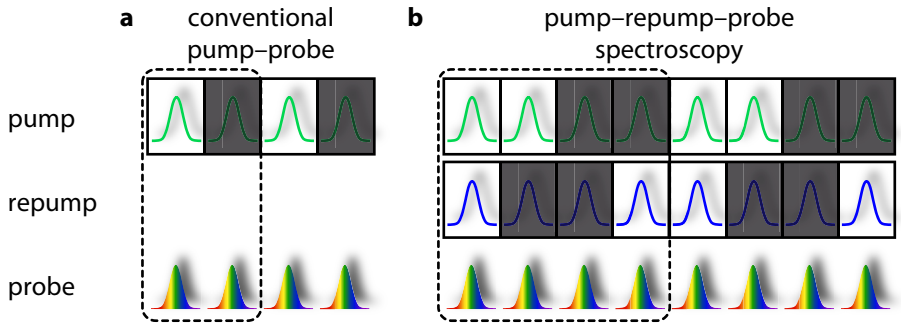

Figure 5.8 | Pulse chopping scheme for conventional pump–probe spectroscopy compared with the principle used for the pump–repump–probe approach. (a) In conventional pump–probe spectroscopy (e.g., in transient absorption) the pump pulse is chopped at half the repetition rate of the laser and the signal is received from the comparison of the probe signal with the preceding pump pulse with the signal without the pump (dashed rectangle). (b) In our pump–repump–probe approach, pump and repump pulses are chopped by a fourth of the repetition rate in addition to a $\pi/2$ phase shift between the two choppers. As a consequence, all four possible combinations of only pump or repump blocked, both pump together with the repump blocked, and none of the pulses blocked are achieved.

tion by interacting twice with molecules already excited to S_1 by two interactions with the pump pulse ("P"). The probe pulse ("Pr") finally gives rise to the fifth interaction with the sample.

For this experiment, the pump pulses were generated with the home-built NOPA centered at $\lambda_P = 590$ nm, which were characterized by the cFROG technique and compressed with the pulse shaper to a pulse duration of 17 fs. For the repump pulses, the commercially available NOPA was tuned to 870 nm of which the SHG signal at $\lambda_R = 435$ nm was used for pumping of the ESA transition.

Since both the conventional third-order transient absorption signal and the much weaker fifth-order repump-induced signal equally satisfy the phase-matching condition, a specific beam chopping arrangement is used in order to extract the background-free fifth-order signal. Two optical choppers are employed, one in the pump and one in the repump beam, operating at 250 Hz (1/4 of the laser's repetition rate) with a $\pi/2$ relative phase shift. The resulting chopping sequence is visualized in Fig. 5.8(b) and compared to the conventional pump–probe approach shown in Fig. 5.8(a). In conventional pump–probe spectroscopy the pump pulses are blocked at half the laser's repetition rate and the transient signal is gained by comparing the probe signal without a pump pulse with the signal in presence of the preceding pump (dashed rectangle). In contrast, in our pump–repump–probe approach, we block pump and repump pulses at 1/4 of the repetition rate of the laser and add a $\pi/2$ phase shift to one of the choppers corresponding to the time delay of one pulse. In this way, all four possible combinations of only pump or repump blocked, pump together with the repump blocked at the same time, and none of the pulses blocked, are obtained.

Similar to all previous time-resolved experiments, all measurements are performed with a multichannel shot-to-shot detection of the continuum probe. Accordingly, four different probe spectra are measured and three optical density changes relative to I_{Pr}

are evaluated:

$$\Delta OD_{\mathrm{PPr}} = -\lg \frac{I_{\mathrm{PPr}}}{I_{\mathrm{Pr}}}, \tag{5.1}$$

$$\Delta OD_{\mathrm{RPr}} = -\lg \frac{I_{\mathrm{RPr}}}{I_{\mathrm{Pr}}}, \tag{5.2}$$

$$\Delta OD_{\mathrm{PRPr}} = -\lg \frac{I_{\mathrm{PRPr}}}{I_{\mathrm{Pr}}}, \tag{5.3}$$

where subscripts denote the unblocked beams. In order to extract the isolated fifth-order signal the differential pump–repump–probe signal $\Delta OD_{\mathrm{diff}}$ is calculated by subtracting contributions from excitations with either only the pump (ΔOD_{PPr}) or the repump pulse (ΔOD_{RPr}) from the signal resulting from the combination of both pulses ($\Delta OD_{\mathrm{PRPr}}$):

$$\Delta OD_{\mathrm{diff}} = \Delta OD_{\mathrm{PRPr}} - \Delta OD_{\mathrm{PPr}} - \Delta OD_{\mathrm{RPr}}. \tag{5.4}$$

5.4.2 Pump–Repump–Probe Results

Figure 5.9 shows the spectrally resolved optical density change $\Delta OD_{\mathrm{diff}}$ as a function of pump–repump delay t_{PR} for a fixed pump–probe delay of $T = 2000$ ps. Positive signals (yellow/red) correspond to an increase, negative ones (blue/purple/black) to a decrease of the combined transient absorption signal.

The most prominent contribution occurs for $0 < t_{\mathrm{PR}} < 250$ ps as a strong negative signal around the probe wavelength of 559 nm. This corresponds to a repump-induced bleach of the merocyanine ground state, i.e., the merocyanine concentration after 2000 ps is additionally reduced by the pump–repump combination compared to the pump-only or repump-only experiments. Blue- and red-shifted to this bleach, two strong and spectrally broad positive signals are detected which indicate the formation of a new long-lived (since probed after 2 ns) product species. Thus, the combination of pump and repump not only leads to internal conversion from S_n states to S_1 from where processes like ring closure or fluorescence take place, but also to a new product.

For increased pump–repump delays these signals disappear, and a small signal offset (positive for $\lambda > 500$ nm, negative for $\lambda < 500$ nm) is evident for all wavelengths. This contribution has the same spectral shape as the pump–probe data after S_1 excitation but with opposite sign [236] and is due to the overestimation of molecules that can be excited from the ground state by the repump [although the absorption in Fig. 5.9(a) is close to zero at 440 nm]. This overestimation is caused by the fact that the preceding pump pulse decreases the concentration of merocyanine molecules remaining in the ground state. Thus, by subtracting ΔOD_{RPr}, which is received by exciting the entire merocyanine concentration, from $\Delta OD_{\mathrm{PRPr}}$, the repump-only signal is overcompensated leading to a transient signal with flipped sign. For $1750 < t_{\mathrm{PR}} < 2000$ ps, this inverted transient signal even increases with the repump approaching the probe pulse. Since the signal for repump-only increases due to merocyanine excited to S_1 that has not yet relaxed back to the ground state, the overcompensation increases, too. A similar argument holds for the signal observed for negative pump–repump delays $t_{\mathrm{PR}} < 0$ ps: In this case, the repump precedes all other pulses; thus the effective concentration is reduced for the subsequent

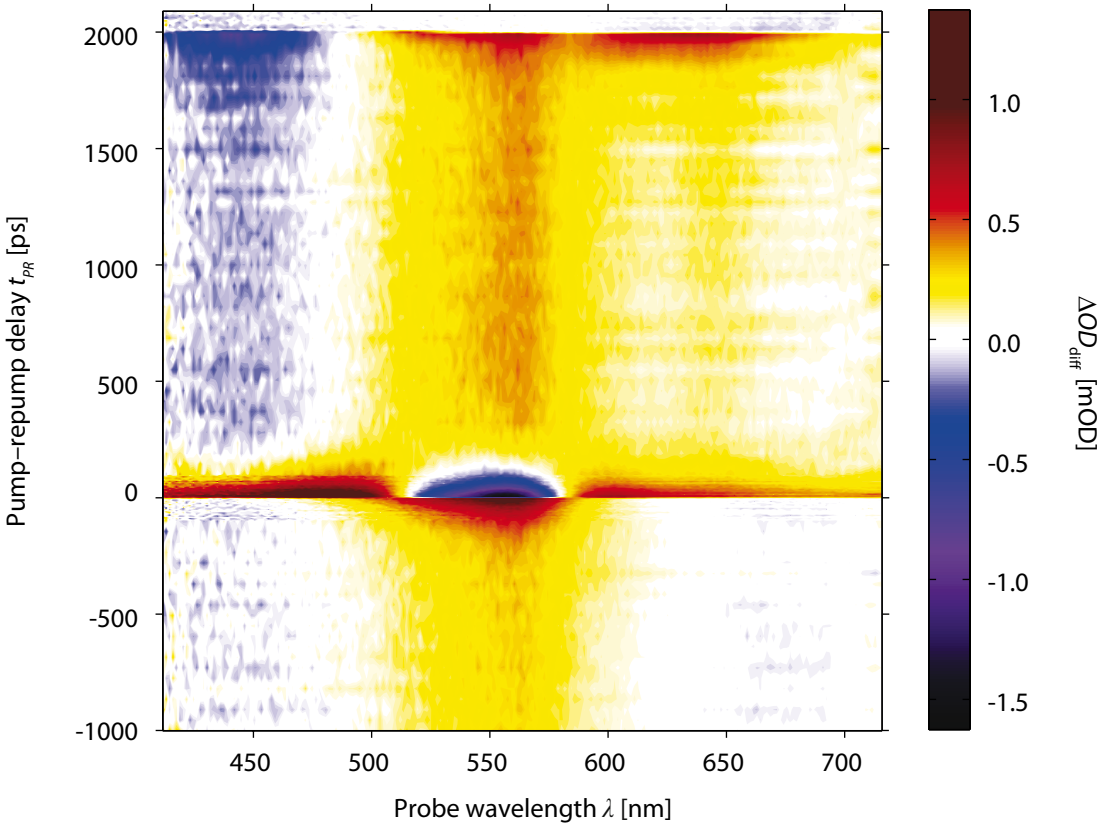

Figure 5.9 | Pump–repump–probe measurement of 6,8-dinitro BIPS in chloroform. The data reflects the spectrally resolved repump-induced change of absorbance $\Delta OD_{\mathrm{diff}}$ as a function of pump–repump delay t_{PR} and probe wavelength λ for a fixed probe delay $T = 2000$ ps. The pump pulses are resonant to the S_0-S_1 excitation and centered at $\lambda_{\mathrm{P}} = 590$ nm while the repump induces the S_1-S_n transition of the ESA at $\lambda_{\mathrm{R}} = 435$ nm. Figure adapted from Ref. [5]. © (2013) by the American Physical Society.

pump pulse. For delays $t_{\mathrm{PR}} > T = 2000$ ps the entire signal vanishes because the repump interacts after the probe and hence no repump-induced signal can be observed.

Figure 5.10(a) shows the data from Fig. 5.9 for three selected wavelengths together with a global exponential fit for pump–repump delays between 0 ps and 500 ps (black dashed line). The fit yields a global decay time of 80 ps for the so far unidentified repump induced product which agrees with the S_1 lifetime of the merocyanine [236]. This evidences that the observed pathway via higher-lying electronic states leading to the product formation is accessible from the S_1 state only. In Fig. 5.10(b) cuts through the same data along the λ-axis are plotted for $t_{\mathrm{PR}} = 30$ ps, 500 ps, and 2020 ps, illustrating the spectral characteristics of the photoproduct with absorption bands around 600 nm and 470 nm (orange squares). For t_{PR} larger than the S_1 lifetime, this signal is no longer detected (purple circles), and for $t_{\mathrm{PR}} > T = 2000$ ps no signal is observed any more (white triangles).

Given the fact that in our case a mixture of molecular isomers, each possessing a multitude of electronic states, is investigated, the nature and the precursor state of the new species has yet to be identified. Both isomers possess an ESA around 440 nm

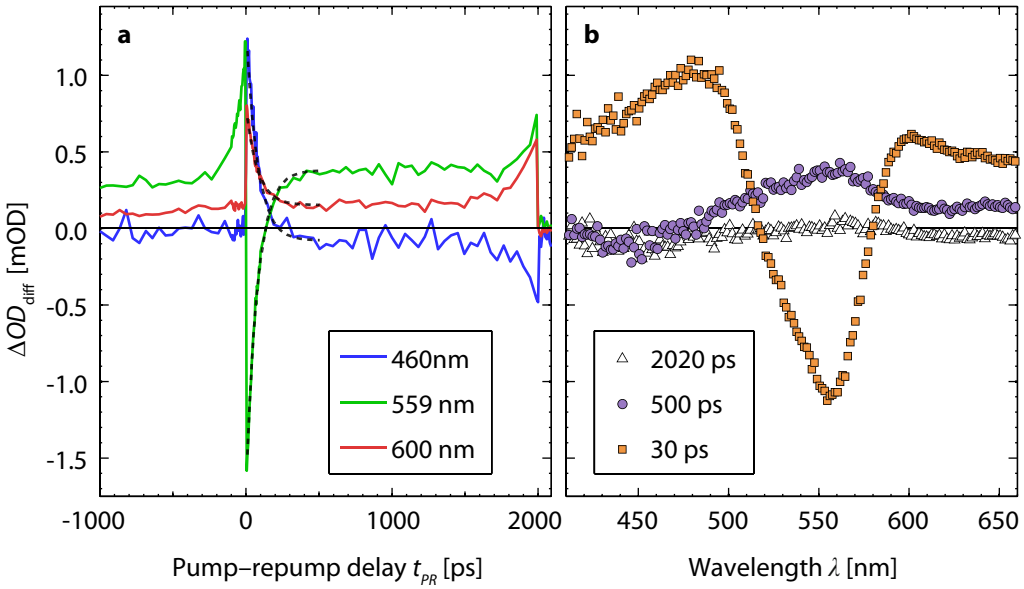

Figure 5.10 | Slices through the pump–repump–probe data map of Fig. 5.9. (a) $\Delta OD_{\mathrm{diff}}$ for selected wavelengths with a global fit (black) revealing a decay time of 80 ps; (b) $\Delta OD_{\mathrm{diff}}$ for selected pump-repump delays t_{PR}. The absorption of the new product is evident from the curve for t_{PR}=30 ps (orange squares). Figure adapted from Ref. [5]. © (2013) by the American Physical Society.

through which higher-lying electronic states are accessible by the repump. The time constant of 80 ps already suggests that TTC might be the relevant isomer in this reaction, as its S_1 lifetime is 96 ps, in contrast to 910 ps for TTT. Nevertheless, for cases where the precursor state cannot be assigned by a characteristic lifetime, further insight is necessary. Electronic TE2D spectroscopy, which will be implemented in the next section, can provide this information by spreading the signal contributions along the pump-frequency axis.

5.5 Triggered-Exchange Two-Dimensional Electronic Spectroscopy

In this section, the common pump–repump–probe approach of the previous section is expanded by establishing coherent electronic TE2D spectroscopy in the visible regime for the investigation of higher-lying electronic states of our model system 6,8-dinitro BIPS. The TE2D technique allows us to correlate the spectral signatures of the reactant in the ground state with those of the photoproduct formed by the interaction with the additional repump pulse between the 2D sequence and the probe pulse. Hence, the observation of the unambiguous signature and the assignment of the corresponding reactive molecular precursor is permitted, which otherwise is not accessible.

For implementing electronic TE2D spectroscopy, the pump is split into a double pulse with the pulse shaper and ΔOD_{PPr}, ΔOD_{RPr}, and $\Delta OD_{\mathrm{PRPr}}$ [Eqs. (5.1)–(5.3)] are

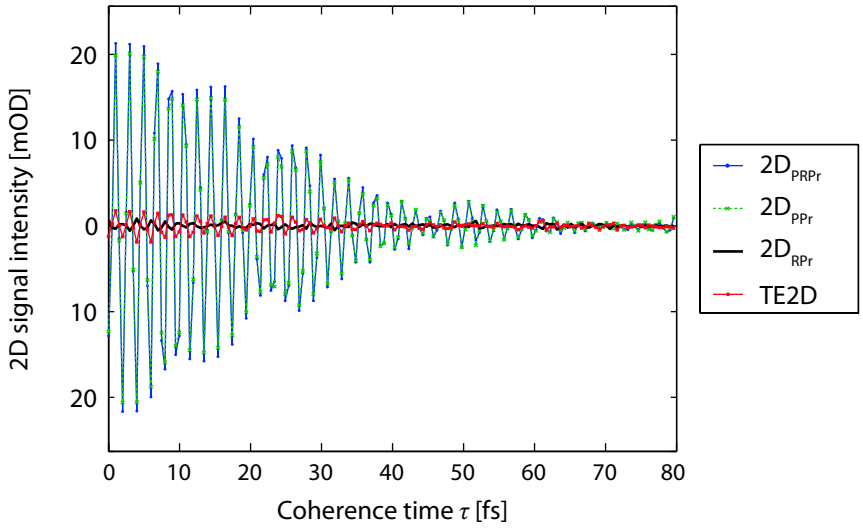

Figure 5.11 | Exemplary time-domain raw data of the electronic TE2D spectra of 6,8-dinitro BIPS as a function of coherence time τ for a probe wavelength of λ = 554 nm, t_{PR} = 500 fs, and T = 2000 ps. The TE2D data (red line) is extracted by subtracting the phase cycled pump-only (dashed green) and repump-only (solid black) from the pump–repump–probe signal (solid blue). Figure adapted from Ref. [6].

measured as a function of coherence time τ, thus generating three different 2D spectra for each waiting time T. The corresponding purely absorptive 2D spectra are obtained by taking the real part of the Fourier transform along τ. A four-step phase cycling scheme allows the retrieval of 2D signals while pump-induced scatter is efficiently reduced (compare Sect. 4.4.2). In this way, the desired fifth-order 2D signal $\Delta OD_{\mathrm{diff}}(\tau,T,t_{\mathrm{PR}})$ is extracted using a combination of pulse chopping and phase cycling.

Figure 5.11 exemplarily shows the phase-cycled TE2D time-domain raw data at a probe wavelength of λ_{Pr} = 554 nm as a function of coherence time τ at fixed pump–repump delay t_{PR} = 500 fs and for a waiting time of T = 2000 ps. We obtain three different signal contributions by analogy with the pump–repump–probe measurements: the 2D data $2\mathrm{D}_{\mathrm{PRPr}}$ corresponding to the case in which the pump pulse pair interacts with the sample together with the repump pulse (solid blue line), the case in which the repump is blocked and only the pump pulse pair excites the sample (dashed green line) corresponding to the conventional 2D signal $2\mathrm{D}_{\mathrm{PPr}}$, and the signal $2\mathrm{D}_{\mathrm{RPr}}$ for the situation where the pump pulses are blocked and only the repump irradiates the sample (solid black). By subtracting the latter two phase-cycled curves from the first one, the isolated fifth-order TE2D data (red), corresponding to the interaction with all four pulses, is extracted. Regarding its small signal magnitude, it becomes obvious that the desired signal is covered by much stronger third-order contributions of those molecules that have been excited to S_1 and not been repumped to higher-lying states.

A TE2D spectrum was measured for t_{PR} = 500 fs and T = 2000 ps and extracted as shown in Figs. 5.12(a)-(d). In all spectra vertical red (TTC) and blue (TTT) dashed lines indicate the spectral maximum of the overlap of the pump spectrum and the corresponding isomer absorption spectrum. The expected positions of ESA, GSB, and SE of

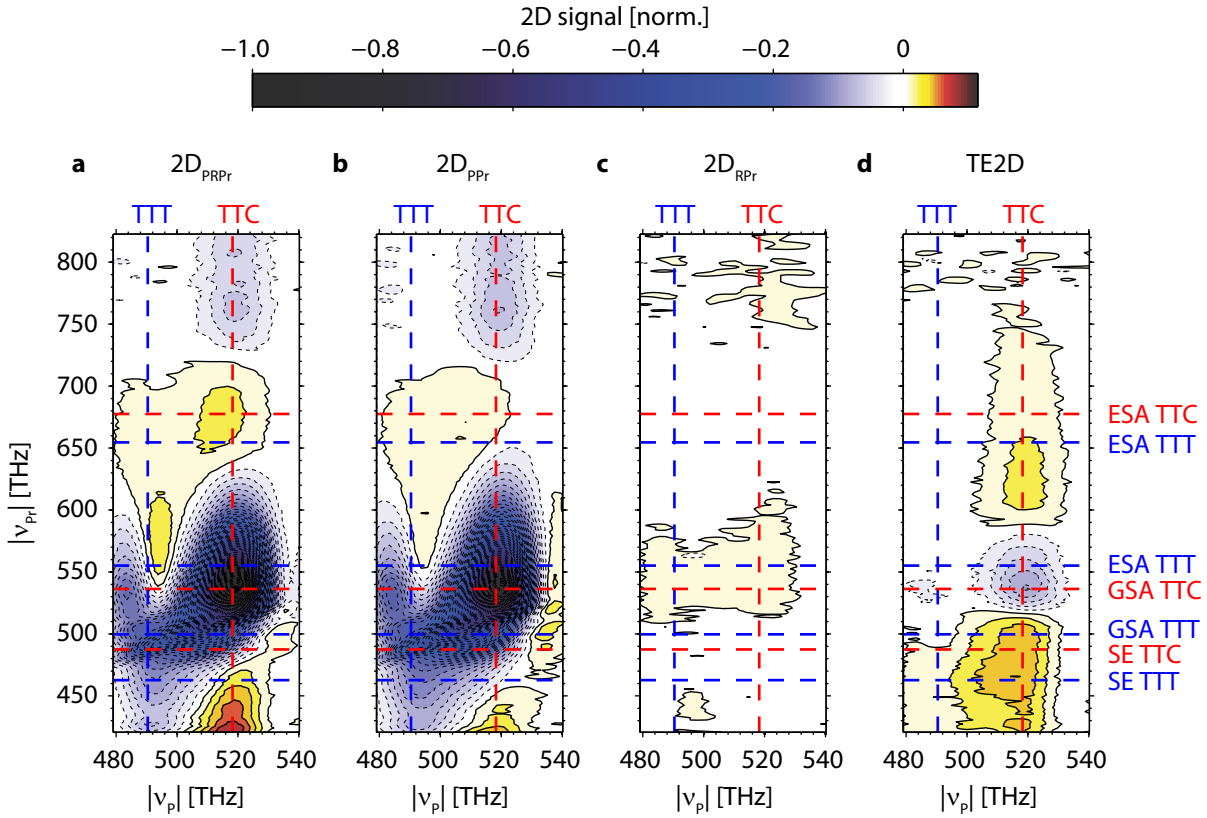

Figure 5.12 | Electronic TE2D spectrum of 6,8-dinitro BIPS. The TE2D signal extraction is demonstrated for $t_{PR} = 0.5$ ps and $T = 2000$ ps. (a) From the $2D_{PRPr}$ data with both pump and repump interacting with the sample, (b) $2D_{PPr}$ and (c) $2D_{RPr}$ are subtracted, yielding (d) the isolated electronic TE2D spectrum. Figure adapted from Ref. [5]. © (2013) by the American Physical Society.

molecules in S_1 are marked with horizontal red (TTC) and blue (TTT) dashed lines. The sign convention is the same as in Fig. 5.9(b), thus positive amplitudes (yellow/red) correspond to an increase of absorption whereas negative ones (blue/purple/black) indicate a decreased absorption.

Figure 5.12(a) shows the $2D_{PRPr}$ spectrum collected in presence of pump and repump pulses. The $2D_{PPr}$ spectrum [Fig. 5.12(b)], obtained by blocking the repump, only exhibits slight differences. No 2D signal (apart from low amplitude noise) is observed when the pump pulse pair is blocked, yielding the $2D_{RPr}$ spectrum [Fig. 5.12(c)]. By subtracting $2D_{PPr}$ and $2D_{RPr}$ from $2D_{PRPr}$ [Eq. (5.4)], the TE2D spectrum is extracted [Fig. 5.12(d)]. This spectrum can be considered as the change in the conventional absorptive 2D electronic spectrum due to the interaction of excited molecules with the repump pulse. Thus, it directly visualizes the correlations between the spectral signatures of the precursor molecule and the response of the repump-induced photoproduct.

The $2D_{PRPr}$ and the $2D_{PPr}$ spectrum are dominated by third-order signals occurring after excitation to S_1 [8]. In essence, distinguishable ESAs, as well as GSB and SE are observed for both isomers, very similar to the 2D spectra discussed in Sect. 5.3. But only the TE2D spectrum visualizes the segregated fifth-order contributions arising from

higher-lying states. It exhibits a distinct GSB located around $|\nu_{\mathrm{Pr}}|$ = 520 - 570 THz, while positive contributions are observed red- and blue-shifted from the bleach between $|\nu_{\mathrm{Pr}}|$ = 400 - 520 THz and 590 - 750 THz. These spectral signatures correspond to those also discussed for the pump–repump–probe data in the previous section [see signal at 30 ps in Fig. 5.10(b)]. With the additional frequency axis in the TE2D spectrum, the S_1-state of the TTC isomer can now nonambiguously be identified as the precursor state of the photoproduct, because all signals are located on the vertical red dashed line corresponding to the excitation of TTC from the ground state.

The negative signal is assigned to TTC GSB, whereas the positive contribution in the TE2D spectrum [Fig. 5.12(d)] and the 30 ps pump–repump difference spectrum [orange squares in Fig. 5.10(b)] evidence a photophysical process: The merocyanine is ionized as a response to the high energetic excitation of roughly 5 eV in total, and an electron is released to the solvent. This electron is not solvated but reacts with chloroform in a dissociative process which does not give rise to any absorption signals in the visible [328]. Hence, the new absorption bands originate from the merocyanine radical cation $MC^{\bullet+}$. In the literature, the characteristic new absorption bands of such a radical cation at the high- and low-energy sides of the GSB have been reported for other merocyanine dyes [329]. The repump pulse thus generates a radical cation $MC^{\bullet+}$ of the merocyanine from excited TTC isomers. The TE2D spectrum can clearly identify this precursor isomer and directly visualizes the interesting finding that the cation $MC^{\bullet+}$ is only formed for one of the isomers (TTC) present in solution.

Other potential photoproducts can be ruled out as discussed in the following. First, an increase of the ring-closure quantum efficiency can be excluded as the origin for the observed signatures, as spiropyran only absorbs in the UV spectral range and therefore would only explain the increased GSB but not the positive product bands in the visible. Second, other merocyanine isomers might be formed just as for 6-nitro BIPS (Chap. 4), but a blue-shifted photostable isomer for 6,8-dinitro BIPS was never observed in the literature and also does not seem plausible from a thermodynamic point of view. Third, while after S_1 excitation only SE and ring closure are directly observed, the repump pulse could enable intersystem crossing from a higher-lying state. However, no participation of triplet states was observed for 6,8-dinitro BIPS and also for other merocyanines [329].

5.6 Reaction Scheme

On the basis of the pump–repump–probe experiments in combination with electronic TE2D spectroscopy direct insight into the photodynamics of 6,8-dinitro BIPS induced after excitation to higher-lying electronic states is obtained. The reaction scheme shown in Fig. 5.13 summarizes the results of the measurements presented in Sects. 5.4 and 5.5 in a schematic and simplified picture. The two merocyanine isomers are located on two separated minima of the ground state potential S_0 of the ring-open configuration. After S_1 excitation both isomers either undergo an ultrafast ring-closure reaction to the spiropyran form SP via a conical intersection or relax back to their electronic ground states via fluorescence or – in addition to this – possibly radiationless through another conical intersection [236, 259]. After reexcitation of the excited-state population by

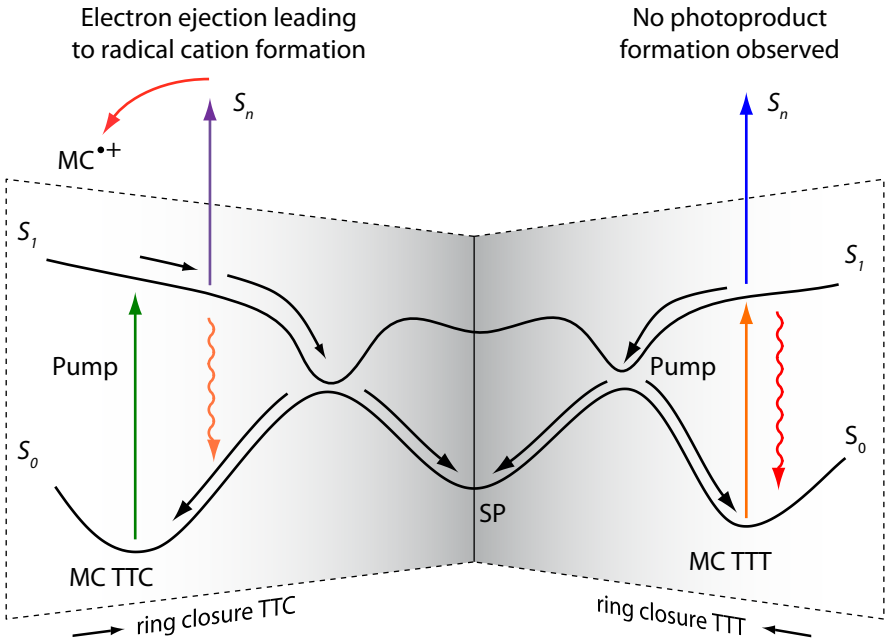

Figure 5.13 | Pump–repump reaction scheme for the two merocyanine isomers TTC and TTT. Both isomers undergo the ring closure reaction to the spiropyran form (SP) after S_1-excitation. By repumping to higher-lying states the radical cation $MC^{\bullet+}$ with a broad absorption band in the visible is formed from the TTC isomer, whereas no long-living species is observed after repumping of the TTT isomer.

pumping the excited-state absorption triggering an $S_1 \rightarrow S_n$ transition, an electron is ejected into the solvent and the radical cation $MC^{\bullet+}$ is formed only from the TTC isomer, whereas no additional photoproduct formation is observed for the TTT isomer.

5.7 Conclusion

In this chapter, novel third- and fifth-order nonlinear time-resolved spectroscopy techniques were implemented that allow the investigation of photophysical and photochemical reaction paths that would be inaccessible by conventional femtosecond time-resolved techniques.

In Sect. 5.3, third-order coherent 2D electronic spectroscopy was used to investigate the photodynamics of the merocyanine form of the molecular switch 6,8-dinitro BIPS after S_1 excitation in more detail as it would be possible with transient absorption spectroscopy. Without any further data modelling, the detected 2D spectra directly visualized the photochemical connectivity between the two merocyanine isomers and unambiguously proved that the *cis–trans* isomerization reaction between the two merocyanine isomers can be ruled out as a dominant reaction path. Thus, no undesired photochemical loss channels competing with the ring-closure reaction exist, which is a very valuable piece of information regarding potential future application of this compound.

In order to explore the role of higher-lying electronic states in the photochemistry of

6,8-dinitro BIPS, pump–repump–probe spectroscopy was implemented in Sect. 5.4. The formation of a so far unobserved long-living new photoproduct, later identified as the merocyanine radical cation $MC^{\bullet+}$, was detected upon S_1-S_n reexcitation.

Finally, the technique of fifth-order TE2D spectroscopy was established for the first time for electronic transitions in Sect. 5.5. Electronic TE2D spectroscopy offers a highly sensitive tool which enables access to the photochemistry within electronically excited states. On the basis of the collected TE2D spectra, it is unequivocally disclosed that the S_1-state of the TTC isomer is the precursor for the radical cation $MC^{\bullet+}$, whereas this reaction path is not involved in the excited-state photochemistry of the TTT isomer. This study demonstrates that fifth-order electronic TE2D spectroscopy is a promising method for the analysis of excited states and associated reaction pathways, with the information from where the reaction started intrinsically preserved.

6 Polarization Pulse Shaping in the von Neumann Formalism for Arbitrary-Order Nonlinearities

In the previous chapters of this thesis it was demonstrated experimentally that third- and fifth-order non-linear optical spectroscopy techniques are capable of providing detailed information about photochemical processes of excited molecular electronic states. What these techniques have in common is that all electronic states located within the broad laser bandwidth may contribute to the resulting signal. As a consequence, this may lead to a conglomeration of various kinds of spectroscopic signatures in which the desired parts of information are veiled by other dominating signals. It was further shown that two- and three-dimensional electronic spectroscopy, making use of phase-cycling and specific pulse chopping configurations, can be used to eliminate some of these drawbacks by spreading the information along several frequency dimensions (Chap. 4) and in addition by extracting exclusively the desired order of optical nonlinearity (Chap. 5). Still, the vectorial character of the laser pulses as well as their spectral profile has been neglected as important control knobs for achieving an improved signal selectivity. For this reason, the so-called von Neumann representation of shaped femtosecond laser pulses is generalized to the description of time-dependent polarization profiles in this chapter. This can have direct implications in multidimensional spectroscopy and quantum-control techniques. The introduced formalism provides a profound basis for exploiting light–matter interactions of almost arbitrary order in polarization-sensitive ultrafast experiments.

A brief motivation for the presented approach is given in Sect. 6.1. Then, the conventional von Neumann representation for linearly polarized laser pulses is reviewed in Sect. 6.2, and the formalism for describing the polarization state in the von Neumann picture is introduced in Sect. 6.3. In Sect. 6.4, two example pulse sequences are discussed. The subject of accuracy of the forward and backward transformations is treated in Sect. 6.5. Finally, an interpretation of the introduced joint time–frequency parameters in time domain is given in Sect. 6.6.

Parts of Sects. 6.1 and 6.3–6.7 of this chapter have been published in Ref. [7][1], (see table on p. v).

[1]Reproduced and adapted with permission from Applied Physics B: Lasers and Optics **107**, 1–9 (2012).

6.1 Motivation

The von Neumann representation (see Sect. 6.2 for details) is a joint time–frequency description of shaped femtosecond laser pulses established by our research group in the field of coherent control [68–70, 330–333]. This formalism allows the description and visualization of the spectro-temporal evolution of linearly polarized laser pulses in time–frequency phase space. Since in many scenarios not only the proper temporal spacing between different subpulses but also the correct frequencies have to be applied in order to achieve the desired transitions, the most effective way to generate the optimal pulse sequence is to define the pulse directly in such a mixed time–frequency representation.

The von Neumann picture has been applied for measuring molecular quantum control landscapes of a fluorescing dye [11] and has also been successfully implemented into an evolutionary algorithm in order to carry out adaptive coherent control experiments [9]. In this chapter the von Neumann basis is extended to the representation of the time-varying polarization state [7, 334] in time–frequency phase-space which may open up new applications in higher-order multidimensional spectroscopy and quantum control using femtosecond polarization pulse shaping as is discussed below.

Femtosecond pulse shaping (see Sect. 3.2) has become a very useful tool for many different time-resolved spectroscopy techniques [57, 59, 210, 213, 216–218, 335–337] and also in the field of quantum control [338–341]. In addition to amplitude and phase shaping of linearly polarized light, polarization shaping makes the modification of both the ellipticity and the elliptical orientation within a single laser pulse possible [88, 89, 342–348]. This can be exploited for systems that are pre-oriented with respect to the laser field. But polarization is also relevant for ensembles of randomly oriented systems, as molecules or aggregates in solution or in the gas phase. In that case, the laser field itself could either be used to actively align the molecules [134, 136, 137], or to select a sub-ensemble of specific alignment on the basis of the first interaction on which further excitations will act.

In all cases of ultrafast spectroscopy or quantum control, not only the phase and amplitude of the driving field but also the time-dependent vectorial character might be relevant and can be exploited. This was demonstrated with CARS spectroscopy in the liquid phase [349, 350], two-photon absorption [351], diatomic molecules in the gas phase [352–354], and also in optical near-field control [355, 356]. Moreover, the advantage of polarization control also in multidimensional spectroscopy has first been utilized in 2DIR spectroscopy [357–360] and has later also been applied in electronic 2D experiments [361].

Various experimental arrangements that are able to alter the polarization state of femtosecond laser pulses were introduced in recent years, involving $4f$ setups and two or more liquid-crystal displays (LCD) [88, 89, 342–347] or acousto-optic modulators [348].

As was described in Sect. 2.1.3 different types of mathematical description for polarization-shaped laser pulses exist. The Fourier representation in frequency and time domain contains all necessary information if amplitude and phase are given for two polarization directions. However, that does not instantaneously reveal the polarization state. The solution lies in a basis transformation to time-dependent "elliptical laser pulse parameters" consisting of polarization ellipticity ϵ, orientation angle θ of the elliptical

principal axis, total intensity I, and total phase φ [see Eqs. (2.49)–(2.51)], which can be plotted in three-dimensional graphs illustrating the temporal evolution [89]. Temporal trajectories of the polarization state in ellipticity-orientation phase space on the Poincaré sphere or in the Poincaré plane (see also Fig. 2.9) can also provide some insight [91].

Concerning the field of quantum control, the choice of pulse parameterization can have a fundamental influence on control performance, speed of convergency of the search algorithm, and on the interpretability of the experimental results in quantum control experiments [362], apart from the purely descriptive nature of pulse representations. Several different basis sets have been exploited in the literature for linearly polarized laser pulses. Typical examples are the "LCD pixel basis" [363], polynomial spectral phase functions [364–367] or sinusoidal phase patterns [59, 60, 335, 368, 369] which all have been successfully applied to many different kinds of experiments. If polarization-shaped laser pulses are considered, these basis sets can, of course, still be employed by applying the modulation functions to two independent polarization directions. However, in most of these cases the resulting polarization states are not accessible immediately. Hence, descriptions which are directly based on the polarization state may be useful. Weise *et al.*, for example, used a parameter set consisting of intensity, position in time, relative phase, chirp, and polarization state to produce polarization-shaped pulse sequences [370].

As shown in Fig. 6.1(a), a formalism which provides the description of the polarization state of a shaped femtosecond laser pulse in the joint–time frequency domain could help to achieve enhanced signal selectivity in multidimensional spectroscopy. In conventional coherent 2D spectroscopy (top, left) typically four broadband laser pulses with the same center frequency and the same linear polarization state (red arrows) are used, separated by τ, T, and t. Since all energy levels of the system within the laser bandwidth may contribute to the detected 2D spectrum (bottom, left), a straight forward data interpretation may be impossible due to an accumulation of many different diagonal and cross peaks. Using a femtosecond pulse shaper in combination with the von Neumann representation, the spectral and temporal location of all subpulses of the pulse sequence can be manipulated independently (top, center), which allows an enhanced spectral selectivity in the 2D data (bottom, center). It was shown that the modification of the polarization state of the employed pulses can be used to suppress certain contributions such as the diagonal peaks [357–361], for example by using a polarization scheme with orientation angles of $\theta = (+60°,-60°,0°,0°)$. In this way, by adding the polarization of the laser pulses as another degree of freedom (top, right), cross peaks may be isolated which are hidden in the conventional 2D spectrum (bottom, right). Consequently, a formalism capable of independent spectro-temporal *and* polarization control in time–frequency phase-space would allow the implementation of cross-peak sensitive multidimensional spectroscopy with enhanced signal selectivity. In addition, using the von Neumann representation an arbitrary number of additional subpulses may be added to the pulse sequence to realize higher-order types of multidimensional spectroscopy such as fifth-order three-dimensional, transient 2D, or triggered-exchange 2D spectroscopy in which all additional pulses can be adjusted independently to match the experimental requirements.

Figure 6.1(b) illustrates potential applications of polarization pulse shaping in von Neumann phase space for coherent control experiments with the help of two examples.

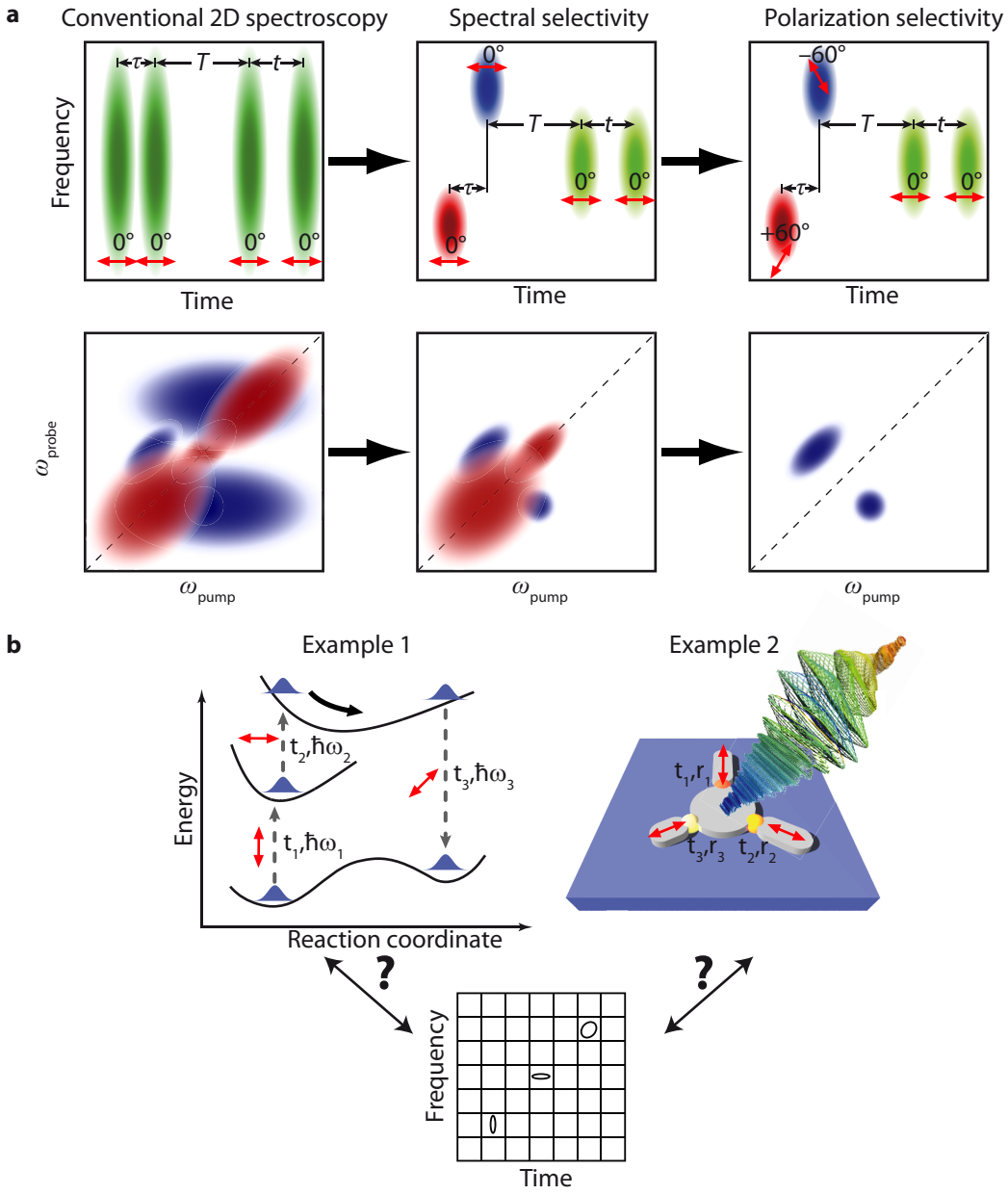

Figure 6.1 | Possible applications of the formalism described in this chapter motivating the ability to describe polarization-shaped pulses in the von Neumann picture. (a) Enhanced selectivity in multidimensional spectroscopy; While in conventional 2D spectroscopy (left) multiple contributions add up to the 2D spectrum spectral selectivity allows the extraction of desired quantum paths. With additional independent control over the polarization state off-diagonal peaks could be isolated. (b) Applications in coherent control; Example 1: A series of subpulses is employed to drive a molecular system from one minimum to another minimum of a double-well potential via a pump–repump–dump sequence. Therefore, different excitation energies at different times and specific polarization states are required. Example 2: A shaped laser pulse is used to control optical near fields in the gap between the central disc and the attached antennas in a plasmonic nanostructure such that at different times different polarization states and excitation frequencies of the driving field are necessary. Figure (b) adapted from Ref. [7].

If a mechanistic and intuitive approach to coherent control is desired, the parameterization may be chosen in such a way that it optimally fits the characteristics of the investigated system. In Example 1, a shaped femtosecond laser pulse could be used to control a molecular transition from the global minimum of a double-well potential to another minimum via a pump–repump–dump sequence. Depending on the Franck–Condon windows this requires well defined subpulse frequencies ω_1, ω_2, and ω_3 at interaction times t_1, t_2, and t_3, respectively. Moreover, the transition probability might be polarization sensitive depending on the symmetry of the problem. In this fictitious example, possible preferential directions of the subpulse polarization are indicated by red double arrows similar to Fig. 6.1(a). In Example 2, polarization-shaped laser pulses are used to control the electromagnetic near field in the gaps at positions r_1, r_2, and r_3 of a plasmonic nanostructure. Assuming that the goal is to achieve an enhancement of the near fields at times t_1, t_2, and t_3, respectively, then the optimal external driving field will consist of a series of pulses with specific temporal subpulse intervals, frequencies and polarization states, as the spatial dimensions (mainly the length) and orientation determine the resonance frequency and the optimal excitation pulse polarization for each individual antenna.

These examples demonstrate why it would be helpful to have available a parameterization in which polarization-shaped laser pulses are defined in a joint time–frequency picture. This chapter provides such a description based on the von Neumann formalism [9, 11, 68–70] but generalized to the case of polarization-shaped laser pulses. It is shown that this formalism can be used to define the polarization ellipticity, the orientation angle, the phase, and the intensity as a function of time *and* frequency simultaneously. It can also be used to represent and analyze general polarization-shaped laser pulses.

6.2 The von Neumann Representation for Linearly Polarized Pulses

Each of the joint time–frequency distributions discussed in Sect. 2.1.2 has its own advantages and is frequently used in the field of femtosecond laser pulses for visualization purposes. However, the fact that they are not analytically invertible (Husimi), that they can not be interpreted in terms of a probability distribution (Wigner), and – most important – that they all contain an enormous amount of redundant information makes it impossible to use them for defining a particular pulse shape. Furthermore, both the Husimi and the Wigner representation contain a high amount of redundant information as a discrete signal defined at N sampling points in time or frequency domain will be mapped on N^2 points in the joint time–frequency domain. As will be shown below, the von Neumann representation circumvents this generation of redundant information. The von Neumann description is closely related to the Husimi representation since it uses the same basis. But in contrast to the continuous basis used in the Husimi distribution, only a subset of coherent states is used for the expansion of the electric field. These basis functions are complex-valued Gaussian functions, centered at fixed coordinates (ω_n,t_m)

in phase space. They can be defined either in frequency domain via

$$\alpha_{\omega_n t_m}(\omega) = \left(\frac{2\alpha}{\pi}\right)^{1/4} \mathrm{e}^{-\alpha(\omega-\omega_n)^2 - \mathrm{i}t_m(\omega-\omega_n)} \tag{6.1}$$

or in time domain:

$$\tilde{\alpha}_{\omega_n t_m}(t) = \left(\frac{1}{2\alpha\pi}\right)^{1/4} \mathrm{e}^{-\frac{1}{4\alpha}(t-t_m)^2 + \mathrm{i}\omega_n t_m}. \tag{6.2}$$

The prefactors are necessary for normalization and the parameter α defines the ratio of the temporal and the spectral FWHM of the basis functions. As mentioned in Sect. 2.1.2, a discrete subset of coherent states can be chosen in such a way that this particular subspace still remains a complete basis set. In 1931 the Austro-Hungarian mathematician John von Neumann introduced such a discrete basis set – the *von Neumann basis* – of which each basis function covers a phase space volume of $V = \Delta\omega \cdot \Delta t = 2\pi$ [371]. The completeness of this basis was not proven until 1971 and it was shown that it is overcomplete by exactly one state [85, 372, 373].

Assuming a phase space that is extending to infinity, the number of states in the von Neumann basis will also be infinity. However, in practice only a limited area of phase space is accessible which in our case is determined by the time and frequency range T and Ω of the pulse shaper, which samples the laser pulse at N points in either domain. The frequency range covered by the pulse shaper then ranges from ω_{min} to $\omega_{max} = \omega_{min} + \Omega$. Consequently, the frequency spacing is given by $\delta\omega = \Omega/N$ and according to the properties of the discrete Fourier transform the temporal window is $T = 2\pi/\delta\omega$. Hence, the temporal spacing between the sampling points is $\delta t = T/N$ and $\Omega = 2\pi/\delta t$. The overall phase-space volume is thus given by

$$V_{ges} = \Omega \cdot T = \frac{2\pi}{\delta t} T = 2\pi N. \tag{6.3}$$

With this smallest possible basis set it is possible to transform a signal which is sampled at N points in pure time- or frequency domain also at N points in the joint time–frequency domain. Thus the von Neumann representation contains exactly the same amount of sampling points in time–frequency phase space as in time or frequency domain, as illustrated in Fig. 6.2. In experiments, the amount of sampling points N would be chosen such that it coincides with the number of sampling points given, e.g., by the amount of pixels of the pulse shaper.

As mentioned above, the parameter α determines the ratio of the spectral and temporal FWHMs σ_ω and σ_t of the basis functions. From Eqs. (6.1) and (6.2) it follows that

$$\sigma_\omega = \sqrt{\frac{4\ln 2}{\alpha}} \tag{6.4}$$

and

$$\sigma_t = \sqrt{16\alpha \ln 2}, \tag{6.5}$$

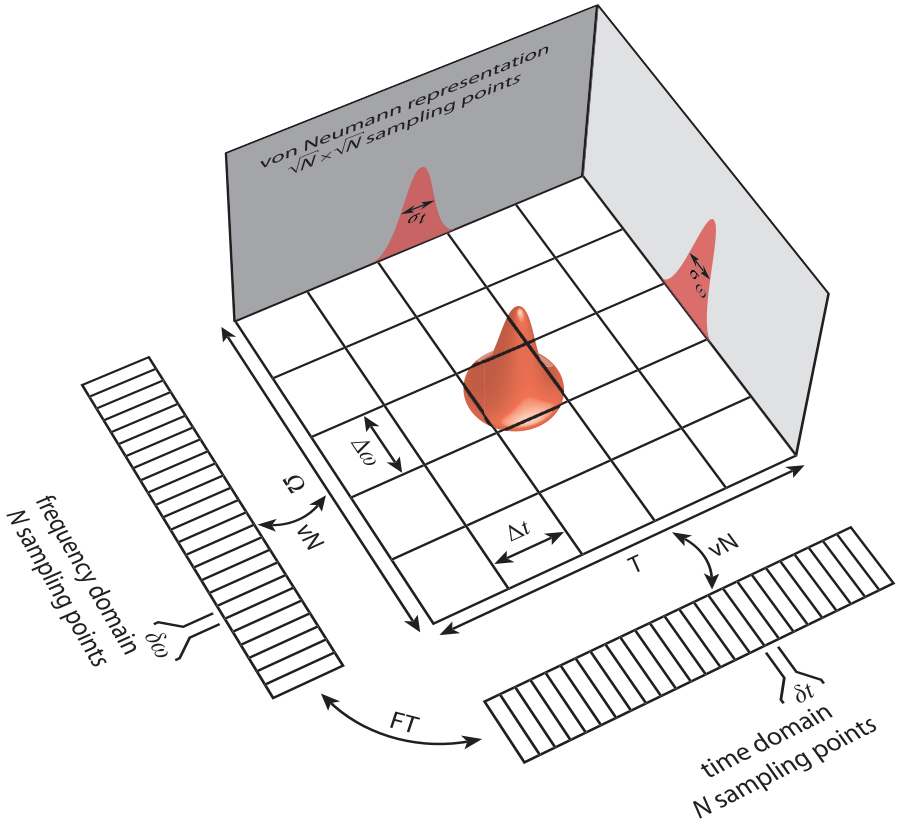

Figure 6.2 | Visualization of the von Neumann plane and associated parameters. In practice, a laser pulse is given by N discrete sampling points either in time or in frequency domain, which are connected via the discrete Fourier transform (FT). In von Neumann phase space, the signal is projected onto a two-dimensional $\sqrt{N} \times \sqrt{N}$ time–frequency plane using Gaussian basis functions (assuming a square lattice). Thus, the information content of the signal is conserved completely since the same number of sampling points is used in both domains.

which results in

$$\alpha = \frac{\sigma_t}{2\sigma_\omega}, \tag{6.6}$$

Assuming a square lattice, i.e., the same number of grid points along the $\omega-$ and $t-$axis, we obtain

$$\alpha = \frac{T}{2\Omega} = \frac{\pi N}{\Omega^2}. \tag{6.7}$$

With above equations the von Neumann basis set is now consistently defined. In the following the transformation between the spectral or temporal domain to the von Neumann space is derived.

For that purpose, the completeness relationship

$$\mathbb{1} = \sum_{(n,m)(i,j)} |\alpha_{\omega_n t_m}\rangle S^{-1}_{(n,m)(i,j)} \langle \alpha_{\omega_i t_j}| \tag{6.8}$$

is required, stating that the von Neumann basis is a set of complete but not orthogonal functions. In Eq. (6.8), $S_{(n,m)(i,j)}$ is the overlap matrix of the basis set. The element $[(n,m)(i,j)]$ of this matrix describes the overlap of the basis function at the phase-space coordinate (ω_n, t_m) with the basis function at the position (ω_i, t_j) which can be calculated using the dot product

$$S_{(n,m)(i,j)} = \langle \alpha_{\omega_n t_m} | \alpha_{\omega_i t_j} \rangle = \int \alpha^*_{\omega_n t_m}(\omega) \alpha_{\omega_i t_j}(\omega) \mathrm{d}\omega. \tag{6.9}$$

An analytical expression for the overlap matrix was found for the case of an infinite von Neumann plane given by

$$S_{(n,m)(i,j)} = (-1)^{(i-n)(j+m-N-1)} \mathrm{e}^{-\frac{\pi}{2}[(i-n)^2+(j-m)^2]} \tag{6.10}$$

which can be inverted numerically [330]. The electric field can then be expanded in terms of coherent states via

$$|E^+\rangle = \sum_{n,m} Q_{\omega_n t_m} |\alpha_{\omega_n t_m}\rangle \tag{6.11}$$

where the expansion coefficients $Q_{\omega_n t_m}$ are obtained by the projection of the electric field onto the basis functions taking into account the inverse overlap matrix

$$\begin{aligned} Q_{\omega_n t_m} &= \sum_{(i,j)} S^{-1}_{(n,m)(i,j)} \langle \alpha_{\omega_i t_j} | E^+ \rangle \\ &= \sum_{(i,j)} S^{-1}_{(n,m)(i,j)} \int \alpha^*_{\omega_i t_j}(\omega) E^+(\omega) \mathrm{d}\omega. \end{aligned} \tag{6.12}$$

As these expansion coefficients are complex-valued quantities, they can also be described by their amplitudes and phases, which in the following are referred to as the *von Neumann amplitude* and *von Neumann phase*, and the square of the absolute value as *von Neumann intensity*. The von Neumann representation can be – just as other time–frequency descriptions – visualized by plotting those quantities on the discrete two-dimensional von Neumann time–frequency grid.

By comparing Eq. (6.12) with Eq. (2.39), it becomes obvious that the expansion coefficients without consideration of the overlap matrix may be considered as a complex-valued Husimi distribution that is defined on a coarse time–frequency grid.

An intuitive interpretation of the von Neumann representation is shown in Fig. 6.3. We consider a laser pulse defined in the von Neumann picture by two non-zero coefficients with relative von Neumann intensities of I_1 =1.0 at ω_1 =2.411 rad/fs and t_1 =407 fs and I_2 =0.75 at ω_2 =2.334 rad/fs and t_2 = −1220 fs [Fig. 6.3(a)]. The phase of these two von Neumann coefficients is set to ϕ_1 =0.6 π and ϕ_2 =-0.4 π, as shown in Fig. 6.3(b). Figure 6.3(c) shows the spectral intensity (blue) and phase (green) of the same laser pulse after transformation to the frequency domain. The intensity profile is given by two Gaussians with the same center frequencies and relative intensities as the two von Neumann coefficients. Furthermore, the spectral phase at the center frequencies is given by the negative values of the von Neumann phases.

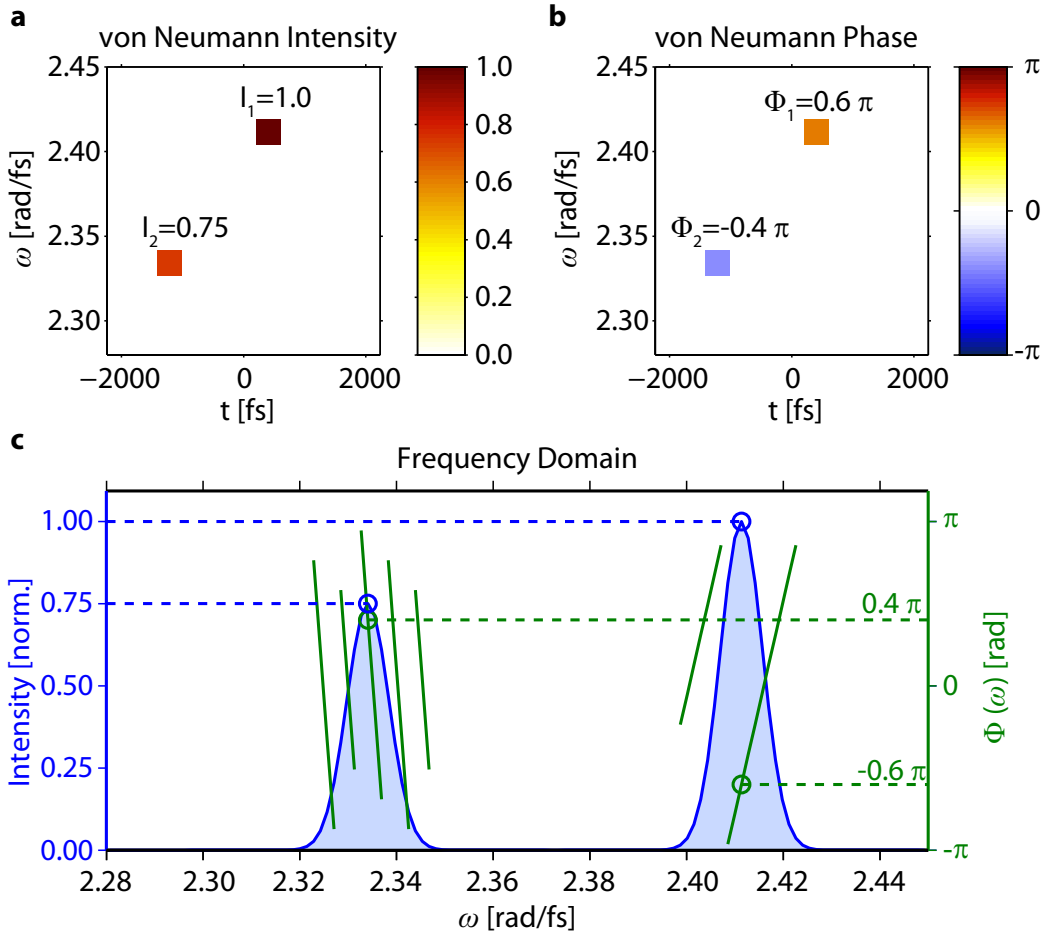

Figure 6.3 | Interpretation of the von Neumann representation. (a) We consider a laser pulse given by two non-zero von Neumann coefficients with relative intensities of 1.0 and 0.75. (b) The corresponding von Neumann phases are set to 0.6 π and -0.4 π. (c) In frequency domain the intensity is given by two separated Gaussians with the same intensities and central frequencies as defined in the von Neumann picture. The spectral phase at the center frequencies is given by the negative values of the von Neumann phases. The phase is not shown for intensity values below 1 %.

This relationship between intensities and phases in von Neumann space and frequency domain is a general property of the von Neumann representation [68, 330] and the formalism introduced in Sect. 6.3 is based on this connection. A similar relationship is found in time domain. However, it has to be emphasized that this strict accordance between the von Neumann parameters and the pure time or frequency domain is only valid for well separated subpulses in time and frequency [68, 330, 331].

Also more complex pulse shapes can be described with the von Neumann picture. To demonstrate this, the von Neumann representation of the example pulse from Figs. 2.6 and 2.5 is illustrated in Fig. 6.4 in terms of the von Neumann amplitude [Fig. 6.4(a)] and von Neumann phase [Fig. 6.4(b)]. In contrast to the von Neumann amplitude, from which the temporal and spectral structure of the laser pulse becomes easily apparent, an intuitive interpretation of the von Neumann phase is not possible for such complicated

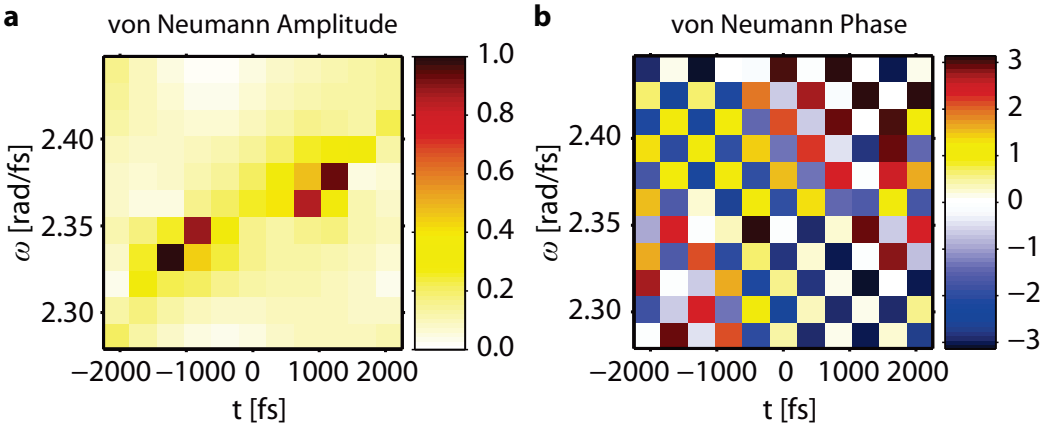

Figure 6.4 | Exemplary von Neumann representation The von Neumann amplitude (a) and phase (b) is shown of the example pulse from Figs. 2.5 in the Wigner distribution and 2.6 in the Husimi representation (adapted from Ref. [332]);

pulse shapes.

It was previously shown that the (for practical reasons unavoidable) truncation of the originally infinitely sized von Neumann phase space to a confined time–frequency range can lead to certain artifacts after back- or forward transformation, especially for pulse shapes that necessitate a larger amount of basis functions for convergence [70, 330, 331]. Several solutions to this issue have been proposed and tested in view of transformation accuracy, bijectivity between von Neumann space and Fourier description, and efficiency. It was shown that the most feasible method to avoid issues arising from the truncated von Neumann lattice is to introduce explicit periodic boundary conditions [70] such that the basis functions satisfy the condition $\alpha_{\omega_n t_m}(\omega+\Omega) = \alpha_{\omega_n t_m}(\omega)$. The same periodicity in time domain is implicitly achieved by the discretization in frequency domain. For all von Neumann transformations employed in this work, this method of periodic boundary conditions for the basis functions was used in order to achieve the best possible accuracy as is demonstrated in Sect.6.5.

6.3 Generalization to Polarization Shaped Laser Pulses

While in the previous section the von Neumann formalism as a joint time–frequency representation for linearly polarized femtosecond laser pulses was reviewed [9, 11, 68–70] this formalism is now transferred to the description of time-dependent polarization profiles [7, 334]. Therefore we consider a time-dependent electric field of a transverse electromagnetic wave with varying polarization state. In analogy to Sect. 2.1.3 this electric field $\vec{E}$ can be described in terms of a linear superposition of two linearly independent field components E_1 and E_2,

$$\vec{E} = \begin{pmatrix} E_1 \\ E_2 \end{pmatrix} , \tag{6.13}$$

and can be expressed in the von Neumann formalism as a superposition of two linearly independent von Neumann basis sets using Dirac's notation:

$$\left|\vec{E}\right\rangle = \sum_{n,m} Q^1_{\omega_n,t_m} \left|\alpha_{\omega_n,t_m}\right\rangle \vec{e}_1 + \sum_{n,m} Q^2_{\omega_n,t_m} \left|\alpha_{\omega_n,t_m}\right\rangle \vec{e}_2. \tag{6.14}$$

Here $Q^k_{\omega_n,t_m}$, $k = 1,2$, denote the complex-valued von Neumann coefficients and $\vec{e}_k$ the unity vectors in polarization directions 1 and 2, respectively. The von Neumann coefficients can, just as for linearly polarized pulses, be expressed by means of the von Neumann amplitude $\left|Q^k_{\omega_n,t_m}\right|$ and the von Neumann phase $\phi^k_{\omega_n,t_m} = \arg\left(Q^k_{\omega_n,t_m}\right)$ as

$$Q^k_{\omega_n,t_m} = \left|Q^k_{\omega_n,t_m}\right| e^{\mathrm{i}\phi^k_{\omega_n,t_m}}, \quad k = 1,2. \tag{6.15}$$

These expansion coefficients can be determined by the projection of the corresponding electric field component onto the basis functions in consideration of the overlap matrix $S_{(n,m)(i,j)} = \langle \alpha_{\omega_n,t_m} \mid \alpha_{\omega_i,t_j} \rangle$ of the basis functions [68–70]:

$$Q^k_{\omega_n,t_m} = \sum_{i,j} S^{-1}_{(n,m)(i,j)} \langle \alpha_{\omega_i,t_j} \mid E_k \rangle. \tag{6.16}$$

An arbitrarily polarized electric field can thus be expressed with the help of the von Neumann amplitudes and phases for both polarization components.

We will now consider the elliptical representation, which was already introduced in Sect. 2.1.3. In the slowly-varying envelope approximation, the time evolution of the electric field vector within one oscillation period at time t can be expressed by an ellipse [91]. This ellipse can be characterized by the following set of time-dependent parameters: The ellipticity $\epsilon(t)$ contains the shape of the ellipse, whereas the orientation angle $\theta(t)$ defines the angle between the major elliptical principal axis and the laboratory axis in polarization direction 1; the total intensity $I(t)$ determines the "size" of the ellipse while the total phase $\varphi(t)$ describes the phase of the electric field oscillation, whose derivative with respect to time can be used to determine the instantaneous frequency of the laser pulse.

Those parameters can be directly transferred to the joint time–frequency domain. A beneficial fact for this is the aforementioned correspondence between the von Neumann amplitudes $\left|Q^k_{\omega_n,t_m}\right|$ and phases $\phi^k_{\omega_n,t_m}$and the spectral amplitudes $|E_k(\omega)|$ and phases $\Phi_k(\omega)$, respectively. As shown previously [68] and as illustrated in Fig. 6.3, one finds the relationships

$$\Phi_k(\omega = \omega_n) = -\phi^k_{\omega_n,t_m}, \tag{6.17}$$

$$|E_k(\omega = \omega_n)| = \left(\frac{2\alpha}{\pi}\right)^{\frac{1}{4}} \left|Q^k_{\omega_n,t_m}\right| \tag{6.18}$$

for temporally and spectrally well-separated subpulses (i.e., vanishing overlap between the corresponding basis functions).

Hence the von Neumann phase $\phi^k_{\omega_n,t_m}$ equals the negative spectral phase $\Phi_k(\omega_n)$ and the von Neumann amplitude describes the field amplitude at the center of the subpulse.

A similar correspondence can be found in time domain [68]. Equations (6.17) and (6.18) provide the motivation for defining elliptical pulse parameters in von Neumann phase space via

$$I_{\omega_n,t_m} = \left|Q^1_{\omega_n,t_m}\right|^2 + \left|Q^2_{\omega_n,t_m}\right|^2, \tag{6.19}$$

$$\begin{aligned}\varphi_{\omega_n,t_m} &= \phi^1_{\omega_n,t_m} + \operatorname{sign}\{\theta_{\omega_n,t_m}\epsilon_{\omega_n,t_m}\} \\ &\quad \times \arccos\left[\sqrt{\frac{I_{\omega_n,t_m}}{|Q^1_{\omega_n,t_m}|^2}}\cos\theta_{\omega_n,t_m}\cos\epsilon_{\omega_n,t_m}\right],\end{aligned} \tag{6.20}$$

$$\begin{aligned}\epsilon_{\omega_n,t_m} &= \frac{1}{2}\arcsin\left[\sin(2\chi_{\omega_n,t_m})\sin\delta_{\omega_n,t_m}\right] \\ &\in \left[-\frac{\pi}{4},\frac{\pi}{4}\right],\end{aligned} \tag{6.21}$$

$$\begin{aligned}\theta_{\omega_n,t_m} &= \tilde{\theta}_{\omega_n,t_m} + \gamma \\ &\in \left[-\frac{\pi}{2},\frac{\pi}{2}\right],\end{aligned} \tag{6.22}$$

$$\gamma = \begin{cases} 0 & \forall\chi_{\omega_n,t_m} \leq \frac{\pi}{4}, \\ +\frac{\pi}{2} & \forall\chi_{\omega_n,t_m} > \frac{\pi}{4} \wedge \tilde{\theta}_{\omega_n,t_m} < 0, \\ -\frac{\pi}{2} & \forall\chi_{\omega_n,t_m} > \frac{\pi}{4} \wedge \tilde{\theta}_{\omega_n,t_m} \geq 0, \end{cases} \tag{6.23}$$

with

$$\tilde{\theta}_{\omega_n,t_m} = \frac{1}{2}\arctan\left[\tan(2\chi_{\omega_n,t_m})\cos\delta_{\omega_n,t_m}\right]. \tag{6.24}$$

The significance of these parameters will be illustrated in Sect. 6.6. The basis transformation in Eqs. (6.19)–(6.24) is analogous to the transformations introduced in Eqs. (2.47–2.51) of Sect. 2.1.3 as adapted from Ref. [91] but replacing the temporal amplitudes and phases with the von Neumann amplitudes and phases in the equation for the elliptical pulse parameters.

The set of parameters now sufficient for a complete description of the electric field are the von Neumann total intensity I_{ω_n,t_m}, the von Neumann total phase φ_{ω_n,t_m}, the von Neumann ellipticity ϵ_{ω_n,t_m}, and the von Neumann orientation angle θ_{ω_n,t_m} at discrete points (ω_n,t_m) in phase space, which we call the von Neumann elliptical laser pulse parameters. The auxiliary parameters δ_{ω_n,t_m} (the phase difference between component 2 and 1) and the angle χ_{ω_n,t_m} in Eqs. (6.21)–(6.24) are in analogy to Eq. (2.45) and (2.46) given by [91]

$$\delta_{\omega_n,t_m} = \phi^2_{\omega_n,t_m} - \phi^1_{\omega_n,t_m} \quad \in [-\pi,\pi] \tag{6.25}$$

and

$$\chi_{\omega_n,t_m} = \arctan\frac{\left|Q^2_{\omega_n,t_m}\right|}{\left|Q^1_{\omega_n,t_m}\right|} \quad \in \left[0,\frac{\pi}{2}\right]. \tag{6.26}$$

Hence the parameter set defined in Eqs. (6.19)–(6.22) can be calculated by the von Neumann coefficients of two orthogonal polarization directions which, in turn, are given by the spectral or temporal electric fields via Eq. (6.16).

It is desirable to define the elliptical pulse parameters directly in von Neumann phase space, in order to be able to control the polarization state in experiments with a pulse shaper. Hence, for a direct definition of arbitrarily polarized fields the inversion of Eqs. (6.19)–(6.26) is required so that the von Neumann amplitudes and phases can be calculated as a function of I_{ω_n,t_m}, φ_{ω_n,t_m}, ϵ_{ω_n,t_m}, and θ_{ω_n,t_m}. Combining Eq. (6.26) with Eq. (6.19) and making use of the relationship $1+\tan^2 x = \frac{1}{\cos^2 x}$ we obtain

$$\left|Q^1_{\omega_n,t_m}\right| = \sqrt{I_{\omega_n,t_m}}\cos\chi_{\omega_n,t_m} \tag{6.27}$$

and

$$\left|Q^2_{\omega_n,t_m}\right| = \sqrt{I_{\omega_n,t_m}}\sin\chi_{\omega_n,t_m} \tag{6.28}$$

for the von Neumann amplitudes. Solving Eq. (6.20) for $\phi^1_{\omega_n,t_m}$ and Eq. (6.25) for $\phi^2_{\omega_n,t_m}$ yields

$$\begin{aligned}\phi^1_{\omega_n,t_m} = \varphi_{\omega_n,t_m} &- \operatorname{sign}\left(\theta_{\omega_n,t_m}\epsilon_{\omega_n,t_m}\right) \\ &\times \arccos\left[\sqrt{\frac{I_{\omega_n,t_m}}{\left|Q^1_{\omega_n,t_m}\right|^2}}\cos\theta_{\omega_n,t_m}\cos\epsilon_{\omega_n,t_m}\right]\end{aligned} \tag{6.29}$$

and

$$\phi^2_{\omega_n,t_m} = \phi^1_{\omega_n,t_m} + \delta_{\omega_n,t_m} \tag{6.30}$$

for the von Neumann phases. To make use of above equations we have to express the phase difference δ_{ω_n,t_m} and the auxiliary angle χ_{ω_n,t_m} as a function of ϵ_{ω_n,t_m} and θ_{ω_n,t_m}. A detailed derivation of these expressions is given in Appendix A.4 of this thesis [see Eqs. (A.10), (A.16), and (A.16)]. We obtain

$$\chi_{\omega_n,t_m} \;=\; \frac{1}{2}\arccos\left[\cos(2\epsilon_{\omega_n,t_m})\cos(2\theta_{\omega_n,t_m})\right] \tag{6.31}$$

and

$$\delta_{\omega_n,t_m} = \begin{cases} +\arccos\left[+\sqrt{1-c}\right], \forall\epsilon_{\omega_n,t_m}\geq 0 \wedge \theta_{\omega_n,t_m}\geq 0 \\ +\arccos\left[-\sqrt{1-c}\right], \forall\epsilon_{\omega_n,t_m}\geq 0 \wedge \theta_{\omega_n,t_m}< 0 \\ -\arccos\left[-\sqrt{1-c}\right], \forall\epsilon_{\omega_n,t_m}< 0 \wedge \theta_{\omega_n,t_m}< 0 \\ -\arccos\left[+\sqrt{1-c}\right], \forall\epsilon_{\omega_n,t_m}< 0 \wedge \theta_{\omega_n,t_m}\geq 0 \end{cases} \tag{6.32}$$

with

$$c = \frac{\sin^2(2\epsilon_{\omega_n,t_m})}{1-\cos^2(2\epsilon_{\omega_n,t_m})\cos^2(2\theta_{\omega_n,t_m})}. \tag{6.33}$$

The four cases of Eq. (6.32) correspond to the four quadrants of the Poincaré plane. The first positive (negative) sign in Eq. (6.32) for the phase difference is chosen for positive (negative) ellipticities, the sign of the argument depends on the orientation angle.

With the mathematical relationship between the electric field in Fourier domain and the polarization parameters in von Neumann time–frequency phase space now established, several example pulse shapes are discussed in the next sections illustrating the formalism and providing an intuitive interpretation of the defined phase-space parameters.

6.4 Example Pulse Shapes

First we consider a pulse sequence defined in von Neumann space (Example 1), consisting of three subpulses at different center frequencies and times. Figure 6.5(a) shows the Fourier description in time and frequency domain. The spectral (top) and temporal (bottom) intensities (solid gray line for polarization component 1, black dashed line for component 2) and phases (blue for component 1, red for component 2) contain all necessary information.

Figure 6.5(b) illustrates the pulse sequence in the Poincaré ellipticity–orientation plane. The three-pulse structure corresponds to three separated ϵ–θ values, one for each subpulse. Here, the values for the ellipticity and the orientation angle are given explicitly. In addition, the subpulse intensity can be specified by the color of the data points.

The same pulse can be illustrated in a time-domain quasi-three-dimensional representation as shown in Fig. 6.5(c) [88, 348, 352, 370]. Here, the temporal evolution of the electric field vector is illustrated by stacking the ellipses associated to the polarization state at every time step along the t axis. Thus, the polarization state and the evolution of intensity can be visualized intuitively. The instantaneous frequency is indicated by the color of the ellipses, where green corresponds to the center frequency of the laser pulse, red to lower frequencies and blue to higher ones. The shadows indicate the envelopes of component 1 (bottom plane of projection) and 2 (back plane). Again, it is obvious that the laser pulse consists of three temporally separated subpulses with different polarization states. The different center frequencies of the subpulses are also directly visible (red, green, blue).

The new representation in von Neumann space [Fig. 6.5(d)] gives an immediate and intuitive time–frequency picture of the investigated pulse shape. An ellipse corresponding to the von Neumann ellipticity and orientation angle is plotted at every grid point in phase space. Dashed and solid lines in addition to an arrow denote the sense of rotation and indicate left (solid) or right (dashed) elliptically polarized light. The associated von Neumann intensity is displayed by the color of the ellipse. Optionally the von Neumann total phase could be illustrated, e.g., by the background color; however, this is not done here in order to keep the diagrams simple.

Now we consider a pulse structure defined in frequency domain (Example 2). The two polarization components are chosen with an identical Gaussian spectral intensity while the amount of second-order phase is chosen differently [Fig. 6.5(e)]. This results in a slightly different temporal pulse structure for the two components.

More insight is provided with a visualization in Poincaré phase space in Fig. 6.5(f). Since phase and spectrum are symmetric with respect to $t = 0$ fs, the evolution of the polarization state is also symmetric. In the beginning (bluish colors), the temporal evolution in ellipticity–orientation space is helical around the point $\epsilon = 0$ rad, $\theta = \pm\pi/2$ rad (note the periodic boundary conditions in Poincaré phase space). At $t = 0$ fs, the curve reaches the reversal point at $\epsilon \approx -\pi/8$ rad, $\theta \approx \pi/4$ rad with maximum intensity (red) and then returns for positive times along the same path as for negative times. This demonstrates that complicated polarization profiles may be generated by very moderate phase differences between the two polarization directions, which would

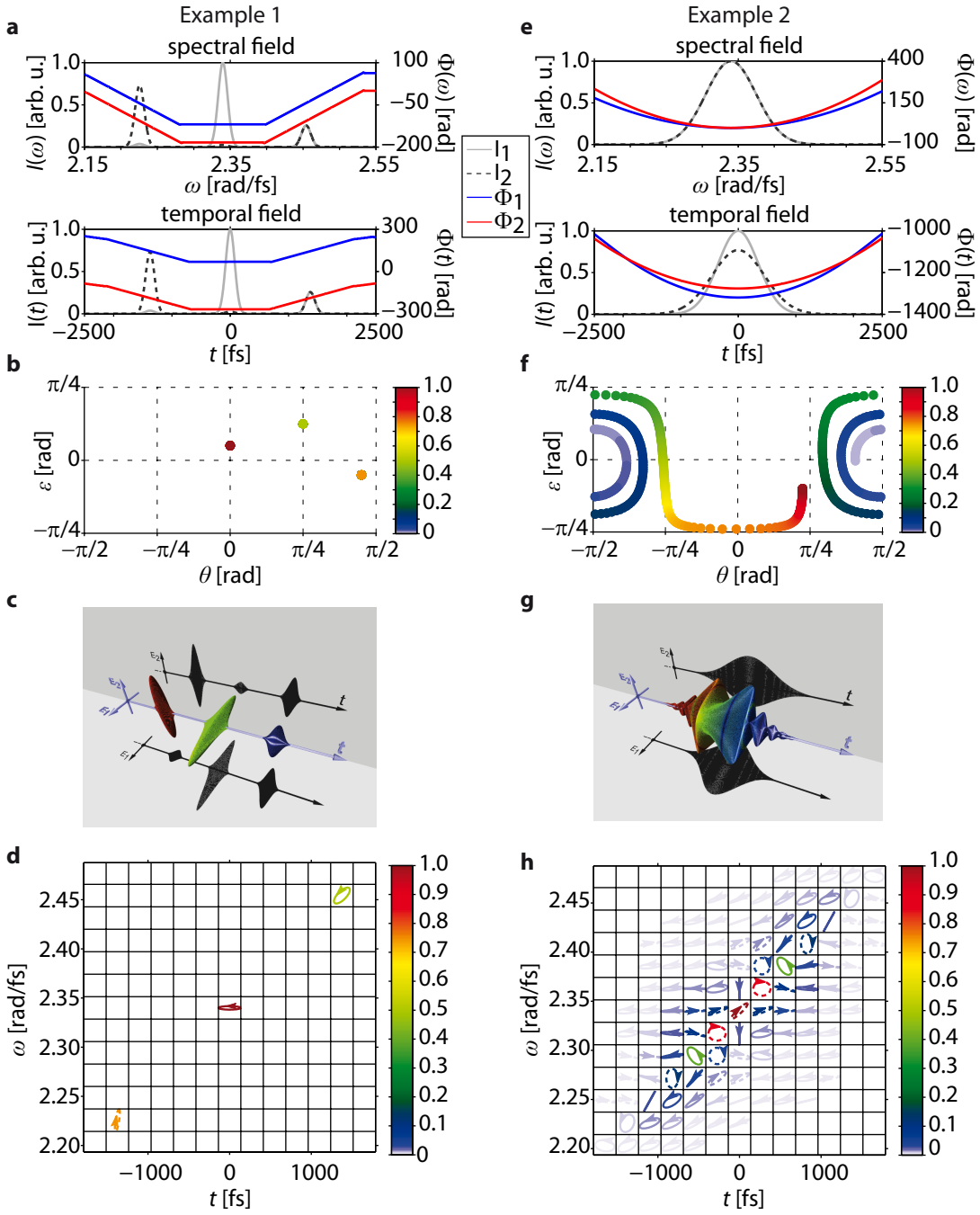

Figure 6.5 | Definition and visualization of polarization-shaped pulses in different representations. In the left column (a-d) a pulse sequence has been defined in the von Neumann basis, in the right column (e-h) a polarization-shaped pulse has been defined in frequency domain. In the Fourier description (a,e) intensities and phases for polarization directions 1/2 are given by gray/black-dashed lines and blue/red lines, respectively. The Poincaré plot (b,f) and the quasi-three-dimensional time-domain description (c,g) can also serve as an intuitive representation. Von Neumann elliptical pulse parameters (d,h) are visualized in joint time–frequency domain. The sense of rotation is indicated by an arrow and the line style (solid lines for right and dashed lines for left elliptically polarized subpulses). Figure adapted from Ref. [7]. © (2012) by Springer Science+Business Media.

not be revealed by only depicting the temporal or spectral fields.

The quasi-three-dimensional representation [Fig. 6.5(g)] also indicates the rapid changes in polarization state. Additionally, the evolution of the instantaneous frequency indicates second-order phase terms that have been applied to the pulse (colors of the ellipses evolving from red to blue indicating up-chirp).

The von Neumann representation of the same pulse is shown in Fig. 6.5(h). The symmetric behavior with respect to $t = 0$ fs in time domain is rendered in a point symmetry with respect to $t = 0$ fs and $\omega = 2.34$ rad/fs in von Neumann space. The second-order spectral phase becomes apparent as the trace of the pulse is located diagonally in the von Neumann plane indicating an up-chirped pulse. It is important to note at this point that the resulting electric field at a specific time t results from the superposition of all basis functions corresponding to this point in time which leads to a mixing of the von Neumann elliptical pulse parameters. Nevertheless, since in this case the intensities of the main subpulses located on the (ω,t)-diagonal dominate, their corresponding von Neumann elliptical pulse parameters are comparable to those in time domain. The evolution of polarization for those von Neumann basis functions matches the behavior in the pseudo-three-dimensional description very well. The consistency of the representations can also be demonstrated by comparing data points in the Poincaré plot and in the von Neumann plot with the same color as both plots share the same intensity color code. The peak of the pulse (reddish colors) consists of right elliptical polarized light (dashed ellipsis in von Neumann plot) as already seen in the Poincaré plot, while for smaller intensities the sense of rotation is alternating.

Each of the four visualization techniques has certain advantages but the amount of contained information in them is not the same. The Fourier description contains all mathematically necessary and sufficient information about the pulse shape. But if only the spectral/temporal amplitudes and phases are considered, the instantaneous frequency and the evolution of the polarization state does not become apparent. The latter information is provided by the Poincaré plot, but no information about the instantaneous frequency and the phase is included and the time axis is only implicit. A quasi-three-dimensional time-domain representation can also serve as an intuitive visualization technique with a pure time basis. Since the von Neumann representation as introduced in Eqs. (6.19)–(6.24) is based on a complete basis set, the amount of contained information is the same as in Fourier space and is also sufficient to describe the laser pulse in its entirety, but provides this information in time–frequency space with direct polarization properties. Furthermore, forward and backward transformations to the Fourier domain can be carried out with the von Neumann elliptical pulse parameters without loss of information as will be demonstrated in Sect. 6.5.

The phase-space representation of polarization states introduced in this section involves the transformation to discrete variables, which are – due to the conservation of information content and the validity of the time–bandwidth product – coarsely distributed in time–frequency space. In some cases the use of a discrete set of parameters may not improve the clarity of illustration of a particular pulse shape due to the low density of data points. However, the representation does illustrate the true number of degrees of freedom. In many cases, it will be helpful to combine different pulse representations to achieve a more comprehensive picture. In order to increase the density of

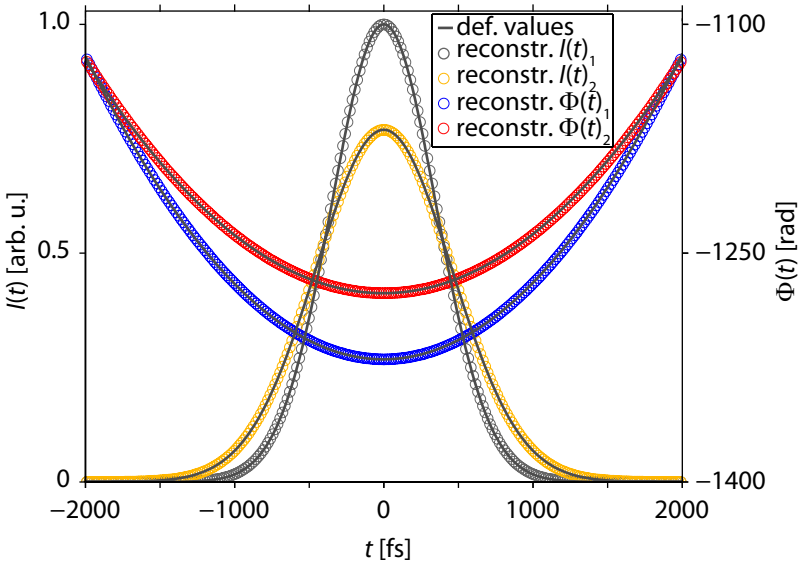

Figure 6.6 | Accuracy of forward- and backward-transformations from Fourier space to von Neumann space with elliptical pulse parameters and back to Fourier space. Perfect agreement is found between originally defined (gray lines) and reconstructed (colored circles) temporal intensities and phases for both polarization directions. Figure adapted from Ref. [7]. © (2012) by Springer Science+Business Media.

data points in phase space, the use of an overcomplete von Neumann basis set is possible as demonstrated in Ref. [70] for the case of linearly polarized fields. This approach can also be transferred to the case of polarization-shaped pulses and can help to increase the level of details at the cost of losing the bijectivity of the transformation.

6.5 Accuracy of Forward- and Backward-Transformations

In this section, the issue of accuracy of the transformation between Fourier-space and von Neumann elliptical pulse parameters is discussed. For this purpose, the same pulse shape as depicted in Fig. 6.5(e) is transformed to the von Neumann parameter set I_{ω_n,t_m}, φ_{ω_n,t_m}, ϵ_{ω_n,t_m}, and θ_{ω_n,t_m} [see Fig. 6.5(h)]. Afterwards, we use Eqs. (6.27)–(6.32) and Eq. (6.14) to reconstruct the temporal electric field amplitudes and phases. The results are shown in Fig. 6.6.

Despite the fact that in von Neumann space many basis functions with completely different polarization states contribute to the signal [compare Fig. 6.5(h)], perfect agreement is found between the originally defined temporal electric field intensities and phases (gray lines) and the reconstructed values (colored circles). A more detailed discussion about the accuracy of the forward and backward transformation between time or frequency space and von Neumann phase space for the case of linearly polarized electric fields can be found in Refs. [70, 330, 331], where it is demonstrated that the introduction of periodic boundary conditions in von Neumann phase-space allows a perfect

reconstruction of arbitrarily shaped laser pulses. The same approach was used in this work, which was applied to both polarization directions. Hence, the equations as introduced in Sect. 6.3 allow for a high-accuracy and bidirectional transformation between purely temporal or spectral field descriptions and von Neumann space, independent of the complexity of the respective parameters.

6.6 Interpretation of the von Neumann Parameters for Polarization-Shaped Pulses

In this section, the von Neumann parameter set for polarization-shaped pulses are compared with purely time-dependent polarization parameters and give an interpretation of the definitions given in Eqs. (6.19)–(6.22). For this comparison, two pulses are defined in von Neumann phase space as an example.

First, we consider Example 1 from Fig. 6.5, i.e., a pulse sequence with temporally and spectrally well separated subpulses, and plot elliptical pulse parameters in Fig. 6.7(a). For reasons of clarity, the linear time-dependent term $[\omega(t) - \omega_0]\, t$ was subtracted from the total temporal phase $\Phi(t)$. The vertical dashed lines indicate the defined temporal centers of the subpulses. A perfect agreement between the temporal (black lines) and the von Neumann parameters (red circles) is found at the positions for which the von Neumann representation is defined (vertical lines) since Eqs. (6.17) and (6.18) are valid due to the negligible phase-space overlap between the subpulses.

If we change the phase-space positions of the subpulses such that they are neighboring each other spectrally and temporally on the von Neumann (ω,t)-diagonal a different result is achieve, as shown in Fig. 6.7(b). All parameters closely match at the pulse centers (dashed vertical lines). However, in this case $\Phi(t)$, $\epsilon(t)$, and $\theta(t)$ are no longer constant during the duration of each subpulse as the polarization state cannot adapt instantaneously between the three subpulses. From this it can be concluded that the von Neumann parameters consistently describe the time dependent parameters at the center of the subpulses. It has to be pointed out that the temporal variation of the parameters as shown in Fig. 6.7(b) is neither a numerical error of the transformation nor a constriction of the accuracy of the transformations, which are exact, as demonstrated in Sect. 6.5; rather only the direct interpretation of von Neumann polarization parameters is limited in spectral–temporal resolution due to the "coarseness" of the grid. Independent of the correspondence between von Neumann parameters and time dependent parameters as compared in Fig. 6.7, von Neumann elliptical parameters can always be used to describe polarization-shaped laser pulses without loss of accuracy.

The results presented in Fig. 6.7 are of high significance especially for those potential applications where it is required that the defined von Neumann parameters match the conventional temporal pulse parameters. One possible scenario would be the use in pulse shaper assisted multidimensional spectroscopy in which phase cycling (see Sect. 4.4.2) is used to extract the desired signal. In such a case the total von Neumann phase $\phi^k_{\omega_n,t_m}$ could be used to easily carry out the desired phase cycling scheme even though a complicated pulse shape with strongly alternating polarization profile may be employed. Apart from that, also cross-peak sensitive multidimensional spectroscopy as

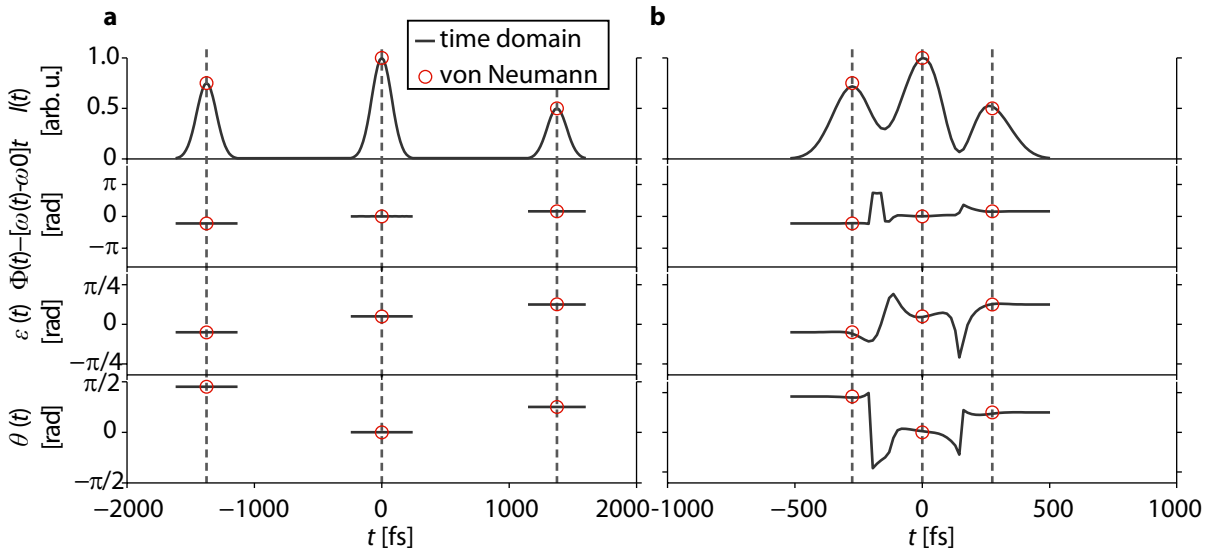

Figure 6.7 | Elliptical pulse parameters total intensity (upper panel), total phase (second panel), ellipticity (third panel), and orientation angle (lower panel) in the time domain (solid lines) compared to the von Neumann parameters (red circles). (a) For spectrally and temporally well separated subpulses, the temporal parameters agree perfectly with the defined von Neumann values. (b) In the case of spectrally and temporally overlapping subpulses von Neumann parameters and temporal parameters still agree very well at the center of the subpulses. However, during the transition between successive subpulses, temporal variations emerge due to the overlap of the basis functions. Figure adapted from Ref. [7].

was proposed in Sect. 6.1 would be feasible since the polarization orientation angle of the laser pulses can be described with very high accuracy with the introduced von Neumann formalism.

6.7 Conclusion

In this chapter the von Neumann joint time–frequency representation for shaped femtosecond laser pulses was generalized to the case of laser pulses with a shaped polarization evolution.The von Neumann formalism for linearly polarized laser pulses was reviewed and the mathematical equations necessary for a basis transformation between Fourier space and the von Neumann time–frequency phase space was introduced for laser pulses with a time-varying polarization profile. Polarization-shaped pulses can be visualized within a single (ω,t)-diagram displaying total intensity, total phase, ellipticity, and orientation angle of the polarization ellipse. The introduced equations allow for high-accuracy forward and backward transformation between Fourier-space and von Neumann elliptical pulse parameters without loss of information. The von Neumann elliptical polarization parameters can be considered as the time–frequency analogues to time-domain elliptical pulse parameters.

Based on the presented results, the von Neumann parameterization can be used as a basis in ultrafast (e.g., multidimensional) spectroscopy or quantum control if an appro-

priate pulse shaper capable of independent amplitude, phase, and polarization control is available. The von Neumann basis may be considered as a natural basis for experiments in which higher-order nonlinearities are exploited and if effects of the laser pulse polarization are expected since the electric field is explicitly encoded in terms of simple and intuitive elliptical laser pulse parameters. Furthermore, the introduced von Neumann picture helps to visualize and to analyze the laser pulse shape in a two-dimensional time–frequency diagram.

7 Summary

Observing chemical reactions in real time with femtosecond laser pulses has evolved into a very popular field of research since it provides fascinating insights into the nature of photochemical transformations. Nevertheless, many photochemical reactions are still too complex for which reason the underlying mechanisms and all engaged species cannot be identified thoroughly. In these cases, conventional time-resolved spectroscopy techniques reach their technical limits and advanced approaches are required to follow the conversion of reactants to their products including all reaction intermediates.

The aim of this work was therefore the development of novel methods for ultrafast spectroscopy of photoreactive systems. Though the concept of coherent multidimensional spectroscopy has so far exclusively been used to explore photophysical phenomena, it also offers great potential for the study of photochemical processes due to its capability of extracting spectroscopic information along several frequency dimensions. This allows resolving the photochemical connectivity between various interconvertible molecular species with ultrafast temporal resolution on the basis of their absorption and emission properties as the spectral correlations are explicitly visualized in the detected spectra.

The ring-open merocyanine form of the photochromic compound 6-nitro BIPS was studied in Chap. 4 of this work. Merocyanines and their associated ring-closed spiropyrans are promising candidates for future applications as, for instance, molecular electronics or optical data storage due to their unique property of being switchable between two stable configurations via light illumination. Transient absorption with sub-50 fs temporal resolution and broadband probing was employed to characterize the photodynamics of this system with variable excitation wavelengths. Using global data analysis, it could be inferred that two different merocyanine isomers with differing excited-state lifetimes exist in solution. These isomers differ in the *cis/trans* configuration in the last bond of the methine bridge. The minority of isomers exist in the all-*trans* configuration (TTT) while the isomer with a *cis* configuration of the third dihedral angle (TTC) is dominant. A characteristic band, detected after long pump–probe delays, was attributed to the unidirectional *cis*→*trans* photoisomerization reaction of the TTC to the TTT form. The quantum yield of the reaction was estimated to be (18±4) %. In addition, pronounced coherent vibrational wave-packet oscillations were observed and it was concluded that these signatures are related to the product formation.

Coherent two-dimensional electronic spectroscopy was successfully implemented using a partially collinear pump–probe beam geometry in combination with a femtosecond pulse shaper. The use of a whitelight probe continuum enabled us to probe contributions far-off the diagonal over the complete visible range. By properly adjusting the relative phase between the first two laser pulses with the pulse shaper, the principle of phase-cycling was explained and it was demonstrated that the measurement can be carried out

in the so-called "rotating frame" in which the observed frequencies detected during the coherence time are shifted to lower values. It was shown that these concepts allow the extraction of the desired background-free photon echo while the amount of necessary data points is highly reduced.

In order to put our proposal of multidimensional spectroscopy of photoreactive systems into practice, third-order two- and three-dimensional spectroscopy was then employed for an in-depth analysis of a photoreactive process, in which the photoisomerization of 6-nitro BIPS served as a model system. The measured two-dimensional spectra revealed the *cis*→*trans* photoisomerization after long population times. By collecting a large data set of two-dimensional spectra for short population times and by applying a Fourier transform along the population time axis, the third-order three-dimensional spectrum was obtained. The novelty of this approach compared to coherent two-dimensional spectroscopy is the introduction of a third axis associated with the vibrational frequencies of the molecular system. In this way, the formation of the reaction product was evidenced and it was shown that the product is formed in its first excited singlet state within 200 fs after excitation. This method hence visualizes the photochemical connections between different reactive molecular species in an intuitive manner and further exposes the normal modes connecting reactant and product. Such conclusions cannot be drawn with conventional third-order techniques such as transient absorption since they are not capable of capturing the full third-order response, but only a subset of it. The reaction mechanism and the role of the observed vibrational modes were uncovered by comparing the experimental data with the results of high-level quantum-chemical calculations performed by our collaborators in the group of Prof. B. Engels from the theoretical chemistry department at the University of Würzburg. Specific calculated molecular normal modes could be assigned to the experimentally observed vibrational frequencies and potential energy surfaces of the electronic ground state and of the first excited state were computed. The technique implemented in this chapter is general and is applicable for the time-resolved analysis of a wide range of chemical reaction networks.

In the first part of Chap. 5, coherent two-dimensional spectroscopy was employed to track the reaction paths of the related 6,8-dinitro BIPS after S_1 excitation. Several differences to the photochemical properties of 6-nitro BIPS were found. From the 2D spectra, the *cis-trans* isomerization between the two merocyanine isomers could be excluded as a major reaction path for this compound. To explore the dynamics after reexcitation to higher-lying electronic states, pump–repump–probe spectroscopy was implemented and the formation of a new species, a radical cation, was observed. To identify the precursor isomer, triggered-exchange two-dimensional spectroscopy, a fifth-order technique previously only available in the infrared regime for vibrational transitions, was implemented for the first time for electronic excitations in the visible. This approach combines the properties of the pump–repump–probe technique with the potential of coherent two-dimensional spectroscopy. It correlates the absorption frequency of a reactive molecular species with the emission signatures of the product formed from this species after an additional absorption of a photon. Using this method, it was unambiguously proven that only the TTC isomer reacts to the radical cation thus forming the precursor species of the reaction. Electronic triggered-exchange two-dimensional spectroscopy is hence another improved technology for time-resolved spectroscopy with applications in

the study of multi-step photoreactions and higher-lying electronic states.

While in the two preceding chapters third- and fifth-order experiments were discussed that neglect the vectorial character of light–matter interactions, Chap. 6 focused on a novel theoretical formalism enabling the description of light fields optimized for polarization-sensitive higher-order nonlinearities. This formalism is based on the von Neumann time–frequency representation of shaped femtosecond laser pulses which permits the definition of multipulse sequences on a discrete time–frequency lattice. Hence, not only the temporal spacing between subpulses is adjustable, but also the center frequencies may be adapted such that they fit the experimental requirements. This method was generalized to the description of pulse sequences with time-varying polarization states. It was shown that by using this description, the polarization ellipticity, orientation angle, relative phase and intensity, and the time–frequency location of each subpulse is explicitly controllable. The accuracy of the transformations from Fourier space to von Neumann domain and vice versa was demonstrated. Moreover, a strict accordance between the von Neumann polarization parameters with the conventional parameters in time domain was found for well separated subpulses. A potential future application of this approach is polarization-sensitive multidimensional spectroscopy in which hidden cross peaks may be isolated by defining the pulses in the von Neumann picture with suitable polarization sequences. This method could also be used in quantum control experiments in which the polarization of the light field is used as a major control knob.

This thesis summarizes our efforts to open the field of femtochemistry to the concept of coherent multidimensional electronic spectroscopy. Making use of femtosecond pulse shaping, sub-50 fs temporal resolution, broadband spectral probing, higher-order nonlinearities, and new types of laser pulse descriptions, the presented methods might stimulate further future advancements in this research area.

Zusammenfassung

Mit Hilfe von Femtosekundenlaserpulsen lassen sich chemische Reaktionen in Echtzeit beobachten, was sich zu einem äußerst populären Forschungsgebiet entwickelt hat, welches faszinierende neue Einblicke in die Natur von photochemischen Transformationen ermöglicht. Nichtdestotrotz sind nach wie vor viele photochemische Reaktionen zu komplex, um die zugrunde liegenden Mechanismen entschlüsseln und alle beteiligten Spezies einwandfrei identifizieren zu können. In diesen Fällen stoßen die konventionellen zeitaufgelösten Techniken an ihre Grenzen, sodass verbesserte Ansätze notwendig sind um der Konversion der Edukte zu den Produkten mit allen reaktiven Zwischenprodukten in Gänze folgen zu können.

Das Ziel der vorliegenden Arbeit war deshalb die Entwicklung neuartiger Methoden in der Ultrakurzzeitspektroskopie photoreaktiver Systeme. Obwohl das Konzept der kohärenten multidimensionalen Spektroskopie bisher ausschließlich zur Erforschung photophysikalischer Phänomene eigesetzt wurde, birgt es angesichts seiner Fähigkeit, spektroskopische Informationen entlang mehrerer Frequenzachsen zu extrahieren, auch großes Potenzial für die Untersuchung photochemischer Prozesse. Diese Eigenschaft ermöglicht die Auflösung des photochemischen Austauschs zwischen untereinander verknüpften molekularen Spezies durch ihre Emissions- und Absorptionseigenschaften, da die spektralen Korrelationen in den gemessenen Spektren unmittelbar visualisiert werden.

In Kap. 4 dieser Arbeit wurde die ringgeöffnete Merocyaninform der photochromen Verbindung 6-nitro BIPS untersucht. Aufgrund ihrer besonderen Eigenschaft, durch Lichteinstrahlung zwischen zwei stabilen Konfigurationen umschalten zu können, sind Merocyanine und ihre assoziierten ringgeschlossenen Spiropyrane vielversprechende Kandidaten für zukünftige Anwendungen auf dem Gebiet der molekularen Elektronik und der optischen Datenspeicherung. Die Photodynamiken dieses Systems wurden mit Hilfe der transienten Absorptionstechnik mit einer zeitlichen Auflösung von unter 50 fs und spektral breitbandiger Abfrage charakterisiert. Die globale Datenanalyse ergab hierbei, dass in Lösung zwei unterschiedliche Merocyaninisomere mit unterschiedlichen Lebensdauern der angeregten Zustände vorliegen. Diese Isomere unterscheiden sich in der *cis/trans*-Anordnung der letzten Bindung der Methinbrücke. Hierbei stellt das Isomer mit *trans-trans-trans* Konfiguration (TTT) die Minderheit dar, während die Mehrzahl der Moleküle eine *cis*-Stellung im dritten Diederwinkel aufweist (TTC). Eine charakteristische spektrale Bande, welche nach langen Pump–Probe-Verzögerungszeiten detektiert wurde, konnte der einfachgerichteten *cis*→*trans* Photoisomerisierungsreaktion der TTC Form zum TTT zugeordnet werden. Die Quantenausbeute dieser Reaktion wurde auf (18±4) % bestimmt. Darüber hinaus wurden stark ausgeprägte Oszillationen eines kohärenten Vibrationswellenpakets beobachtet wobei geschlussfolgert wurde, dass diese Signaturen mit der Entstehung des Reaktionsprodukts zusammenhängen.

Die Technik der kohärenten zweidimensionalen elektronischen Spektroskopie wurde auf Basis einer partiell kollinearen Pump–Probe Strahlgeometrie und in Kombination mit einem Femtosekundenpulsformer erfolgreich implementiert. Dabei ermöglichte die Verwendung eines Weißlichtkontinuums als Abfragepuls auch die Erfassung von Beiträgen, welche weit entfernt von der Diagonalen lokalisiert sind und sich über den gesamten sichtbaren Spektralbereich erstrecken. Durch eine geeignete Anpassung der relativen Phase zwischen den ersten beiden Laserpulsen mit Hilfe des Pulsformers konnte das Prinzip des "phase cyclings" umgesetzt werden. Darüber hinaus wurde demonstriert, dass die Messung im sogenannten "rotating frame" durchgeführt werden kann wobei die Oszillationsfrequenzen, welche während der Kohärenzzeit detektiert werden, zu niedrigeren Werten verschoben werden. Es wurde gezeigt, dass mit diesen Konzepten das erwünschte hintergrundfreie Photonenecho extrahiert und darüber hinaus das Signal mit einer deutlich niedrigeren Anzahl an notwendigen Datenpunkten erfasst werden kann.

Um unsere Idee der multidimensionalen Spektroskopie an photoreaktiven Systemen in die Praxis umzusetzen, wurde anschließend die zwei- und dreidimensionale Spektroskopie dritter Ordnung zur eingehenden Untersuchung eines photoreaktiven Prozesses angewandt, wobei die Photoisomerisierungsreaktion von 6-nitro BIPS als Modellreaktion herangezogen wurde. Die gemessenen zweidimensionalen Spektren offenbarten unmittelbar die *cis*→*trans* Photoisomerisierung nach längeren Populationszeiten. Das dreidimensionale Spektrum dritter Ordnung konnte generiert werden, indem ein großer Datensatz an zweidimensionalen Spektren für kleine Populationszeiten aufgenommen und anschließend die Fouriertransformation entlang der Populationszeitachse bestimmt wurde. Die Neuartigkeit dieses Verfahrens besteht darin, dass eine dritte Achse eingeführt wird, welche mit der Schwingungsfrequenz des molekularen Systems assoziiert ist. Dadurch konnte die Entstehung des Reaktionsprodukts eindeutig belegt werden. Außerdem konnte so gezeigt werden, dass es innerhalb von 200 fs im ersten angeregten Singulettzustand erzeugt wird. Somit vermag diese Methode einerseits die photochemischen Beziehungen zwischen unterschiedlichen reaktiven Spezies auf intuitive Art und Weise zu visualisieren und andererseits ermöglicht sie die Enthüllung derjenigen Normalschwingungen, welche Edukt und Produkt miteinander verbinden. Derartige Schlussfolgerungen können nicht mit konventionellen Techniken dritter Ordnung, wie beispielsweise der transienten Absorption, gezogen werden, da sie nicht in der Lage sind die vollständige Antwortfunktion dritter Ordnung, sondern lediglich ein Teil davon, zu erfassen. Durch Abgleich der experimentellen Daten mit den Resultaten von umfassenden quantenchemischen Berechnungen unserer Kollaborationspartner der Gruppe von Prof. B. Engels aus dem Fachbereich der theoretischen Chemie der Universität Würzburg, konnten der Reaktionsmechanismus sowie die Rolle der beobachteten Vibrationsmoden entschlüsselt werden. Dabei konnten spezifische berechnete Normalschwingungen den experimentell beobachteten Frequenzen zugeordnet und die Potentialhyperflächen des elektronischen Grundzustands und des ersten angeregten Zustands bestimmt werden. Die Technik, welche in diesem Kapitel eingesetzt wurde, ist universell und zur zeitaufgelösten Untersuchung einer großen Zahl an chemischen Reaktionsnetzwerken anwendbar.

Im ersten Teil von Kap. 5 wurden die Reaktionspfade der sehr ähnlichen Verbindung 6,8-dinitro BIPS nach S_1-Anregung mittels kohärenter zweidimensionaler Spektroskopie untersucht. Dabei zeigten sich zahlreiche Unterschiede zu den photochemischen Eigen-

schaften von 6-nitro BIPS. Auf Basis der 2D Spektren konnte für diese Verbindung die *cis-trans* Isomerisierung zwischen den beiden Merocyaninisomeren als bedeutender Reaktionspfad ausgeschlossen werden. Zur Erforschung der Dynamik nach der Wiederanregung in höher angeregte elektronische Zustände, wurde die Anrege–Wiederanrege–Abfrage Spektroskopie implementiert, wobei die Bildung einer neuen Spezies – des Radikalkations – beobachtet wurde. Zur Identifikation des Vorläuferisomers wurde die Technik der zweidimensionalen Spektroskopie mit ausgelöster Umwandlung ("triggered-exchange 2D", TE2D) erstmals mit elektronischen Anregungen im Sichtbaren realisiert. Bisher stand diese Technik ausschließlich im infraroten Spektralbereich für Vibrationsübergänge zur Verfügung. Diese Methode vereinigt die Eigenschaften der Anrege–Wiederanrege–Abfrage Technik mit dem Leistungsvermögen der kohärenten zweidimensionalen Spektroskopie. Sie stellt die Korrelation zwischen der Absorptionsfrequenz einer reaktiven molekularen Spezies mit der Emissionssignatur eines Produkts dar, welches von der ersten Spezies durch die zusätzliche Absorption eines weiteren Photons erzeugt wurde. Durch die Zuhilfenahme dieser Methode konnte eindeutig gezeigt werden, dass nur das TTC Isomer zum Radikalkation reagiert, weshalb es somit als Vorläuferisomer der Reaktion aufgefasst werde kann. Die elektronische TE2D Spektroskopie stellt somit eine weitere verbesserte Technologie in der zeitaufgelösten Spektroskopie mit möglichen Anwendungen bei der Untersuchung von mehrstufigen Photoreaktionen und höher angeregten elektronischen Zuständen dar.

Während in den beiden vorhergehenden Kapiteln Experimente dritter und fünfter Ordnung unter Vernachlässigung des vektoriellen Charakters von Licht–Materie-Wechselwirkungen diskutiert wurden, befasste sich Kap. 6 mit einem neuartigen theoretischen Formalismus, welcher die Beschreibung von Lichtfeldern ermöglicht, welche für polarisationssensitive Nichtlinearitäten höherer Ordnung optimiert sind. Dieser Formalismus basiert auf der von Neumann Zeit–Frequenz Darstellung von geformten Laserpulsen, welche es gestattet, Mehrfachpulssequenzen auf einem diskreten Zeit–Frequenz Gitter zu definieren. Somit kann nicht nur der zeitliche Abstand zwischen den Teilpulsen eingestellt, sondern auch die Zentralfrequenz derart angepasst werden, dass sie den experimentellen Ansprüchen gerecht wird. Diese Methode wurde für die Beschreibung von Pulsformen mit einem zeitabhängigen Polarisationsprofil verallgemeinert. Es wurde gezeigt, dass mit Hilfe dieser Darstellung die Elliptizität, der Orientierungswinkel, die relative Phase und Intensität der Polarisationsellipse, sowie die Zeit–Frequenz Position jedes einzelnen Teilpulses explizit kontrolliert werden können. Die Genauigkeit der Transformationen vom Fourier- in den von Neumann Raum und wieder zurück wurde demonstriert. Überdies wurde festgestellt, dass im Falle von deutlich getrennten Teilpulsen die von Neumann Parameter exakt mit den konventionellen Polarisationsparametern im Zeitraum übereinstimmen. Eine der möglichen zukünftigen Anwendungen dieser Methode ist die polarisationssensitive multidimensionale Spektroskopie, mit deren Hilfe verborgene Cross Peaks durch die Definition der Pulssequenz in der von Neumann Darstellung unter Verwendung geeigneter Polarisationsabfolgen isoliert werden können. Dieser Formalismus könnte außerdem bei Quantenkontrollexperimenten Anwendung finden, bei denen die Polarisation des Lichtfelds der entscheidende Kontrollparameter darstellt.

Diese Dissertation fasst unsere Bemühungen zusammen, das Feld der Femtochemie

auch für das Konzept der multidimensionalen Spektroskopie zu eröffnen. Durch die Verwendung der Femtosekundenpulsformung, einer zeitlichen Auflösung von unter 50 fs, spektral breitbandiger Abfrage, Nichtlinearitäten höherer Ordnung sowie das Ausnutzen neuartiger Beschreibungen von Laserpulsen könnten die präsentierten Methoden Anreize für weitere zukünftige Entwicklungen auf diesem Forschungsgebiet schaffen.

Appendix

A.1 Molecular Geometry of Ring-Open 6-nitro BIPS in the First Excited State

Table A.1 | Excited-state (S_1) molecular geometry of the merocyanine form of 6-nitro BIPS at the transition-state geometry with $\gamma = 90°$ optimized in the gas phase on the CAM-B3LYP/cc-pVDZ level of theory. Table taken from Ref. [4].

Element	X [Å]	Y [Å]	Z [Å]
C	2.78022	1.77769	0.54890
C	2.25569	0.59955	-0.13750
C	3.11765	-0.43910	-0.44237
C	4.46048	-0.35410	-0.08586
C	5.01340	0.75791	0.58229
C	4.19232	1.80116	0.89459
C	0.81963	0.56217	-0.48882
C	-0.13325	0.06766	0.38475
C	-1.50773	-0.01500	0.19667
N	-2.35727	-0.52333	1.16328
C	-3.68328	-0.50685	0.72632
C	-3.73638	0.03151	-0.56318
C	-2.33552	0.40316	-1.01717
C	-4.95024	0.15324	-1.21390
C	-6.11871	-0.26740	-0.56896
C	-6.05192	-0.80201	0.71440
C	-4.83308	-0.93126	1.38378
C	-1.91853	-1.00245	2.44792
C	-1.95067	-0.39261	-2.27661
C	-2.23977	1.91708	-1.27717
N	5.34766	-1.47570	-0.41808
O	6.51820	-1.37779	-0.09617
O	2.03753	2.73547	0.82824
O	4.85792	-2.43036	-0.99281
H	4.55703	2.68987	1.40966
H	-0.92063	-0.17761	-2.59078
H	-2.03536	-1.47399	-2.09847
H	-2.62275	-0.12977	-3.10735
H	-2.53565	2.48662	-0.38507
H	-1.21844	2.21713	-1.54642
H	-2.91083	2.19973	-2.10234
H	-1.39184	-0.21093	3.00434
H	-2.78445	-1.31949	3.03778
H	-1.23743	-1.86229	2.34086
H	-7.08187	-0.17644	-1.07215
H	-6.96640	-1.12882	1.21218
H	-4.80085	-1.35357	2.38804
H	-5.00028	0.57285	-2.22080
H	0.24011	-0.29607	1.34450
H	0.54424	0.95969	-1.46349
H	6.07359	0.74765	0.82639
H	2.76796	-1.33210	-0.95585

A.2 Normal Modes of Ring-Open 6-nitro BIPS in the First Excited State

Table A.2 | Calculated excited-state normal-mode wavenumbers (unscaled), reduced masses, and IR intensities of the MC form of 6-nitro BIPS at $\gamma = 90°$ calculated in the gas phase (CAM-B3LYP/cc-pVDZ). Table taken from Ref. [4].

#	$\bar{\nu}$ [cm^{-1}]	m_{red} [amu]	Intensity [$10^3 \frac{\mathrm{m}}{\mathrm{mol}}$]
1	22.01	5.51	0.05
2	30.36	5.96	0.16
3	38.39	8.42	0.09
4	56.55	4.53	0.35
5	58.81	4.61	0.52
6	100.93	2.36	0.06
7	103.94	8.31	7.33
8	112.85	3.67	1.43
9	121.99	2.56	0.37
10	135.34	1.87	0.05
11	177.46	2.61	0.43
12	184.57	3.50	1.00
13	221.12	1.25	0.26
14	237.62	1.25	0.19
15	243.20	4.78	4.57
16	258.47	2.79	0.18
17	287.20	3.32	0.42
18	299.08	3.38	0.45
19	303.37	3.15	1.18
20	328.44	4.50	5.34
21	333.30	2.96	0.54
22	360.71	4.09	0.18
23	362.42	5.45	0.38
24	376.14	5.25	2.97
25	455.40	3.53	15.63
26	470.52	6.93	4.91
27	478.09	3.25	4.28
28	516.39	4.72	0.72
29	542.42	6.50	2.26
30	559.03	5.30	9.83
31	561.45	4.00	1.27
32	576.07	4.88	0.00
33	587.26	3.64	0.00
34	607.10	4.57	2.46
35	621.50	4.95	4.63
36	638.59	4.42	0.58
37	643.00	4.20	13.80
38	678.69	5.27	0.00
39	716.87	4.63	0.00
40	754.32	3.94	28.42
41	770.49	1.26	0.00
42	786.93	4.14	0.00
43	787.27	4.53	2.89
44	804.04	3.18	2.64
45	831.69	3.46	0.00
46	847.14	2.29	7.99
47	858.18	5.05	0.00
48	866.30	2.09	0.00
49	879.52	1.46	0.18
50	908.33	1.67	0.00
51	953.59	1.43	0.00
52	957.45	2.18	14.79
53	961.91	2.66	0.00
54	965.68	1.37	0.00
55	981.07	1.80	13.04
56	1008.18	1.30	0.00
57	1022.62	1.32	0.12
58	1029.97	1.32	1.21
59	1063.02	2.06	0.00
60	1081.85	2.68	0.00

#	$\bar{\nu}$ [cm^{-1}]	m_{red} [amu]	Intensity [$10^3 \frac{\mathrm{m}}{\mathrm{mol}}$]
61	1095.16	1.88	44.39
62	1108.61	2.22	0.00
63	1138.49	1.31	0.00
64	1140.96	1.45	10.03
65	1146.84	1.49	0.00
66	1156.48	1.66	0.00
67	1178.06	1.16	4.19
68	1187.02	2.48	0.00
69	1188.04	4.01	0.00
70	1210.36	2.31	5.45
71	1251.12	1.56	0.00
72	1259.96	2.04	0.00
73	1270.27	1.95	27.59
74	1302.73	2.23	0.00
75	1317.50	2.23	0.00
76	1346.78	3.04	114.22
77	1354.35	3.63	0.00
78	1390.63	1.24	0.00
79	1398.16	3.06	37.25
80	1412.40	1.44	0.00
81	1417.31	2.50	0.00
82	1432.00	6.98	389.93
83	1437.74	2.94	0.00
84	1455.34	1.79	0.00
85	1458.96	1.05	0.76
86	1459.67	1.05	1.54
87	1462.14	1.04	8.72
88	1467.25	1.53	4.81
89	1476.58	1.08	0.00
90	1482.95	1.15	0.00
91	1499.80	1.59	51.79
92	1525.06	2.67	10.00
93	1547.09	5.02	0.00
94	1552.68	3.85	563.07
95	1555.88	7.94	0.00
96	1615.81	5.35	0.00
97	1628.04	6.00	9.62
98	1688.03	7.35	0.00
99	1699.91	7.51	0.00
100	1706.83	10.96	458.67
101	1715.90	0.00	0.00
102	3047.79	0.00	0.00
103	3065.56	1.04	13.90
104	3068.70	1.04	0.00
105	3107.55	1.10	0.00
106	3143.55	1.10	8.01
107	3147.01	1.10	0.00
108	3159.79	1.10	0.00
109	3163.76	1.10	20.17
110	3189.45	1.10	6.40
111	3197.01	1.09	4.37
112	3199.42	1.09	3.21
113	3208.30	1.09	6.35
114	3223.83	1.09	0.00
115	3232.06	1.10	12.13
116	3238.30	1.09	0.56
117	3243.48	1.08	5.93
118	3262.93	1.09	7.04
119	3264.55	1.10	3.35
120	5198.17	1.35	0.00

A.3 Analysis of the Normal Modes of Ring-Open 6-nitro BIPS in the First Excited State

In order to analyze which normal modes might be triggered by *cis-trans* isomerization, the optimized molecular geometry (i.e. bond lengths, bond angles, and torsional angles) was analyzed for different fixed torsional angles γ of the C–C bond around which isomerization occurs.

A.3.1 Modulation of Bond Lengths

Concerning the bond lengths, the strongest variation as a function of the torsional angle is found in the isomerizing C–C bond itself as discussed in Sect. 4.6.2. Normal modes that involve a strong stretching of this bond are identified at the experimentally measured vibrational frequency [see Figs. 4.25(a) and 4.25(b) in Sect. 4.6.2]. Apart from the C–C bond, we also find a strong elongation of the C–N bonds connecting the nitro group with the benzene ring at position 6 and of one of the C–N bonds in the pyrrole moiety. As shown in Fig. A.1(a) the normal modes 22-24 in the range between 361 and 376 cm^{-1} strongly modulate the C–N bond of the nitro group which matches the experimentally observed higher frequency oscillation centered at 363 cm^{-1} (HFM, gray shaded area). The same normal modes lead to a stretching of the pyrrole C–N bond, as illustrated in Fig. A.1(b).

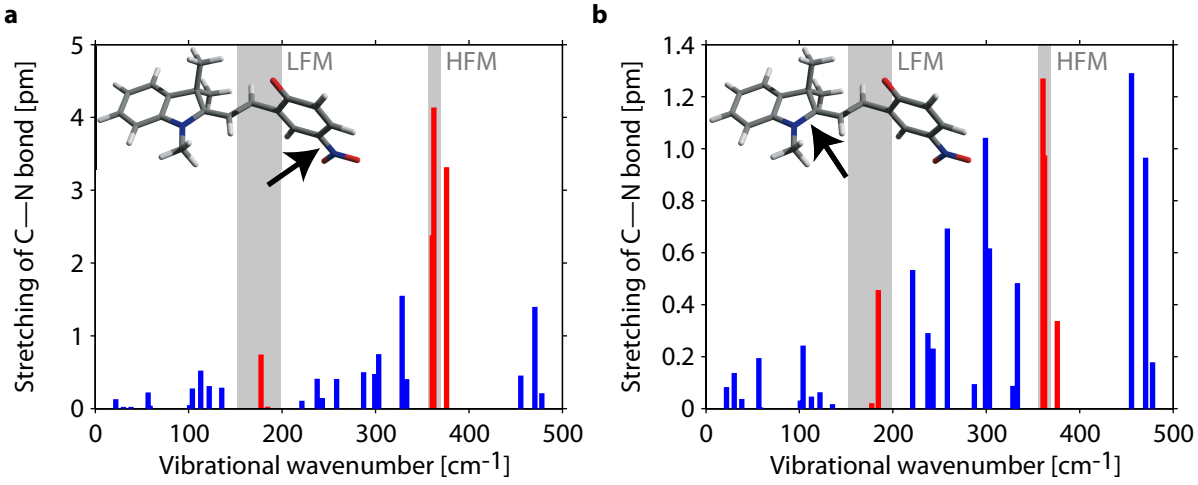

Figure A.1 | Calculated modulation of the two C–N bond lengths (arrows) for the S_1 low-frequency normal modes at the transition-state geometry as a function of the vibrational wavenumber. (a) Excited-state geometry optimizations at the transition state predict a moderate elongation of the C–N bond connecting the nitro group to the benzene ring. The normal-mode analysis shows that this bond is strongly modulated by normal modes 22-24 which match the experimentally observed higher-frequency oscillation (HFM). (b) The same normal modes lead to a pronounced modulation of the C–N bond in the pyrrole moiety which is also found to be affected by photoisomerization. Figure adapted from Ref. [4].

A.3.2 Bending of Bond Angles

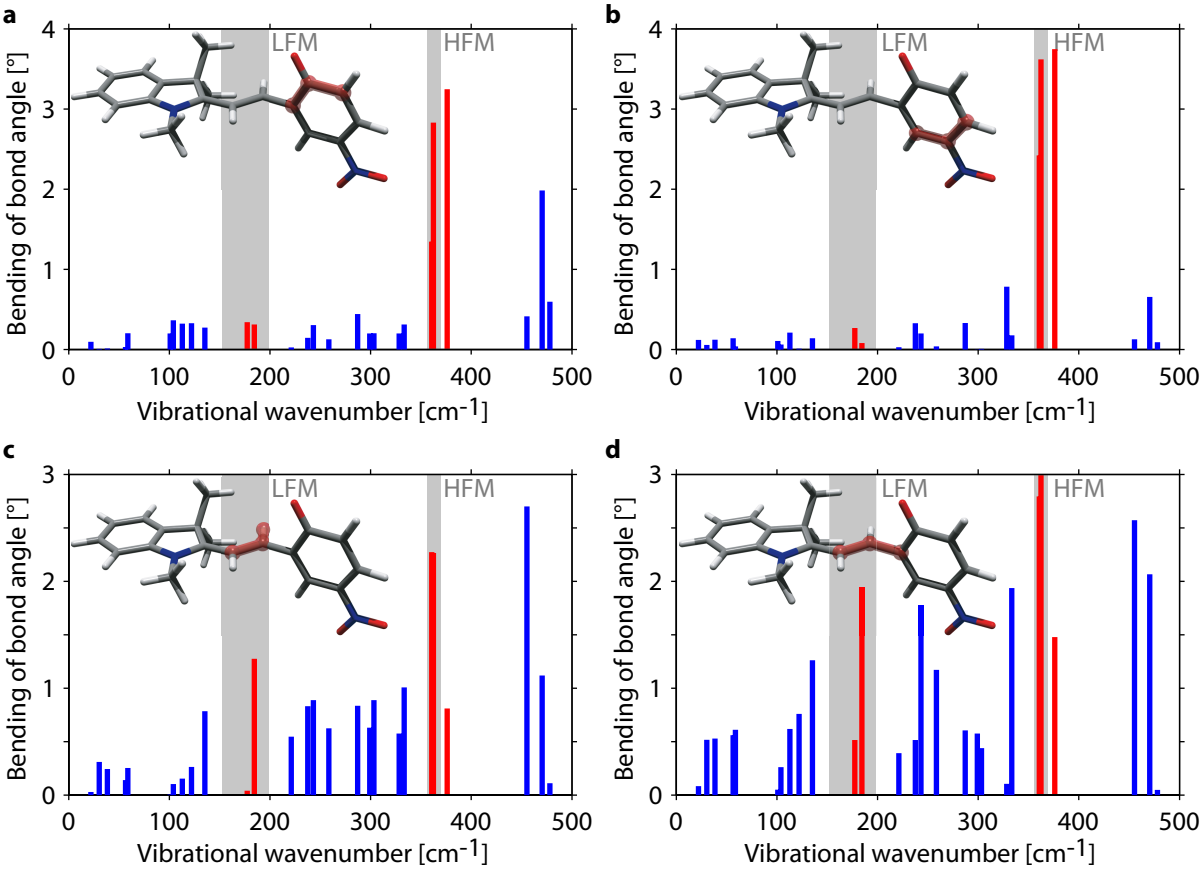

Figure A.2 | Calculated bending of selected bond angles (highlighted in red in the molecular structure) for the S_1 low-frequency normal modes at the transition-state geometry. A squeezing of the benzene ring at the transition-state configuration results in a bending of the two C–C–C bond angles shown in (a) and (b). For both bond angles the normal modes 22-24 (between 361 and 376 cm^{-1}) play a major role. The bending of the highlighted C–C–H angle in the methine chain illustrated in (c) and of the C–C–C bond angle in (d) is also dominated by modes that are located in the experimentally observed frequency range (HFM). Figure adapted from Ref. [4].

The results of the DFT geometry optimizations show that the benzene ring which is rotated during isomerization is slightly distorted and squeezed at the twisted transition-state geometry. It is very likely that this distortion causes vibrational motions that involve a bending of the internal benzene C–C–C bond angles. As shown in Figs. A.2(a) and A.2(b) the normal modes 22-24 (361-376 cm^{-1}) induce a pronounced bending of both considered bond angles (highlighted in red) which is again in agreement with the higher-frequency oscillations observed in the experiment (gray shaded area).

Moreover, the methine chain also exhibits a strong distortion caused by the molecular torsional motion. Figures A.2(c) and A.2(d) show that the bending motion of the highlighted C–C–H bond angle and the C–C–C bond angle (including the isomerizing C–C bond) is – apart from two normal modes above 400 cm^{-1} – dominated in the

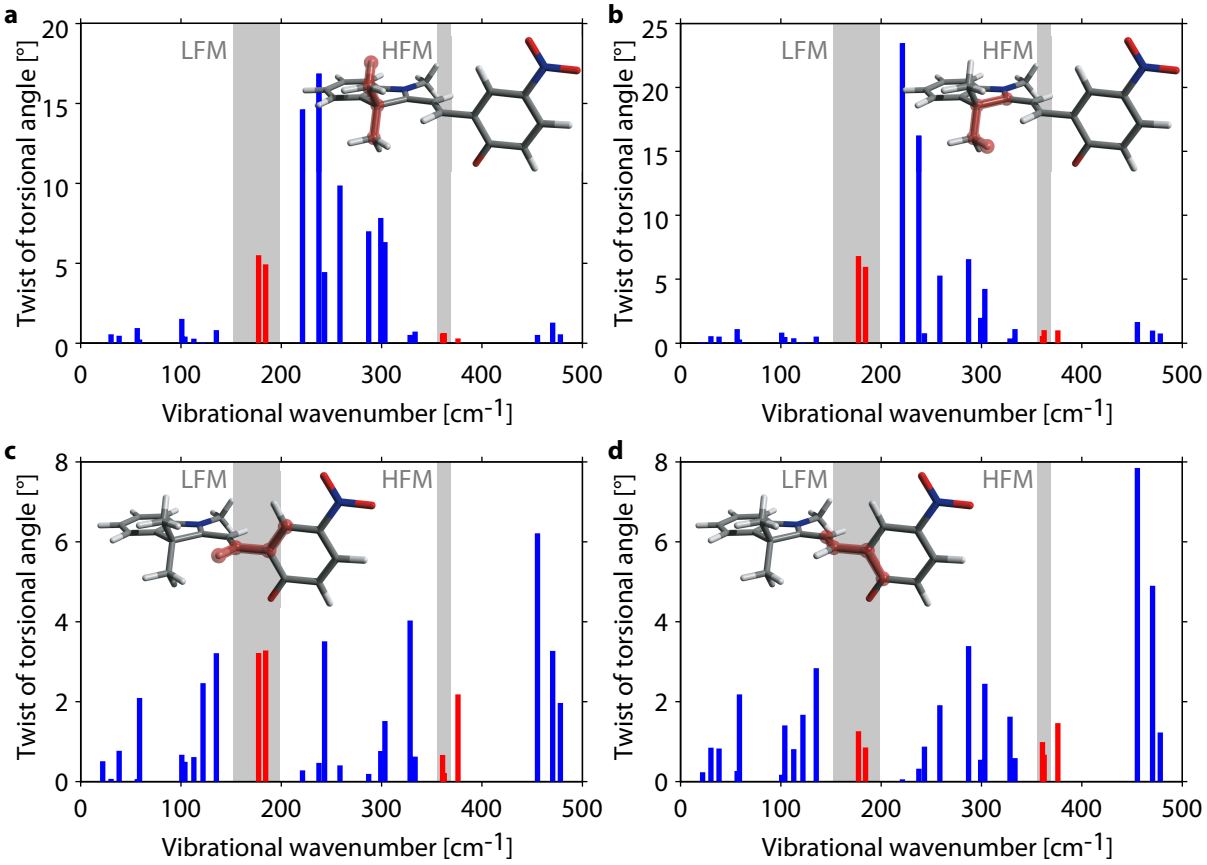

Figure A.3 | Calculated twisting amplitudes of selected torsional angles (highlighted in red in the molecular structure) for the S_1 low-frequency normal modes at the transition-state geometry. (a) The C–C–C–H torsional angle connecting the two out-of-plane methyl groups is not affected by normal modes below 150 cm^{-1}. Mode 11 at 177 cm^{-1}, which is in the experimentally observed wavenumber region, is the lowest-frequency normal mode that leads to a significant twisting of the torsional angle. (b) This is also the case for the C–C–C–H torsional angle describing a twisting of the methyl group with respect to the pyrrole moiety. (c) No dominant normal mode is identified on the basis of the H–C–C–C torsional motion along the methine chain where isomerization occurs. (d) This is also the case for the C–C–C–C torsional angle γ along the methine backbone. Figure adapted from Ref. [4].

low-frequency range by mode 12 at 185 cm^{-1}, which is consistent with the observed lower-frequency mode (LFM), and modes 22 and 23 at 361 cm^{-1} and 362 cm^{-1}, respectively.

A.3.3 Torsional Motions

As *cis-trans* isomerizations involve a torsional motion around one or several molecular bonds, torsional motions are expected to play a significant role in such a photoreaction. We analyzed the change of all torsional angles (also called dihedral angle and defined as the angle between two planes each of which is spanned by two adjacent molecular bonds, i.e. each torsional angle is defined by the spatial coordinates of four atoms)

caused by *cis-trans* isomerization in the excited state. The geometry optimizations show that (apart from the torsional motion in the methine chain resulting from *cis-trans* isomerization itself) the torsional angles defined by the two out-of-plane methyl groups are most affected by the photoreaction.

In analogy to the bond lengths and bond angles discussed above, all molecular normal modes were analyzed regarding their influence on the molecular torsional angles. The twisting amplitudes of two selected C–C–C–H torsional angles (highlighted in red) as a function of the normal-mode wavenumber are shown in Figs. A.3(a) and A.3(b) for all lower-frequency vibrational modes. The two depicted angles describe either a torsion of one of the methyl groups compared to the opposing methyl group [Fig. A.3(a)] or a twisting of a methyl group with respect to the pyrrole moiety [Fig. A.3(b)]. It becomes obvious that the methyl groups are not significantly affected by the molecular normal modes 1-10 at vibrational wavenumbers below 150 cm^{-1}. Figures A.3(a) and A.3(b) also show that normal modes 11 and 12 at 177 and 185 cm^{-1} are the lowest-frequency modes that involve a notable torsional motion of the methyl groups. Both modes are located in the experimentally observed lower-frequency range (LFM).

In Figs. A.3(c) and A.3(d) C–C–C–H and C–C–C–C torsional angles are analyzed that describe the tilting of the benzene ring with respect to the methine chain by rotation of the C–C bond around which isomerization is observed. No dominant molecular normal mode can be deduced from Figs. A.3(c) and A.3(d) which leads to the conclusion that the observed vibrational motion is not a pure torsional motion around the isomerizing C–C bond.

A.4 Auxiliary Calculations for Section 6.3

In the following a detailed derivation of Eqs. (6.26)–(6.33) for δ_{ω_n,t_m} and χ_{ω_n,t_m} as a function of the ellipticity ϵ_{ω_n,t_m} and the orientation angle θ_{ω_n,t_m} is given. The subscript ω_n,t_m will be omitted for reasons of clarity. The calculations are adopted from Ref. [334].

We start with Eqs. (6.21) and (6.22)

$$\epsilon = \frac{1}{2}\arcsin[\sin(2\chi)\sin\delta] \tag{A.1}$$

$$\theta = \frac{1}{2}\arctan[\tan(2\chi)\cos\delta] \tag{A.2}$$

and rewrite both equations to

$$\sin(2\epsilon) = \sin(2\chi)\sin\delta = \sin(2\chi)\sqrt{(1-\cos^2\delta)} \tag{A.3}$$

$$\tan(2\theta) = \tan(2\chi)\cos\delta. \tag{A.4}$$

Solving Eq. (A.3) for $\cos^2\delta$ one obtains

$$\cos^2\delta = 1 - \frac{\sin^2(2\epsilon)}{\sin^2(2\chi)} \tag{A.5}$$

and combining this with the squared of Eq. (A.4) yields

$$\tan^2(2\theta) = \tan^2(2\chi)\left(1 - \frac{\sin^2(2\epsilon)}{\sin^2(2\chi)}\right). \tag{A.6}$$

This expression can be rearranged to

$$\tan^2(2\theta)\cos^2(2\chi) = \sin^2(2\chi) - \sin^2(2\epsilon). \tag{A.7}$$

Adding $\cos^2(2\chi)$ to this term and by using the relationship $\sin^2(2\chi)+\cos^2(2\chi) = 1$ yields

$$\cos^2(2\chi) = \frac{1-\sin^2(2\epsilon)}{1+\tan^2(2\theta)}. \tag{A.8}$$

Equation (A.8) can now be solved for χ:

$$\chi = \frac{1}{2}\arccos\left[\pm\sqrt{\frac{1-\sin^2(2\epsilon)}{1+\tan^2(2\theta)}}\right] \tag{A.9}$$

which can be simplified to

$$\chi = \frac{1}{2}\arccos[\cos(2\epsilon)\cos(2\theta)] \tag{A.10}$$

finally yielding Eq. (6.31) of Sect. 6.3. In the last step the two relationships $\cos x = \sqrt{1-\sin^2 x}$ and $\cos x = \frac{1}{\sqrt{1+\tan^2 x}}$ are used. Hence, the auxiliary angle χ may solely be expressed as a function of ϵ and θ.

In order to further describe the phase difference δ as a function of these two parameters we add $\sin^2(2\chi)$ to Eq. (A.8) which results in

$$\sin^2(2\chi) = \sqrt{1 - \frac{1 - \sin^2(2\epsilon)}{1 + \tan^2(2\theta)}}. \tag{A.11}$$

Inserting Eq. (A.11) into Eq. (A.5) yields

$$\cos^2\delta = 1 - \frac{\sin^2(2\epsilon)}{1 - \cos^2(2\epsilon)\cos^2(2\theta)} \tag{A.12}$$

from which the following expression for δ is obtained:

$$\cos\delta = \pm\sqrt{1 - \frac{\sin^2(2\epsilon)}{1 - \cos^2(2\epsilon)\cos^2(2\theta)}} \tag{A.13}$$

$$\delta = \arccos\left(\pm\sqrt{1 - \frac{\sin^2(2\epsilon)}{1 - \cos^2(2\epsilon)\cos^2(2\theta)}}\right) \tag{A.14}$$

Considering the possible values achieved with Eq. (A.14) it becomes evident that the required range of $\delta \in [-\pi,\pi]$ is not entirely covered by this expression. By accounting for the symmetry

$$\cos(\delta) = \cos(-\delta) \tag{A.15}$$

of the cosine function in Eq. (A.14) we then obtain a correct expression of δ as a function of ϵ and θ:

$$\delta = \begin{cases} +\arccos\left[+\sqrt{1-c}\right], \forall\epsilon \geq 0 \wedge \theta \geq 0 \\ +\arccos\left[-\sqrt{1-c}\right], \forall\epsilon \geq 0 \wedge \theta < 0 \\ -\arccos\left[-\sqrt{1-c}\right], \forall\epsilon < 0 \wedge \theta < 0 \\ -\arccos\left[+\sqrt{1-c}\right], \forall\epsilon < 0 \wedge \theta_{\omega_n,t_m} \geq 0 \end{cases} \tag{A.16}$$

where

$$c = \frac{\sin^2(2\epsilon)}{1 - \cos^2(2\epsilon)\cos^2(2\theta)}. \tag{A.17}$$

As given behind the curly bracket, the four cases of Eq. (A.16) determine the signs needed for the calculation of δ depending on in which of the four quadrants of the Poincaré plane the polarization is defined.

List of Abbreviations

2D	two-dimensional
2D-NMR	two-dimensional nuclear magnetic resonance
2D-IR	two-dimensional infrared
3D	three-dimensional
BBO	β-Barium borate
CEP	carrier envelope phase
CI	conical intersection
CPA	chirped pulse amplification
cw	continuous wave
DADS	decay-associated difference spectra
DFG	difference-frequency generation
ESA	excited-state absorption
Fl	fluorescence
FROG	frequency-resolved optical gating
FWHM	full width at half maximum
FWM	four-wave mixing
GSA	ground-state absorption
GSB	ground-state bleaching
HFM	high-frequency mode
IC	internal conversion
IRF	instrument response function
ISC	intersystem crossing
ITO	indium tin oxide
JTFR	joint time–frequency representations
LCD	liquid-crystal display
LFM	low-frequency mode
NIR	near infrared
NOPA	noncollinear optical parametric amplification
OD	optical density
OPA	optical parametric amplification
OR	optical rectification
P	pump pulse
PA	photoproduct absorption
Pr	probe pulse
Ph	phosphorescence
PES	potential energy surface
R	repump pulse
RMS	root mean square

RWA rotating-wave approximation
SE stimulated emission
SFG sum-frequency generation
SHG second-harmonic generation
SLM spatial-light modulator
SPM self-phase modulation
STFT short-time Fourier transform
SVEA slowly varying envelope approximation
TE2D triggered-exchange 2D
TEM transversal electromagnetic mode
TOD third-order dispersion
TS transition state
UV ultraviolet
VC vibrational cooling
WLG white-light generation

Bibliography

[1] C. Consani, S. Ruetzel, P. Nuernberger, and T. Brixner.
Quantum Control Spectroscopy of Competing Reaction Paths in a Molecular Switch.
in preparation (2014).

[2] S. Ruetzel, M. Diekmann, P. Nuernberger, C. Walter, B. Engels, and T. Brixner.
Photoisomerization Among Ring-Open Merocyanines. Part I: Reaction Dynamics and Wave-Packet Oscillations Induced by Tunable Femtosecond Pulses.
submitted for publication (2014).

[3] C. Walter, S. Ruetzel, M. Diekmann, P. Nuernberger, T. Brixner, and B. Engels.
Photoisomerization Among Ring-Open Merocyanines. Part II: A Computational Study.
submitted for publication (2014).

[4] S. Ruetzel, M. Diekmann, P. Nuernberger, C. Walter, B. Engels, and T. Brixner.
Multidimensional spectroscopy of photoreactivity.
Proc. Natl. Acad. Sci. USA, in press, doi: 10.1073/pnas.1323792111 (2014).

[5] S. Ruetzel, M. Kullmann, J. Buback, P. Nuernberger, and T. Brixner.
Tracing the steps of photoinduced chemical reactions in organic molecules by coherent two-dimensional electronic spectroscopy using triggered exchange.
Phys. Rev. Lett. **110**, 148305 (2013).

[6] S. Ruetzel, M. Kullmann, J. Buback, P. Nuernberger, and T. Brixner.
Exploring Higher-Lying Electronic States of a Molecular Switch by Coherent Triggered-Exchange 2D Electronic Spectroscopy.
EPJ Web of Conferences **41**, 05001 (2013).

[7] S. Rützel, A. Krischke, and T. Brixner.
The von Neumann representation as a joint time–frequency parameterization for polarization-shaped femtosecond laser pulses.
Appl. Phys. B **107**, 1–9 (2012).

[8] M. Kullmann, S. Ruetzel, J. Buback, P. Nuernberger, and T. Brixner.
Reaction Dynamics of a Molecular Switch Unveiled by Coherent Two-Dimensional Electronic Spectroscopy.
J. Am. Chem. Soc. **133**, 13074–13080 (2011).

[9] S. Ruetzel, C. Stolzenberger, F. Dimler, D. J. Tannor, and T. Brixner.
Adaptive coherent control using the von Neumann basis.
Phys. Chem. Chem. Phys. **13**, 8627–8636 (2011).

[10] D. Reitzenstein, T. Quast, F. Kanal, M. Kullmann, S. Ruetzel, M. S. Hammer, C. Deibel, V. Dyakonov, T. Brixner, and C. Lambert.
Synthesis and Electron Transfer Characteristics of a Neutral, Low-Band-Gap, Mixed-Valence Polyradical.
Chem. Mater. **22**, 6641–6655 (2010).

[11] S. Ruetzel, C. Stolzenberger, S. Fechner, F. Dimler, T. Brixner, and D. J. Tannor.
Molecular quantum control landscapes in von Neumann time-frequency phase space.
J. Chem. Phys. **133**, 164510 (2010).

[12] A. H. Zewail.
Femtochemistry: atomic-scale dynamics of the chemical bond.
J. Phys. Chem. A **104**, 5660–5694 (2000).

[13] A. H. Zewail.
Femtochemistry. Past, present, and future.
Pure Appl. Chem. **72**, 2219–2231 (2000).

[14] J. D. Hybl, A. W. Albrecht, S. M. Gallagher Faeder, and D. M. Jonas.
Two-dimensional electronic spectroscopy.
Chem. Phys. Lett. **297**, 307–313 (1998).

[15] J. D. Hybl, A. A. Ferro, and D. M. Jonas.
Two-dimensional Fourier transform electronic spectroscopy.
J. Chem. Phys. **115**, 6606 (2001).

[16] S. Mukamel.
Multidimensional Femtosecond Correlation Spectroscopies of Electronic and Vibrational Excitations.
Annu. Rev. Phys. Chem. **51**, 691–729 (2000).

[17] D. M. Jonas.
Two-dimensional femtosecond spectroscopy.
Annu. Rev. Phys. Chem. **54**, 425–463 (2003).

[18] R. M. Hochstrasser.
Two-dimensional spectroscopy at infrared and optical frequencies.
Proc. Natl. Acad. Sci. USA **104**, 14190–14196 (2007).

[19] M. Cho.
Coherent two-dimensional optical spectroscopy.
Chem. Rev. **108**, 1331–1418 (2008).

[20] J. P. Ogilvie and K. J. Kubarych.
Multidimensional Electronic and Vibrational Spectroscopy: An Ultrafast Probe of Molecular Relaxation and Reaction Dynamics (Chapter 5).
Adv. At. Mol. Opt. Phys. **57**, 249–321 (2009).

[21] T. Brixner, J. Stenger, H. M. Vaswani, M. Cho, R. E. Blankenship, and G. R. Fleming.
Two-dimensional spectroscopy of electronic couplings in photosynthesis.
Nature **434**, 625–628 (2005).

[22] G. S. Engel, T. R. Calhoun, E. L. Read, T. Ahn, T. Mančal, Y. Cheng, R. E. Blankenship, and G. R. Fleming.
Evidence for wavelike energy transfer through quantum coherence in photosynthetic systems.
Nature **446**, 782–786 (2007).

[23] E. Collini, C. Y. Wong, K. E. Wilk, P. M. G. Curmi, P. Brumer, and G. D. Scholes.
Coherently wired light-harvesting in photosynthetic marine algae at ambient temperature.
Nature **463**, 644–647 (2010).

[24] J. A. Myers, K. L. M. Lewis, F. D. Fuller, P. F. Tekavec, C. F. Yocum, and J. P. Ogilvie.
Two-Dimensional Electronic Spectroscopy of the D1-D2-cyt b559 Photosystem II Reaction Center Complex.
J. Phys. Chem. Lett. **1**, 2774–2780 (2010).

[25] M. Cho, H. M. Vaswani, T. Brixner, J. Stenger, and G. R. Fleming.
Exciton Analysis in 2D Electronic Spectroscopy.
J. Phys. Chem. B **109**, 10542–10556 (2005).

[26] A. V. Pisliakov, T. Mančal, and G. R. Fleming.
Two-dimensional optical three-pulse photon echo spectroscopy. II. Signatures of coherent electronic motion and exciton population transfer in dimer two-dimensional spectra.
J. Chem. Phys. **124**, 234505 (2006).

[27] P. Kjellberg, B. Brüggemann, and T. Pullerits.
Two-dimensional electronic spectroscopy of an excitonically coupled dimer.
Phys. Rev. B **74** (2006).

[28] F. Milota, J. Sperling, A. Nemeth, T. Mančal, and H. F. Kauffmann.
Two-dimensional electronic spectroscopy of molecular excitons.
Acc. Chem. Res. **42**, 1364–1374 (2009).

[29] S. Woutersen, Y. Mu, G. Stock, and P. Hamm.
Hydrogen-Bond Lifetime Measured by Time-Resolved 2D-IR Spectroscopy: N-Methylacetamide in Methanol.
Chem. Phys. **266**, 137–147 (2001).

[30] J. B. Asbury, T. Steinel, C. Stromberg, K. J. Gaffney, I. R. Piletic, A. Goun, and M. D. Fayer.
Hydrogen Bond Dynamics Probed with Ultrafast Infrared Heterodyne-Detected Multidimensional Vibrational Stimulated Echoes.
Phys. Rev. Lett. **91**, 237402 (2003).

[31] J. Zheng, K. Kwak, J. Asbury, X. Chen, I. R. Piletic, and M. D. Fayer.
Ultrafast Dynamics of Solute-Solvent Complexation Observed at Thermal Equilibrium in Real Time.
Science **309**, 1338–1343 (2005).

[32] Y. S. Kim and R. M. Hochstrasser.
Chemical Exchange 2D IR of Hydrogen-Bond Making and Breaking.
Proc. Natl. Acad. Sci. USA **102**, 11185 –11190 (2005).

[33] J. Zheng, K. Kwak, J. Xie, and M. D. Fayer.
Ultrafast Carbon-Carbon Single-Bond Rotational Isomerization in Room-Temperature Solution.
Science **313**, 1951–1955 (2006).

[34] P. Hamm, J. Helbing, and J. Bredenbeck.
Two-Dimensional Infrared Spectroscopy of Photoswitchable Peptides.
Annu. Rev. Phys. Chem. **59**, 291–317 (2008).

[35] M. Fayer.
Dynamics of Liquids, Molecules, and Proteins Measured with Ultrafast 2D IR Vibrational Echo Chemical Exchange Spectroscopy.
Annu. Rev. Phys. Chem. **60**, 21–38 (2009).

[36] O. Bixner, V. Lukeš, T. Mančal, J. Hauer, F. Milota, M. Fischer, I. Pugliesi, M. Bradler, W. Schmid, E. Riedle, H. F. Kauffmann, and N. Christensson.
Ultrafast photo-induced charge transfer unveiled by two-dimensional electronic spectroscopy.
J. Chem. Phys. **136**, 204503–204503–12 (2012).

[37] C. Consani, G. Auböck, F. van Mourik, and M. Chergui.
Ultrafast Tryptophan-to-Heme Electron Transfer in Myoglobins Revealed by UV 2D Spectroscopy.
Science **339**, 1586–1589 (2013).

[38] P. Hamm.
Three-dimensional-IR spectroscopy: Beyond the two-point frequency fluctuation correlation function.
J. Chem. Phys. **124**, 124506 (2006).

[39] F. Ding and M. T. Zanni.
Heterodyned 3D IR spectroscopy.
Chem. Phys. **341**, 95–105 (2007).

[40] S. Garrett-Roe and P. Hamm.
What can we learn from three-dimensional infrared spectroscopy?
Acc. Chem. Res. **42**, 1412–1422 (2009).

[41] D. B. Turner, K. W. Stone, K. Gundogdu, and K. A. Nelson.
Three-dimensional electronic spectroscopy of excitons in GaAs quantum wells.
J. Chem. Phys. **131**, 144510 (2009).

[42] A. F. Fidler, E. Harel, and G. S. Engel.
Dissecting hidden couplings using fifth-order three-dimensional electronic spectroscopy.
J. Phys. Chem. Lett. **1**, 2876–2880 (2010).

[43] J. A. Davis, C. R. Hall, L. V. Dao, K. A. Nugent, H. M. Quiney, H. H. Tan, and C. Jagadish.
Three-dimensional electronic spectroscopy of excitons in asymmetric double quantum wells.
J. Chem. Phys. **135**, 044510 (2011).

[44] D. Hayes and G. S. Engel.
Extracting the excitonic Hamiltonian of the Fenna-Matthews-Olson complex using three-dimensional third-order electronic spectroscopy.
Biophys. J. **100**, 2043–2052 (2011).

[45] Z. Zhang, K. L. Wells, and H.-S. Tan.
Purely absorptive fifth-order three-dimensional electronic spectroscopy.
Opt. Lett. **37**, 5058–5060 (2012).

[46] H. Li, A. D. Bristow, M. E. Siemens, G. Moody, and S. T. Cundiff.
Unraveling quantum pathways using optical 3D Fourier-transform spectroscopy.
Nat. Commun. **4**, 1390 (2013).

[47] J. Diels and W. Rudolph.
Ultrashort Laser Pulse Phenomena.
Second edition. Academic Press, Burlington (2006).

[48] F. Träger.
Springer handbook of lasers and optics.
Springer handbooks, second edition. Springer, Berlin (2012).

[49] A. Apolonski, A. Poppe, G. Tempea, C. Spielmann, T. Udem, R. Holzwarth, T. W. Hänsch, and F. Krausz.
Controlling the Phase Evolution of Few-Cycle Light Pulses.
Phys. Rev. Lett. **85**, 740–743 (2000).

[50] D. J. Jones, S. A. Diddams, J. K. Ranka, A. Stentz, R. S. Windeler, J. L. Hall, and S. T. Cundiff.
Carrier-Envelope Phase Control of Femtosecond Mode-Locked Lasers and Direct Optical Frequency Synthesis.
Science **288**, 635 –639 (2000).

[51] G. G. Paulus, F. Grasbon, H. Walther, P. Villoresi, M. Nisoli, S. Stagira, E. Priori, and S. D. Silvestri.
Absolute-phase phenomena in photoionization with few-cycle laser pulses.
Nature **414**, 182–184 (2001).

[52] A. Baltuška, T. Udem, M. Uiberacker, M. Hentschel, E. Goulielmakis, C. Gohle, R. Holzwarth, V. S. Yakovlev, A. Scrinzi, T. W. Hänsch, and F. Krausz.
Attosecond control of electronic processes by intense light fields.
Nature **421**, 611–615 (2003).

[53] D. Meshulach and Y. Silberberg.
Coherent quantum control of multiphoton transitions by shaped ultrashort optical pulses.
Phys. Rev. A **60**, 1287 (1999).

[54] M. Renard, R. Chaux, B. Lavorel, and O. Faucher.
Pulse trains produced by phase-modulation of ultrashort optical pulses: tailoring and characterization.
Opt. Express **12**, 473–482 (2004).

[55] G. Vogt, P. Nuernberger, R. Selle, F. Dimler, T. Brixner, and G. Gerber.
Analysis of femtosecond quantum control mechanisms with colored double pulses.
Phys. Rev. A **74**, 033413 (2006).

[56] P. Nuernberger.
Differences and analogies between linearly chirped and colored double pulses in the femtosecond regime.
Opt. Commun. **282**, 227–235 (2009).

[57] N. Dudovich, D. Oron, and Y. Silberberg.
Single-pulse coherently controlled nonlinear Raman spectroscopy and microscopy.
Nature **418**, 512–514 (2002).

[58] N. Dudovich, D. Oron, and Y. Silberberg.
Single-pulse coherent anti-Stokes Raman spectroscopy in the fingerprint spectral region.
J. Chem. Phys. **118**, 9208–9215 (2003).

[59] D. Meshulach and Y. Silberberg.
Coherent quantum control of two-photon transitions by a femtosecond laser pulse.
Nature **396**, 239–242 (1998).

[60] M. Wollenhaupt, A. Präkelt, C. Sarpe-Tudoran, D. Liese, T. Bayer, and T. Baumert.
Femtosecond strong-field quantum control with sinusoidally phase-modulated pulses.
Phys. Rev. A **73**, 063409 (2006).

[61] L. Cohen.
Time frequency-distributions - a review.
Proc. IEEE **77**, 941–981 (1989).

[62] L. Cohen.
Time Frequency Analysis: Theory and Applications.
Facsimile edition. Prentice Hall (1995).

[63] S. Qian and D. Chen.
Joint Time-Frequency Analysis: Method and Application.
Prentice Hall, New York (1996).

[64] P. Flandrin.
Time-Frequency/Time-Scale Analysis.
First edition. Academic Press, Paris (1998).

[65] L. Debnath.
Wavelet Transforms and Time Frequency Signal Analysis.
Birkhäuser, Boston (2001).

[66] C. Blatter.
Wavelets. Eine Einführung.
Second edition. Vieweg+Teubner (2003).

[67] Y. Nievergelt.
Wavelets made easy.
Modern Birkhäuser classics, reprint of the 2001 ed. edition. Springer, New York [u.a.] (2013).

[68] S. Fechner, F. Dimler, T. Brixner, G. Gerber, and D. J. Tannor.
The von Neumann picture: A new representation for ultrashort laser pulses.
Opt. Express **15**, 15387–15401 (2007).

[69] A. Rodenberg, S. Fechner, F. Dimler, D. J. Tannor, and T. Brixner.
Experimental implementation of ultrashort laser pulses in the von Neumann picture.
Appl. Phys. B **93**, 763–772 (2008).

[70] F. Dimler, S. Fechner, A. Rodenberg, T. Brixner, and D. J. Tannor.
Accurate and efficient implementation of the von Neumann representation for laser pulses with discrete and finite spectra.
New J. Phys. **11**, 105052 (2009).

[71] E. P. Wigner.
On the Quantum Correction For Thermodynamic Equilibrium.
Phys. Rev. **40**, 749–759 (1932).

[72] W. Schleich.
Quantum optics in phase space.
First edition. Wiley-VCH, Berlin [u.a.] (2001).

[73] M. O. Scully.
Quantum optics.
Fifth edition. Cambridge Univ. Press, Cambridge [u.a.] (2006).

[74] J. Paye.
The chronocyclic representation of ultrashort light pulses.
IEEE J. Quantum Electron. **28**, 2262–2273 (1992).

[75] B. Kohler, J. L. Krause, F. Raksi, C. Rose-Petruck, R. M. Whitnell, K. R. Wilson, V. V. Yakovlev, Y. Yan, and S. Mukamel.
Mode-locking matter with light.
J. Phys. Chem. **97**, 12602–12608 (1993).

[76] B. Kohler, J. L. Krause, F. Raksi, K. R. Wilson, V. V. Yakovlev, R. M. Whitnell, and Y. Yan.
Controlling the Future of Matter.
Acc. Chem. Res. **28**, 133–140 (1995).

[77] T. Meier and S. Mukamel.
Femtosecond Spectroscopic Signatures of Electronic Correlations in Conjugated Polyenes and Semiconductor Nanostructures.
Phys. Rev. Lett. **77**, 3471–3474 (1996).

[78] R. Hudson.
When is the Wigner quasi-probability density non-negative?
Rep. Math. Phys. **6**, 249–252 (1974).

[79] D. Lalović, D. M. Davidović, and N. Bijedić.
Quantum mechanics in terms of non-negative smoothed Wigner functions.
Phys. Rev. A **46**, 1206–1212 (1992).

[80] R. O'Connell and E. Wigner.
Some properties of a non-negative quantum-mechanical distribution function.
Phys. Lett. A **85**, 121–126 (1981).

[81] K. Husimi.
Some formal properties of the density matrix.
Proc. Phys. Math. Soc. Japan **22**, 264–314 (1940).

[82] J. R. Klauder and B. Skagerstam.
Coherent states.
World Scientific, Singapore (1985).

[83] J. Gazeau.
Coherent states in quantum physics.
WILEY-VCH, Weinheim (2009).

[84] D. J. Tannor.
Introduction to Quantum Mechanics: A Time-Dependent Perspective.
University Science Books, Sausalito (2007).

[85] A. M. Perelomov.
On the completeness of a system of coherent states.
Theor. Math. Phys. **6**, 156–164 (1971).

[86] M. Born and E. Wolf.
Principles of Optics: Electromagnetic Theory of Propagation, Interference and Diffraction of Light.
7th edition. Cambridge University Press (1999).

[87] E. Hecht.
Optics.
Fourth edition. Addison Wesley, San Francisco; Munich [u.a.] (2002).

[88] T. Brixner and G. Gerber.
Femtosecond polarization pulse shaping.
Opt. Lett. **26**, 557–559 (2001).

[89] T. Brixner, G. Krampert, P. Niklaus, and G. Gerber.
Generation and characterization of polarization-shaped femtosecond laser pulses.
Appl. Phys. B **74**, 133–144 (2002).

[90] M. A. Porras.
Propagation-induced changes in the instantaneous polarization state, phase, and carrier–envelope phase of few-cycle pulsed beams.
J. Opt. Soc. Am. B **30**, 1652–1659 (2013).

[91] T. Brixner.
Poincaré representation of polarization-shaped femtosecond laser pulses.
Appl. Phys. B **76**, 531–540 (2003).

[92] H. Poincaré.
Théorie mathématique de la lumière II. Nouvelles études sur la diffraction.–Théorie de la dispersion de Helmholtz., volume 2.
Georges Carré, Paris (1892).

[93] D. H. Goldstein.
Polarized light.
Optical engineering; 83, second edition. Dekker, New York (2003).

[94] A. E. Siegman.
Lasers.
University Science Books, Sausalito (1986).

[95] D. Meschede.
Optics, light and lasers.
Physics textbook, second edition. Wiley-VCH, Weinheim (2007).

[96] R. W. Boyd.
Nonlinear Optics.
Third edition. Academic Press, Burlington (2008).

[97] Y. R. Shen.
Principles of Nonlinear Optics.
Wiley classics edition. Wiley & Sons, New York, NY (2002).

[98] P. A. Franken, A. E. Hill, C. W. Peters, and G. Weinreich.
Generation of Optical Harmonics.
Phys. Rev. Lett. **7**, 118 (1961).

[99] R. Menzel.
Photonics.
Second edition. Springer, Berlin [u.a.] (2007).

[100] M. Bass.
Handbook of Optics.
Second edition. McGraw-Hill, New York (1995).

[101] D. Eimerl, L. Davis, S. Velsko, E. K. Graham, and A. Zalkin.
Optical, mechanical, and thermal properties of barium borate.
J. Appl. Phys. **62**, 1968–1983 (1987).

[102] R. R. Alfano.
The Supercontinuum Laser Source.
Second edition. Springer, New York (2006).

[103] R. Alfano and S. Shapiro.
Observation of Self-Phase Modulation and Small-Scale Filaments in Crystals and Glasses.
Phys. Rev. Lett. **24**, 592–594 (1970).

[104] R. L. Fork, C. V. Shank, C. Hirlimann, R. Yen, and W. J. Tomlinson.
Femtosecond white-light continuum pulses.
Opt. Lett. **8**, 1–3 (1983).

[105] A. Brodeur and S. L. Chin.
Band-Gap Dependence of the Ultrafast White-Light Continuum.
Phys. Rev. Lett. **80**, 4406 (1998).

[106] C. Nagura, A. Suda, H. Kawano, M. Obara, and K. Midorikawa.
Generation and Characterization of Ultrafast White-Light Continuum in Condensed Media.
Appl. Opt. **41**, 3735–3742 (2002).

[107] M. Bradler, P. Baum, and E. Riedle.
Femtosecond continuum generation in bulk laser host materials with sub-μJ pump pulses.
Appl. Phys. B **97**, 561–574 (2009).

[108] A. Major, F. Yoshino, I. Nikolakakos, J. S. Aitchison, and P. W. E. Smith.
Dispersion of the nonlinear refractive index in sapphire.
Opt. Lett. **29**, 602–604 (2004).

[109] G. Yang and Y. R. Shen.
Spectral broadening of ultrashort pulses in a nonlinear medium.
Opt. Lett. **9**, 510–512 (1984).

[110] B. Gross and J. T. Manassah.
Supercontinuum in the anomalous group-velocity dispersion region.
J. Opt. Soc. Am. B **9**, 1813–1818 (1992).

[111] A. L. Gaeta.
Catastrophic Collapse of Ultrashort Pulses.
Phys. Rev. Lett. **84**, 3582–3585 (2000).

[112] J. M. Dudley, G. Genty, and S. Coen.
Supercontinuum generation in photonic crystal fiber.
Rev. Mod. Phys. **78**, 1135 (2006).

[113] J. J. Sakurai.
Modern Quantum Mechanics.
Rev. edition. Addison Wesley (1993).

[114] P. Klán and J. Wirz.
Photochemistry of organic compounds.
Postgraduate chemistry series, first edition. Wiley, Chichester (2009).

[115] M. Born and R. Oppenheimer.
Zur Quantentheorie der Molekeln.
Annalen der Physik **389**, 457–484 (1927).

[116] M. Kasha.
Characterization of electronic transitions in complex molecules.
Discuss. Faraday Soc. **9**, 14 (1950).

[117] N. J. Turro, V. Ramamurthy, and J. C. Scaiano.
Modern Molecular Photochemistry of Organic Molecules.
Palgrave Macmillan (2010).

[118] D. R. Yarkony.
Diabolical Conical Intersections.
Rev. Mod. Phys. **68**, 985 (1996).

[119] D. R. Yarkony.
Conical Intersections: The New Conventional Wisdom.
J. Phys. Chem. A **105**, 6277–6293 (2001).

[120] W. Domcke, D. R. Yarkony, and H. Köppel.
Conical Intersections: Electronic Structure, Dynamics and Spectroscopy.
World Scientific Publishing, Singapore (2004).

[121] W. Domcke and D. R. Yarkony.
Role of Conical Intersections in Molecular Spectroscopy and Photoinduced Chemical Dynamics.
Annu. Rev. Phys. Chem. **63**, 325–352 (2012).

[122] R. Leonhardt, W. Holzapfel, W. Zinth, and W. Kaiser.
Terahertz quantum beats in molecular liquids.
Chem. Phys. Lett. **133**, 373–377 (1987).

[123] D. Mcmorrow, W. T. Lotshaw, and G. A. Kenney-Wallace.
Femtosecond Raman-induced Kerr effect. Temporal evolution of the vibrational normal modes in halogenated methanes.
Chem. Phys. Lett. **145**, 309–314 (1988).

[124] J. Chesnoy and A. Mokhtari.
Resonant impulsive-stimulated Raman scattering on malachite green.
Phys. Rev. A **38**, 3566–3576 (1988).

[125] P. C. Becker, H. L. Fragnito, J. Y. Bigot, C. H. B. Cruz, R. L. Fork, and C. V. Shank.
Femtosecond photon echoes from molecules in solution.
Phys. Rev. Lett. **63**, 505–507 (1989).

[126] T. Baumert, M. Grosser, R. Thalweiser, and G. Gerber.
Femtosecond Time-Resolved Molecular Multiphoton Ionization: The Na_2 System.
Phys. Rev. Lett. **67**, 3753–3756 (1991).

[127] T. S. Rose, M. J. Rosker, and A. H. Zewail.
Femtosecond real-time observation of wave packet oscillations (resonance) in dissociation reactions.
J. Chem. Phys. **88**, 6672–6673 (1988).

[128] A. Mokhtari, P. Cong, J. L. Herek, and A. H. Zewail.
Direct femtosecond mapping of trajectories in a chemical reaction.
Nature **348**, 225–227 (1990).

[129] E. D. Potter, J. L. Herek, S. Pedersen, Q. Liu, and A. H. Zewail.
Femtosecond laser control of a chemical reaction.
Nature **355**, 66–68 (1992).

[130] R. Schoenlein, L. Peteanu, R. A. Mathies, and C. V. Shank.
The First Step in Vision: Femtosecond Isomerization of Rhodopsin.
Science **254**, 412–415 (1991).

[131] M. H. Vos, F. Rappaport, J.-C. Lambry, J. Breton, and J.-L. Martin.
Visualization of coherent nuclear motion in a membrane protein by femtosecond spectroscopy.
Nature **363**, 320–325 (1993).

[132] Q. Wang, R. W. Schoenlein, L. A. Peteanu, R. A. Mathies, and C. V. Shank.
Vibrationally Coherent Photochemistry in the Femtosecond Primary Event of Vision.
Science **266**, 422–424 (1994).

[133] M. Morgen, W. Price, L. Hunziker, P. Ludowise, M. Blackwell, and Y. Chen.
Femtosecond Raman-induced polarization spectroscopy studies of rotational coherence in O_2, N_2 and CO_2.
Chem. Phys. Lett. **209**, 1–9 (1993).

[134] B. Friedrich and D. Herschbach.
Alignment and Trapping of Molecules in Intense Laser Fields.
Phys. Rev. Lett. **74**, 4623 (1995).

[135] T. Seideman.
Rotational excitation and molecular alignment in intense laser fields.
J. Chem. Phys. **103**, 7887–7896 (1995).

[136] H. Sakai, C. P. Safvan, J. J. Larsen, K. M. Hilligsøe, K. Hald, and H. Stapelfeldt.
Controlling the alignment of neutral molecules by a strong laser field.
J. Chem. Phys. **110**, 10235 (1999).

[137] H. Stapelfeldt and T. Seideman.
Colloquium: Aligning molecules with strong laser pulses.
Rev. Mod. Phys. **75**, 543–557 (2003).

[138] M. K. Lawless and R. A. Mathies.
Excited-state structure and electronic dephasing time of Nile blue from absolute resonance Raman intensities.
J. Chem. Phys. **96**, 8037–8045 (1992).

[139] C. J. Bardeen and C. V. Shank.
Femtosecond electronic dephasing in large molecules in solution using mode suppression.
Chem. Phys. Lett. **203**, 535–539 (1993).

[140] T. Joo and A. Albrecht.
Electronic dephasing studies of molecules in solution at room temperature by femtosecond degenerate four wave mixing.
Chem. Phys. **176**, 233–247 (1993).

[141] P. Cong, H. P. Deuel, and J. D. Simon.
Using optical coherence to measure the ultrafast electronic dephasing of large molecules in room-temperature liquids.
Chem. Phys. Lett. **212**, 367–373 (1993).

[142] R. L. Fork, B. I. Greene, and C. V. Shank.
Generation of optical pulses shorter than 0.1 psec by colliding pulse mode locking.
Appl. Phys. Lett. **38**, 671–672 (1981).

[143] A. Finch, G. Chen, W. Sleat, and W. Sibbett.
Pulse Asymmetry in the Colliding-pulse Mode-locked Dye Laser.
J. Mod. Opt. **35**, 345–354 (1988).

[144] H. Kubota, K. Kurokawa, and M. Nakazawa.
29-fsec pulse generation from a linear-cavity synchronously pumped dye laser.
Opt. Lett. **13**, 749–751 (1988).

[145] D. E. Spence, P. N. Kean, and W. Sibbett.
60-fsec pulse generation from a self-mode-locked Ti:sapphire laser.
Opt. Lett. **16**, 42–44 (1991).

[146] M. T. Asaki, C. Huang, D. Garvey, J. Zhou, H. C. Kapteyn, and M. M. Murnane.
Generation of 11-fs pulses from a self-mode-locked Ti:sapphire laser.
Opt. Lett. **18**, 977–979 (1993).

[147] A. Stingl, C. Spielmann, F. Krausz, and R. Szipöcs.
Generation of 11-fs pulses from a Ti:sapphire laser without the use of prisms.
Opt. Lett. **19**, 204–206 (1994).

[148] U. Morgner, F. X. Kärtner, S. H. Cho, Y. Chen, H. A. Haus, J. G. Fujimoto, E. P. Ippen, V. Scheuer, G. Angelow, and T. Tschudi.
Sub-two-cycle pulses from a Kerr-lens mode-locked Ti:sapphire laser.
Opt. Lett. **24**, 411–413 (1999).

[149] R. Ell, U. Morgner, F. X. Kärtner, J. G. Fujimoto, E. P. Ippen, V. Scheuer, G. Angelow, T. Tschudi, M. J. Lederer, A. Boiko, and B. Luther-Davies.
Generation of 5-fs pulses and octave-spanning spectra directly from a Ti:sapphire laser.
Opt. Lett. **26**, 373–375 (2001).

[150] D. Strickland and G. Mourou.
Compression of amplified chirped optical pulses.
Opt. Commun. **56**, 219–221 (1985).

[151] P. Maine, D. Strickland, P. Bado, M. Pessot, and G. Mourou.
Generation of Ultrahigh Peak Power Pulses by Chirped Pulse Amplification.
IEEE J. Quantum Electron. **24**, 398–403 (1988).

[152] G. Cheriaux, P. Rousseau, F. Salin, J. P. Chambaret, B. Walker, and L. F. DiMauro.
Aberration-free stretcher design for ultrashort-pulse amplification.
Opt. Lett. **21**, 414–416 (1996).

[153] E. Treacy.
Optical Pulse Compression with Diffraction Gratings.
IEEE J. Quantum Electron. **QE 5**, 454–& (1969).

[154] G. Cerullo and S. D. Silvestri.
Ultrafast Optical Parametric Amplifiers.
Rev. Sci. Instrum. **74**, 1–18 (2003).

[155] T. Wilhelm, J. Piel, and E. Riedle.
Sub-20-fs pulses tunable across the visible from a blue-pumped single-pass noncollinear parametric converter.
Opt. Lett. **22**, 1494–1496 (1997).

[156] G. Cerullo, M. Nisoli, and S. D. Silvestri.
Generation of 11 fs pulses tunable across the visible by optical parametric amplification.
Appl. Phys. Lett. **71**, 3616–3618 (1997).

[157] G. Cerullo, M. Nisoli, S. Stagira, and S. D. Silvestri.
Sub-8-fs pulses from an ultrabroadband optical parametric amplifier in the visible.
Opt. Lett. **23**, 1283–1285 (1998).

[158] A. Shirakawa, I. Sakane, and T. Kobayashi.
Pulse-front-matched optical parametric amplification for sub-10-fs pulse generation tunable in the visible and near infrared.
Opt. Lett. **23**, 1292–1294 (1998).

[159] T. Kobayashi and A. Baltuska.
Sub-5 fs pulse generation from a noncollinear optical parametric amplifier.
Meas. Sci. Technol. **13**, 1671–1682 (2002).

[160] A. M. Weiner.
Femtosecond Pulse Shaping Using Spatial Light Modulators.
Rev. Sci. Instrum. **71**, 1929–1960 (2000).

[161] A. M. Weiner.
Ultrafast Optics.
First edition. John Wiley & Sons Inc., Hoboken (2009).

[162] A. Monmayrant, S. Weber, and B. Chatel.
A newcomer's guide to ultrashort pulse shaping and characterization.
J. Phys. B: At. Mol. Opt. Phys. **43**, 103001 (2010).

[163] A. M. Weiner.
Ultrafast optical pulse shaping: A tutorial review.
Opt. Commun. **284**, 3669–3692 (2011).

[164] A. M. Weiner, J. P. Heritage, and J. A. Salehi.
Encoding and decoding of femtosecond pulses.
Opt. Lett. **13**, 300–302 (1988).

[165] A. M. Weiner, J. P. Heritage, and E. M. Kirschner.
High-resolution femtosecond pulse shaping.
J. Opt. Soc. Am. B **5**, 1563–1572 (1988).

[166] A. Weiner, D. Leaird, J. Patel, and J. Wullert.
Programmable shaping of femtosecond optical pulses by use of 128-element liquid-crystal phase modulator.
IEEE J. Quantum Electron. **28**, 908–920 (1992).

[167] M. M. Wefers and K. A. Nelson.
Analysis of programmable ultrashort waveform generation using liquid-crystal spatial light modulators.
J. Opt. Soc. Am. B **12**, 1343–1362 (1995).

[168] J. Vaughan, T. Feurer, K. Stone, and K. Nelson.
Analysis of replica pulses in femtosecond pulse shaping with pixelated devices.
Opt. Express **14**, 1314–1328 (2006).

[169] M. Wefers and K. Nelson.
Space-time profiles of shaped ultrafast optical waveforms.
IEEE J. Quantum Electron. **32**, 161–172 (1996).

[170] F. Frei, A. Galler, and T. Feurer.
Space-time coupling in femtosecond pulse shaping and its effects on coherent control.
J. Chem. Phys. **130**, 034302–14 (2009).

[171] D. Brinks, R. Hildner, F. D. Stefani, and N. F. van Hulst.
Beating spatio-temporal coupling: implications for pulse shaping and coherent control experiments.
Opt. Express **19**, 26486–26499 (2011).

[172] D. Kane and R. Trebino.
Characterization of arbitrary femtosecond pulses using frequency-resolved optical gating.
IEEE J. Quantum Electron. **29**, 571–579 (1993).

[173] R. Trebino, K. W. DeLong, D. N. Fittinghoff, J. N. Sweetser, M. A. Krumbügel, B. A. Richman, and D. J. Kane.
Measuring Ultrashort Laser Pulses in the Time-Frequency Domain Using Frequency-Resolved Optical Gating.
Rev. Sci. Instrum. **68**, 3277–3295 (1997).

[174] R. Trebino.
Frequency-Resolved Optical Gating: The Measurement of Ultrashort Laser Pulses.
Har/Cdr edition. Springer Netherlands (2002).

[175] K. W. DeLong, R. Trebino, J. Hunter, and W. E. White.
Frequency-resolved optical gating with the use of second-harmonic generation.
J. Opt. Soc. Am. B **11**, 2206–2215 (1994).

[176] K. W. DeLong, D. N. Fittinghoff, R. Trebino, B. Kohler, and K. Wilson.
Pulse retrieval in frequency-resolved optical gating based on the method of generalized projections.
Opt. Lett. **19**, 2152–2154 (1994).

[177] I. Amat-Roldán, I. Cormack, P. Loza-Alvarez, E. Gualda, and D. Artigas.
Ultrashort Pulse Characterisation with SHG Collinear-FROG.
Opt. Express **12**, 1169–1178 (2004).

[178] G. Stibenz and G. Steinmeyer.
Interferometric frequency-resolved optical gating.
Opt. Express **13**, 2617–2626 (2005).

[179] A. Galler and T. Feurer.
Pulse Shaper Assisted Short Laser Pulse Characterization.
Appl. Phys. B **90**, 427–430 (2008).

[180] D. E. Wilcox, F. D. Fuller, and J. P. Ogilvie.
Fast second-harmonic generation frequency-resolved optical gating using only a pulse shaper.
Opt. Lett. **38**, 2980 (2013).

[181] R. G. W. Norrish and G. Porter.
Chemical Reactions Produced by Very High Light Intensities.
Nature **164**, 658 (1949).

[182] G. Porter.
Flash Photolysis and Spectroscopy. A New Method for the Study of Free Radical Reactions.
Proc. R. Soc. Lond. A **200**, 284–300 (1950).

[183] W. T. Pollard and R. A. Mathies.
Analysis of Femtosecond Dynamic Absorption Spectra of Nonstationary States.
Annu. Rev. Phys. Chem. **43**, 497–523 (1992).

[184] S. A. Kovalenko, A. L. Dobryakov, J. Ruthmann, and N. P. Ernsting.
Femtosecond Spectroscopy of Condensed Phases with Chirped Supercontinuum Probing.
Phys. Rev. A **59**, 2369–2384 (1999).

[185] U. Megerle, I. Pugliesi, C. Schriever, C. Sailer, and E. Riedle.
Sub-50 fs Broadband Absorption Spectroscopy with Tunable Excitation: Putting the Analysis of Ultrafast Molecular Dynamics on Solid Ground.
Appl. Phys. B **96**, 215–231 (2009).

[186] R. Berera, R. van Grondelle, and J. T. M. Kennis.
Ultrafast transient absorption spectroscopy: principles and application to photosynthetic systems.
Photosynth. Res. **101**, 105–118 (2009).

[187] J. Buback.
Femtochemistry of Pericyclic Reactions and Advances towards Chiral Control.
Dissertation, Universität Würzburg (2011).

[188] H. E. Lessing and A. V. Jena.
Separation of Rotational Diffusion and Level Kinetics in Transient Absorption Spectroscopy.
Chem. Phys. Lett. **42**, 213–217 (1976).

[189] I. H. M. van Stokkum, D. S. Larsen, and R. van Grondelle.
Global and Target Analysis of Time-Resolved Spectra.
Biochim. Biophys. Acta, Bioenerg. **1657**, 82–104 (2004).

[190] J. J. Snellenburg, S. P. Laptenok, R. Seger, K. M. Mullen, and I. H. M. van Stokkum.
Glotaran: a Java-Based Graphical User Interface for the R-Package TIMP.
J. Stat. Softw. **49**, 1–22 (2012).

[191] K. M. Mullen and I. H. M. van Stokkum.
TIMP: An R Package for Modeling Multi-way Spectroscopic Measurements.
J. Stat. Softw. **18**, 1–46 (2007).

[192] M. Rasmusson, A. N. Tarnovsky, E. Åkesson, and V. Sundström.
On the Use of Two-Photon Absorption for Determination of Femtosecond Pump-Probe Cross-Correlation Functions.
Chem. Phys. Lett. **335**, 201–208 (2001).

[193] K. Ekvall, P. van der Meulen, C. Dhollande, L. Berg, S. Pommeret, R. Naskrecki, and J. Mialocq.
Cross Phase Modulation Artifact in Liquid Phase Transient Absorption Spectroscopy.
J. Appl. Phys. **87**, 2340 (2000).

[194] M. Lorenc, M. Ziolek, R. Naskrecki, J. Karolczak, J. Kubicki, and A. Maciejewski.
Artifacts in Femtosecond Transient Absorption Spectroscopy.
Appl. Phys. B **74**, 19–27 (2002).

[195] B. Dietzek, T. Pascher, V. Sundström, and A. Yartsev.
Appearance of coherent artifact signals in femtosecond transient absorption spectroscopy in dependence on detector design.
Laser Phys. Lett. **4**, 38–43 (2007).

[196] W. P. Aue, E. Bartholdi, and R. R. Ernst.
Two-dimensional spectroscopy. Application to nuclear magnetic resonance.
J. Chem. Phys. **64**, 2229–2246 (1976).

[197] G. E. Martin.
Two-dimensional NMR methods for establishing molecular connectivity.
Methods in stereochemical analysis. VCH Publ., New York, NY [u.a.] (1988).

[198] R. R. Ernst.
Principles of nuclear magnetic resonance in one and two dimensions.
The international series of monographs on chemistry ; 14, reprint. edition. Clarendon Press, Oxford (2004).

[199] P. Hamm, M. Lim, and R. M. Hochstrasser.
Structure of the Amide I Band of Peptides Measured by Femtosecond Nonlinear-Infrared Spectroscopy.
J. Phys. Chem. B **102**, 6123–6138 (1998).

[200] M. C. Asplund, M. T. Zanni, and R. M. Hochstrasser.
Two-dimensional infrared spectroscopy of peptides by phase-controlled femtosecond vibrational photon echoes.
Proc. Natl. Acad. Sci. USA **97**, 8219–8224 (2000).

[201] M. T. Zanni and R. M. Hochstrasser.
Two-dimensional infrared spectroscopy: a promising new method for the time resolution of structures.
Curr. Opin. Struct. Biol. **11**, 516–522 (2001).

[202] T. Brixner, T. Mančal, I. V. Stiopkin, and G. R. Fleming.
Phase-Stabilized Two-Dimensional Electronic Spectroscopy.
J. Chem. Phys. **121**, 4221–4236 (2004).

[203] T. Brixner, I. V. Stiopkin, and G. R. Fleming.
Tunable Two-Dimensional Femtosecond Spectroscopy.
Opt. Lett. **29**, 884–886 (2004).

[204] M. L. Cowan, J. P. Ogilvie, and R. J. D. Miller.
Two-dimensional Spectroscopy Using Diffractive Optics Based Phased-Locked Photon Echoes.
Chem. Phys. Lett. **386**, 184–189 (2004).

[205] S. Mukamel.
Principles of Nonlinear Optical Spectroscopy.
First edition. Oxford University Press, New York (1995).

[206] M. Cho.
Two-Dimensional Optical Spectroscopy.
CRC Press, Boca Raton, FL (2009).

[207] P. Hamm and M. Zanni.
Concepts and Methods of 2D Infrared Spectroscopy.
First edition. Cambridge University Press, New York (2011).

[208] L. Lepetit, G. Chériaux, and M. Joffre.
Linear Techniques of Phase Measurement by Femtosecond Spectral Interferometry for Applications in Spectroscopy.
J. Opt. Soc. Am. B **12**, 2467–2474 (1995).

[209] C. Dorrer, N. Belabas, J. Likforman, and M. Joffre.
Experimental implementation of Fourier-transform spectral interferometry and its application to the study of spectrometers.
Appl. Phys. B **70**, 99–107 (2000).

[210] P. Tian, D. Keusters, Y. Suzaki, and W. S. Warren.
Femtosecond phase-coherent two-dimensional spectroscopy.
Science **300**, 1553–1555 (2003).

[211] P. F. Tekavec, G. A. Lott, and A. H. Marcus.
Fluorescence-detected two-dimensional electronic coherence spectroscopy by acousto-optic phase modulation.
J. Chem. Phys. **127**, 214307–21 (2007).

[212] S. Rahav and S. Mukamel.
Multidimensional attosecond photoelectron spectroscopy with shaped pulses and quantum optical fields.
Phys. Rev. A **81**, 063810 (2010).

[213] M. Aeschlimann, T. Brixner, A. Fischer, C. Kramer, P. Melchior, W. Pfeiffer, C. Schneider, C. Strüber, P. Tuchscherer, and D. V. Voronine.
Coherent two-dimensional nanoscopy.
Science **333**, 1723–1726 (2011).

[214] O. Golonzka, M. Khalil, N. Demirdöven, and A. Tokmakoff.
Vibrational Anharmonicities Revealed by Coherent Two-Dimensional Infrared Spectroscopy.
Phys. Rev. Lett. **86**, 2154–2157 (2001).

[215] E. H. G. Backus, S. Garrett-Roe, and P. Hamm.
Phasing problem of heterodyne-detected two-dimensional infrared spectroscopy.
Opt. Lett. **33**, 2665–2667 (2008).

[216] S. Shim, D. B. Strasfeld, Y. L. Ling, and M. T. Zanni.
Automated 2D IR Spectroscopy Using a Mid-IR Pulse Shaper and Application of this Technology to the Human Islet Amyloid Polypeptide.
Proc. Natl. Acad. Sci. USA **104**, 14197–14202 (2007).

[217] E. M. Grumstrup, S. Shim, M. A. Montgomery, N. H. Damrauer, and M. T. Zanni.
Facile collection of two-dimensional electronic spectra using femtosecond pulse-shaping technology.
Opt. Express **15**, 16681–16689 (2007).

[218] S. Shim and M. T. Zanni.
How to Turn Your Pump–Probe Instrument into a Multidimensional Spectrometer: 2D IR and VIS Spectroscopies via Pulse Shaping.
Phys. Chem. Chem. Phys. **11**, 748–761 (2009).

[219] S. M. Gallagher Faeder and D. M. Jonas.
Two-Dimensional Electronic Correlation and Relaxation Spectra: Theory and Model Calculations.
J. Phys. Chem. A **103**, 10489–10505 (1999).

[220] L. P. DeFlores, R. A. Nicodemus, and A. Tokmakoff.
Two-dimensional Fourier transform spectroscopy in the pump-probe geometry.
Opt. Lett. **32**, 2966–2968 (2007).

[221] J. A. Myers, K. L. Lewis, P. F. Tekavec, and J. P. Ogilvie.
Two-Color Two-Dimensional Fourier Transform Electronic Spectroscopy with a Pulse-Shaper.
Opt. Express **16**, 17420–17428 (2008).

[222] P. F. Tekavec, J. A. Myers, K. L. M. Lewis, and J. P. Ogilvie.
Two-Dimensional Electronic Spectroscopy with a Continuum Probe.
Opt. Lett. **34**, 1390–1392 (2009).

[223] C. Tseng, S. Matsika, and T. C. Weinacht.
Two-dimensional ultrafast Fourier transform spectroscopy in the deep ultraviolet.
Opt. Express **17**, 18788–18793 (2009).

[224] N. Krebs, I. Pugliesi, J. Hauer, and E. Riedle.
Two-dimensional Fourier transform spectroscopy in the ultraviolet with sub-20 fs pump pulses and 250–720 nm supercontinuum probe.
New J. Phys. **15**, 085016 (2013).

[225] H.-S. Tan.
Theory and Phase-Cycling Scheme Selection Principles of Collinear Phase Coherent Multi-Dimensional Optical Spectroscopy.
J. Chem. Phys. **129**, 124501 (2008).

[226] S. Yan and H.-S. Tan.
Phase cycling schemes for two-dimensional optical spectroscopy with a pump–probe beam geometry.
Chem. Phys. **360**, 110–115 (2009).

[227] P. Hamm, M. Lim, W. F. DeGrado, and R. M. Hochstrasser.
The two-dimensional IR nonlinear spectroscopy of a cyclic penta-peptide in relation to its three-dimensional structure.
Proc. Natl. Acad. Sci. USA **96**, 2036–2041 (1999).

[228] V. Cervetto, J. Helbing, J. Bredenbeck, and P. Hamm.
Double-resonance versus pulsed Fourier transform two-dimensional infrared spectroscopy: An experimental and theoretical comparison.
J. Chem. Phys. **121**, 5935–5942 (2004).

[229] J. C. Crano and R. J. Guglielmetti.
Organic Photochromic and Thermochromic Compounds: Volume 2: Physicochemical Studies, Biological Applications, and Thermochromism.
First edition. Kluwer Academic Publishers, New York (1999).

[230] H. Dürr and H. Bouas-Laurent.
Photochromism: Molecules and Systems.
Elsevier, Amsterdam (2003).

[231] B. S. Lukyanov and M. B. Lukyanova.
Spiropyrans: Synthesis, Properties, and Application. (Review).
Chem. Heterocycl. Compd. **41**, 281–311 (2005).

[232] Y. Kawanishi, K. Seki, T. Tamaki, M. Sakuragi, and Y. Suzuki.
Tuning reverse ring closure in the photochromic and thermochromic transformation of 1',3',3'-trimethyl-6-nitrospiro[2H-1-benzopyran-2,2'-indoline] analogues by ionic moieties.
J. Photochem. Photobiol. A **109**, 237–242 (1997).

[233] J. Hobley, U. Pfeifer-Fukumura, M. Bletz, T. Asahi, H. Masuhara, and H. Fukumura.
Ultrafast Photo-Dynamics of a Reversible Photochromic Spiropyran.
J. Phys. Chem. A **106**, 2265–2270 (2002).

[234] B. C. Bunker, B. I. Kim, J. E. Houston, R. Rosario, A. A. Garcia, M. Hayes, D. Gust, and S. T. Picraux.
Direct Observation of Photo Switching in Tethered Spiropyrans Using the Interfacial Force Microscope.
Nano Lett. **3**, 1723–1727 (2003).

[235] J. Buback, M. Kullmann, F. Langhojer, P. Nuernberger, R. Schmidt, F. Würthner, and T. Brixner.
Ultrafast Bidirectional Photoswitching of a Spiropyran.
J. Am. Chem. Soc. **132**, 16510–16519 (2010).

[236] J. Buback, P. Nuernberger, M. Kullmann, F. Langhojer, R. Schmidt, F. Würthner, and T. Brixner.
Ring-closure and isomerization capabilities of spiropyran-derived merocyanine isomers.
J. Phys. Chem. A **115**, 3924–3935 (2011).

[237] J. Kohl-Landgraf, M. Braun, C. Özçoban, D. P. N. Gonçalves, A. Heckel, and J. Wachtveitl.
Ultrafast Dynamics of a Spiropyran in Water.
J. Am. Chem. Soc. **134**, 14070–14077 (2012).

[238] D. Parthenopoulos and P. Rentzepis.
Three-Dimensional Optical Storage Memory.
Science **245**, 843–845 (1989).

[239] D. Dattilo, L. Armelao, G. Fois, G. Mistura, and M. Maggini.
Wetting Properties of Flat and Porous Silicon Surfaces Coated with a Spiropyran.
Langmuir **23**, 12945–12950 (2007).

[240] J. Andersson, S. Li, P. Lincoln, and J. Andréasson.
Photoswitched DNA-Binding of a Photochromic Spiropyran.
J. Am. Chem. Soc. **130**, 11836–11837 (2008).

[241] R. Heiligman-Rim, Y. Hirshberg, and E. Fischer.
Photochromism in spiropyrans. Part IV.1 Evidence for the existence of several forms of the colored modification.
J. Phys. Chem. **66**, 2465–2470 (1962).

[242] N. P. Ernsting, B. Dick, and T. Arthen-Engeland.
The primary photochemical reaction step of unsubstituted indolino-spiropyrans.
Pure Appl. Chem. **62**, 1483–1488 (1990).

[243] N. Ernsting and T. Arthenengeland.
Photochemical ring-opening reaction of indolinospyropyrans studied by subpicosecond transient absorption.
J. Phys. Chem. **95**, 5502–5509 (1991).

[244] S. M. Aldoshin and L. O. Atovmyan.
The Structure of Open Merocyanine Forms of Photochromic Indoline Spiropyrans and the Mechanism of Their Structural Conversions.
Mol. Cryst. Liq. Cryst. **149**, 251–290 (1987).

[245] J. Hobley, V. Malatesta, R. Millini, L. Montanari, and W. O. Parker.
Proton exchange and isomerisation reactions of photochromic and reverse photochromic spiropyrans and their merocyanine forms.
Phys. Chem. Chem. Phys. **1**, 3259–3267 (1999).

[246] Y. Futami, M. L. S. Chin, S. Kudoh, M. Takayanagi, and M. Nakata.
Conformations of nitro-substituted spiropyran and merocyanine studied by low-temperature matrix-isolation infrared spectroscopy and density-functional-theory calculation.
Chem. Phys. Lett. **370**, 460–468 (2003).

[247] Y. Sheng, J. Leszczynski, A. A. Garcia, R. Rosario, D. Gust, and J. Springer.
Comprehensive Theoretical Study of the Conversion Reactions of Spiropyrans: Substituent and Solvent Effects.
J. Phys. Chem. B **108**, 16233–16243 (2004).

[248] Y. Hirshberg and E. Fischer.
Photochromism and reversible multiple internal transitions in some spiroPyrans at low temperatures. Part II.
J. Chem. Soc. pp. 3129–3137 (1954).

[249] Y. Hirshberg and E. Fischer.
Photochromism and reversible multiple internal transitions in some spiropyrans at low temperatures. Part I.
J. Chem. Soc. pp. 297–303 (1954).

[250] A. Holm, M. Rini, E. T. J. Nibbering, and H. Fidder.
Femtosecond UV/mid-IR study of photochromism of the spiropyran 1',3'-dihydro-1',3',3'-trimethyl-6-nitrospiro[2H-1-benzopyran-2,2'-(2H)-indole] in solution.
Chem. Phys. Lett. **376**, 214–219 (2003).

[251] A. Holm, O. F. Mohammed, M. Rini, E. Mukhtar, E. T. J. Nibbering, and H. Fidder.
Sequential Merocyanine Product Isomerization Following Femtosecond UV Excitation of a Spiropyran.
J. Phys. Chem. A **109**, 8962–8968 (2005).

[252] A. K. Chibisov and H. Görner.
Photoprocesses in spiropyran-derived merocyanines.
J. Phys. Chem. A **101**, 4305–4312 (1997).

[253] H. Görner.
Photochromism of Nitrospiropyrans: Effects of Structure, Solvent and Temperature.
Phys. Chem. Chem. Phys. **3**, 416–423 (2001).

[254] C. J. Wohl and D. Kuciauskas.
Excited-state dynamics of spiropyran-derived merocyanine isomers.
J. Phys. Chem. B **109**, 22186–22191 (2005).

[255] G. Cottone, R. Noto, G. L. Manna, and S. L. Fornili.
Ab initio study on the photoisomers of a nitro-substituted spiropyran.
Chem. Phys. Lett. **319**, 51–59 (2000).

[256] G. Cottone, R. Noto, and G. L. Manna.
Theoretical study of spiropyran-merocyanine thermal isomerization.
Chem. Phys. Lett. **388**, 218–222 (2004).

[257] I. Baraldi, F. Momicchioli, G. Ponterini, A. S. Tatikolov, and D. Vanossi.
Photoisomerization of Simple Merocyanines: a Theoretical and Experimental Comparison with Polyenes and Symmetric Cyanines.
Phys. Chem. Chem. Phys. **5**, 979–987 (2003).

[258] G. Cottone, R. Noto, and G. L. Manna.
Density Functional Theory Study of the Trans-Trans-Cis (TTC)→Trans-Trans-Trans (TTT) Isomerization of a Photochromic Spiropyran Merocyanine.
Molecules **13**, 1246–1252 (2008).

[259] M. Sanchez-Lozano, C. M. Estévez, J. Hermida-Ramón, and L. Serrano-Andres.
Ultrafast Ring-Opening/Closing and Deactivation Channels for a Model Spiropyran–Merocyanine System.
J. Phys. Chem. A **115**, 9128–9138 (2011).

[260] R. Kobayashi and R. D. Amos.
Theoretical investigation of the isomerisation of merocyanine.
Mol. Phys. **111**, 1574–1579 (2013).

[261] M. Diekmann.
Kohärente multidimensionale Spektroskopie an Merocyanin-Isomeren.
Diploma thesis, Universität Würzburg (2012).

[262] S. J. Rosenthal, X. Xie, M. Du, and G. R. Fleming.
Femtosecond solvation dynamics in acetonitrile: Observation of the inertial contribution to the solvent response.
J. Chem. Phys. **95**, 4715–4718 (1991).

[263] M. L. Horng, J. A. Gardecki, A. Papazyan, and M. Maroncelli.
Subpicosecond Measurements of Polar Solvation Dynamics: Coumarin 153 Revisited.
J. Phys. Chem. **99**, 17311–17337 (1995).

[264] D. Polli, P. Altoe, O. Weingart, K. M. Spillane, C. Manzoni, D. Brida, G. Tomasello, G. Orlandi, P. Kukura, R. A. Mathies, M. Garavelli, and G. Cerullo.
Conical intersection dynamics of the primary photoisomerization event in vision.
Nature **467**, 440–443 (2010).

[265] U. Åberg, E. Åkesson, and V. Sundström.
Excited state dynamics of barrierless isomerization in solution.
Chem. Phys. Lett. **215**, 388–394 (1993).

[266] Q. Xu and G. R. Fleming.
Isomerization Dynamics of 1,1'-Diethyl-4,4'-Cyanine (1144C) Studied by Different Third-Order Nonlinear Spectroscopic Measurements.
J. Phys. Chem. A **105**, 10187–10195 (2001).

[267] P. Nuernberger, G. Vogt, G. Gerber, R. Improta, and F. Santoro.
Femtosecond study on the isomerization dynamics of NK88. I. Ground-state dynamics after photoexcitation.
J. Chem. Phys. **125**, 044512 (2006).

[268] G. Vogt, P. Nuernberger, T. Brixner, and G. Gerber.
Femtosecond Pump-Shaped-Dump Quantum Control of Retinal Isomerization in Bacteriorhodopsin.
Chem. Phys. Lett. **433**, 211–215 (2006).

[269] B. Dietzek, A. Yartsev, and A. N. Tarnovsky.
Watching Ultrafast Barrierless Excited-State Isomerization of Pseudocyanine in Real Time.
J. Phys. Chem. B **111**, 4520–4526 (2007).

[270] A. Weigel, M. Pfaffe, M. Sajadi, R. Mahrwald, R. Improta, V. Barone, D. Polli, G. Cerullo, N. P. Ernsting, and F. Santoro.
Barrierless photoisomerisation of the "simplest cyanine": Joining computational and femtosecond optical spectroscopies to trace the full reaction path.
Phys. Chem. Chem. Phys. **14**, 13350–13364 (2012).

[271] J. Briand, O. Bräm, J. Réhault, J. Léonard, A. Cannizzo, M. Chergui, V. Zanirato, M. Olivucci, J. Helbing, and S. Haacke.
Coherent Ultrafast Torsional Motion and Isomerization of a Biomimetic Dipolar Photoswitch.
Phys. Chem. Chem. Phys. **12**, 3178 (2010).

[272] B. G. Levine and T. J. Martínez.
Isomerization Through Conical Intersections.
Annu. Rev. Phys. Chem. **58**, 613–634 (2007).

[273] J. Dasgupta, R. R. Frontiera, K. C. Taylor, J. C. Lagarias, and R. A. Mathies.
Ultrafast excited-state isomerization in phytochrome revealed by femtosecond stimulated Raman spectroscopy.
Proc. Natl. Acad. Sci. USA **106**, 1784–1789 (2009).

[274] M. Seel, S. Engleitner, and W. Zinth.
Wavepacket motion and ultrafast electron transfer in the system oxazine 1 in N,N-dimethylaniline.
Chem. Phys. Lett. **275**, 363–369 (1997).

[275] C. J. Bardeen, Q. Wang, and C. V. Shank.
Femtosecond Chirped Pulse Excitation of Vibrational Wave Packets in LD690 and Bacteriorhodopsin.
J. Phys. Chem. A **102**, 2759–2766 (1998).

[276] K. Horikoshi, K. Misawa, and R. Lang.
Rapid motion capture of mode-specific quantum wave packets selectively generated by phase-controlled optical pulses.
J. Chem. Phys. **127**, 054104 (2007).

[277] T. J. Dunn, J. N. Sweetser, I. A. Walmsley, and C. Radzewicz.
Experimental determination of the dynamics of a molecular nuclear wave packet via the spectra of spontaneous emission.
Phys. Rev. Lett. **70**, 3388–3391 (1993).

[278] R. S. S. Kumar, L. Lüer, D. Polli, M. Garbugli, and G. Lanzani.
Primary Photo-Events in a Metastable Photomerocyanine of Spirooxazines.
Opt. Mater. Express **1**, 293–304 (2011).

[279] M. J. Rosker, M. Dantus, and A. H. Zewail.
Femtosecond Real Time Probing of Reactions I: The Technique.
J. Chem. Phys. **89**, 6113–6127 (1988).

[280] A. H. Zewail.
Femtosecond transition-state dynamics.
Faraday Discuss. Chem. Soc. **91**, 207 (1991).

[281] N. Pugliano, D. K. Palit, A. Z. Szarka, and R. M. Hochstrasser.
Wave packet dynamics of the HgI_2 photodissociation reaction in solution.
J. Chem. Phys. **99**, 7273–7276 (1993).

[282] U. Banin, A. Waldman, and S. Ruhman.
Ultrafast photodissociation of I3- in solution: Direct observation of coherent product vibrations.
J. Chem. Phys. **96**, 2416–2419 (1992).

[283] U. Banin and S. Ruhman.
Ultrafast photodissociation of I3. Coherent photochemistry in solution.
J. Chem. Phys. **98**, 4391–4403 (1993).

[284] S. Pedersen, L. Bañares, and A. H. Zewail.
Femtosecond vibrational transition-state dynamics in a chemical reaction.
J. Chem. Phys. **97**, 8801–8804 (1992).

[285] S. L. Dexheimer, Q. Wang, L. A. Peteanu, W. T. Pollard, R. A. Mathies, and C. V. Shank.
Femtosecond impulsive excitation of nonstationary vibrational states in bacteriorhodopsin.
Chem. Phys. Lett. **188**, 61–66 (1992).

[286] T. Nägele, R. Hoche, W. Zinth, and J. Wachtveitl.
Femtosecond photoisomerization of cis-azobenzene.
Chem. Phys. Lett. **272**, 489–495 (1997).

[287] T. Kobayashi, T. Saito, and H. Ohtani.
Real-time spectroscopy of transition states in bacteriorhodopsin during retinal isomerization.
Nature **414**, 531–534 (2001).

[288] K. Heyne, J. Herbst, D. Stehlik, B. Esteban, T. Lamparter, J. Hughes, and R. Diller.
Ultrafast Dynamics of Phytochrome from the Cyanobacterium Synechocystis, Reconstituted with Phycocyanobilin and Phycoerythrobilin.
Biophys. J. **82**, 1004–1016 (2002).

[289] N. Mataga, H. Chosrowjan, Y. Shibata, Y. Imamoto, M. Kataoka, and F. Tokunaga.
Ultrafast photoinduced reaction dynamics of photoactive yellow protein (PYP): observation of coherent oscillations in the femtosecond fluorescence decay dynamics.
Chem. Phys. Lett. **352**, 220–225 (2002).

[290] S. Takeuchi, S. Ruhman, T. Tsuneda, M. Chiba, T. Taketsugu, and T. Tahara.
Spectroscopic Tracking of Structural Evolution in Ultrafast Stilbene Photoisomerization.
Science **322**, 1073–1077 (2008).

[291] J. Conyard, K. Addison, I. A. Heisler, A. Cnossen, W. R. Browne, B. L. Feringa, and S. R. Meech.
Ultrafast dynamics in the power stroke of a molecular rotary motor.
Nat. Chem. **4**, 547–551 (2012).

[292] G. N. Lewis and M. Calvin.
The Color of Organic Substances.
Chem. Rev. **25**, 273–328 (1939).

[293] D. B. Turner, R. Dinshaw, K. Lee, M. S. Belsley, K. E. Wilk, P. M. G. Curmi, and G. D. Scholes.
Quantitative investigations of quantum coherence for a light-harvesting protein at conditions simulating photosynthesis.
Phys. Chem. Chem. Phys. **14**, 4857–4874 (2012).

[294] D. A. Blank, L. J. Kaufman, and G. R. Fleming.
Fifth-order two-dimensional Raman spectra of CS_2 are dominated by third-order cascades.
J. Chem. Phys. **111**, 3105–3114 (1999).

[295] K. J. Kubarych, C. J. Milne, and R. J. D. Miller.
Fifth-order two-dimensional Raman spectroscopy: A new direct probe of the liquid state.
Int. Rev. Phys. Chem. **22**, 497–532 (2003).

[296] B. Brüggemann and T. Pullerits.
Nonperturbative modeling of fifth-order coherent multidimensional spectroscopy in light harvesting antennas.
New J. Phys. **13**, 025024 (2011).

[297] P. Nuernberger, K. F. Lee, and M. Joffre.
Femtosecond Spectroscopy from the Perspective of a Global Multidimensional Response Function.
Acc. Chem. Res. **42**, 1433–1441 (2009).

[298] F. Milota, V. I. Prokhorenko, T. Mančal, H. von Berlepsch, O. Bixner, H. F. Kauffmann, and J. Hauer.
Vibronic and vibrational coherences in two-dimensional electronic spectra of supramolecular J-aggregates.
J. Phys. Chem. A **117**, 6007–6014 (2013).

[299] D. Keusters, H.-S. Tan, and W. S. Warren.
Role of pulse phase and direction in two-dimensional optical spectroscopy.
J. Phys. Chem. A **103**, 10369–10380 (1999).

[300] J. C. Vaughan, T. Hornung, K. W. Stone, and K. A. Nelson.
Coherently Controlled Ultrafast Four-Wave Mixing Spectroscopy.
J. Phys. Chem. A **111**, 4873–4883 (2007).

[301] S. Shim, R. Gupta, Y. L. Ling, D. B. Strasfeld, D. P. Raleigh, and M. T. Zanni.
Two-dimensional IR spectroscopy and isotope labeling defines the pathway of amyloid formation with residue-specific resolution.
Proc. Natl. Acad. Sci. USA **106**, 6614 –6619 (2009).

[302] P. F. Tekavec, J. A. Myers, K. L. M. Lewis, F. D. Fuller, and J. P. Ogilvie.
Effects of Chirp on Two-Dimensional Fourier Transform Electronic Spectra.
Opt. Express **18**, 11015–11024 (2010).

[303] P. A. Tekavec, K. L. Lewis, F. D. Fuller, J. A. Myers, and J. P. Ogilvie.
Toward Broad Bandwidth 2-D Electronic Spectroscopy: Correction of Chirp From a Continuum Probe.
IEEE J. Sel. Top. Quantum Electron. **18**, 210–217 (2012).

[304] F. Jensen.
Introduction to computational chemistry.
Second edition. Wiley, Chichester [u.a.] (2007).

[305] T. Yanai, D. P. Tew, and N. C. Handy.
A New Hybrid Exchange–Correlation Functional Using the Coulomb-Attenuating Method (CAM-B3LYP).
Chem. Phys. Lett. **393**, 51–57 (2004).

[306] M. J. Frisch, G. W. Trucks, H. B. Schlegel, G. E. Scuseria, M. A. Robb, J. R. Cheeseman, G. Scalmani, V. Barone, B. Mennucci, G. A. Petersson, H. Nakatsuji, M. Caricato, X. Li, H. P. Hratchian, A. F. Izmaylov, J. Bloino, G. Zheng, J. L. Sonnenberg, M. Hada, M. Ehara, K. Toyota, R. Fukuda, J. Hasegawa, M. Ishida, T. Nakajima, Y. Honda, O. Kitao, H. Nakai, T. Vreven, J. J. A. Montgomery, J. E. Peralta, F. Ogliaro, M. Bearpark, J. J. Heyd, E. Brothers, K. N. Kudin, V. N. Staroverov, R. Kobayashi, J. Normand, K. Raghavachari, A. Rendell, J. C. Burant, S. S. Iyengar, J. Tomasi, M. Cossi, N. Rega, J. M. Millam, M. Klene, J. E. Knox, J. B. Cross, V. Bakken, C. Adamo, J. Jaramillo, R. Gomperts, R. E. Stratmann, O. Yazyev, A. J. Austin, R. Cammi, C. Pomelli, J. W. Ochterski, R. L. Martin, K. Morokuma, V. G. Zakrzewski, G. A. Voth, P. Salvador, J. J. Dannenberg, S. Dapprich, A. D. Daniels, O. Farkas, J. B. Foresman, J. V. Ortiz, J. Cioslowski, and D. J. Fox.
Gaussian 09, Revision B.01 (2009).
Gaussian Inc. Wallingford CT 2009.

[307] S. L. Logunov, V. V. Volkov, M. Braun, and M. A. El-Sayed.
The Relaxation Dynamics of the Excited Electronic States of Retinal in Bacteriorhodopsin by Two-Pump-Probe Femtosecond Studies.
Proc. Natl. Acad. Sci. USA **98**, 8475 –8479 (2001).

[308] D. S. Larsen, E. Papagiannakis, I. H. M. van Stokkum, M. Vengris, J. T. M. Kennis, and R. van Grondelle.
Excited State Dynamics of β-Carotene Explored with Dispersed Multi-Pulse Transient Absorption.
Chem. Phys. Lett. **381**, 733–742 (2003).

[309] E. Papagiannakis, M. Vengris, D. S. Larsen, I. H. M. van Stokkum, R. G. Hiller, and R. van Grondelle.
Use of Ultrafast Dispersed Pump-Dump-Probe and Pump-Repump-Probe Spectroscopies to Explore the Light-Induced Dynamics of Peridinin in Solution.
J. Phys. Chem. B **110**, 512–521 (2006).

[310] S. Draxler, T. Brust, S. Malkmus, J. A. DiGirolamo, W. J. Lees, W. Zinth, and M. Braun.
Ring-Opening Reaction of a Trifluorinated Indolylfulgide: Mode-Specific Photochemistry after Pre-Excitation.
Phys. Chem. Chem. Phys. **11**, 5019–5027 (2009).

[311] D. J. Tannor and S. A. Rice.
Control of Selectivity of Chemical Reaction via Control of Wave Packet Evolution.
J. Chem. Phys. **83**, 5013–5018 (1985).

[312] F. Gai, J. C. McDonald, and P. A. Anfinrud.
Pump–Dump–Probe Spectroscopy of Bacteriorhodosin: Evidence for a Near-IR Excited State Absorbance.
J. Am. Chem. Soc. **119**, 6201–6202 (1997).

[313] S. Ruhman, B. Hou, N. Friedman, M. Ottolenghi, and M. Sheves.
Following Evolution of Bacteriorhodopsin in Its Reactive Excited State via Stimulated Emission Pumping.
J. Am. Chem. Soc. **124**, 8854–8858 (2002).

[314] D. S. Larsen, I. H. van Stokkum, M. Vengris, M. A. van der Horst, F. L. de Weerd, K. J. Hellingwerf, and R. van Grondelle.
Incoherent Manipulation of the Photoactive Yellow Protein Photocycle with Dispersed Pump-Dump-Probe Spectroscopy.
Biophys. J. **87**, 1858–1872 (2004).

[315] G. Vogt, P. Nuernberger, G. Gerber, R. Improta, and F. Santoro.
Femtosecond study on the isomerization dynamics of NK88. II. Excited-state dynamics.
J. Chem. Phys. **125**, 044513 (2006).

[316] P. Marquetand, P. Nuernberger, G. Vogt, T. Brixner, and V. Engel.
Properties of Wave Packets Deduced from Quantum Control Fitness Landscapes.
Europhys. Lett. **80**, 53001 (2007).

[317] J. Bredenbeck, J. Helbing, R. Behrendt, C. Renner, L. Moroder, J. Wachtveitl, and P. Hamm.
Transient 2D-IR Spectroscopy: Snapshots of the Nonequilibrium Ensemble during the Picosecond Conformational Transition of a Small Peptide.
J. Phys. Chem. B **107**, 8654–8660 (2003).

[318] J. Bredenbeck, J. Helbing, and P. Hamm.
Transient two-dimensional infrared spectroscopy: Exploring the polarization dependence.
J. Chem. Phys. **121**, 5943–5957 (2004).

[319] C. Kolano, J. Helbing, M. Kozinski, W. Sander, and P. Hamm.
Watching hydrogen-bond dynamics in a β-turn by transient two-dimensional infrared spectroscopy.
Nature **444**, 469–472 (2006).

[320] H. S. Chung, Z. Ganim, K. C. Jones, and A. Tokmakoff.
Transient 2D IR Spectroscopy of Ubiquitin Unfolding Dynamics.
Proc. Natl. Acad. Sci. USA **104**, 14237 –14242 (2007).

[321] H. S. Chung, M. Khalil, A. W. Smith, and A. Tokmakoff.
Transient two-dimensional IR spectrometer for probing nanosecond temperature-jump kinetics.
Rev. Sci. Instrum. **78**, 063101 (2007).

[322] J. Bredenbeck, J. Helbing, C. Kolano, and P. Hamm.
Ultrafast 2D–IR Spectroscopy of Transient Species.
ChemPhysChem **8**, 1747–1756 (2007).

[323] J. Bredenbeck, J. Helbing, and P. Hamm.
Labeling Vibrations by Light: Ultrafast Transient 2D-IR Spectroscopy Tracks Vibrational Modes during Photoinduced Charge Transfer.
J. Am. Chem. Soc. **126**, 990–991 (2004).

[324] J. Bredenbeck, J. Helbing, K. Nienhaus, G. U. Nienhaus, and P. Hamm.
Protein ligand migration mapped by nonequilibrium 2D-IR exchange spectroscopy.
Proc. Natl. Acad. Sci. USA **104**, 14243–14248 (2007).

[325] C. R. Baiz, M. J. Nee, R. McCanne, and K. J. Kubarych.
Ultrafast Nonequilibrium Fourier-Transform Two-Dimensional Infrared Spectroscopy.
Opt. Lett. **33**, 2533–2535 (2008).

[326] B. L. Feringa.
Molecular Switches.
Wiley-VCH Verlag GmbH, Berlin (2001).

[327] S. Ruhman, A. G. Joly, and K. A. Nelson.
Time-Resolved Observations of Coherent Molecular Vibrational Motion and the General Occurrence of Impulsive Stimulated Scattering.
J. Chem. Phys. **86**, 6563–6565 (1987).

[328] C. Xia, J. Peon, and B. Kohler.
Femtosecond Electron Ejection in Liquid Acetonitrile: Evidence for Cavity Electrons and Solvent Anions.
J. Chem. Phys. **117**, 8855–8866 (2002).

[329] S. Yang, H. Tian, H. Xiao, X. Shang, X. Gong, S. Yao, and K. Chen.
Photodegradation of Cyanine and Merocyanine Dyes.
Dyes Pigments **49**, 93–101 (2001).

[330] S. Fechner.
Quantenkontrolle im Zeit-Frequenz-Phasenraum.
Dissertation, Universität Würzburg (2008).

[331] A. Rodenberg.
Kohärente Kontrolle im Zeit-Frequenz-Phasenraum.
Diploma thesis, Universität Würzburg (2008).

[332] S. Rützel.
Adaptive Synthese von Femtosekunden-Laserpulsen im Zeit-Frequenz-Phasenraum.
Master's thesis, Universität Würzburg (2009).

[333] C. Stolzenberger.
Die von Neumann-Darstellung als eine Alternative zur Frequenzbasis in Quantenkontroll-Experimenten.
Master's thesis, Universität Würzburg (2009).
00000.

[334] A. Krischke.
Polarisationsgeformte Femtosekundenlaserpulse im Zeit-Frequenz-Phasenraum.
Diploma thesis, Universität Würzburg (2010).

[335] J. L. Herek, W. Wohlleben, R. J. Cogdell, D. Zeidler, and M. Motzkus.
Quantum control of energy flow in light harvesting.
Nature **417**, 533–535 (2002).

[336] I. Pastirk, J. D. Cruz, K. Walowicz, V. Lozovoy, and M. Dantus.
Selective two-photon microscopy with shaped femtosecond pulses.
Opt. Express **11**, 1695–1701 (2003).

[337] T. Hornung, J. C. Vaughan, T. Feurer, and K. A. Nelson.
Degenerate four-wave mixing spectroscopy based on two-dimensional femtosecondpulse shaping.
Opt. Lett. **29**, 2052–2054 (2004).

[338] S. A. Rice and M. Zhao.
Optical Control of Molecular Dynamics.
Wiley-Interscience, New York (2000).

[339] P. W. Brumer and M. Shapiro.
Principles of the Quantum Control of Molecular Processes.
Wiley-Interscience, New York (2003).

[340] T. Brixner and G. Gerber.
Quantum Control of Gas-Phase and Liquid-Phase Femtochemistry.
ChemPhysChem **4**, 418–438 (2003).

[341] P. Nuernberger, G. Vogt, T. Brixner, and G. Gerber.
Femtosecond quantum control of molecular dynamics in the condensed phase.
Phys. Chem. Chem. Phys. **9**, 2470–2497 (2007).

[342] L. Polachek, D. Oron, and Y. Silberberg.
Full control of the spectral polarization of ultrashort pulses.
Opt. Lett. **31**, 631–633 (2006).

[343] M. Plewicki, F. Weise, S. M. Weber, and A. Lindinger.
Phase, amplitude, and polarization shaping with a pulse shaper in a Mach-Zehnder interferometer.
Appl. Opt. **45**, 8354–8359 (2006).

[344] S. M. Weber, F. Weise, M. Plewicki, and A. Lindinger.
Interferometric generation of parametrically shaped polarization pulses.
Appl. Opt. **46**, 5987–5990 (2007).

[345] M. Ninck, A. Galler, T. Feurer, and T. Brixner.
Programmable common-path vector field synthesizer for femtosecond pulses.
Opt. Lett. **32**, 3379–3381 (2007).

[346] O. Masihzadeh, P. Schlup, and R. A. Bartels.
Complete polarization state control ofultrafast laser pulses with a single linearspatial light modulator.
Opt. Express **15**, 18025–18032 (2007).

[347] F. Weise and A. Lindinger.
Full control over the electric field using four liquid crystal arrays.
Opt. Lett. **34**, 1258–1260 (2009).

[348] C. T. Middleton, D. B. Strasfeld, and M. T. Zanni.
Polarization shaping in the mid-IR and polarization-based balanced heterodyne detection with application to 2D IR spectroscopy.
Opt. Express **17**, 14526–14533 (2009).

[349] D. Oron, N. Dudovich, and Y. Silberberg.
Femtosecond Phase-and-Polarization Control for Background-Free Coherent Anti-Stokes Raman Spectroscopy.
Phys. Rev. Lett. **90**, 213902 (2003).

[350] T. Polack, D. Oron, and Y. Silberberg.
Control and measurement of a non-resonant Raman wavepacket using a single ultrashort pulse.
Chem. Phys. **318**, 163–169 (2005).

[351] N. Dudovich, D. Oron, and Y. Silberberg.
Quantum Control of the Angular Momentum Distribution in Multiphoton Absorption Processes.
Phys. Rev. Lett. **92**, 103003 (2004).

[352] T. Brixner, G. Krampert, T. Pfeifer, R. Selle, G. Gerber, M. Wollenhaupt, O. Graefe, C. Horn, D. Liese, and T. Baumert.
Quantum Control by Ultrafast Polarization Shaping.
Phys. Rev. Lett. **92**, 208301 (2004).

[353] T. Suzuki, S. Minemoto, T. Kanai, and H. Sakai.
Optimal Control of Multiphoton Ionization Processes in Aligned I_2 Molecules with Time-Dependent Polarization Pulses.
Phys. Rev. Lett. **92**, 133005 (2004).

[354] F. Weise, S. M. Weber, M. Plewicki, and A. Lindinger.
Application of phase, amplitude, and polarization shaped pulses for optimal control on molecules.
Chem. Phys. **332**, 313–317 (2007).

[355] T. Brixner, F. J. G. de Abajo, J. Schneider, and W. Pfeiffer.
Nanoscopic ultrafast space-time-resolved spectroscopy.
Phys. Rev. Lett. **95**, 093901–4 (2005).

[356] M. Aeschlimann, M. Bauer, D. Bayer, T. Brixner, F. J. G. de Abajo, W. Pfeiffer, M. Rohmer, C. Spindler, and F. Steeb.
Adaptive subwavelength control of nano-optical fields.
Nature **446**, 301–304 (2007).

[357] S. Woutersen and P. Hamm.
Structure determination of trialanine in water using polarization sensitive two-dimensional vibrational spectroscopy.
J. Phys. Chem. B **104**, 11316–11320 (2000).

[358] R. M. Hochstrasser.
Two-dimensional IR-spectroscopy: polarization anisotropy effects.
Chem. Phys. **266**, 273–284 (2001).

[359] M. T. Zanni, N. Ge, Y. S. Kim, and R. M. Hochstrasser.
Two-dimensional IR spectroscopy can be designed to eliminate the diagonal peaks and expose only the crosspeaks needed for structure determination.
Proc. Natl. Acad. Sci. USA **98**, 11265–11270 (2001).

[360] J. Dreyer, A. M. Moran, and S. Mukamel.
Tensor components in three pulse vibrational echoes of a rigid dipeptide.
Bull. Korean Chem. Soc. **24**, 1091–1096 (2003).

[361] E. L. Read, G. S. Engel, T. R. Calhoun, T. Mančal, T. K. Ahn, R. E. Blankenship, and G. R. Fleming.
Multidimensional Ultrafast Spectroscopy Special Feature: Cross-peak-specific two-dimensional electronic spectroscopy.
Proc. Natl. Acad. Sci. USA **104**, 14203–14208 (2007).

[362] F. Langhojer, D. Cardoza, M. Baertschy, and T. C. Weinacht.
Gaining mechanistic insight from closed loop learning control: The importance of basis in searching the phase space.
J. Chem. Phys. **122**, 014102 (2005).

[363] D. Yelin, D. Meshulach, and Y. Silberberg.
Adaptive femtosecond pulse compression.
Opt. Lett. **22**, 1793–1795 (1997).

[364] C. J. Bardeen, Q. Wang, and C. V. Shank.
Selective Excitation of Vibrational Wave Packet Motion Using Chirped Pulses.
Phys. Rev. Lett. **75**, 3410–3413 (1995).

[365] B. Kohler, V. V. Yakovlev, J. Che, J. L. Krause, M. Messina, K. R. Wilson, N. Schwentner, R. M. Whitnell, and Y. Yan.
Quantum Control of Wave Packet Evolution with Tailored Femtosecond Pulses.
Phys. Rev. Lett. **74**, 3360–3363 (1995).

[366] C. J. Bardeen, V. V. Yakovlev, K. R. Wilson, S. D. Carpenter, P. M. Weber, and W. S. Warren.
Feedback quantum control of molecular electronic population transfer.
Chem. Phys. Lett. **280**, 151–158 (1997).

[367] A. Bartelt, A. Lindinger, C. Lupulescu, S. Vajda, and L. Wöste.
One parameter fs-pulse form control on NaK and Na2K.
Phys. Chem. Chem. Phys. **5**, 3610–3615 (2003).

[368] T. Hornung, R. Meier, D. Zeidler, K. Kompa, D. Proch, and M. Motzkus.
Optimal control of one- and two-photon transitions with shaped femtosecond pulses and feedback.
Appl. Phys. B **71**, 277–284 (2000).

[369] A. F. Bartelt, T. Feurer, and L. Wöste.
Understanding optimal control results by reducing the complexity.
Chem. Phys. **318**, 207–216 (2005).

[370] F. Weise and A. Lindinger.
Full parametric pulse shaping in phase, amplitude, and polarization using an effective four-array modulator.
Appl. Phys. B **101**, 79–91 (2010).

[371] J. v. Neumann.
Die Eindeutigkeit der Schrödingerschen Operatoren.
Math. Ann. **104**, 570–578 (1931).

[372] V. Bargmann, P. Butera, L. Girardello, and J. R. Klauder.
On the completeness of the coherent states.
Rep. Math. Phys. **2**, 221–228 (1971).

[373] M. Boon and J. Zak.
Amplitudes on von Neumann lattices.
J. Math. Phys. **22**, 1090–1099 (1981).

Acknowledgements

At this point, I would like to express my deep gratitude to all who contributed to this work and supported me during the last few years. This thesis is the result of an outstanding working atmosphere, excellent team work, and fruitful collaborations. Special thanks go to

- my supervisor **Prof. Dr. Tobias Brixner** for giving me the great opportunity to work in this exciting field of research and for providing us with such unique working conditions. I am grateful for his trust in my abilities, his enthusiasm, and his helpful and constructive advices. I also appreciate the freedom he gave me to pursue my own ideas and the possibilities to productively participate in the research community.
- **Prof. Dr. Patrick Nürnberger** for all the stimulating discussions, for his invaluable knowledge of literature, and his extraordinary support and advices in various projects.
- **Prof. Dr. Bernd Engels** for the theoretical support and the insightful discussions within the 6-nitro BIPS project.
- **Prof. Dr. David Tannor** for the fruitful cooperation within the von Neumann project.
- **Prof. Dr. Frank Würthner** and **Dr. Ralf Schmidt** for the synthesis of 6,8-dinitro BIPS.
- **Dr. Martin Kullmann** for sharing all the days and nights with me in the lab and for being such a helpful and kind colleague.
- **Christof Walter** for performing the DFT calculations in the framework of the 6-nitro BIPS project.
- **Meike Diekmann** for her experimental support in the 6-nitro BIPS project during her diploma thesis.
- **Anja Krischke** for her valuable contributions to the von Neumann project.
- **Andreas Steinbacher**, **Prof. Dr. Patrick Nürnberger**, **Dr. Cristina Consani**, **Dr. Martin Kullmann**, **Dr. Monika Pawłowska**, and **Sabrina Donnert** for thoroughly proofreading this thesis.
- **Christoph Schwarz** for his efforts concerning the office workstations, his help in diverse software issues, and for the daily coffee breaks.

- **Dr. Johannes Buback** and **Andreas Steinbacher** for the administration and maintenance of the VI pool and the lab computers.

- **Philipp Rudolf** for managing our reference data base and for joining me on our unforgettable trip to N.Y.C.

- **Dr. Susanne Fechner**, **Dr. Florian Langhojer**, **Frank Dimler**, **Dr. Johannes Buback**, and **Dr. Ulrike Selig-Parthey** for everything they taught me about femtosecond laser pulses, ultrafast optics, and spectroscopy, and their previous achievements forming an essential technical basis for large parts of the experiments discussed in this thesis.

- all members of the mechanic and electronic workshop, in particular **Wolfgang Liebler**, **Reiner Eck**, and **Jürgen Zimmermann**.

- the technical staff **Belinda Böhm** and **Sabine Fuchs** for their daily assistance, and our secretary **Andrea Gehring**.

- my office colleagues **Christoph Schwarz**, **Andreas Steinbacher**, and **Christian Kramer** for creating such a unique and pleasant working atmosphere.

- **Dr. Martin Kullmann**, **Christoph Stolzenberger**, and **Daniel Neumann** for the weekly lunchtime meetings and the coffee breaks.

- all current and past members of the **Lehrstuhl für Physikalische und Theoretische Chemie I (PC1)**, namely **Andreas Reiserer, Andreas Reuß, Andreas Steinbacher, Anja Krischke, Arthur Hipke, Bernhard Huber, Björn Gieseking, Carl-Friedrich Schleußner, Christian Dreher, Christian Kramer, Christian Rewitz, Christoph Schwarz, Christoph Stolzenberger, Dr. Cristina Consani, Dr. Dmitri Voronine, Fabian Ebert, Federico Koch, Florian Kanal, Dr. Florian Langhojer, Frank Dimler, Dr. Johannes Buback, Johannes Knorr, Marco Schmid, Dr. Martin Kullmann, Michael Förster, Dr. Monika Pawłowska, Nadja Bertleff, Ole Hüter, Dr. Philip Tuchscherer, Philipp Rudolf, Philipp Terberger, Dr. Pramod Kumar Verma, Sabine Keiber, Sebastian Götz, Sebastian Röding, Sebastian Schott, Simon Draeger, Stephanie Karg, Dr. Susanne Fechner, Dr. Tatjana Quast, Thomas Keitzl, Tom Bolze**, and **Dr. Ulrike Selig-Parthey**.

- my parents **Maria** and **Hubert** for their longstanding support, their encouragement, and for giving me free rein to do what I really enjoy doing.

- my girlfriend **Sabrina** for the countless beautiful and happy moments together, for her warmhearted nature, her support, and her love.